Luminescent and Conductive Hybrid Materials based on Nanoscale Metal-Organic Frameworks and (Bio)Polymers

Kumulative Dissertationsschrift zur Erlangung des akademischen Grades

Doctor rerum naturalium

(Dr. rer. nat.)

vorgelegt von

Moritz Maxeiner

aus Born (Hessen)

Institut für Anorganische und Analytische Chemie

Fachbereich Biologie und Chemie

Justus-Liebig-Universität Gießen

Mai 2025

1. Gutachter: Prof. Dr. Klaus Müller-Buschbaum

2. Gutachter: Prof. Dr. Bernd Smarsly

Eingereicht am: 14.Mai.2025

Eidesstattliche Versicherung

„Ich erkläre: Ich habe die vorgelegte Dissertation selbstständig und ohne unerlaubte fremde Hilfe und nur mit den Hilfen angefertigt, die ich in der Dissertation angegeben habe. Alle Textstellen, die wörtlich oder sinngemäß aus veröffentlichten Schriften entnommen sind, und alle Angaben, die auf mündlichen Auskünften beruhen, sind als solche kenntlich gemacht. Ich stimme einer evtl. Überprüfung meiner Dissertation durch eine Antiplagiat-Software zu. Bei den von mir durchgeführten und in der Dissertation erwähnten Untersuchungen habe ich die Grundsätze guter wissenschaftlicher Praxis, wie sie in der „Satzung der Justus-Liebig-Universität Gießen zur Sicherung guter wissenschaftlicher Praxis“ niedergelegt sind, eingehalten.“

Angaben zu auf künstlicher Intelligenz (KI) basierender Hilfen wie ChatGPT oder SchulKI von OpenAI oder Gemini von Google zur Erstellung meiner Dissertation (Zutreffendes angekreuzt):

☐ Ich habe bei der Erstellung dieses Textes kein KI-Tool verwendet.

☒ Ich habe ein KI-Tool in den folgenden Bereichen eingesetzt (Mehrfachnennungen möglich):

- ☐ Ideen finden, meine Kreativität anregen
- ☐ Verstehen von Konzepten, Recherche von Fakten und Definitionen
- ☒ Optimierung eines von mir verfassten Textes
- ☐ Erstellen ganzer Textpassagen nach meinen Vorgaben

Folgende KI-Tools habe ich verwendet, damit aufgeführte Teile meines Textes von dem Tool wie folgt profitiert haben:

Die sprachliche Überarbeitung aller Texte wurde mit Unterstützung der im Folgenden genannten KI-Werkzeuge durchgeführt.

ChatGPT (*OpenAI*)

JLUkiCHAT (*ki@JLU*)

DeepL Write (*DeepL SE*)

Datum: _____ Unterschrift: _____

Danksagung

Ich möchte an dieser Stelle allen voran **Prof. Dr. Klaus Müller-Buschbaum** meinen aufrichtigsten Dank aussprechen. Er hat mich auf das Herzlichste in seine Gruppe aufgenommen. Sein Engagement, seine wertvollen Ratschläge, seine Expertise und sein Feedback haben maßgeblich zum Gelingen beigetragen und mir stets weitergeholfen.

Meinem Zweitgutachter **Prof. Dr. Bernd Smarsly** danke ich für die Zeit und Mühe, die er in die Begutachtung meiner Dissertation investiert hat.

Für ihre Bereitschaft, der Prüfungskommission meiner Disputation anzugehören, danke ich **Prof. Dr. Richard Göttlich** und **Prof. Dr. Peter Friedhoff**.

Bei **Dr. Thomas Kasper** möchte ich mich in beruflicher als auch privater Hinsicht besonders bedanken. Egal ob MOFs, Spongebob's Quallen-Disco oder zusammen auf der Bühne als *Mayhem Freqs.*; es war immer ein Vergnügen mit dir Zeit zu verbringen.

Ein Dank gilt auch **Dr. Christian Würtele** und **Julian Burkhart** für die Korrekturlesung meiner Dissertation und ihrer ehrlichen Worte.

Ich danke allen **Kooperationspartner** und **Co-Autoren**, mit denen ich auf die gemeinsame Veröffentlichung von erfolgreichen Arbeiten zurückschauen kann.

Meiner Master-Studentin **Lea Wittig** und meinem Bachelor-Studenten **Murat Cuvalli** möchte ich für ihre verantwortungsbewusste und teilweise aufopferungsvolle Mitarbeit an meinen Projekten danken. Ihr habt sehr gute Erfolge erzielt und selbst sehr schöne Arbeiten verfasst.

Ich möchte mich herzlich bei der ganzen **Arbeitsgruppe** bedanken. Wir hatten eine schöne Zeit, sowohl an der Universität als auch außerhalb. Ja, ich bin mir bewusst, dass ich öfter dabei hätte sein können. Aber auch ein Biologie-Studium ist schließlich nicht von selbst gemacht.

Und zum Schluss möchte ich noch etwas sagen, was mir sehr am Herzen liegt. Denn ohne **meine Familie**, **Freundin** und **Freunde** wäre ich sicher nicht an diesem Punkt in meinem Leben angekommen. Die Auszeiten in meiner Heimat waren immer das perfekte Gegenstück zu meiner Zeit in Gießen.

Ganz sicher sind mir Menschen begegnet, die ich hier nicht erwähnt habe. Aber auch ihr sollt wissen, dass jede **Begegnung** mich zu dem gemacht hat, der ich jetzt bin. Dafür möchte ich mich bei euch allen bedanken.

„In der grossen Verkettung von Ursachen und Wirkungen darf kein Stoff, keine Thätigkeit isolirt betrachtet werden."

Alexander von Humboldt, 1807

„No pressure, no diamonds."

Bear Grylls, Never Give Up, 2022

Anmerkung meines sechsjährigen Ichs:

„Leb' deinen Traum, denn er wird wahr, geh' deinen Weg, stelle dich der Gefahr. Alles, was wichtig ist wirst du erkennen, wenn die Zeit gekommen ist, ja. Greif' nach den Sternen, du bist bereit. Glaub' an dich, bald ist es so weit. Wir werden bei dir sein. Sei bereit!"

Frank Schindel, Digimon Adventure, 1999

Abstract

This PhD thesis is centred around a unifying theme: the design and fabrication of hybrid materials that integrate nanoscale metal-organic frameworks (nanoMOFs) with (bio)polymers, targeting advancements in materials science and greener chemistry. A multi-faceted research approach has been applied to address this topic, with three main objectives: first, to synthesise nanoscale versions of bulk MOFs known from the literature; second, to develop nanoMOF@polymer hybrid materials with multi-level anti-counterfeiting mechanisms; and third, to synthesise environmentally friendly nanoMOF@biopolymer materials according to green chemistry principles. During the elaboration of the set scientific scope, all key objectives were successfully achieved, leading to notable achievements in the areas studied.

A surfactant-assisted bottom-up synthesis route has successfully produced nanoMOFs with enhanced photophysical and morphological properties compared to their bulk versions. Mixed-matrix-membranes (MMMs) and powders composed of lanthanide-containing nanoMOFs (nLn^{3+}-MOFs) and anthropogenic polymers (APs) have been developed, exhibiting multi-level anti-counterfeiting with interconnected properties, making them highly secure and difficult to replicate, thereby suitable for security-related applications. Aiming towards sustainability, developed nLn^{3+}-MOFs were combined successfully with biopolymers yielding biodegradable and recyclable MMMs, hydrogels and cryogels. These bio-based materials demonstrating high regeneration capacity and stability over multiple recycling steps, align with green chemistry principles.

Dispersibility and particle distribution benefit from the nanocharacter of nLn^{3+}-MOF particles, which is a critical requirement for stable and resilient hybrid materials. The visible (Vis= Eu^{3+}, Tb^{3+}) and invisible (NIR= Yb^{3+}) photoluminescence of developed nLn^{3+}-BDC (BDC^{2-}= benzene-1,4-dicarboxylate), together with the conductivity of the APs polystyrene sulfonate (PSS) and pyrolysed resorcinol-formaldehyde (pRF) were used to create an additive multi-level anti-counterfeiting. Each feature (Vis-light, NIR-light, conductivity) represents a certain level of security, while they are interconnected by optical and physical properties – changing one will inevitably change another of the levels. The materials developed are designed to be difficult to replicate for unambiguous marking of valuable goods. As materials science has to address sustainability to overcome environmentally relevant challenges in the future, APs have been replaced by biodegradable nature-based biopolymers agar and gelatine. Luminescent MMMs made from nEu^{3+}-BDC@biopolymers have been successfully recycled ten-times, while the red luminescence allows for the monitoring of the material's condition. Resilient nEu^{3+}-BDC in boiling water and freezing temperatures as well as water-based synthesis routes, render these materials suitable alternatives for AP-based hybrid materials.

Altogether: improved synthesis techniques, application-driven approaches and biodegradable alternatives enable the creation of advanced nanoMOF@(bio)polymer hybrid materials supporting anti-counterfeiting, sustainability and circular economy.

Kurzzusammenfassung

Diese Doktorarbeit behandelt das zentrale Thema: Design und Herstellung von Hybridmaterialien, die nanoskalige metall-organische Gerüstverbindungen (nanoMOFs) mit (Bio-)polymeren verbinden, um Fortschritte in der Material-wissenschaft und nachhaltiger Chemie zu erreichen. Ein vielschichtiger Forschungsansatz mit drei Hauptzielen wurde gewählt, um dieses Thema zu adressieren: erstens, nanoskalige Versionen von aus der Literatur bekannten MOFs zu synthetisieren; zweitens, nanoMOF@Polymer-Hybridmaterialien mit mehrstufigen Fälschungsschutzmechanismen zu entwickeln; und drittens, umweltfreundliche nanoMOF@Biopolymer-Hybridmaterialien nach den Prinzipien der nachhaltigen Chemie zu synthetisieren. Während der Bearbeitung des festgelegten wissenschaftlichen Rahmens, wurden alle gesetzten Ziele erreicht, was zu bedeutenden Erkenntnissen in den untersuchten Bereichen führte.

Durch einen Tensid-gestützten bottom-up-Syntheseweg wurden erfolgreich nanoMOFs mit verbesserten photophysikalischen und morphologischen Eigenschaften entwickelt. Mischmatrixmembranen (MMMs) und Pulver, die aus lanthanidhaltigen nanoMOFs (nLn^{3+}-MOFs) und anthropogenen Polymeren (APs) bestehen, wurden synthetisiert. Sie weisen mehrstufigen Fälschungsschutz mit ineinandergreifenden Eigenschaften auf, wodurch sie außergewöhnlich sicher und schwer zu replizieren sind, und sich somit für sicherheitsrelevante Anwendungen eignen. Um den Aspekt der Nachhaltigkeit zu berücksichtigen, wurden die entwickelten nLn^{3+}-MOFs erfolgreich mit Biopolymeren kombiniert, was zu biologisch abbaubaren und recycelbaren MMMs, Hydrogelen und Kryogelen führte. Diese biobasierten Materialien zeigen eine hohe Regenerationsfähigkeit und Stabilität über mehrere Recycling-Schritte hinweg, was im Einklang mit den Prinzipien nachhaltiger Chemie steht.

Die Dispergierbarkeit und Partikelverteilung profitieren vom Nanocharakter des nLn^{3+}-MOFs, welcher eine kritische Anforderung für stabile und widerstandsfähige Hybridmaterialien darstellt. Die sichtbare (Vis= Eu^{3+}, Tb^{3+}) und unsichtbare (NIR= Yb^{3+}) Photolumineszenz des entwickelten nLn^{3+}-BDC (BDC^{2-}= Benzol-1,4-dicarboxylat), zusammen mit der Leitfähigkeit der APs Polystyrolsulfonat (PSS) und pyrolysiertem Resorcin-Formaldehyd (pRF), wurden genutzt, um einen additiven mehrstufigen Fälschungsschutz zu kreieren. Jede Eigenschaft (Vis-Licht, NIR-Licht, Leitfähigkeit) repräsentiert ein bestimmtes Sicherheitslevel, während sie durch optische und physikalische Eigenschaften miteinander verbunden sind – die Veränderung einer Eigenschaft wird unvermeidlich die Veränderung einer weiteren zur Folge haben. Die entwickelten Materialien wurden so entworfen, dass sie schwer zu replizieren sind und eine eindeutige Kennzeichnung geschützter Güter ermöglichen. Da sich besonders die Materialwissenschaft mit Nachhaltigkeit auseinandersetzen muss, um zukünftige umweltrelevante Herausforderungen zu meistern, wurden APs durch biologisch abbaubare, naturbasierte Biopolymere, wie Agar und Gelatine, ersetzt. Lumineszente MMMs aus nEu^{3+}-BDC@Biopolymeren wurden erfolgreich zehnfach recycelt, während die rote Lumineszenz die Überwachung des Materialzustands

ermöglicht. Die Beständigkeit von nEu^{3+}-BDC in kochendem Wasser und bei Temperaturen unter dem Gefrierpunkt, sowie die wasserbasierten Syntheserouten qualifizieren diese Materialien als geeignete Alternativen zu AP-basierten Hybridmaterialien.

Insgesamt ermöglichen verbesserte Synthesetechniken, anwendungsorientierte Ansätze und biologisch abbaubare Alternativen, die Herstellung fortschrittlicher nanoMOF@(Bio-)polymer-Hybridmaterialien in den Bereichen Fälschungssicherheit, Nachhaltigkeit und Kreislaufwirtschaft.

Table of Content

Outline

This PhD thesis is concerned with the synthesis of luminescent nanosized lanthanide-containing metal-organic frameworks (nLn^{3+}-MOFs) and their functionalisation by combination with (bio)polymers as mixed-matrix-membranes (MMMs) or other hybrid materials such as hydrogels or cryogels. The materials are subject to analysis regarding their structural, photophysical and morphological properties, as well as their conductivity, chemical stability, and recyclability.

Chapter 1 provides an overview of the current state of knowledge regarding the research topic investigated in this PhD thesis. It introduces the structural composition of MOFs, unique photophysical properties of lanthanides and recent research topic-relevant applications of nLn^{3+}-MOFs. Furthermore, it introduces the concept of (bio)polymers, highlighting their distinctive structure and inherent conductivity, which are key features of the developed anti-counterfeiting hybrid materials. It also shades light on greener chemistry and sustainable approaches towards a circular economy in the field of materials science.

Chapter 2 concludes the theoretical introduction by outlining the research objectives and providing a graphical overview of what to achieve throughout this PhD thesis.

Chapter 3 is concerned with the presentation of scientific contributions that have been published with lead authorship in high-ranking scientific journals. Each subchapter represents a separate publication, while they are linked by the common theme: nLn^{3+}-MOFs and their functionalisation as hybrid materials by combination with (bio)polymers.

Chapter 3.1 presents a successful bottom-up synthesis of a total of nine novel nanoscale lanthanide-containing MOFs, namely nLn^{3+}-BDC, nDUT-5(Al):Ln^{3+} and nMOF-253(Al):Ln^{3+} (Ln^{3+}= Eu^{3+}, Tb^{3+}), employing a surfactant-assisted approach. The bulk Ln^{3+}-MOFs and nLn^{3+}-MOFs are subjected to a comprehensive comparative analysis with respect to their morphological characteristics and photophysical properties. The findings indicate a correlation between the photophysical processes and both, the particle size and the Ln^{3+}-linker pair, suggesting that the nanoMOFs represent an advancement over their bulk versions.

Chapter 3.2 outlines the incorporation of luminescent (Vis/NIR) nLn^{3+}-BDC (Ln^{3+}= Eu^{3+}, Tb^{3+}, Yb^{3+}) into conductive (PSS, pRF) and non-conductive (PSUd) matrices, resulting in the successful synthesis of nine novel hybrid materials. These materials cannot be easily replicated, as their distinctive features are not arbitrary and cannot be modified without affecting a second or even a third feature, thus acting as an anti-counterfeiting material with an interdependent multi-level structure. The principle has been demonstrated in a real-world scenario as a proof-of-concept experiment.

Chapter 3.3 addresses the environmental impact of nanoMOF-based hybrid

materials by combining the luminescent nEu^{3+}-BDC with the biopolymers agar and gelatine instead of anthropogenic polymers (APs). As MMMs, hydrogels and cryogels, nEu^{3+}-BDC@biopolymers demonstrate biodegradability and effective recyclability over ten reproduction cycles, while the red luminescence functions as an "on-the-fly"-status probe for the material's condition. Moreover, features such as the reversible deformability of agar cryogels exemplify the potential of biopolymer-based materials to compete with or surpass conventional technologies using APs.

Chapter 4 recaps the results presented in the published works by interpreting the results in the context of the set objectives and existing literature. It also links the findings that have been published separately and integrates these into a unified perspective, allowing a comprehensive conclusion to be drawn on the common thread of multifunctional nanoMOF-based hybrid materials.

Chapter 5 provides a summary of this PhD thesis and outlines the most important achievements with respect to the set research objectives. A short outlook gives ideas about the potential further development of presented achievements and materials.

Overall, the successful implementation of nLn^{3+}-MOFs in various (bio)polymers has opened up the vast field of hybrid material design with an exciting combination of properties, contributing to a more sophisticated, sustainable future beyond classic membrane technology.

1 Introduction

1.1 Lanthanides – the 4f element series

Lanthanides (Ln) are 15 elements with the atomic numbers 57 to 71 in the periodic table of elements, including the elements from lanthanum (La, 57) to lutetium (Lu, 71). The term 'lanthanide' is an old compound word consisting of the element lanthanum and the suffix *–ide* (usually denoting an anion), which is still used in parallel with the more recent term 'lanthanoid' (Greek: suffix -οειδής, (*–oid*) meaning 'similar to'), but also includes lanthanum in the International Union of Pure and Applied Chemistry (IUPAC) nomenclature.[1] Another common terminology used for the lanthanides is '4f-elements' and refers to their unique set of valence shell 4f-orbitals (together with the actinide's 5f-orbitals). The term 'rare earth elements' (REE) extends the terminology of the lanthanide series to include the elements scandium (Sc, 21) and yttrium (Y, 39), making them 17 elements that are considered 'critical' in terms of availability[2,3] (see **Figure 1**). It is important to note that the term 'critical' is not related to the abundance of REEs in the Earth's crust; rather, it is a reference to the challenging mining conditions and purification procedures, that result from the simultaneous presence of multiple REEs in the ores due to their ionic radii alike.[4] The similar ionic radii of REEs result in the formation of a multitude of minerals that each contain trace concentrations of multiple REEs. This renders the mining process costly and necessitates the implementation of sophisticated purification techniques.[4]

With a general electronic configuration of $[Xe]4f^n5d^06s^2$ as gaseous elemental atoms starting at La (n= 0) to Lu (n= 14)[5] the 4f-orbitals of lanthanides are progressively filled up with electrons through the 4f-series, with the energy-favoured exceptions La ($[Xe]4f^05d^16s^2$), cerium (Ce, 58; $[Xe]4f^15d^16s^2$), gadolinium (Gd, 64; $[Xe]4f^75d^16s^2$) and Lu ($[Xe]4f^{14}5d^16s^2$). Multivalent cations are formed during deionization from Ln^{2+} to Ln^{4+}, with Ln^{3+} being the most stable oxidation state. This stability is attributed to the overlapping of the diffuse very broad 5d-bands with the narrower 4f-bands, as indicated by the metal's band structure.[5] Due to the shielding effect of 5s- and 5p-

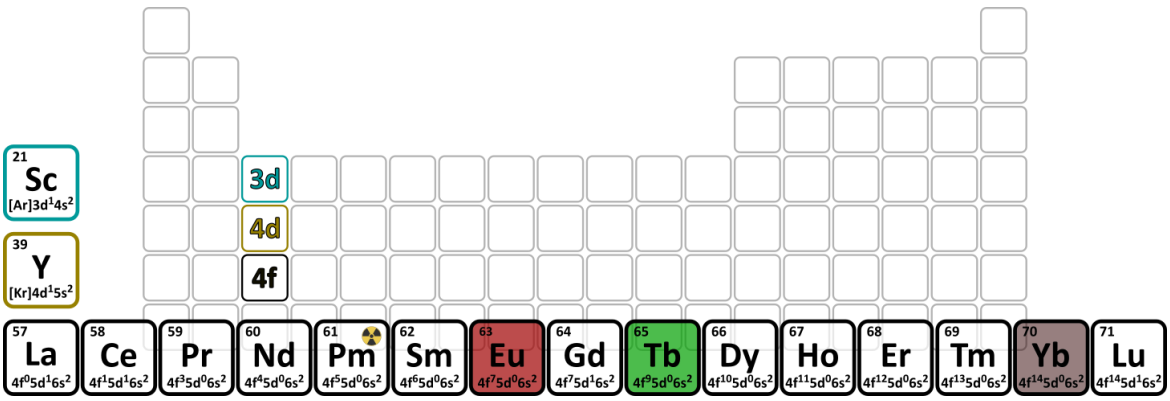

Figure 1. REEs with their corresponding valence shell electron configurations. Lanthanides of particular interest are highlighted in their typical photoluminescence (PL) emission colours (Eu^{3+}= red, Tb^{3+}= green, Yb^{3+} is depicted in brown to visualise emission in the near-infrared (NIR) region).

orbitals and a strong effective nuclear charge derived by the nuclei, the 4f-orbitals are minimally influenced by the coordination environment, resulting in their negligible participation in binding with adjacent molecules or ions.[5,6] Furthermore, it is observed that the ionic radii of the trivalent lanthanides decrease within the lanthanide series as a consequence of the poor shielding properties of the diffuse 4f-orbitals and the increasing nuclear charge. As a result, the 4f-orbitals are subject to an increasing effective nuclear charge - a phenomenon known as 'lanthanide contraction'.[5] The chemistry of lanthanides is notably alike across the entire 4f-series, largely due to the unique properties of the 4f-orbitals described above.

In solid state, the sesquioxides Ln_2O_3, also termed 'rare earths', represent one of the most stable oxides formed with Ln^{3+}. In particular, terbium (Tb, 65; along with praseodymium, Pr, 59) can form stable intermediates between LnO_2 and Ln_2O_3 with mixed oxidation states of +IV and +III, respectively.[7] The coordination behaviour of lanthanides in solution is predominantly governed by electrostatic interactions (mostly of ionic character), rather than covalent bonding, which can result in a coordination number (C.N.) of trivalent lanthanides of up to twelve per Ln^{3+}. The coordination behaviour is significantly influenced by the ionic radii, with larger Ln^{3+} ions forming complexes with higher C.N. than Ln^{3+} ions with smaller ionic radii.[8] A high C.N., together with a high *Lewis* acidity[9,10] makes Ln^{3+} ideal candidates for the coordination with multidentate chelates. Furthermore, Ln^{3+} ions are considered hard acids within the concept of 'hard and soft acids and bases' (HSAB).[8,11] Together with organic ligands, containing hard *Lewis* base functional groups, with O- and N-donors,[10] and a rigid aromatic backbone structure, lanthanides are highly suitable for the formation of multidimensional complexes.[12,13]

1.2 Photophysical properties of lanthanides

In general, the intensities of electronic transitions between defined energy levels (*e.g.*, the singlet vibronic fundamental level $S_{0,0}$ and the excited singlet vibronic level $S_{\varepsilon,v}$, with ε= electronic state and v= vibrational state) are dependent on transition probabilities, which in turn are described as the integral of overlapping wavefunctions $\psi(S_{0,0})$ and $\psi(S_{\varepsilon,v})$.[6] Moreover, the *Franck-Condon* principle[14,15] further defines the overlapping of $\psi(S_{0,0})$ and $\psi(S_{\varepsilon,v})$ as follows: the probability of a molecule transitioning from one electronic state to another is contingent on the compatibility of the vibrational part of the wavefunctions $\psi(S_{0,0})$ and $\psi(S_{\varepsilon,v})$, *i.e.*, the presence of a maximum at the same nuclear distance. Consequently, vibronic transitions are more probable in cases where the nuclear spacing remains constant. Hence, selection rules based on the principle of transition probabilities allow the prediction of how the transition will behave in terms of intensity. Mainly, two types of transitions play a role in lanthanide photoluminescence (PL) – electric dipole (ED) and magnetic dipole (MD) interactions, with the first one being many magnitudes more intense than the latter one. A third type of transition, the electric quadrupole interactions (EQ), are neglectable due to its relative low intensity compared to the others.[6]

The term symbol $^{2S+1}L_J$ defines energy states by means of quantum numbers. The spin

multiplicity $M = 2S+1$ (with $M = 1$: singlet, $M = 2$: doublet, ...; and S= total spin angular moment) is equal to the number of unpaired electrons (plus one) and its value at maximum for the lowest energy state, according to *Hund*'s rule.[6,16] The total orbital angular momentum quantum number $L = \Sigma(-(l-1), ..., -1, 0, 1, ..., (l-1), l)$, where l is the orbital angular moment with $l = 3$ for f-orbitals, describes the splitting into different terms starting at the electronic configuration of the element under discussion ($L = 0$: S, $L = 1$: P, $L = 2$: D, $L = 3$: F, continuing with the alphabet except for J). The total angular momentum quantum number $J = (|L-S|, ..., L+S-1, L+S)$ splits the terms further in levels caused by spin-orbit coupling, also called *Russel-Saunders* coupling,[17] while the coordination environment (also called ligand-field) further divides these levels into sublevels according to $2J+1$ depending on the local symmetry.[6] It needs to be considered that the most stable sublevel in a half-filled shell is the lowest possible J value and *vice versa*.

Lanthanides are subject to certain selection rules, first and foremost the 'parity selection rule' ($\Delta L \neq 1$). Here, ED interactions must cause a change in parity during an electronic transition and needs to be $g \leftrightarrow u$ (German: g= gerade (even), u= ungerade (odd)) with respect to a centrosymmetric centre as *Laporte*[18] describes. However, transitions between two f-orbitals are $u \leftrightarrow u$,[6,19,20] therefore violating *Laporte*'s rule, making ED f-f transitions 'forbidden'. Yet, f-f transitions may become partially allowed after mixing with parity-even d-orbitals during transition in a low symmetric coordination environment, called 'induced electric dipole' (IED) interactions. If the f-d-orbital mixing is occurring without the presence of a local inversion symmetry, transitions are also referred to as 'hypersensitive transitions'.[6,19] In contrast, MD interactions must not change in parity ($\Delta L = 0$) during an f-f transition, which makes them insensitive to the local environment.[6] Furthermore, the total spin angular moment S must not change since the overall spin of the system needs to be preserved during the transition. Consequently, this so-called 'spin selection rule' ($\Delta S = 0$) requires the multiplicity M to be constant during a transition between electronic states. However, *JJ'*-coupling starts to dominate over *Russel-Saunders* coupling due to a stronger spin-orbit coupling than interactions between spin-spin (SS) or orbit-orbit (LL) angular moments with an increasing nuclear charge per atom.[6] As consequence, spin-forbidden transitions become progressively more allowed with heavier atoms involved. By recalling the IED interactions, the *Judd-Ofelt* theory[21,22] further defines the selection rule for transitions of mixed states; if the transition holds $\Delta J = 2, 4, 6$ (if $J = 0$ or $J' = 0$, but only for $\Delta J \leq 6$) it is an allowed process, which may become weakened due to the described *JJ'*-coupling.

An additional phenomenon has an impact on the described 4f-5d orbital mixing and is called the 'nephelauxetic effect' (Greek: -νεφος (*-nephos*), meaning 'cloud' and -αυξάνομαι (*-auxanomai*), meaning 'expansion').[19] *Jørgensen*[23] described an expansion of orbitals upon interaction with a ligand. This results in reduced electron repulsion within the 5d-orbitals, leading to a favourable loss in energy. Therefore, transitions in lanthanides based on the 4f-5d orbitals, such as in divalent europium, are influenced by a shift between the corresponding energy levels in relation to the

coordination environment.[19]

Unique photophysical properties are provided by the special role of 4f-electrons throughout the lanthanide series, with the exception of La and Lu, which have empty ($4f^0$) and full ($4f^{14}$) 4f-orbitals, respectively, and therefore no electronic transitions between 4f-states appear. The emissive properties of lanthanide ions are defined by the possibilities to populate their excited states and to minimise the non-radiative deactivation pathways. If the energy gap between the excited state and the fundamental state is about the energy of non-radiative de-excitation processes (*e.g.*, O–H vibrations of water), the emission is partly quenched or completely quenched without emitting any light. Although Gd has only half-filled 4f-orbitals ($4f^7$), Gd only emits under harsh conditions due to its high-energy electron states. Gd is also known for its effective energy transfer to electron states of trivalent europium (Eu^{3+}) as an alternative non-radiative de-excitation pathway.[24] In contrast, the elements with the atomic numbers 63 (Eu), 65 (Tb), and 70 (ytterbium, Yb) show a sufficiently large energy gap to mostly avoid described quenching processes. Moreover, they are of particular interest due to their emission in the visible (Vis; Eu^{3+}, Tb^{3+}) and near-infrared (NIR; Yb^{3+}) wavelength region.[24–26]

Lanthanides are particularly noted for their PL when irradiated with ultraviolet (UV) light. However, PL depends not only on the lanthanide of choice, but also from its oxidation state and chemical environment.[19] The trivalent cations, Eu^{3+}, Tb^{3+} and Yb^{3+}, which exhibit the most stable oxidation state with $4f^n$, are characterised by their predominantly colourless appearance under daylight conditions,[8] but have the potential to show red (Eu^{3+}) and green (Tb^{3+}) emissions as well as emission in the NIR (Yb^{3+}) upon excitation by UV light. However, the PL of lanthanides is not readily available through direct 4f-4f excitation due to the parity forbidden 4f-4f transitions and very narrow absorption bands, which are giving very low molar absorption coefficients (typically, <3 M^{-1} s^{-1}).[24] Therefore, an UV light harvesting antenna ligand, possessing a conjugated π-system coordinated to the lanthanide, is necessary. Once the antenna ligand is excited, it transfers its energy to the lanthanide through a cascade of different energy transfer processes. In the best case, the lanthanide then loses its energy by emitting characteristic light. Non-radiative de-excitation processes may also take place at the same time, though, partly quenching the emitted light. Absorption of UV light followed by an energy transfer cascade to a lanthanide is known as the 'antenna effect' or 'sensitisation'.[19–22,27]

A simplified *Jablonski* diagram as well as an accompanying illustration, presented in **Figure 2**, gives an overview of the sensitisation process between an antenna ligand and Ln^{3+}. The diagram focuses exclusively on the most pertinent energy states and the most significant processes, accompanied by their respective lifetimes, while the 4f-4f-based excitation and emission of Eu^{3+}, Tb^{3+} and Yb^{3+} is presented in more detail. Electron states are set in relation to each other by means of empirically determined energies,[27] thus allowing the attribution of transitions between two different states. *Latva*[28] empirically defined the energy gap to be ideal with 2000 – 4000 cm^{-1} between the triplet donor state $T_{1,0}$ of the ligand and the excited acceptor state $^{2S+1}L_J^*$ of the

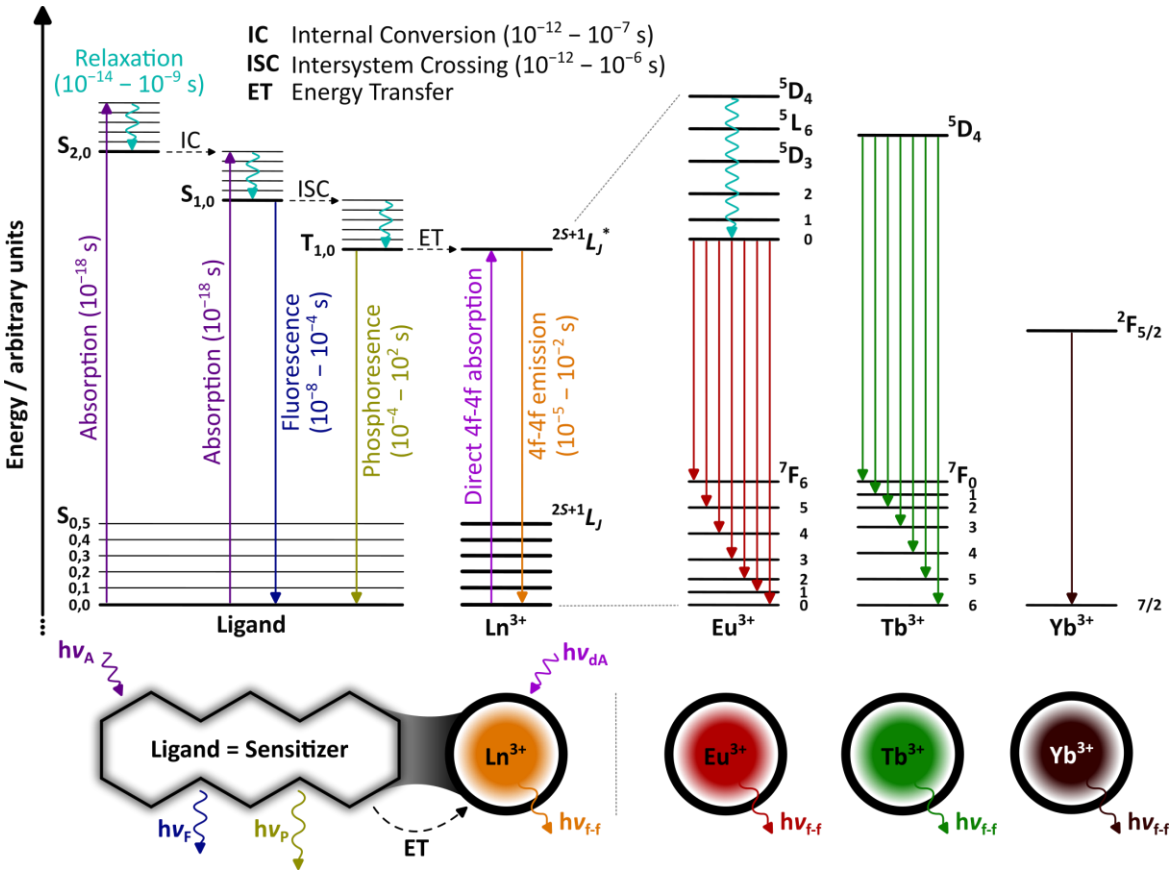

Figure 2. A simplified *Jablonski* diagram of Ln^{3+} (Ln^{3+}= Eu^{3+}, Tb^{3+}, Yb^{3+}) coordinated to a sensitising ligand, as demonstrated in a simplified representation of the sensitisation process. Photophysical processes are given with its characteristic lifetimes, with solid lines representing excitation (A= absorption, dA= direct 4f-4f absorption) and emission (F= Fluorescence, P= Phosphorescence, f-f= 4f-4f-based emission), dashed lines representing non-radiative processes, and turquoise waved lines representing vibrational relaxation. Relevant energy states of the ligand are denoted in vibronic terms $S_{\varepsilon,v}$ (singlet) or $T_{\varepsilon,v}$ (triplet), with ε= electronic state and v= vibrational state. Relevant Ln^{3+} 4f-energy levels are denoted with corresponding term symbols $^{2S+1}L_J$ with *S*= total spin angular momentum, *L*= total orbital angular momentum, and *J*= total angular momentum.

lanthanide at room temperature. The most efficient energy transfer occurs when energy is transferred between energy states within this energy gap, thereby avoiding energy back-transfer. In particular, it is not clear whether the energy transfer mechanism is *Dexter* energy transfer or *Förster* resonance energy transfer, given the short distance between the organic molecule and the lanthanide.[29] It was also observed that Ln^{3+} with $4f^n$ and $4f^{14-n}$ are 'spectroscopic twins'[6] as their energy levels behaving similar but in reversed order (*e.g.*, Eu^{3+}= $4f^6$ and Tb^{3+}= $4f^8$).

Absorption processes push electrons into excited vibronic states upon UV light irradiation as observed in organic ligands as π*←π transitions ($S_{\varepsilon,v}$←$S_{0,0}$) or, to a lesser extent, as direct 4f-4f absorptions in lanthanides ($^{2S+1}L_J$*←$^{2S+1}L_J$), with typical lifetimes of 10^{-18} s[30]. Upon vibrational relaxation (10^{-14} – 10^{-9} s),[31] isoenergetic non-radiative processes such as internal conversion (IC, 10^{-12} – 10^{-7} s)[31] or intersystem crossing (ISC, 10^{-12} – 10^{-6} s)[31] lead to transitions with constant multiplicity ($S_{2,0}$→$S_{1,v}$) or transitions where a spin-flip yields a triplet multiplicity ($S_{1,0}$→$T_{1,v}$), respectively. For vibrational relaxation is an extremely fast process, emission always occurs from the vibrational fundamental level.[19,32] Fluorescence (10^{-12} – 10^{-7} s)[30,32] describes the rapid

radiative emission process of $S_{1,0} \rightarrow S_{0,v}$. The radiative processes $T_{1,0} \rightarrow S_{0,v}$ and $^{2S+1}L_J^* \rightarrow {}^{2S+1}L_J$ are referred to as phosphorescence (10^{-5} – 10^{2} s)[30,32] and 4f-4f-based emissions (10^{-5} – 10^{-2} s),[30,32] respectively, and appear to be slower than fluorescence due to required spin-flip processes during the de-excitation.

1.3 Luminescent nanoscale metal-organic frameworks

Reticular chemistry is a field that focuses on the design and synthesis of complex molecular frameworks using the principles of connectivity and modularity. It primarily involves the assembly of small building blocks by a combination of organic molecules (called linker or ligand) and inorganic cations or clusters (called inorganic building unit, IBU), into larger structures through various interactions like covalent binding, coordination binding, or hydrogen binding.[33–37] Amongst others such as covalent organic frameworks (COFs),[35] this approach has also led to the discovery of coordination polymers (CPs).[35,36] CPs consist of repeating entities in one, two, or three dimensions. The development of metal-organic frameworks (MOFs) was eventually initiated by thinking in three dimensions, first published by Omar M. Yaghi in 1995.[38] Despite efforts to standardise MOF nomenclature, there are multiple concepts for naming MOFs. These include naming after the eponymous research institutes, the IBU-linker combination, or numbering them consecutively as MOF-XXX, which makes it hard to get information only from the nomenclature. It should also be noted that one MOF with a certain crystal structure may have multiple names.

A MOF is defined as a three-dimensional coordination network constituted of inorganic and organic building blocks, constructed in accordance with principles of lock-and-key mechanisms. The three-dimensionality is the result of connected subunits by a combination of multivalent metal cations or metal clusters with multidentate organic ligands. The modularity in designing these subunits allows for the creation of highly tuneable structures. The subunits are arranged in three dimensions with well-ordered repeating patterns, yielding often high crystallinity with a constant ratio of constituents. Consequently, each MOF exhibits an inherent microporous (pore size: <2 nm), mesoporous (2 – 50 nm) or macroporous (>50 nm) pore system, depending on the selected linker and metal cation/cluster combination.[39] Those porous networks possess two distinguishable surfaces: an outer surface describing the outbound interface of MOF to the surrounding medium (*e.g.*, to a solvent), and an inner surface describing the inbound interface of a volume confined by the subunits within the crystal structure of a MOF. The outer surface can be modified to alter dispersion behaviour, solubility or interactions with other materials,[35] while the inner 'active' surface becomes accessible *via* pore channels made up by the IBU-linker framework after a process called 'activation', and is subject to various sorption applications as outlined in more detail later in this chapter. A MOF is heated to an elevated temperature (usually under reduced pressure) with the objective of removing adsorbents that occupy the inner surface, most often solvent molecules, to give a wide range of accessible BET (*Brunauer-Emmett-Teller*) surface areas from a few $m^2\,g^{-1}$ up to 7000 $m^2\,g^{-1}$. It should be noted that adsorbents must

enter the pore channels through pore windows, giving the MOF structure an intrinsic molecular filter function dependent on the pore window size.[33–35,37,38,40,41]

The pursuit of enhancing MOF properties entails more than just selecting the best IBU and linker combination. MOFs with crystallite sizes in the nanometre range, so-called 'nanoMOFs' or short 'nMOFs', combine size-related advantages (*i.e.*, higher outer-to-inner surface ratio and better dispersibility)[42] with the described properties of their bulk counterparts. The outer surface area of nanoMOFs is significantly larger (as commonly known for nanoparticles), while the inner surface area remains almost unchanged but with the advantage of far better accessible pores than in bulk MOFs. For instance, a nMOF-74(Yb)[43] ($^{\infty}_{3}$[Yb(btc)], with btc^{3-}= benzene-1,3,5-tricarboxylate) exhibits an improved adsorption behaviour due to the smaller crystallite size. The smaller the crystallite size of a MOF the shorter are the pore channels, hence the diffusion pathway of adsorbents become shorter, and the pores become better accessible. Besides, monodispersed particles of nanosized copper (Cu)-BTC[44] MOF demonstrates increased dispersibility, which eases the synthesis of nanoMOF-based hybrid materials, which have thus far been inaccessible using their bulk counterparts. The formation of stable dispersions can be attributed to two key factors. Firstly, the presence of smaller particles, which are less susceptible to sedimentation processes. Secondly, a more reactive outer surface, which facilitates increased interactions with the surrounding environment.[45]

Guided synthesis routes are used to produce nanoMOFs by controlling the crystal growth process. These routes involve physical conditions (*e.g.*, temperature) and/or additives, particularly surfactants.[37,45] The term 'surfactant' is a combination of the words 'surface-active agent', which clearly identifies the surface as the site of action. Their amphiphilic nature drives them to self-assemble in solutions, making them useful for template-guided synthesis routes. For instance, crystal growth is controlled by polymers or micelle-forming detergents, such as polyvinyl pyrrolidone (PVP)[46] or cetyltrimethylammonium bromide (CTAB),[40] respectively, creating confined spaces allowing only a limited amount of educts to react within these spaces. In addition, surfactants can also act as templates that influence the particle morphology, so that a PVP-guided MOF-5 grows particles in cubic and in octahedral shape.[40,46] Further examples have been reported, where CTAB-guided synthesis routes yielded MOF nanorods of HKUST-1(Cu) (*Hong Kong University of Science and Technology*, $^{\infty}_{3}$[$Cu_3(btc)_2(H_2O)_3$]).[40,45] Another approach used to synthesis nanoMOFs is called 'reverse microemulsion', where micelle-forming surfactants are dispersed in an aqueous phase and an organic phase, thereby again forming confined spaces by means of polarity.[47] However, once nanoMOFs are formed, the surfactants are usually needed to prevent particle agglomeration/aggregation, thereby remaining on the MOF's surface and effecting MOF properties. Although micelle-formation is a dynamic process, the BET surface area decreases in the presence of CTAB, since the pores are less accessible due to the coverage of CTAB onto the MOF outer surface, as observed for a nanosized Cu-BTC.[45] Moreover, ionic surfactants can compete with the linker for coordination sites, making the choice of surfactants important when using a

surfactant-guided synthesis approach.[45]

Given the virtually unlimited possibilities for combining linkers and IBUs to porous networks, one approach for choosing proper combinations utilises the previously discussed concepts of *Pearson*[11] and *Lewis*.[10] For instance, the inorganic *Lewis* acids aluminium (Al^{3+})[48–50] or Ln^{3+} (*e.g.*, Ln^{3+}= Eu^{3+}, Tb^{3+}, Yb^{3+})[34,51–56] in combination with the organic *Lewis* bases benzene-1,4-dicarboxylate (BDC^{2-}),[33–35,46,50–54,57–63] 1,1'-biphenyl-4,4'-dicarboxylate ($BPDC^{2-}$)[33,35,48,51–53,61,63,64] or 2,2'-bipyridine-5,5'-dicarboxylate ($BPyDC^{2-}$)[38,49,52,53,59,60] yield archetype bulk MOFs well known in literature (see **Scheme 1**). The simplicity, structural similarities, good accessibility, multidentate carboxylate groups and easy handling of BDC^{2-}, $BPDC^{2-}$ as well as $BPyDC^{2-}$ make them ideal linkers for MOFs. The presence of guest molecules (*e.g.*, solvent or water molecules), either coordinated to a metal site[34,48,49,51] or captured in the MOF's pore system by *van der Waals* interactions, is commonly observed.[44,52,53,59,61–66] Sometimes, import and export of guests into the pores causes the MOF structure to reversibly expand and contract, so called 'breathing',[57] as observed for the MIL-53(Al) (*Matériaux de l'Institut Lavoisier*, $^{\infty}_{3}$[Al(OH)(bdc)]).[50] The loading of the pore system is principally governed by diffusion, which is delineated as 'movement along a potential gradient' (*i.e.*, the concentration of the guest). *Fick*'s first law,[67] which relates the concentration gradient to a temperature-dependent diffusion coefficient, provides a mathematical description of this phenomenon. Given that ions are charged objects, parameters such as electric charge and electron mobility must be taken into account, as elucidated in the *Einstein-Smoluchowski* relation.[68,69] The 'host-guest interactions' can be tuned by increasing the linker backbone length, as demonstrated with $BPDC^{2-}$ compared to BDC^{2-}, which in turn impacts the crucial pore window size at which guests enter the pores. Alternatively, the addition of a higher number of potential coordination sites (*i.e.*, N-donors), as demonstrated with $BPyDC^{2-}$ compared to $BPDC^{2-}$, is a further option to consider.[33,34,57] It has been demonstrated that the crystal structure of a MOF can be further tuned by the use of different IBUs.[34–37,40,41,54,58,70]

For instance, Al^{3+} comes with empty 3s and 3p orbitals, which allows the formation of three coordination bonds per Al^{3+}, as observed in DUT-5(Al)[48] (*Dresden University of Technology*, $^{\infty}_{3}$[Al(OH)(bpdc)]) or MOF-253(Al)[49] ($^{\infty}_{3}$[Al(OH)(bpydc)]) with both crystal structures shown in **Figure 3**. Alternative examples utilise Ln^{3+}ions owing to their

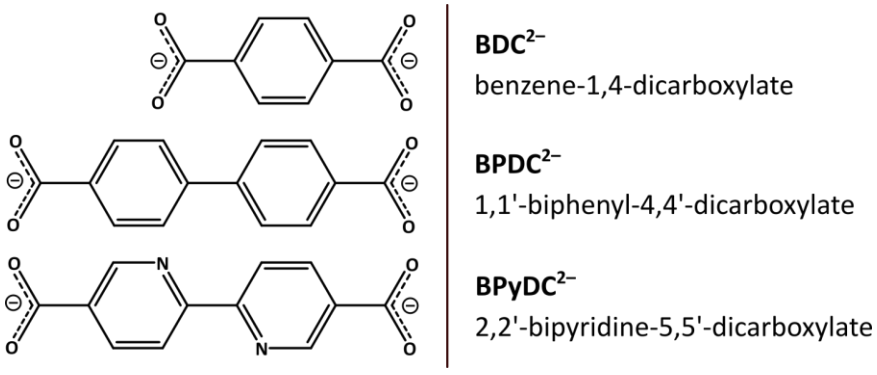

Scheme 1. Selected multidentate aromatic linkers of archetype MOFs well known in literature.

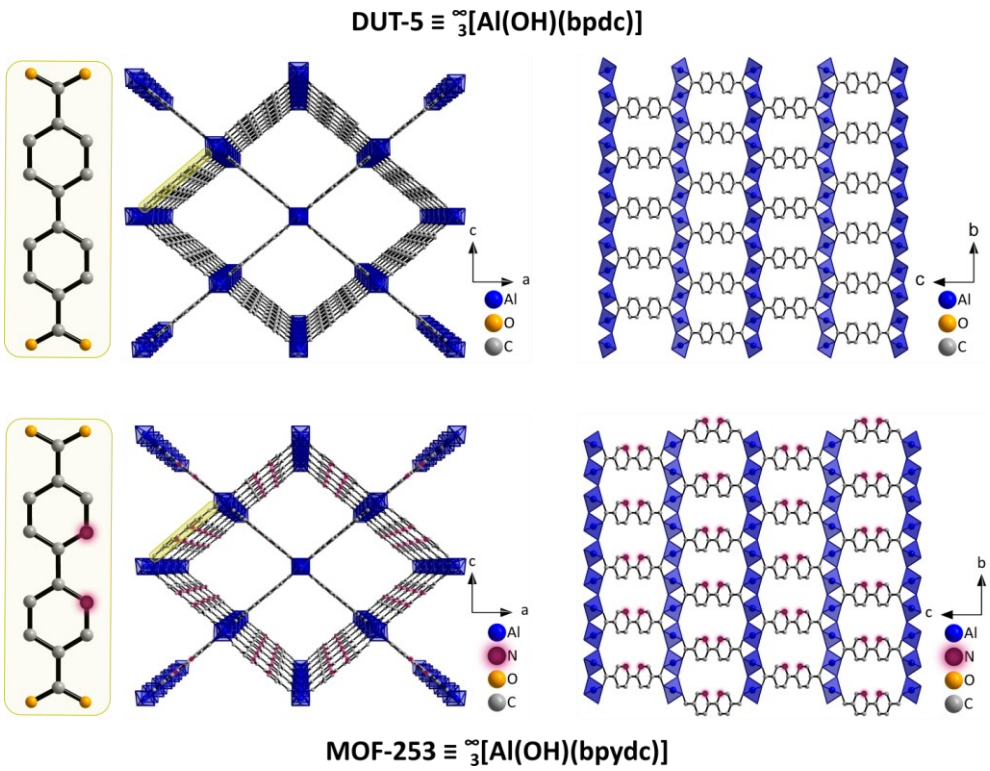

Figure 3. The crystal structures of isostructural DUT-5(Al) (top) and MOF-253(Al) (bottom) are displayed here, with the viewing directions indicated along the a-axis (right) and the b-axis (left). The yellow boxes present the linkers $BPDC^{2-}$ of DUT-5(Al) (top left) and $BPyDC^{2-}$ of MOF-253(Al) (bottom left) in enlarged excerpts. Colour code: blue (aluminium), violet (nitrogen), orange (oxygen), grey (carbon). Hydrogen atoms are omitted for clarity.

ability to form multiple coordination bonds at each metal centre. In the case of Ln^{3+}-BDC, this results in a C.N. of eight. Since there are no consistent rules for naming MOFs, the definition of Ln^{3+}-BDC is ambiguous as it is considered to describe at least two different modifications of the same IBU-linker combination as shown in **Figure 4**, namely $^{\infty}_{3}[Ln_3(bdc)_{4.5}(dmf)_2(H_2O)_3]$[34] and $^{\infty}_{3}[Ln_2(bdc)_3(H_2O)_4]$.[51] Among other reported cases,[45,50,52,53,71] these selected Ln^{3+}-MOFs clearly demonstrate the need to consider IBU-solvent interactions during MOF formation.

As the unique luminescence of lanthanides is provoked by the organic ligand *via* sensitisation, Ln^{3+}-MOFs containing one or more lanthanides emit light in the Vis and NIR region.[72] Typical red (Eu^{3+}-MOF,[73–77] trivalent samarium (Sm^{3+})-MOF[73,75]), green (Tb^{3+}-MOF),[74,75,77] blue (Ce^{3+}-MOF[74,75]), or NIR emission (Yb^{3+}-MOF,[75] trivalent erbium (Er^{3+})-MOF[75,78], trivalent neodymium (Nd^{3+})-MOF[75,79]) have been observed. Since Gd^{3+} emits light in the UV if any,[73] the linker-based emission of Gd^{3+}-MOFs is detectable, allowing the energy of the donor state $T_{1,0}$ responsible for the energy transfer to the lanthanide to be determined (*cf.*, Figure 2).[72] Linker-based emission is also employed in conjunction with Ln^{3+} emission in optical thermometers,[80] utilising the temperature-dependent emission shift. While the temperature-dependent change in linker emission can be rationalised by the reduced availability of vibrational degrees of freedom for excitation at low temperatures, the influence of temperature on the energy transfer from linker to lanthanide remains to be fully elucidated.[81] It was observed, however, that an incomplete energy transfer to a lanthanide ion can be indicated by the presence of linker-based emission in the PL spectrum.[70] A mixture of

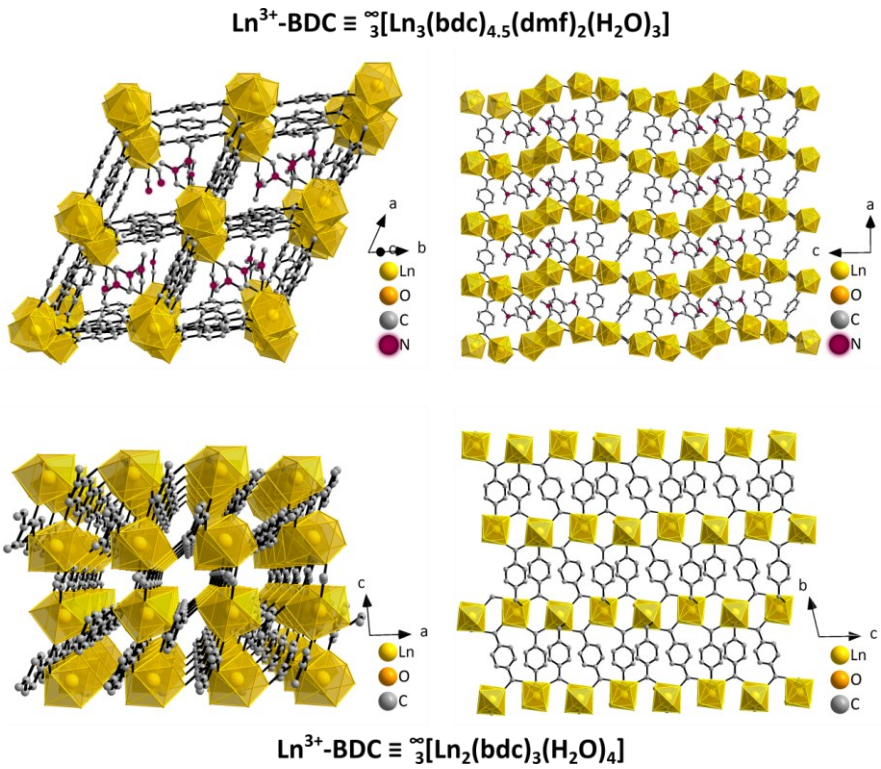

Figure 4. An overview of the crystal structures of two solvent-dependent modifications of Ln^{3+}-BDC, displaying their structural intricacies under various viewing directions. Colour code: yellow (lanthanide), violet (nitrogen), orange (oxygen), grey (carbon). Hydrogen atoms are omitted for clarity.

light emitting lanthanides results in an overall emission tuneable by means of the ratio of used amounts of lanthanide, often applied in ratiometric assays (*e.g.*, overall emission of orange to yellow for a Eu^{3+}/Tb^{3+}-MOF).[74,77] The principle is also applicable to Vis/NIR emitter mixtures, as demonstrated in Eu^{3+}/Eu^{2+}-MOFs.[76]

While qualitative PL spectra describe the emission colour of lanthanides, PL can be quantified by means of PL quantum yield (PLQY). PLQY is defined as the ratio of the number of photons emitted to the number of photons absorbed by a system. Put simply, what percentage of energy is converted into light, ranging from 0% to 100%. Besides the energy transfer processes described, additional non-radiative processes compromise the energy conversion to light, such as vibrational relaxation or heat generation (*cf.*, Figure 2). It is important to note that PLQY is dramatically reduced for lanthanides due to the forbiddance of 4f-4f transitions. However, the antenna effect can relativise the loss to a certain extent. Hence, common PLQYs of Ln^{3+}-MOFs are located at 10 – 50% in solid-state.[82] Only few exceptions are known, showing PLQYs up to 93%, as observed for $^{\infty}_{3}[Tb(H_2O)_3(hl)]$ (with hl^{3-}= 5,5'-(pyridine-2,5-diyl)-diisophthalate).[77]

When taking all the described properties into account, MOFs are highly versatile compounds with tuneable functions making them excellent materials for applications ranging from gas storage[61,65] and separation[62,63,71] to catalysis[43,44,60,64] or drug delivery,[58,59,66] and many more.[41] Together with the unique photophysical properties of lanthanides, Ln^{3+}-MOFs show even higher functionality and therefore have been intensively studied as potential sensors,[52,53] anti-counterfeiting materials,[55,56] or luminescent tags in bioimaging applications.[54,58,59] The present PhD thesis explores

the synthesis design of nLn^{3+}-MOFs, employing surfactants to yield suitable, functional materials. These materials are intended for application in the development of hybrid materials.

1.4 Hybrid materials based on (nano)MOFs and (bio)polymers

Following their conception by natural processes, hybrid materials are widely defined as those materials comprising a minimum of two constituent components that are blended at the molecular level. Hybrid materials are classified by means of interactions between the blended moieties: either weak physical interactions such as *van der Waals*, H-bonding or ionic bonding (class I); or strong chemical interactions such as coordinative or covalent bonding (class II).[83] In order to define hybrid materials more precisely, two terms need to be introduced: 'matrix' and 'additive' (with the latter sometimes called 'filler'). The matrix consists of compounds of an organic or inorganic nature, often forming amorphous or crystalline networks capable of hosting the second component. The additive, in fact, is usually composed of molecules, particles, or fibres of organic or inorganic nature. The combination of the matrix and the additive gives rise to a number of distinct properties – the huge advantage hybrid materials are bearing. In most cases, these properties can be attributed either to one of the two components or both. Furthermore, properties originate from one of the two components may be altered under the influence of the properties of the second component. Perhaps most significantly of all, the combination of matrix and additive can result in the creation of completely new properties.[72,83,84] Moreover, reducing the size of one component to the nanoscale allows for more homogeneous materials, since the dispersibility benefits from the smaller particle size.[83,85] **Figure 5** provides a schematic overview of the concept of hybrid material design. It should be noted that the selection of additives and matrices is arbitrary and does not imply completeness. In literature, hybrid materials are often appointed with an '@' between the additive and the matrix (additive@matrix), signifying the association of the two.

Out of almost infinite combinations possible using the described design approach, mixed-matrix-membranes (MMMs)[84] consist of film-forming organic polymers as a matrix (*e.g.*, polyimide (PI)[85]) with embedded organic or inorganic materials, or a combination of both, such as MOFs (MOF-MMMs). Hybrid materials of this kind demonstrate excellent performance in gas sorption and separation, while also

Figure 5. An overview of the concept of hybrid material design, which involves the combination of various additives and matrices. It should be noted that this overview does not imply the completeness of additives and matrices used for hybrid material synthesis, as only selected examples are given.

exhibiting mechanical and thermal stability[84–87] – properties contributed from both the MOF and the polymer. In general, polymers are highly relevant in all kinds of industries and being a vital part of modern life with a wide range of applications. Depending on the field of application, polymers can display significant properties such as low density, chemical resistance, electrical and thermal insulating behaviour, or mechanical stability. In addition, the processing of polymers is rapid and energy-efficient.[83] Apart from gas sorption and separation, PL of Ln^{3+}-MOF@matrix MMMs has been the subject of numerous publications in fields such as sensorics[87,88] or anti-counterfeiting applications.[77,89,90] However, it is rarely observed that the matrix has a role other than the described properties in MMMs. Only a few cases are reported in literature, where the polymer adds features such as conductivity for electronic functionalisation purposes in MMMs.[91–94] To pave the way for the creation of even more sophisticated hybrid materials, the matrix should contribute properties beyond classic membrane technology, in addition to its chemical and mechanical durability.

A key objective in Ln^{3+}-MOF-MMM research is to explore the potential of utilising electric current as an alternative energy source to UV light.[95] However, two major drawbacks need to be overcome in the future: (I) MOFs are mostly insulators, so the polymer needs to be electrically conductive, and (II) the electrical charge needs to be transferred from the conductive polymer to the Ln^{3+}-MOF (equivalent to an energy transfer from the antenna ligand to the metal site using UV light). Potential matrices conducting electricity have conjugated sp^2-hybridised carbon (C) atoms or are doped by either electron poor (p-type) or electron rich (n-type) atoms.[95,96] So far, conductivity is currently tuned by dopants such as iodine (I_2).[97] The mechanism of charge transport in conductive polymers is described as 'hopping' of charge carriers, which is influenced by temperature.[98] Consequently, the *Mott*-model identifies two key factors – the '*Boltzmann* factor' and the 'tunnelling factor' – which have been described in detail mathematically.[98,99] The interest in conductive polymers peaked with a Nobel Prize in Chemistry "[...] for the discovery and development of conductive polymers [...]" in 2000.[100] Among other techniques, the electrochemical impedance spectroscopy (EIS) gives access to quantify conductivity.[101] Impedance can be described as a complex number, with both a real part (resistance) and an imaginary part (reactance). Resistance is the opposition to current flow in a purely resistive material, and it is independent of the frequency of the applied signal. Conversely, reactance is frequency-dependent and accounts for the effects of inductance and capacitance, which cause the current to lag or lead the voltage. The impedance, therefore, combines both resistance and reactance to describe how much the material resists or impedes the current. The results are typically presented in a *Nyquist* plot by plotting the real part of impedance against the imaginary part of impedance in ohmic units.[102] It is crucial to emphasise that the real part is the only relevant component for conductivity calculations, as this ensures direct access to the resistance value from the *Nyquist* plot. As the electrical resistance is directly proportional to the length (or thickness) of the MMMs under consideration, the MMMs should be as thin as structural stability, additive particle size and the polymer-based

electron conduction path will allow in order to achieve the highest possible conductivity.

In general, MOF-MMMs show limited conductivity, with only a few exceptions reported for special linker design or MMM post-modification. For instance: a cadmium (Cd)-MOF:I_2@PVP-PVDF (with PVDF= polyvinylidene fluoride)[97] shows 10^{-4} S cm^{-1} after I_2 doping. Thanks to a special metallocene-like sandwich structure, a zirconium (Zr)-FDC@chitsoan (with FDC^{2-}= ferrocenyl dicarboxylate)[103] exhibit increased conductivity of 10^{-2} S cm^{-1}. Whereas a ZIF-8(Zn)@NPC (zeolitic imidazolate frameworks, $^{\infty}_{3}[Zn(im)_2]$, with Zn= zinc, im^-= imidazolate and NPC= nanoporous carbons)[104] gives 10 S cm^{-1} due to a biased growth orientation yielded from electrospinning, evidently, has the potential to enhance conductivity to a considerable degree. Concurrently, the MOF contributes to the porosity and associated properties of the hybrid material, which are characteristic of a MOF's three-dimensionality, albeit with reduced conductivity due to its insulating nature.

Besides the application-driven designing of hybrid materials, the focus should also include the promotion of long-term reusability, as opposed to a single-use approach, to also address sustainability. Within the concept of sustainability, the term 'circular economy' refers to the reduction of waste, the reuse of materials and the recycling of products. **Figure 6** gives an overview what the process of designing sustainable hybrid materials needs to address.[105] However, only a few publications have taken the principles of a circular economy into account when developing hybrid materials, for instance, a five-time recycled MOF@polyurethane membrane, albeit lacks biodegradability.[106] Moreover, the term 'high-quality (HQ) recycling' refers to the process of avoiding the use of pristine material in the recycling process. Instead, the material obtained from the recycled product is used to fabricate an exact replica of the product at the start of the recycling process.

The prevalence of anthropogenic polymers (AP) in nature-based alternatives is evident across diverse industrial sectors, attributable to their expeditious, cheap and large-scale synthesis. Concurrently, the global recycling rate of APs exhibits stagnation, attaining a mere 10% (35.5 million tonnes per year).[107] Furthermore, there are significant consequences of releasing APs into nature, whether intentionally or unintentionally, which must not be ignored. The beneficial properties of APs, including chemical inertness and stability as described above, must be considered in the

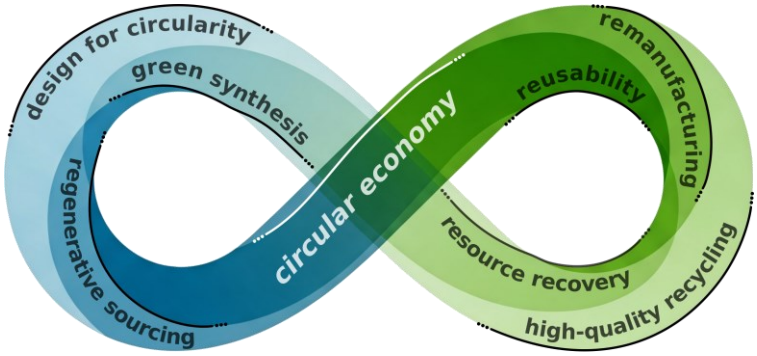

Figure 6. An overview of aspects defining circular economy with focus on materials science. It should be noted that this overview does not imply completeness but highlights certain aspects.

context of the potential risks to the flora, fauna and water bodies in the environment. The United Nations (UN) has published a risk assessment of chemicals related to the production of APs in 2023.[108] The aforementioned assertions are reinforced by the published UN report, which underscores the necessity for immediate action. Several publications addressed the urge for more sustainable MOF hybrid materials by introducing polysaccharides or polypeptides as biodegradable matrices, so called 'biopolymers'.[109] Reports have been made not only of luminescent biodegradable (bio)-MOF-MMMs such as Eu-BTC@cotton[110] films, or bimetallic manganese (Mn)Zn-MOF@starch nanoparticles[111] but also of multifunctional gels, as represented by magnetic UiO-66(Zr)@agarose (*Universitetet i Oslo*, $^{\infty}_{3}[Zr_6O_4(OH)_4(bdc)_6]$) particles.[112] While the environmental benefits of biodegradability are clear, there are potential drawbacks for specific applications: a constant trade-off exists between durability and stability on the one hand, and biodegradability on the other hand in the event of material release into the environment. When speaking of MOFs, it is particularly important to consider the toxicity of IBU and linkers separately for risk assessment. Therefore, the selection of additive and matrix for bio-based hybrid materials is contingent on factors such as water solubility, pH and temperature stability, or resistance against UV light along with other environmental stressors. It is important to note that conditions in the laboratory often do not accurately reflect real environmental conditions. Notably, chemical processes carried out by microorganisms (*e.g.*, aerobic/anaerobic respiration or digestion) or elevated ion concentrations in seawater differ significantly from those found in demineralised water, which is typically used in laboratory settings. Consequently, the development of non-harmful bio-based hybrid materials will necessitate a risk assessment based on substrates obtained from nature, which should be implemented in experimental procedures. This PhD thesis is pioneering as there are no other published HQ recycling of nanoMOF-based hybrid materials using biopolymers. It delivers crucial data on an increasingly important topic and is a significant addition to the field.

2 Research Objectives

The following paragraphs set out the progression chapter by chapter: from the synthesis of nanoMOFs; to a combinatorial approach for multifunctional nanoMOF@polymer hybrid materials; to biodegradable nanoMOF@biopolymer alternatives. The utilisation of nanoMOF-based hybrid materials is discussed in the context of anti-counterfeiting, with subsequent development towards greater sustainability. A graphical overview of the set research objectives is presented in **Figure 7**.

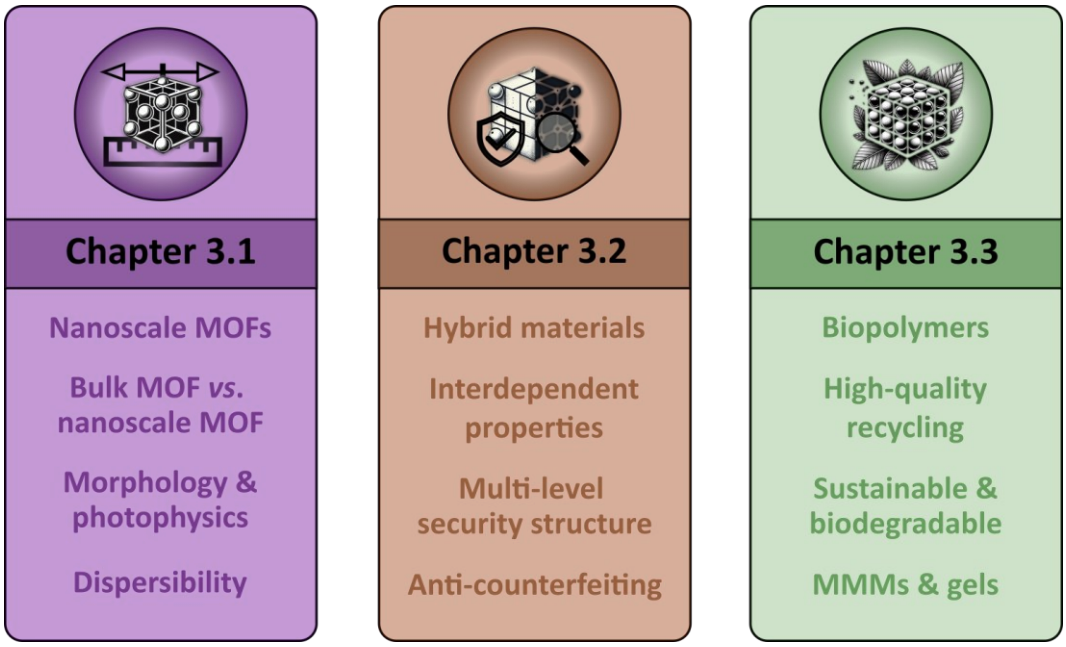

Figure 7. Chapter-wise overview of the research objectives to be achieved. Keywords are defined as the most significant aspects related to the research conducted within the designated chapter, without excluding other aspects investigated.

In general, nanoparticles offer a number of distinct advantages, including enhanced dispersibility and an increased surface-to-volume ratio in comparison to their bulk counterparts.[42] However, it should be noted that a reduction in particle size can result in an increase in surface energy, which may potentially lead to undesirable processes such as particle agglomeration/aggregation.[42] **Chapter 3.1** seizes the idea of particle size reduction and its application to literature-known luminescent Ln^{3+}-containing archetype bulk MOFs. The central questions guiding this investigation are whether the synthesis of nanoMOFs can be achieved with controllable particle sizes by employing a bottom-up surfactant-based strategy, and how the size of lanthanide-containing MOFs impacts their photophysical and morphological properties. Following this, it is recommended that the yield is scaled up. In addition, the work addresses the question of whether the insertion of lanthanide ions during synthesis or post-synthetically exerts an influence on the properties of nanoMOFs. In this regard, it is also worthwhile investigating whether the choice of lanthanide makes a difference on the particle size and *vice versa*. All aspects will be discussed in relation to their bulk counterparts.

In view of the remarkable photophysical properties and enhanced dispersibility of nanoMOFs in comparison with their bulk MOF counterparts, **Chapter 3.2** proposes a combination of luminescent nanosized MOFs with conductive APs as multifunctional hybrid materials. It is suggested that the potential for multifunctionality may be able to be organised in a way that creates a multi-level structure, where each level would be defined by a specific property. The intention is that these levels (= properties) should be interconnected, with the aim of ensuring that the multi-level design is not only an additive approach, but also very difficult to imitate. In order to achieve this, it is necessary to consider both visible and hidden properties for the naked eye, while the material design should allow for tuneable interdependency of the properties. The intended outcome of this work is to integrate optical and electronic characteristics to achieve the described multi-level structure design provided by nLn^{3+}-MOF@polymer hybrid materials for a highly secure anti-counterfeiting. It is anticipated that the synthesised hybrid materials will benefit from the size-related photophysical and morphological features of nanosized Ln^{3+}-MOFs. As Ln^{3+} emits light in the Vis and NIR (invisible to the naked eye) wavelength regions upon excitation, PL is going to be investigated as a visible/invisible security feature in anti-counterfeiting hybrid materials. While polymers are mostly used as matrices due to their mechanical stability, chemical resistance and other properties described in Chapter 1.4, this work aims on the introduction of conductive polymers, providing an additional hidden security feature as conductivity is also invisible to the naked eye. In order to investigate the conductivity of MMMs, a new setup needs to be developed.

Nowadays, the presence of non-biodegradable APs continues to inflict considerable harm upon the natural environment, as their incorporation into our daily lives has not been accompanied by adequate recycling initiatives.[107] This situation is mainly driven by single-use plastics in a wide range of sectors. Tackling this problem requires a multi-sectoral, multidisciplinary approach to achieve the most appropriate solutions. **Chapter 3.3** tentatively employs an interdisciplinary strategy that combines synthetic chemistry with molecular biology. This approach is proposed to be a potential eco-friendly alternative in the field of materials science, particularly in the area of membrane technologies. The strategy involves substituting APs with biodegradable alternatives inspired by natural polymers. However, this research should not be limited to the development of membranes but is also proposed to look into the design of hybrid materials with other physical textures. The work also aims to address sustainability by developing nanoMOF-based materials whose recyclability over multiple cycles contributes to a circular economy. Furthermore, the research seeks to identify alternatives to MMMs by modifying the synthesis parameters and exploring the possibilities offered by gelation. In addition to the end products, the synthesis routes are a source of environmental concern and should be investigated as well. Besides environmental concerns, the intention behind the development of bio-based hybrid materials is to provide potential for applications. It is therefore proposed that the PL of the used nLn^{3+}-MOFs could function as a status probe for the material's condition throughout the recycling process. This would require nLn^{3+}-MOFs to be stable in

aqueous environments, over a broad pH region, or in the presence of high ion concentrations as found in marine water bodies.

In summary, the objective of all publications collectively is to address the development of nLn^{3+}-MOF-based (bio)polymer hybrid materials that combine the characteristics of all components for advanced applications, and to achieve more sustainable materials by using biodegradable component alternatives.

3 Published Scientific Contributions

3.1 Nano *vs.* bulk: surfactant-controlled photophysical and morphological features of luminescent lanthanide MOFs

published in the *Journal of Materials Chemistry A*
as part of the themed collection “Functional Framework Materials”.

Moritz Maxeiner, Lea Wittig, Alexander E. Sedykh, Thomas Kasper, and Klaus Müller-Buschbaum

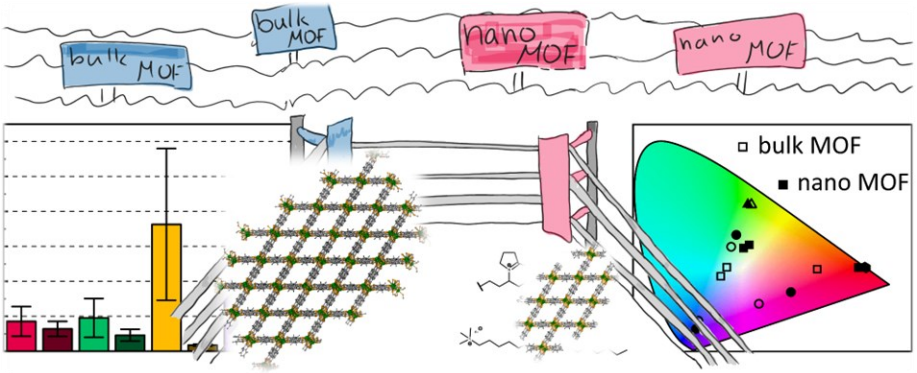

Supporting Information is available in
Appendix A – Supporting Information – Chapter 3.1.

Supporting video material is available online.

Reprinted with permission from *J. Mater. Chem. A* **2023**, 11, 22478–22491.

DOI: 10.1039/D3TA05219B

Journal of Materials Chemistry A

ROYAL SOCIETY OF CHEMISTRY

PAPER

Cite this: J. Mater. Chem. A, 2023, 11, 22478

Nano *vs.* bulk: surfactant-controlled photophysical and morphological features of luminescent lanthanide MOFs†

Moritz Maxeiner, [a] Lea Wittig,[a] Alexander E. Sedykh, [a] Thomas Kasper[a] and Klaus Müller-Buschbaum *[ab]

A surfactant-assisted bottom-up synthesis route provides access to nanoscale metal–organic frameworks (nMOFs) that exploit size-dependent property advantages. This includes an increased surface-to-volume ratio, improved dispersibility and superior morphological properties by a narrow size distribution compared to the bulk analogues. Photophysical properties such as photoluminescence are also influenced by particle size, surfactant components and post-synthetic modification. The series of the related organic linkers (H_2bdc, H_2bpdc and H_2bpydc) together with trivalent lanthanides (Ln^{3+} = Eu^{3+}, Tb^{3+}) in synthesis and post-synthetic modification together with surface-active agents (CTAB, PVP) were used to assemble luminescent nMOFs for three archetype MOFs: nLn^{3+}-bdc, nDUT-5:Ln^{3+} and nMOF-253:Ln^{3+}. Both, dispersibility and morphology benefit from the CTAB- and PVP-controlled bottom-up particle downsizing down to 35 nm. DLS confirms homogeneous, narrow particle size distributions down to ±5 nm, which is 21-times smaller than the bulk analogues. Moreover, excellent luminescence QYs of up to 78.1(3)% were determined for the Ln^{3+}-containing nMOFs. Successful post-synthetic modification with trivalent lanthanide ions of nMOFs was accomplished showing an improved photoluminescence sensitization effect compared to the bulk MOFs and exhibiting increased Ln^{3+}-to-linker emission intensity ratios. The amount and photophysical properties of surfactants encapsulating the nMOFs were further quantified by DTA/TG-MS and UV-Vis-DRS. Finally, this work aims to elaborate thoroughly on the previously mentioned properties of nMOFs by comparison with their bulk analogues. Since surfactants play a key role in this synthesis route, the pros and cons of this approach were also assessed concerning several nMOF features.

Received 30th August 2023
Accepted 8th October 2023

DOI: 10.1039/d3ta05219b

rsc.li/materials-a

Introduction

Metal–organic frameworks (MOFs) combine a wide variety of chemical adaptability with intrinsic potentially occupiable interstices, leading to a vast range of applications such as gas storage,[1–3] medical implementation,[4–6] catalysis,[7–9] sorption matrix,[10–12] sensors[13–15] or ionic conductors.[16–18] The ability to play a role in such a variety of applications is given by the vast possibility of combinations of various inorganic building units (IBUs) and organic linkers. The properties of MOFs strongly depend on the structure, electronic states, functional groups, and synthesis parameters, making MOFs highly tuneable porous materials.[19] Trivalent lanthanide (Ln^{3+})-containing MOFs are of a particular interest, as their unique photophysical properties render them highly suitable for the use as optical sensors.[20–22] The light uptake by direct excitation of Ln^{3+} ions is low, due to the non-binding character of electronically isolated 4f-orbitals and the parity-prohibition of 4f–4f transitions according to Laporte's rule.[23,24] However, the light uptake of Ln^{3+} can be significantly enhanced indirectly by a proper organic linker capable of a high light absorption followed by an energy transfer to Ln^{3+} ions, from which light is emitted. Thereby, this 'antenna effect' or 'sensitization' overall enhances the luminescence properties of the composite material.[25] This includes lanthanide ions inside MOF pores.[26] The range of emitted light covers both, the vis-region from 400 nm to 800 nm and also the NIR-region from 800 nm to 1700 nm is possible.[27] This is an interesting endorsement of the photophysical capability of lanthanide MOFs and provides excess to applications such as luminescent MOF barcodes.[28]

The interest in nanoparticles has grown enormously over the last two decades due to their unique size-dependent properties, which can be readily influenced by limiting their particle growth. As a result, they outperform their bulk analogues with

[a]Institute of Inorganic and Analytical Chemistry, Justus-Liebig-University Giessen, Heinrich-Buff-Ring 17, 35392 Giessen, Germany. E-mail: kmbac@uni-giessen.de; Web: https://www.uni-giessen.de/de/fbz/fb08/Inst/iaac/mueller-buschbaum

[b]Center for Materials Research (LAMA), Justus-Liebig-University Giessen, Heinrich-Buff-Ring 16, 35392 Giessen, Germany

† Electronic supplementary information (ESI) available. See DOI: https://doi.org/10.1039/d3ta05219b

higher surface-to-volume ratios, increased solvent affinity, enhanced particle penetration rates, and newly acquired photophysical properties.[29] Nowadays, the importance of functionalized nanomaterials extends to a multitude of sectors, for instance, electronics[30–32] and medical applications.[33–35] However, the generation of novel nanomaterials is still challenging, as inevitable processes such as Ostwald ripening or agglomeration must be overcome. Therefore, well-designed synthesis routes with size limiting features are required. Several methods have been established using either chemical additives or physical concepts in bottom-up and top-down routes, respectively.[36,37]

The contradicting idea of reducing an extended three-dimensional network in size, which is defined by its long-range order, crystallinity, and an enormous number of pores as in bulk MOFs, consequently, takes these specific properties away but leads to nano-scaled MOF (nMOF) particles consisting of only a couple of unit cells. Furthermore, nMOFs offer the advantages stated above of bulk MOFs, plus those given by their nano-character.[38] The bottom-up downsizing results in a higher specific surface area and less gravitational influence on dispersibility compared to bulk MOFs, as well as defined optical properties through the incorporation of luminophores.[39] Therefore, distinct improvements can be achieved in the synthesis and application of composites containing nLn^{3+}-MOFs compared to their bulk analogues. For instance, enhanced homogeneity and stability of a dispersion or ameliorated sorption efficiency.

In principle, nLn^{3+}-MOFs can be synthesized by a bottom-up[40] or top-down approach.[41] In this work, the bottom-up approach implements a template-based method by using surface-active agents (surfactants).[42] Scheme 1 shows the behaviour of the cationic tenside *N*,*N*,*N*-trimethylhexadecan-1-ammonium bromide (CTAB) and polyvinylpyrrolidone (M_w = 40 000 g mol^{-1}, PVP$_{40\,000}$) in solution prior to the synthesis of the nMOF, enclosing both the IBU (Ln^{3+} or Al^{3+}) and the deprotonated linker in a confined synthesis space, which is the key to yield nMOFs and the method of choice in this work.

Ln^{3+} were incorporated into MOFs either during the MOF synthesis or by post-synthetic modification of the synthesized MOF. The Ln^{3+}-bdc (Ln^{3+} = Eu^{3+}, Tb^{3+}) has been prepared by mixing Eu^{3+}- or Tb^{3+}-salts as IBU with benzene-1,4-dicarboxylic acid (H_2bdc) as linker. For the post-synthetic modification approach, MOFs have been synthesized with Al^{3+}-salts as IBU with biphenyl-4,4′-dicarboxylic acid (H_2bpdc) or 2,2′-bipyridine-5,5′-dicarboxylic acid (H_2bpydc) as linkers. These MOFs are hereafter referred to as DUT-5:Ln^{3+} and MOF-253:Ln^{3+} (Ln^{3+} = Eu^{3+}, Tb^{3+}) according to their impregnation with Eu^{3+} ions or Tb^{3+} ions. An overview of the MOFs used in this work and the type of Ln^{3+}-incorporation is given in Table 1.

A variety of analytical techniques were used to fully characterize the systems. Powder X-ray diffraction (PXRD), dynamic light scattering (DLS), scanning electron microscopy (SEM), microwave plasma – atomic emission spectroscopy (MP-AES), organic elemental analysis (OES) and simultaneous differential thermoanalysis/thermogravimetry combined with mass spectrometry (DTA/TG-MS) were carried out to entirely characterize the structure, composition, and particle morphology. In order to provide photophysical data, a spectrophotometer was used equipped with different setups for

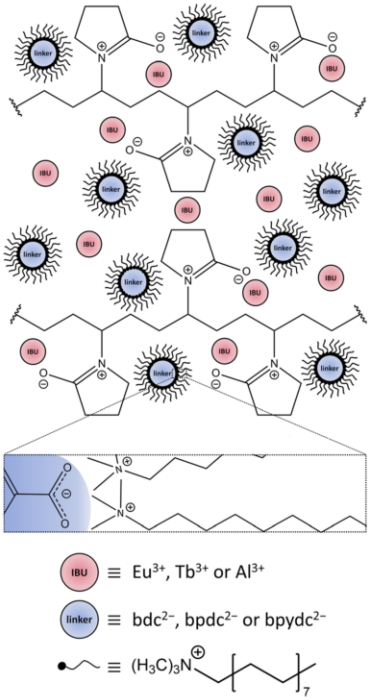

Scheme 1 Depiction of the confined space made up by the surfactants CTAB and PVP$_{40\,000}$, enclosing the IBU and linker ions prior to the synthesis. Red circles represent the IBU cations Eu^{3+} for Eu^{3+}-bdc, Tb^{3+} for Tb^{3+}-bdc, and Al^{3+} for DUT-5 and MOF-253, respectively. Blue circles represent the deprotonated linkers bdc^{2-}, bpdc^{2-} and bpydc^{2-} for Ln^{3+}-bdc, DUT-5 and MOF-253, respectively. The linkers are surrounded by black, tailed symbols representing reverse micelles, which are formed by CTAB. The enlarged rectangular box shows Coulomb-attraction between the negatively charged carboxylate group of the linker and the positively charged ammonium part of the CTAB in more detail. PVP$_{40\,000}$ forms layers enclosing a limited amount of IBU and the linker-containing reverse micelles. Both, CTAB and PVP$_{40\,000}$ set up the steric synthesis parameters for nMOFs. Solvent molecules, NO_3^- and Br^- counterions have been omitted for clarity. The dimensions do not correspond to reality.

Table 1 MOF nomenclature with respect to IBU, linker and Ln^{3+} incorporation approach

MOF[a]	IBU	Linker	Ln^{3+} incorporation approach
Eu^{3+}-bdc	Eu^{3+}	H_2bdc	Synthesis
Tb^{3+}-bdc	Tb^{3+}		
DUT-5	Al^{3+}	H_2bpdc	—
DUT-5:Ln^{3+}			Post-synthetic
MOF-253		H_2bpydc	—
MOF-253:Ln^{3+}			Post-synthetic

[a] Nomenclature is valid for both bulk MOF and nMOF.

excitation and emission spectra (PL), luminescence decay (lifetime τ), quantum yield (QY) and linker triplet state determination. A UV-Vis diffuse reflectance spectrophotometer (UV-Vis-DRS) complemented the photophysical data acquisition.

For this work, three archetype MOFs were both synthesized as bulk (Ln^{3+}-bdc, DUT-5, MOF-253, the latter two were post-synthetically modified with Ln^{3+}: DUT-5:Ln^{3+}, MOF-253:Ln^{3+}) and nano (nLn^{3+}-bdc, nDUT-5:Ln^{3+}, nMOF-253:Ln^{3+}) batch materials and discussed concerning their properties. A comparison of bulk MOFs and nMOFs on morphological and photophysical properties reveals the potential of nanomaterials.

Results and discussion

Crystal structures of Ln^{3+}-bdc, DUT-5 and MOF-253

The successful bottom-up surfactant-assisted downsizing of Ln^{3+}-bdc, DUT-5 and MOF-253 to nMOFs has been confirmed by PXRD in terms of crystallinity, purity, and potential side phases. Fig. 1 shows the PXRD results of nLn^{3+}-bdc, nDUT-5 and nMOF-253 as well as the simulated diffractograms for the single-crystal data of Ln^{3+}-bdc, DUT-5 and MOF-253, respectively. Moreover, the diffractograms of the corresponding bulk MOFs are shown in Fig. SI3–6.† All synthesized bulk MOFs and nMOFs correspond to the simulated powder patterns based on single crystal structure data. The crystal structures of the archetype MOFs Tb^{3+}-bdc,[43] DUT-5 [44] and MOF-253 [45] are well known (for clarity, they are depicted in Fig. SI1 and 2†). PXRD reveals nEu^{3+}-bdc and nTb^{3+}-bdc to be isostructural and therefore called nLn^{3+}-bdc (with Ln^{3+} = Eu^{3+}, Tb^{3+}). While the crystal structures of nDUT-5 and nMOF-253 are directly related. A broadening of the reflections is apparent for all nMOFs compared to the diffraction patterns of their bulk analogues. This can be explained by the reduction of crystallinity due to the decrease in particle size. The described phenomenon was already previously observed for other nMOFs.[46] However, crystallite size determination using the Scherrer equation is not applicable due to broad, unseparated reflections. A slight overall shift of 2θ is noticeable in the diffractograms of MOF-253 and nMOF-253 compared to the simulated powder pattern of MOF-253, which was also previously observed by Deng *et al.* for the archetype MOF-253.[47]

Noteworthy is a broad reflection between 15–30° for nDUT-5 and nMOF-253, which belongs to the surface-located CTAB. This was also shown by Chhetri *et al.* for CTAB-functionalized MoS_2. They described both CTAB attached and intercalated to the surface and in between MoS_2 nanolayers, respectively.[48] In our work, the cationic tenside CTAB forms reversible reverse micelles due to Coulomb-interactions with the unsaturated anionic carboxylate groups at the MOF surface. In contrast to micelles, the hydrophilic heads of reverse micelles face the centre, while at the outside, the tails form a hydrophobic interface with the solvent. A dynamic process of enclosing the MOF is essential to allow MOF synthesis. But the surfactant limits particle growth and also affects particle shape and dispersibility.[49,50] Moreover, the presence of small amounts of residual amorphous polymer $PVP_{40\,000}$ cannot be excluded by PXRD since this method is sensitive to the diffraction of crystalline materials only and therefore unable to detect thin layers of amorphous materials as $PVP_{40\,000}$. In fact, $PVP_{40\,000}$ forms non-linear layers in solution that resemble a confined space synthesis by encapsulating all the reactants. Particle growth becomes limited and unidirectional due to the limited amount of IBU and linker within this space.[51]

Besides, the results do not show reflections of the reagents, side phases or other non-assignable reflections, respectively.

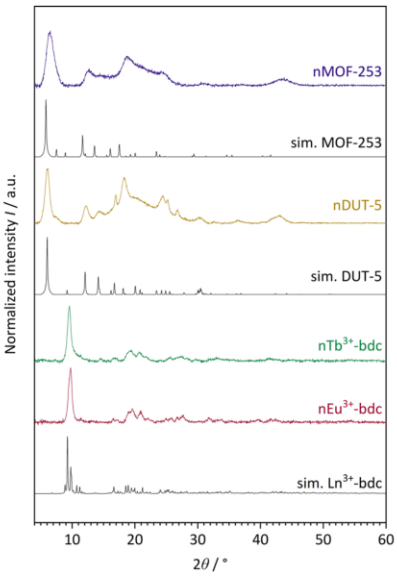

Fig. 1 Experimental powder patterns of the investigated nMOFs: nEu^{3+}-bdc, nTb^{3+}-bdc, nDUT-5 and nMOF-253. Furthermore, simulated (sim.) powder patterns for single crystal data of Tb^{3+}-bdc,[43] DUT-5 (ref. 44) and MOF-253 (ref. 45) are shown. Since nEu^{3+}-bdc and nTb^{3+}-bdc are isostructural they are denoted as nLn^{3+}-bdc (with Ln^{3+} = Eu^{3+}, Tb^{3+}). Both, experimental and single crystal data were acquired at room temperature and at ambient air atmosphere.

Composition and morphology

Characterisation of non-post-synthetically modified bulk MOFs and nMOFs. DLS reveals successful particle size reduction and more homogeneous, narrower particle size distributions of the nMOFs compared to the corresponding bulk MOFs. An overview of particle sizes and their distributions is shown in Fig. 2 and stated in Table 2. DLS gives 125 ± 40 nm for nEu^{3+}-bdc (Fig. 3b), 90 ± 35 nm for nTb^{3+}-bdc (Fig. 3d), 35 ± 5 nm for nDUT-5 (Fig. 3f) and 90 ± 20 nm for nMOF-253 (Fig. 3h), respectively. It needs to be considered that DLS measures the hydrodynamic radius of the nMOFs, which includes the surrounding surfactant as well as solvent molecules bound by electrostatic interactions to the nMOF and therefore leads to larger particles than the determination by electron microscopy (20–60 nm for nLn^{3+}-bdc, 10–20 nm for nDUT-5 and 15–30 nm for nMOF-253). SEM images confirm homogenous nLn^{3+}-bdc (Fig. 3a and c), nDUT-5 (Fig. 3e) and nMOF-253 (Fig. 3g) particles in terms of size distribution and shape. However,

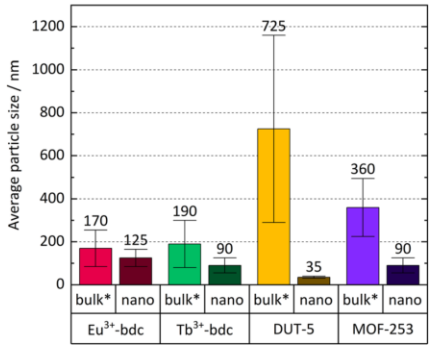

Fig. 2 Comparison of average particle size and particle size distribution (error bars) of Ln^{3+}-bdc, nLn^{3+}-bdc ($Ln^{3+} = Eu^{3+}$, Tb^{3+}), DUT-5, nDUT-5, MOF-253 and nMOF-253. Bulk MOF sizes supposed to be larger than stated due to an unavoidable sedimentation of larger particles in the dispersion during the DLS measurement and are therefore marked with an asterisk.

nanoparticle boundaries become blurred for nDUT-5 and nMOF-253 due to an increased amount of surfactants.

Bulk MOF synthesis results in clefted microparticles (>400 nm) for Ln^{3+}-bdc, and spherical particles (>1000 nm) for DUT-5 and MOF-253, respectively, as SEM demonstrates. Furthermore, particle size determination based on DLS reveals particles sizes of 170 ± 85 nm for Eu^{3+}-bdc, 190 ± 110 nm for Tb^{3+}-bdc, 725 ± 430 nm for DUT-5 and 360 ± 135 nm for MOF-253. However, bulk MOF particle sizes again supposed to be even higher due to an unavoidable sedimentation process during the DLS data acquisition (Fig. SI10†).

As PXRD and SEM already indicated the presence of surfactants at the outside of the nMOFs, coverage with $PVP_{40\,000}$ as well as the reverse micelle formation of CTAB lead to narrow particle size distributions and smaller particle sizes (Fig. 3b, d, f and h). In addition and beneficially, a dispersion with nMOFs is stabilized by residual surfactants and prevents sedimentation during DLS data acquisition. Scheme 2 illustrates how the surfactants are enclosing a nMOF particle which leads to the stabilization effect. It should be emphasized that nDUT-5 particles were significantly reduced in size by a factor of ≈21 and remarkably homogenized compared to DUT-5 (see Fig. 2).

Further information on the presence of surfactants on bulk MOFs and nMOFs was obtained by DTA/TG-MS using synthetic air as the working gas, which can oxidize the MOF instead of typical inert gases such as Ar/N_2. DTA/TG-MS results are shown in Fig. 4 and as enlarged graphics in Fig. SI14–16 in the ESI.† DTA/TG confirm an exothermic mass loss of 15 wt% and 7 wt% for Tb^{3+}-bdc (Fig. 4a) and nTb^{3+}-bdc (Fig. 4b), respectively, at 230–270 °C. MS signals identify these mass losses as the solvent molecules H_2O and DMF either located in the pores or at the surface of the MOFs. The mass loss of DUT-5 (Fig. 4c) with 40 wt% is higher than the mass loss of nDUT-5 (Fig. 4d) with 10 wt% at 100–250 °C. Consequently, both nTb^{3+}-bdc and nDUT-5 contain less solvents than their bulk analogues, suggesting that surfactants partially replace solvents in the pores and on the surface of nMOFs.

Table 2 Overview of quantitative data for the investigated Ln^{3+}-bdc, nLn^{3+}-bdc, DUT-5:Ln^{3+}, nDUT-5:Ln^{3+}, MOF-253:Ln^{3+} and nMOF-253:Ln^{3+} ($Ln^{3+} = Eu^{3+}$, Tb^{3+})

		Particle size/nm			Wavelength λ_{max}/nm		QY/%		Lifetime τ/ms	
		DLS[a]								
	Ln^{3+}/wt%	MeCN	EtOH	SEM	PL ex	PL em	Ln^{3+}	Linker	τ_1	τ_2
Eu^{3+}-bdc	32	n/a[g]	170 ± 85	>1000	288	614	33(2)	n/a[e]	0.9055(6)	n/a[f]
nEu^{3+}-bdc	32	n/a[g]	125 ± 40	20–60	296	614	23.7(3)	n/a[e]	0.701(4)	1.071(3)
Tb^{3+}-bdc	38	n/a[g]	190 ± 110	>1000	300	544	94(2)	n/a[e]	1.396(2)	n/a[f]
nTb^{3+}-bdc	33	n/a[g]	90 ± 35	20–60	286	543	78.1(3)	n/a[e]	1.04(4)	1.612(3)
DUT-5	n/a[c]	n/a[g]	725 ± 430	>400	307	376[b]	n/a[c]	5.1(5)	$2.49(6) \times 10^{-6}$	n/a[f]
nDUT-5	n/a[c]	n/a[g]	35 ± 5	10–20	326	378[b]	n/a[c]	14.8(6)	$3.6(1) \times 10^{-6}$	n/a[f]
DUT-5:Eu^{3+}	2	265 ± 115	500 ± 90	>400	307	616	2.1(2)	10.4(3)	0.288(6)	0.596(6)
nDUT-5:Eu^{3+}	2	175 ± 55	110 ± 10	20–50	310	616	3.6(1)	4.5(3)	0.306(8)	0.70(1)
DUT-5:Tb^{3+}	2	290 ± 110	385 ± 260	>400	416	544	n/a[d]	11.5(3)	n/a[d]	n/a[d]
nDUT-5:Tb^{3+}	1	160 ± 35	105 ± 10	20–50	427	544	n/a[d]	4.6(2)	n/a[d]	n/a[d]
MOF-253	n/a[c]	n/a[g]	360 ± 135	>400	370	440[b]	n/a[c]	<1	$1.19(6) \times 10^{-6}$	$6.4(1) \times 10^{-6}$
nMOF-253	n/a[c]	n/a[g]	90 ± 20	15–30	366	536[b]	n/a[c]	<1	$0.559(7) \times 10^{-6}$	$2.13(5) \times 10^{-6}$
MOF-253:Eu^{3+}	3	185 ± 180	150 ± 60	>400	327	616	2.0(1)	n/a[e]	0.204(3)	0.432(3)
nMOF-253:Eu^{3+}	4	135 ± 70	155 ± 80	20–50	310	616	1.79(3)	n/a[e]	0.14(2)	0.308(6)
MOF-253:Tb^{3+}	7	155 ± 70	130 ± 45	>400	374	544	n/a[d]	<1	n/a[d]	n/a[d]
nMOF-253:Tb^{3+}	2	100 ± 10	155 ± 70	20–50	371	544	n/a[d]	<1	n/a[d]	n/a[d]

[a] Particle sizes of bulk MOFs are supposed to be even higher due to sedimentation. [b] Recording of linker-based emission spectrum. [c] No Ln^{3+} present in the sample. [d] Only linker-based emission observable, no sufficient energy transfer from linker to Tb^{3+}. [e] No linker-based emission intensity observable in PL spectra. [f] An exponential fit of first order was used. [g] Measurements not carried out in MeCN.

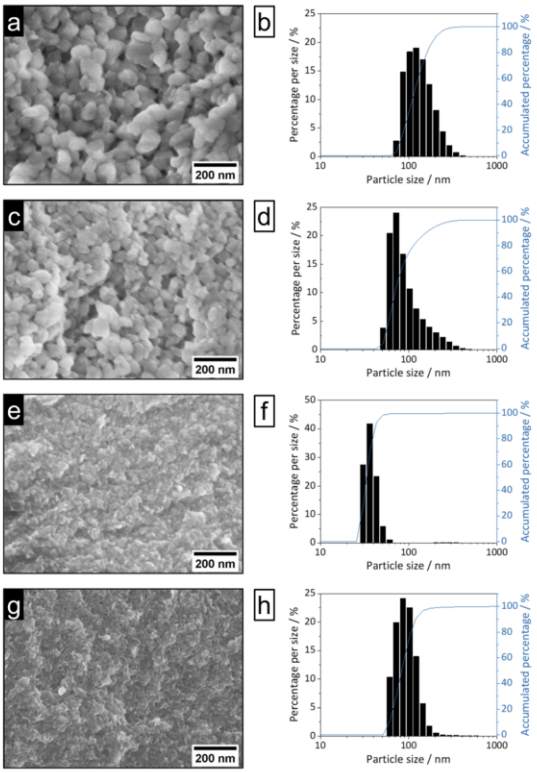

Fig. 3 SEM images (100k magnification, left) and DLS particle size distributions (right) of nEu^{3+}-bdc (a and b), nTb^{3+}-bdc (c and d), nDUT-5 (e and f) and nMOF-253 (g and h).

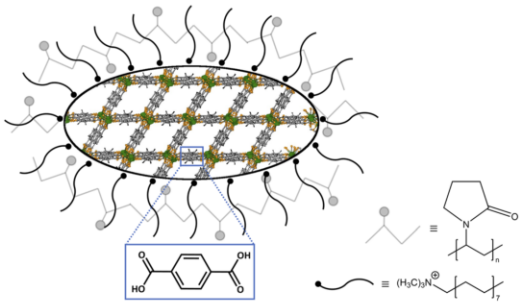

Scheme 2 Depiction of a surfactant-stabilized nMOF particle. The Tb^{3+}-bdc crystal structure is shown within the particle-shaped area and represents the MOFs used. Atom color code: green (Tb), yellow (O), grey (C), black (H). The nMOF is surrounded by black, tailed symbols representing reverse micelles, which are formed by CTAB. $PVP_{40\,000}$ impacts the particle shape by enclosing the nMOF depicted as pale-grey chains. The blue box shows exemplarily the H_2bdc in Tb^{3+}-bdc as representative for the linkers used.

In Fig. 4b, mass losses of 1 wt% at 305–345 °C and 13 wt% at 400–500 °C were observed for nTb^{3+}-bdc, attributed to the oxidation of CTAB and $PVP_{40\,000}$, respectively. Results from MS allow for the identification of CO_2, NO and H_2O as oxidation products, confirming the oxidation of surfactants, for the deprotonated linker bdc^{2-} does not contain nitrogen. In the oxidation process, a shorter aliphatic chain as in CTAB requires less energy to be cracked than a longer polymeric chain as in $PVP_{40\,000}$. In fact, this effect has been previously reported for CTAB[52] and $PVP_{40\,000}$ (ref. 53) for the above-mentioned temperature ranges. The powder pattern of nTb^{3+}-bdc does not show any broad reflection at 12–30° (Fig. 1), therefore the amount of surfactant must be lower than for nDUT-5 and nMOF-253. In corroboration, both, nDUT-5 and nMOF-253 show a higher mass loss of 30 wt% at 300–470 °C (Fig. 4d and f). Moreover, NO signals at 310–420 °C and 300–470 °C for nDUT-5 and nMOF-253, respectively, are indicating surfactant oxidation and further confirm this assignment.

NO signals starting at 500 °C can be assigned to the oxidation of the N-containing linker $bpydc^{2-}$ (Fig. 4e and f). Additionally, the ongoing oxidation of organic linkers is also indicated by the CO_2 signal starting at 400 °C for Tb^{3+}-bdc and nTb^{3+}-bdc while the oxidation of the linkers of DUT-5, nDUT-5, MOF-253 and nMOF-253 continues at 500 °C. The DTA/TG-MS results do not show any NO signals at 320–420 °C for the investigated bulk MOFs, thus the mass loss can be attributed to the amount of surfactants present in the investigated nMOFs by comparing bulk MOF and nMOF results.

At temperatures higher than 650 °C, Tb^{3+}-bdc and nTb^{3+}-bdc become fully oxidized accompanied by an altogether mass loss of 60 wt% with Tb_4O_7 being formed (Fig. 4a and b). Higher temperatures, starting at 850 °C are necessary to fully oxidize DUT-5 and nDUT-5 as well as MOF-253 and nMOF-253 to Al_2O_3 with an altogether mass loss of 85 wt% (Fig. 4c–f). Both, Tb_4O_7 and Al_2O_3 are confirmed as oxidation products by PXRD (Fig. SI9†).

Characterisation of post-synthetically modified bulk MOF:Ln^{3+} and nMOF:Ln^{3+}. To study the effect of post-synthetic modification with Ln^{3+} ions on the composition as well as on particle size and particle size distribution of DUT-5, nDUT-5, MOF-253 and nMOF-253, they were impregnated with solutions of Eu^{3+}- and Tb^{3+}-salts. Details of the impregnation procedure are described in the Experimental section.

The amount of Ln^{3+} was determined by MP-AES and the results are presented in Table 2. Ln^{3+}-bdc and nLn^{3+}-bdc contain 32–38 wt% Ln^{3+} depending on the lanthanide and MOF. In contrast, the post-synthetically modified DUT-5:Ln^{3+} and nDUT-5:Ln^{3+} contain only 1–2 wt% Ln^{3+}, while MOF-253:Ln^{3+} and nMOF-253:Ln^{3+} contain 2–7 wt% Ln^{3+}, again depending on lanthanide and MOF. The difference in the amount of Ln^{3+} between both synthesis approaches is explainable by the function of Ln^{3+} ions in the MOFs. As main connectivity centre, Ln^{3+} is much more present in Ln^{3+}-bdc than by impregnation of DUT-5:Ln^{3+} and MOF-253:Ln^{3+}. It can be seen that the surfactants do not have a distinct impact on the uptake of Ln^{3+} ions, as the amount of Ln^{3+} do not follow any comprehensible trend between bulk MOFs and nMOFs.

Powder patterns of DUT-5:Ln^{3+} and nDUT-5:Ln^{3+} (Fig. SI7†) as well as MOF-253:Ln^{3+} and nMOF-253:Ln^{3+} (Fig. SI8†) reveal stable crystal structures for MOF:Ln^{3+}s impregnated with Eu^{3+}

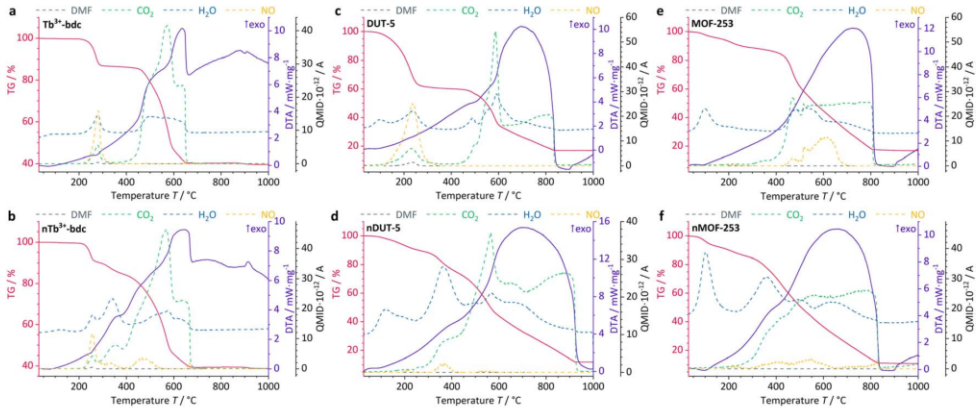

Fig. 4 DTA/TG-MS results of investigated bulk MOFs and nMOFs at synthetic air atmosphere. Tb^{3+}-bdc (a), nTb^{3+}-bdc (b), DUT-5 (c), nDUT-5 (d), MOF-253 (e) and nMOF-253 (f). NO signal (yellow) is given in QMID × 10^{-13}. A for a more detailed insight.

and Tb^{3+}. As a side effect of the post-synthetic modification process, the broad reflection at 12–30° 2θ in the diffractograms of nDUT-5 and nMOF-253 is less intense than in the diffractograms of nDUT-5:Ln^{3+} and nMOF-253:Ln^{3+}. Hence, SEM images of nDUT-5:Ln^{3+} and nMOF-253:Ln^{3+} modified in MeCN were recorded to check whether a reduced amount of surfactant can be observed. The partial purification from surfactants results in distinguishable particles for nDUT-5:Ln^{3+} and nMOF-253:Ln^{3+} (Fig. 5) meaning a lesser amount of surfactants are covering nMOF particles.

Complementary results on particle size and its distribution for the post-synthetically modified MOF:Ln^{3+} and nMOF:Ln^{3+} were obtained by DLS and are given in Table 2. DLS reveals the influence of the reduced amount of surfactants on the morphological properties and particle growth indicated by increasing particle sizes (130–140 nm for nDUT-5:Ln^{3+} and 10–50 nm for nMOF-253:Ln^{3+}, respectively, see also Fig. SI11†). Processes such as crystal growth during post-synthetic modification due to a more accessible nMOF surface, which was previously covered with surfactants, or swelling of the crystal structure due to Ln^{3+} insertion are likely to be responsible for the determined increased particle sizes. In addition, penetration of the crystal structure by surfactants or formation of holes/defects by anions to compensate for the positive charge brought in by Ln^{3+} also contribute to the swelling effect.[54] This increase in particle size is more prominent for nDUT-5:Ln^{3+} than for nMOF-253:Ln^{3+} due to the smaller particle size of nDUT-5. The smaller the particles, the higher the surface energy and the more distinct surface energy reducing mechanisms become, such as Ostwald-ripening, which consequently leads to crystal growth.[55] In addition, bulk MOF:Ln^{3+} particle sizes are hardly comparable with non-modified bulk MOF particle sizes due to sedimentation processes described above during the DLS data acquisition, and therefore, do not follow any discernible trend (Fig. SI12 and 13†).

Altogether, these results point to the presence of residual surfactants after the post-synthetic modification process, that allows nDUT-5:Ln^{3+} and nMOF-253:Ln^{3+} to form stable and homogeneous dispersions with slightly increased particle sizes, due to a swelling of the crystal structure and less coverage by surfactants.

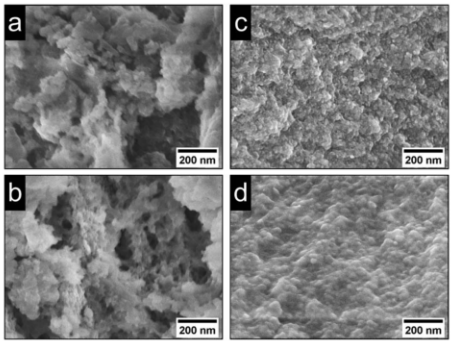

Fig. 5 SEM images (100k magnification) of (a) nDUT-5:Eu^{3+}, (b) nDUT-5:Tb^{3+}, (c) nMOF-253:Eu^{3+} and (d) nMOF-253:Tb^{3+}.

Photophysical properties

The evaluation of the photophysical properties of bulk MOFs and nMOFs was accomplished by comparing the obtained results of qualitative PL spectra, overall luminescence decay times τ, QYs and linker triplet state energy determinations, as well as UV-Vis-DRS.

Comparison of the photophysical properties of the investigated bulk MOFs and nMOFs. PL spectra were recorded for all Ln^{3+}-containing MOFs and nMOFs, with Ln^{3+} = Eu^{3+}, Tb^{3+} (see Fig. 6 for excitation and emission spectra). For excitation, a broad band at 280–350 nm appears in the excitation spectra of all investigated MOFs and nMOFs at similar wavelengths and with similar band shapes that represent the $\pi^* \leftarrow \pi$ excitation of the linkers. Subsequently, the excited π-electrons of the linker undergo an intersystem crossing to a triplet state followed by an energy transfer to excited 4f-states of the trivalent

lanthanides – this describes the so-called 'antenna effect'. Other obvious features in the excitation spectra shown in Fig. 6 are direct excitations of Ln^{3+} that are prominent for Eu^{3+}-bdc and nEu^{3+}-bdc (Eu^{3+}: $^5D_{1,2,4}$, $^5L_6 \leftarrow {}^7F_0$ and $^5D_{1,3,4} \leftarrow {}^7F_1$ at 525 nm, 464 nm, 392 nm, 361 nm and 533 nm, 414 nm, 379 nm, respectively) and weak to hardly observable in the excitation spectra of Tb^{3+}-bdc and nTb^{3+}-bdc (Tb^{3+}: $^5D_2 \leftarrow {}^7F_6$, $^5L_{10} \leftarrow {}^7F_6$, $^5D_3 \leftarrow {}^7F_6$ and $^5D_4 \leftarrow {}^7F_6$ at 351 nm, 368 nm, 376 nm and 489 nm, respectively). Although quantum mechanically unfavoured, these peaks demonstrate the weak receptivity of these Ln^{3+}-MOFs to absorb light in a direct way without participation of the linker, indicating the preferred route of an excitation *via* a sensitizer linker, as the broad $\pi^* \leftarrow \pi$ excitations of the linkers surpass the direct excitations of the investigated Ln^{3+}-MOFs in terms of intensity.

The emission spectra of the investigated Eu^{3+}-containing MOFs and nMOFs show the typical Eu^{3+} transitions $^5D_0 \rightarrow {}^7F_0$, $^5D_0 \rightarrow {}^7F_1$, $^5D_0 \rightarrow {}^7F_2$, $^5D_0 \rightarrow {}^7F_3$, $^5D_0 \rightarrow {}^7F_4$, $^5D_0 \rightarrow {}^7F_5$ and $^5D_0 \rightarrow {}^7F_6$, which correspond to the emission signals at 580 nm, 593 nm, 616 nm, 652 nm, 700 nm, 753 nm, and 810 nm, respectively. The emission bands differ in terms of relative intensity and shape. For instance, the coordinated Eu^{3+} in Eu^{3+}-bdc and nEu^{3+}-bdc causes a splitting of the $^5D_0 \rightarrow {}^7F_2$ and $^5D_0 \rightarrow {}^7F_4$ transitions, while Eu^{3+} inside the pores of DUT-5:Eu^{3+} and MOF-253:Eu^{3+} gives broader, single-maxima emission bands. This signal broadening is indicative for multiple, different local electric fields of Eu^{3+} in the pores or on the MOF surface, which differs from the distinct crystallographic Ln^{3+}-positions in Ln^{3+}-bdc and nLn^{3+}-bdc. For the post-synthetic modification, the MOF pores allow for multiple locations inside the pores for Eu^{3+}. In addition, the relative intensities of $^5D_0 \rightarrow {}^7F_2$ and $^5D_0 \rightarrow {}^7F_4$ vary between DUT-5:Eu^{3+} and MOF-253:Eu^{3+}, depending on the specific Eu^{3+} position within the crystal structure. Both effects are well known in the literature[56] and provide evidence for different electrostatic environments for Eu^{3+} inside the pores. Furthermore, the asymmetry ratio of Eu^{3+} provides valuable insights concerning its local environment and is defined as the ratio of the integrated intensities $I(^5D_0 \rightarrow {}^7F_2)$ and $I(^5D_0 \rightarrow {}^7F_1)$. As the $^5D_0 \rightarrow {}^7F_1$ transition is predominantly unaffected by the local environment,[57] a low asymmetry ratio indicates minimal distortions in the electric field, with $^5D_0 \rightarrow {}^7F_2$ being comparatively weaker and Eu^{3+} is located at distinct positions. However, when the distortion in the electrostatic environment of Eu^{3+} increases, *i.e.* Eu^{3+} is located at positions with different local environments, the intensity of the $^5D_0 \rightarrow {}^7F_2$ transition also increases, resulting in a higher asymmetry ratio. The calculated asymmetry ratios for bulk Eu^{3+}-bdc and nEu^{3+}-bdc are 5.07 and 6.57, respectively. This observation supports the assertion that surfactants remain present in the pores and/or at the surface of nEu^{3+}-bdc after the washing procedure, leading to distortion of the local environment of Eu^{3+}. The post-synthetically modified MOF-253:Eu^{3+} and nMOF-253:Eu^{3+} also following the described trend indicative by the asymmetry ratios 4.47 and 6.49, respectively. Additionally, in the case of the post-synthetically modified MOFs, the higher average diffusion pathway affords improved pore occupancy of Eu^{3+}, resulting in even more

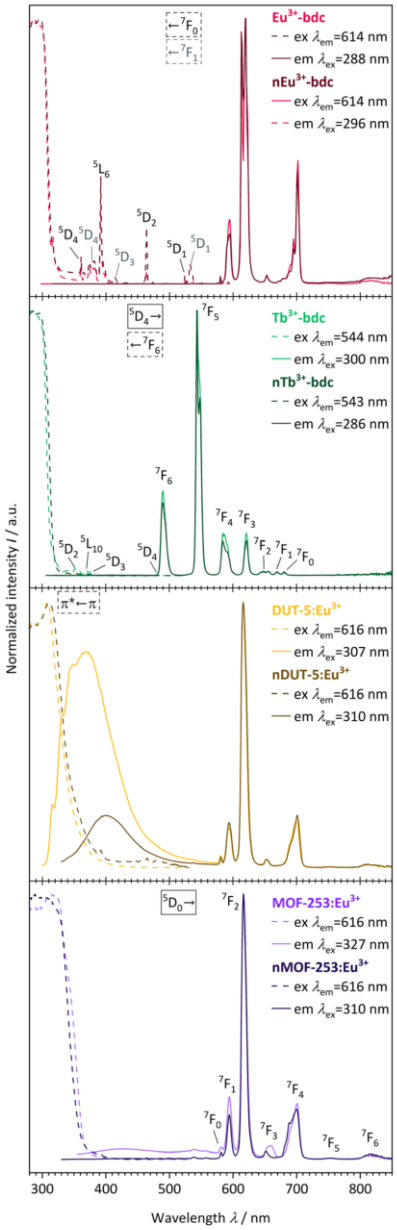

Fig. 6 Qualitative PL excitation and emission spectra of Eu^{3+}-bdc (pale red), nEu^{3+}-bdc (dark red), Tb^{3+}-bdc (pale green), nTb^{3+}-bdc (dark green), DUT-5:Eu^{3+} (pale yellow), nDUT-5:Eu^{3+} (dark yellow), MOF-253:Eu^{3+} (pale violet) and nMOF-253:Eu^{3+} (dark violet). Electronic states are exemplarily denoted for clarity with the corresponding electronic transitions for the linker, Eu^{3+} and Tb^{3+}, respectively.[56,58]

different electrostatic environments than in Ln^{3+}-bdc. Asymmetry ratios of 6.34 and 6.35 are observed for DUT-5:Eu^{3+} and nDUT-5:Eu^{3+}, respectively. These ratios indicate a more distorted local environment for Eu^{3+} in DUT-5:Eu^{3+} compared to

MOF-253:Eu^{3+} and Eu^{3+}-bdc, while the environment of Eu^{3+} in nDUT-5:Eu^{3+} is similar to other nMOF-253:Eu^{3+} and Eu^{3+}-bdc.

The emission spectra of Tb^{3+}-bdc and nTb^{3+}-bdc exhibit the typical emission pattern of Tb^{3+} with the transitions $^5D_4 \rightarrow {}^7F_6$, $^5D_4 \rightarrow {}^7F_5$, $^5D_4 \rightarrow {}^7F_4$, $^5D_4 \rightarrow {}^7F_3$, $^5D_4 \rightarrow {}^7F_2$, $^5D_4 \rightarrow {}^7F_1$ and $^5D_4 \rightarrow {}^7F_0$, which can be attributed to sharp bands at 489 nm, 543 nm, 584 nm, 621 nm, 647 nm, 669 nm, and 680 nm, respectively.[58] Tb^{3+} does not show emission in post-synthetically modified DUT-5:Tb^{3+}, nDUT-5:Tb^{3+}, MOF-253:Tb^{3+} and nMOF-253:Tb^{3+} since the sensitization of Tb^{3+} by the energy transfer from the linkers to Tb^{3+} is not preferred (Fig. SI21 and 22†). In order to investigate the reasons for the neglectable energy transfer, the donor triplet state energies of the linkers were determined and subsequently compared with the emitting energy state level $^5D_4$ of Tb^{3+} in terms of energy. Latva *et al.*[59] state that donor–acceptor energy states should be optimally separated by 2000–4000 cm^{-1}. The emitting state $^5D_4$ of Tb^{3+} is located at 20 470 cm^{-1},[60] whereas the donor triplet states of Tb^{3+}-bdc, DUT-5 and MOF-253 are located at 24 691 cm^{-1}, 21 079 cm^{-1} and 20 877 cm^{-1}, respectively (Fig. SI23–25†). Since the energy states for DUT-5 and MOF-253 are energetically too close to the Tb^{3+} energy state $^5D_4$, high energy back-transfer rates dominate the systems, and therefore no Tb^{3+}-based emissions are observed. In contrast, Eu^{3+} has two energetic states $^5D_{1,2}$ at 19 026 cm^{-1} and 21 499 cm^{-1}, respectively, which get addressed to as acceptor states[61] for the sensitization energy transfer from the linker to Eu^{3+} and is in accordance with Latva's rule.

Altogether, the comparison of Ln^{3+}-containing MOFs and nMOFs show a benefit of nanoscale particles regarding the sensitizing efficiency as indicated by a strong decrease in the intensity of the linker-based emission bands.

The previously described emission processes were further characterised by performing luminescence overall decay time measurements to determine lifetimes τ (Fig. SI26–31†), with the results being given in Table 2. Lifetimes of the emitting states in millisecond range indicate quantum mechanically unfavoured phosphorescent emission processes caused by parity forbidden 4f–4f transitions of the Ln^{3+} ions. Typical lifetimes for phosphorescence processes are 0.9055(6) ms for Eu^{3+}-bdc or 0.701(4) ms for nEu^{3+}-bdc, for instance. However, for the non-Ln^{3+}-containing MOFs, lifetimes in nanosecond range were recorded and are indicative for fluorescence processes of the linker-based emission with 2.49(6) ns for DUT-5 or 3.6(1) ns for nDUT-5, for instance.

In fact, an important aspect when considering the efficiency of the emission of the Ln^{3+}-MOFs is its residual linker-based emission intensity. The presence and intensity of the emission band of the linker is a reciprocal indicator for the efficiency of the sensitizing effect. The better the energy transfer from the linker to Ln^{3+}, the lower the emission band intensity of the linker. This energy transfer is strongly depending on the donor–acceptor distance *i.e.*, linker and Ln^{3+}. As nDUT-5:Ln^{3+} and nMOF-253:Ln^{3+} are smaller in size than their bulk analogues, the average Ln^{3+} diffusion pathway becomes shorter, and a better pore occupancy can be achieved. Accordingly, the linker-based emission intensity in the emission spectrum of nDUT-5:Eu^{3+} at 400 nm is lower than the bulk analogue. This is in corroboration with a decreased linker-based QY from 10.4(3)% to 4.5(3)% for DUT-5:Eu^{3+} and nDUT-5Eu^{3+}, respectively. The linker-based emission band of nMOF-253:Eu^{3+} yet diminishes completely. Both reveal nicely the advantages of nanoparticles. Interestingly, although the MOF-253, nMOF-253, MOF-253:Tb^{3+} and nMOF-253:Tb^{3+} show linker-based emission bands in their PL spectra QYs are <1%, which, however, is consistent with the low emission intensities observed with the naked eye (Fig. 7). This is also evidence for energy release by rather non-radiative processes than light emission. Moreover, the undoped DUT-5 and nDUT-5 show linker-based QYs of 5.1(5)% and 14.8(6)%, respectively, which is in accordance with the observed higher intensity of nDUT-5 compared to its bulk analogue, accompanied by a bathochromic shift as explained later in more detail. On the other hand, Ln^{3+}-bdc and nLn^{3+}-bdc do not show any linker-based emission bands at all, which confirms a highly efficient energy transfer. This results in excellent Ln^{3+}-based QYs as the ratio of emitted to absorbed photons of 94(2)% and 78.1(3)% for Tb^{3+}-bdc and nTb^{3+}-bdc, respectively (see Table 2). The respective Ln^{3+}-based QYs of 33(2)% for Eu^{3+}-bdc and 23.7(3)% for nEu^{3+}-bdc are lower than the Ln^{3+}-based QYs of their Tb^{3+}-analogues indicating a better energetical match between the excited states of the sensitizer for Tb^{3+}. Different to Ln^{3+}-coordination sites of these MOFs, post-synthetically modified MOF:Ln^{3+}s show lower Ln^{3+}-QYs as the Ln^{3+}-to-linker distances increase (Ln^{3+}-based QY of 2.0(1)% for MOF-253:Eu^{3+}, for instance). As discussed early, DUT-5:Tb^{3+} and nDUT-5:Tb^{3+} do not show Tb^{3+}-based emission due to the mismatch of Tb^{3+}-linker energy states while the linker-based QYs also decreasing from 11.5(3)% to 4.6(2)% from DUT-5:Tb^{3+} to nDUT-5:Tb^{3+}. For nDUT-5:Eu^{3+}, however, the Ln^{3+}-based QY can exceed the bulk MOF (Ln^{3+}-based QYs: 3.6(1)% compared to 2.1(2)%) corroborated by a longer lifetime τ (see Table 2). Accordingly, a decreased Ln^{3+}-based QY may be concluded as a result of the surfactant influence, although there is no general trend.

In addition, light absorption was investigated by UV-Vis-DRS. In general, it reveals broad absorption from 200–320 nm for all investigated MOFs, which can be assigned to the $\pi^* \leftarrow \pi$ transition of the linkers and fits nicely the excitation spectra seen in Fig. 6. However, all absorption spectra of the investigated nMOFs show this broad absorption band starting at 200 nm but instead of tailing at 320 nm, the absorption band shows tailing up to 700 nm for nTb^{3+}-bdc, for instance, which implies a contribution of further absorption processes along with the $\pi^* \leftarrow \pi$ transition. The range of this multiple-process absorption band varies with each investigated MOF and is displayed in Fig. SI17–20.† Since this broader absorption band appears exclusively in investigated nMOF absorption spectra, the absorption band is attributed to the surfactants CTAB and $PVP_{40\,000}$. Therefore, the investigated nMOFs appear yellow at daylight compared to their colourless bulk analogues (Fig. 7 and SI33† as well as a video download). In addition, only Eu^{3+}-bdc and nEu^{3+}-bdc spectra show low-intensity, sharp absorption peaks at 395 nm, 466 nm and 535 nm which can again be assigned to the respective 4f–4f transitions $^5L_6 \leftarrow {}^7F_0$, $^5D_2 \leftarrow$

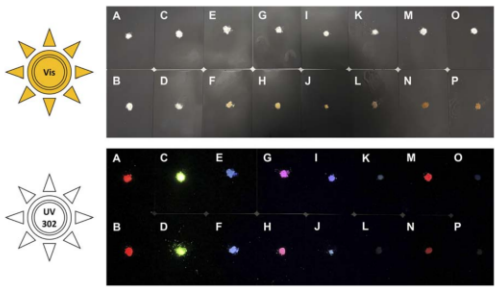

Fig. 7 Photographs of powders of investigated bulk MOFs and nMOFs exposed to Vis-light (top) and UV-light (302 nm, bottom). A = Eu^{3+}-bdc, B = nEu^{3+}-bdc, C = Tb^{3+}-bdc, D = nTb^{3+}-bdc, E = DUT-5, F = nDUT-5, G = DUT-5:Eu^{3+}, H = nDUT-5:Eu^{3+}, I = DUT-5:Tb^{3+}, J = nDUT-5:Tb^{3+}, K = MOF-253, L = nMOF-253, M = MOF-253:Eu^{3+}, N = nMOF-253:Eu^{3+}, O = MOF-253:Tb^{3+}, P = nMOF-253:Tb^{3+}.

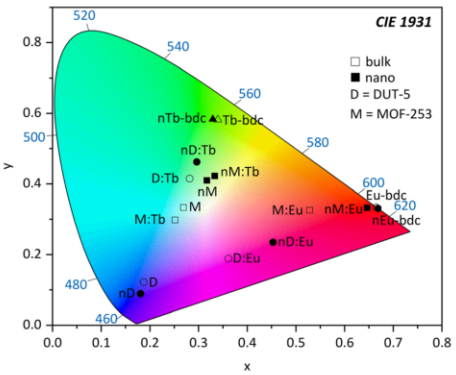

Fig. 8 Chromaticity diagram according to CIE 1931 calculated from PL data of Ln^{3+}-bdc, nLn^{3+}-bdc, DUT-5, nDUT-5, MOF-253, nMOF-253, DUT-5:Ln^{3+}, nDUT-5:Ln^{3+}, MOF-253:Ln^{3+} and nMOF-253:Ln^{3+} (Ln^{3+} = Eu^{3+}, Tb^{3+}) investigated in this work. Hexagon = Eu^{3+}-bdc; triangle = Tb^{3+}-bdc; square = MOF-253 and MOF-253:Ln^{3+}; circle = DUT-5 and DUT-5:Ln^{3+}; D = DUT-5; and M = MOF-253. Empty symbols represent bulk MOFs, while filled symbols represent nMOFs.

$^7F_1$ and $^5D_1 \leftarrow {}^7F_1$ already observed in the excitation spectra of Eu^{3+}-bdc and nEu^{3+}-bdc.

Comparison of the chromaticity of investigated bulk MOFs and nMOFs. The contributions of linker-based emission and Ln^{3+}-based emission to the overall light emission as a specific colour by each MOF is shown in a chromaticity diagram according to CIE 1931 (Fig. 8). It was calculated from the PL data of all bulk MOFs and nMOFs investigated and clearly shows the effect of an improved energy transfer from the linker to Ln^{3+} in nMOFs compared to bulk MOFs. This corroborates the observed emission spectra and results in an emission colour shift. In general, the emission of nEu^{3+}-bdc and nTb^{3+}-bdc is less influenced by the nano-character of the particles than the emission of the post-synthetically modified nDUT:Ln^{3+} and nMOF-253:Ln^{3+}. Both, nDUT-5 and nMOF-253 show shifted overall luminescence but to opposing wavelength regions. *E.g.*, the emission band of nDUT-5 is shifted by 18 nm from 377 nm to 395 nm compared to DUT-5. In contrast, nMOF-253 does not show the additional emission band of MOF-253, as explained earlier, which shifts the chromaticity towards green. This means that a combination of the processes of all MOF components, post-synthetic modification and the surfactants influence the overall luminescence and its chromaticity. An overview is given in Fig. 7 and SI33,† as well as a video download.

Conclusion

This work presents new aspects of the impact of nanoparticle formation on morphological and photophysical properties compared to the bulk archetype MOFs for Ln^{3+}-MOFs and archetype MOFs doped post-synthetically modified by impregnation with lanthanide ions, shown for Ln^{3+}-bdc, DUT-5:Ln^{3+} and MOF-253:Ln^{3+} (Ln^{3+} = Eu^{3+}, Tb^{3+}). Nanoscale variants of the three archetype MOFs have been successfully achieved by surfactant-assisted bottom-up synthesis as fully-characterised nMOFs.

The nMOFs were synthesized with particle sizes down to 35 nm as nDUT-5 demonstrates (21-times smaller than DUT-5). Consequently, a particle consists of only a couple unit cells of the 3D framework. Furthermore, particle size distributions were tremendously narrowed down to ≈1% of their original bulk particle size distribution and stabilized in dispersion by $PVP_{40\,000}$ and CTAB. After post-synthetic modification, the nMOFs:Ln^{3+} benefit from residual surfactants as good as non-post-synthetically modified nMOFs in terms of dispersibility and particle size. The shorter average free path of the diffusion of Ln^{3+} in nMOF:Ln^{3+} leads to a better pore occupancy and an improved energy transfer from the linker to the Ln^{3+}. The importance of suitable energy differences of the excited states of the MOFs and incorporated Ln^{3+}-ions becomes evident for the non-preferred sensitization of Tb^{3+} in nMOF:Tb^{3+} combinations. In contrast, MOFs and nMOFs with Ln^{3+} as connectivity centres show higher QYs up to 94% and 78% for Tb^{3+}-bdc and nTb^{3+}-bdc, as an energy transfer *via* the electronic system of the MOF is available. This results in chromaticity shifts between MOFs and nMOFs being either bathochromic or hypsochromic.

Altogether, this work provides insights into the photophysical and morphological properties of nano-sized lanthanide-containing MOFs, the pros and cons associated with the usage of surfactants as well as two different ways of functionalizing of these versatile three-dimensional compounds. We demonstrate, how the synthesis of nMOFs can be controlled by reagents such as surfactants, how the light emission of Ln^{3+}-containing MOFs can be influenced either by changing the size and morphology of the particles or by incorporate the lanthanide at different stages of the synthesis process (early in the synthesis procedure or post-synthetic), as well as how the choice of IBU-linker-Ln^{3+} combination affects the energy transfer efficiency and luminescence efficiency.

Experimental

All chemicals were used as purchased without further purification. The rare-earth nitrates $Ln(NO_3)_3 \cdot 6H_2O$ (Ln = Eu, Tb, Gd;

99.9% pur.); the organic linkers benzene-1,4-dicarboxylic acid (H_2bdc, 98% pur.), biphenyl-4,4′-dicarboxylic acid (H_2bpdc, 97% pur.) and 2,2′-bipyridine-5,5′-dicarboxylic acid (H_2bpydc, 97% pur.); and the aluminium salt $AlCl_3 \cdot 6H_2O$ (99% pur.) have been supplied from abcr. In addition, the aluminium salts $Al(NO_3)_3 \cdot 9H_2O$ (≥98% ACS gra.); the surfactants *N*,*N*,*N*-trimethylhexadecan-1-ammonium bromide (CTAB, ≥96% pur.) and 1-ethenylpyrrolidin-2-one ($PVP_{40\,000}$, avg. mol. wt. 40 000, MQ: 200); and the reference material polytetrafluoroethylene (PTFE, 1 μm particle size) and magnesium oxide (MgO, MQ: 300) were purchased from Sigma-Aldrich (Merck). Moreover, the solvents *N*,*N*-dimethylformamide (DMF, 99% pur., purchased from Grüssing), ethanenitrile (MeCN, ≥99.8% pur., purchased from Chemsolute (Th. Geyer)), ethanol (EtOH, ≥99.8% abs., Fischer Scientific) and triethylamine (TEA, 99% pur., Fischer Scientific) did not undergo any additional drying process. Nitric acid (HNO_3, tech. qual.) was purchased from STOCKMEIER Chemie. Furthermore, only demineralized water (H_2O) was used for synthesis, analysis, and product purification processes.

Synthesis and post-synthetic modification procedure

Synthesis of Eu^{3+}-bdc and Tb^{3+}-bdc. The synthesis according to Guo *et al.*[43] was modified in certain steps and started by mixing of 80 mg (0.179 mmol) $Eu(NO_3)_3 \cdot 6H_2O$ or 80 mg (0.177 mmol) $Tb(NO_3)_3 \cdot 6H_2O$, respectively, and 32 mg (0.193 mmol) H_2bdc inside a 30 mL snap-on cap glass vial. Subsequent dilution in 20 mL DMF, 4 mL abs. EtOH and 4 mL H_2O resulted in a colourless, transparent solution. After the addition of four drops of TEA, the solution became opaque. After shaking for 60 s, five drops of 6 M HNO_3 were added until the dispersion became transparent again. The vial was closed with a lid, sealed with Parafilm® and placed in an autoclave (Heraeus) at 55 °C for 7 d. Finally, the colourless precipitate was washed stepwise with 10 mL of DMF and EtOH, consecutively, and centrifuged at 10 565 g (rcf) for 10 min after each step.

Eu^{3+}-bdc. Drying under vacuum gave 38 mg (0.026 mmol, 1472.72 g mol^{-1}, 15%) of a colourless powder. Organic elemental analysis ($^3_\infty[Eu_3(bdc)_{4.5}] \cdot 3.3DMF \cdot 0.9H_2O$, found: C, 37.9; H, 3.0; N, 3.2. Calc. for $Eu_3C_{45.9}H_{42.9}N_{3.3}O_{22.2}$: C, 37.4; H, 2.9; N, 3.1%).

Tb^{3+}-bdc. Drying under vacuum gave 48 mg (0.032 mmol, 1510.96 g mol^{-1}, 18%) of a colourless powder. Organic elemental analysis ($^3_\infty[Tb_3(bdc)_{4.5}] \cdot 3.7DMF \cdot 1.4H_2O$, found: C, 37.4; H, 3.0; N, 3.5. Calc. for $Tb_3C_{47.1}H_{46.7}N_{3.7}O_{23.1}$: C, 37.4; H, 3.1; N, 3.4%).

Synthesis of nEu^{3+}-bdc and nTb^{3+}-bdc. The synthesis according to Neufeld *et al.*[46] was modified in certain steps and started by dissolving 280 mg (0.628 mmol) $Eu(NO_3)_3 \cdot 6H_2O$ or 280 mg (0.618 mmol) $Tb(NO_3)_3 \cdot 6H_2O$, respectively, and 4220 mg (29.90 mmol) $PVP_{40\,000}$, separately, in 40 mL DMF under vigorous stirring. Subsequently, 190 mg (1.14 mmol) H_2bdc and 3220 mg (8.78 mmol) CTAB were dissolved in 200 mL DMF inside a 500 mL three-necked round-bottomed flask equipped with a reflux condenser, under vigorous stirring at 55 °C for 60 min. Afterwards, the previously prepared solutions were then gradually added, followed by the addition of 200 μL of TEA. The reaction mixture became slightly opaque and was stirred vigorously for a further 60 min at 55 °C. Further heating at 90 °C for 6 h resulted in a thick opaque, pale yellowish dispersion, which was washed with 10 mL DMF (1×) and 10 mL EtOH (2×), consecutively, and centrifuged at 17 855 g (rcf) for 10 min after each step.

nEu^{3+}-bdc. Drying under vacuum gave 188 mg of a pale yellowish powder.

nTb^{3+}-bdc. Drying under vacuum gave 121 mg of a pale yellowish powder.

Synthesis of DUT-5. The synthesis according to Senkovska *et al.*[44] started by suspending 521 mg (2.15 mmol) H_2bpdc in 15 mL DMF and stirring at 55 °C for 30 min. Then, 1042 mg (2.778 mmol) $Al(NO_3)_3 \cdot 9H_2O$ were added and dissolved. The reaction mixture was kept in a closed 120 mL pressure tube (Ace Glass) for 24 h at 120 °C. Subsequent liquid/solid separation by centrifugation (6762 g (rcf), 10 min) yielded a colourless solid. Final drying under vacuum gave 946 mg (1.923 mmol, 492.05 g mol^{-1}, 89%) of a colourless powder. Organic elemental analysis ($^3_\infty[Al(OH)bpdc] \cdot 2.4DMF \cdot 1.8H_2O$, found: C, 51.8; H, 5.5; N, 6.8. Calc. for $AlC_{21.1}H_{29.4}N_{2.4}O_{9.2}$ C, 51.6; H, 6.0; N, 6.8%).

Synthesis of nDUT-5. The synthesis according to Neufeld *et al.*[46] was modified in certain steps and started with the dissolution of 392 mg (1.62 mmol) H_2bpdc and 2250 mg (6.174 mmol) CTAB in 200 mL DMF at 55 °C. At the same time, 1051 mg (6.174 mmol) $PVP_{40\,000}$ and 417 mg (1.11 mmol) $Al(NO_3)_3 \cdot 9H_2O$ were dissolved in 40 mL and 20 mL DMF, respectively, and gradually added to the reaction mixture. After 5 min of stirring, adding of 300 μL of TEA made the solution opaque. This was followed by a further 1 h of stirring at 55 °C. Afterwards, the reaction mixture was treated at 120 °C for 24 h in a reflux apparatus. First, the purification process was started by separating the precipitate by centrifugation at 17 855 g (rcf) for 10 min. Second, washing with 15 mL DMF (4×) and 10 mL H_2O (4×), followed by the above-mentioned centrifugation procedure after each step, yielded a pale brownish residue. Finally, the specimen was dried under vacuum to give 467 mg of a pale brownish powder.

Synthesis of MOF-253. The synthesis according to Bloch *et al.*[45] was modified in certain steps and started by suspending 306 mg (1.25 mmol) H_2bpydc in 30 mL DMF and stirring at 55 °C for 30 min. After dissolving 303 mg (1.26 mmol) $AlCl_3 \cdot 6H_2O$, the reaction mixture was heated for 24 h at 120 °C in a closed pressure tube (Ace Glass). The pale greenish precipitate was centrifuged (10 565 g (rcf), 10 min) and subsequently reheated for 15 min in 20 mL DMF under reflux for purification. After a short cooling period, the product was centrifuged again (1690 g (rcf), 10 min) and the supernatant removed. Repeated purification with 20 mL DMF (1×) and 20 mL EtOH (2×), followed by vacuum drying yielded 324 mg (0.852 mmol, 380.29 g mol^{-1}, 68%) of a colourless powder. Organic elemental analysis ($^3_\infty[Al(OH)bpydc] \cdot 1.3EtOH \cdot 1.9H2O$, found: C, 46.1; H, 4.9; N, 7.4. Calc. for $AlC_{14.6}H_{18.6}N_2O_{8.2}$: C, 46.1; H, 5.0; N, 7.4%).

Synthesis of nMOF-253. The synthesis according to Neufeld *et al.*[46] was modified in certain steps and started by dissolving of 159 mg (0.651 mmol) H_2bpydc and 899 mg (2.47 mmol) CTAB in 80 mL DMF at 55 °C. Simultaneously, 421 mg (2.98 mmol) PVP_{40}

$_{000}$ were dissolved in 16 mL DMF and gradually added to the reaction mixture. Additionally, 108 mg (0.447 mmol) $AlCl_3 \cdot 6H_2O$ were added as solid. After 5 min of stirring, adding of 120 μL of TEA made the solution opaque. This was followed by another 1 h of stirring at 55 °C. Afterwards, the reaction mixture was treated at 120 °C for 24 h in a reflux apparatus. First, the purification process was started by separating the precipitate by centrifugation at 17 855 g (rcf) for 10 min. Second, washing with 10 mL DMF (4×) and 10 mL EtOH (4×), followed by the aforementioned centrifugation procedure after each step, yielded in a dark brownish residue. Finally, the specimen was dried under vacuum, yielding 136 mg of a dark brownish powder.

Post-synthetic modification of DUT-5, nDUT-5, MOF-253 and nMOF-253. Two different approaches going to be stated in the following section. For post-synthetic modification, different amounts of $Eu(NO_3)_3 \cdot 6H_2O$ and $Tb(NO_3)_3 \cdot 6H_2O$ were used in combination with different temperatures and solvents to yield DUT-5:Ln^{3+}, nDUT-5:Ln^{3+}, MOF-253:Ln^{3+} and nMOF-253:Ln^{3+}.

The first post-synthetic modification approach was carried out at room temperature (RT) in a snap-on cap glass vial. Previously, $Ln(NO_3)_3 \cdot 6H_2O$ has been dissolved in EtOH. Then, 40 mg specimen were soaked with 1 mL of a 0.1 M Ln^{3+}-solution. After 5 min of sonicating, the vial was closed and left untouched for one week. After rinsing the specimen out of the vial, it was centrifuged at 17 855 g (rcf) for 10 min. Ultimately, the post-synthetically modified sample was washed with 2 mL of EtOH, centrifuged and dried under vacuum to obtain a powder.

The second post-synthetic modification approach was carried out at 65 °C in a closed pressure tube (Ace Glass) according to the procedure of Lu *et al.*,[62] with some modifications. Previously, 45 mg $Ln(NO_3)_3 \cdot 6H_2O$ were dissolved in 10 mL MeCN (0.01 M). After adding 40 mg MOF to the mixture, the mixture was again dispersed with 5 mL MeCN and sonicated for 5 min. This was followed by a heating step for 24 h and the final purification process, consisting of centrifugation (17 855 g (rcf), 10 min), washing (10 mL MeCN) and sonication (5 min) three times consecutively. After drying under vacuum, the post-synthetically modified sample was obtained as powder.

Analytical methods

Powder X-ray diffraction (PXRD). Structural information has been acquired using a X'Pert Pro MPD with Data Collector (ver. 5.4.0.90) software from PANalytical. The X-ray beam was generated by an Empyrean Cu LFF X-ray tube ($\lambda_{Cu\text{-}K\alpha} = 154.06$ pm) at 40 kV and 40 mA. After focusing the incident beam by Soller slits (0.04 rad), a beam mask (10 mm) and a fixed anti-scatter slit (1°), a flattened sample presented on a silicon waver diffracted the beam, which then passed through an angled anti-scatter slit (0.5°), again Soller slits (0.04 rad) and a Beta-filter Nickel towards an X'Celerator with a FASS detector. The measurement was performed in Bragg–Brentano geometry between 3.5° and 60° in 2θ on account of a PW3050/60 goniometer at RT and ambient atmosphere. Finally, the diffractogram was background corrected using DIFFRAC.EVA (ver. 5.2.0.5, Bruker) and plotted using OriginPro 2023 (ver. 10.0.0.154, OriginLab).

Dynamic light scattering (DLS). Particle size and its distribution were determined using a StabiSizer® PMX 200CS from Particle Metrix. The Microtrac FLEX Application Software (ver. 10.5.4.) from Mictrotrac was used for data acquisition. The sample preparation began by rinsing and filling up to half of the volume of the snap-on cap glass vials with EtOH. Subsequently, a spatula tip of sample was added to one of the vials and sonicated for 10 min at 30 °C. After checking the stability of the dispersion, data acquisition was performed, first for the blank (EtOH only) and then for the dispersion. Additionally, for improving statistics, the measurement was carried out three times, for 120 s each. The particle size distribution plots shown in this work represent the average of these three measurements and have been plotted using OriginPro 2023 (ver. 10.0.0.154, OriginLab). Furthermore, the average value for particle size is denoted with $\pm 2\sigma$.

Scanning electron microscopy (SEM). Particle morphology was examined using a GeminiSEM 560 and the software SMART SEM (ver. 6.08) from Carl Zeiss NTS. Ground samples were waved onto a sticky carbon pad attached to an aluminium carrier. The surface was cleaned by carefully blowing off loose material with pressurized air, to ensure no contamination within the vacuum chamber of the instrument. The electron images were recorded with a 7.5 μm aperture and an acceleration voltage of 3 kV at a working distance of 3 mm using a Schottky field emitter as electron source. Moreover, a SE-InLens detector afforded the images from secondary electrons. Particle sizes were determined using ImageJ (ver. 1.53f51) from National Institute of Health.

Microwave plasma–atomic emission spectroscopy (MP-AES). The amounts of Eu^{3+} and Tb^{3+} in the samples were determined by a 4210 MP-AES with MP Expert Software (ver. 1.6.0.9255) from Agilent Technologies using the external calibration method. Standard solutions for Al (22102, Grüssing), Eu (2414.1, Carl Roth) and Tb (2476.1, Carl Roth) were diluted to give standard solutions of 0.05 mg L^{-1}, 0.10 mg L^{-1}, 0.50 mg L^{-1}, 1.00 mg L^{-1}, 5.00 mg L^{-1} and 10.00 mg L^{-1} for external calibration. First, the sample was dissolved in HNO_3 (wt 1%). For DUT-5:Ln^{3+}, nDUT-5:Ln^{3+}, MOF-253:Ln^{3+} and nMOF-253:Ln^{3+}, the sample did not dissolve completely, so that an additional step of centrifugation (20 707 g (rcf), 15 min) was carried out to remove the linker (stem solution). Subsequently, the procedure was the same to all MOFs. Several dilutions were prepared from stem solution to theoretically match the concentration range of the external calibration. Intensity was recorded at characteristic atomic emission wavelengths (Al: 394.401 nm, 396.152 nm; Eu: 381.967 nm, 412.973 nm; Tb: 350.917 nm, 384.874 nm) were used to determine the concentration of the analytes. The instrument required 90 min for sample uptake, followed by 30 min for rinsing and 15 min for flow stabilization. This procedure was repeated after each dilution.

UV-Vis diffuse reflectance spectroscopy (UV-Vis-DRS). Diffuse reflectance spectra were acquired using a Cary 5000 UV-Vis-NIR spectrophotometer and the Cary WinUV Scan Application software (ver. 6.3.0.1595) from Agilent Technologies. The

instrument was equipped with a Praying Mantis™ Diffuse Reflectance Accessory from Harrick Scientific Products and operated in double beam mode with reduced slit height. Raw data is given in reflectance units. Since this is a relative method, PTFE was chosen as reference material. Both, reference and MOF were ground and successively filled into a DRP-SAP microsample-cup (Harrick Scientific Products) and flattened with a spatula. Finally, the reflectance spectrum was recorded and corrected by PTFE according to the following operation: $\%R_{corr}^{MOF} = \%R_{raw}^{MOF}/\%R_{raw}^{PTFE}$.

Photophysical methods for the determination of qualitative and quantitative properties. Qualitative PL excitation and emission spectra were recorded using a Jobin Yvon Fluorolog 3 with the FluorEssence™ for Windows® (ver. 3.9.0.1) software supplied by HORIBA. A Xe short-arc lamp (USHIO) was used in conjunction with a double-grated monochromator at the excitation site, while another monochromator was used in conjunction with a photomultiplier tube R928P (HAMAMATSU PHOTONICS K.K.) at the emission site to record the spectra. Additionally, mathematical corrections for monochromators and detectors were provided by the manufacturer. The spectral distribution of the lamp is measured by a reference detector (R signal) and corrected *in situ*. For measurement, the sample was filled into a cylindric synthetic-quartz glass cuvette (proQuarz) and positioned in the focus point of the beam. To acquire a full spectrum, a long-pass edge filter 550 (Newport) was placed in the beam path between the sample and the detector. The excitation and emission spectra were recorded separately and then plotted together in one graph with OriginPro 2023 (ver. 10.0.0.154) from OriginLab.

QY determination was performed using a Jobin Yvon Fluorolog 3 with the FluorEssence™ for Windows® (ver. 3.9.0.1) software equipped with a Quanta-φ Integrating Sphere F-3029 from HORIBA. For the measurement, the reference and sample, respectively, were filled into a micro cell cuvette 18-F/ST/C/Q/10 from Starna Scientific. The quantum yield determination was repeated three times for each specimen and related to the reference material MgO. An additional check using another standard material γ-$[Tb_4(OAc)_{12}(ptpy)_2]$ verified the calibration of the Quanta-φ Integrating Sphere ($\lambda_{ex} = 310$ nm, $\lambda_{em} = 450$–700 nm; $\Phi_{exp} = 46(1)\%$, $\Phi_{lit} = 46(3)\%$ (ref. 63)). Ln^{3+}-based QYs were determined with $\lambda_{ex} = 310$ nm and $\lambda_{em} = 450$–700 nm. Linker-based QYs were determined with $\lambda_{ex} = 310$ nm, $\lambda_{em} = 315$–520 nm for DUT-5; $\lambda_{ex} = 310$ nm, $\lambda_{em} = 335$–570 nm for nDUT-5; $\lambda_{ex} = 310$ nm, $\lambda_{em} = 330$–540 nm for DUT-5:Tb^{3+} and nDUT-5:Tb^{3+}; $\lambda_{ex} = 310$ nm, $\lambda_{em} = 330$–550 nm for DUT-5:Eu^{3+} and nDUT-5:Eu^{3+} and $\lambda_{ex} = 360$ nm, $\lambda_{em} = 370$–700 nm for MOF-253, nMOF-253, MOF-253:Tb^{3+} and nMOF-253:Tb^{3+}.

Lifetime determinations were carried out by recording the overall luminescence decay times (τ) using a Jobin Yvon Fluorolog 3 with the Data Station (ver. 2.7.4) software for data acquisition and the Decay Analysis Software (ver. 6.8.16) for raw data fitting, respectively, from HORIBA. For this purpose, the instrument was upgraded with a TCSPC (time-correlated single-photon counting) and UV Xenon FX-1102 flashlamp from Excelitas Technologies. However, a pulsed Delta Diode™ 278 nm (HORIBA) was necessary for linker emission decay determination. Moreover, for this method, the sample was filled into a cylindrical synthetic-quartz glass cuvette (proQuarz) and placed in the focus of the beam. Subsequently after recording the overall emission decay, the lifetime has been calculated by exponentially fitting the data with $I(t) = A + B_1 \cdot e^{-(t-t_0/\tau_1)} + B_2 \cdot e^{-(t-t_0/\tau_2)}$, where $I(t)$ is the emission intensity depending on time, A is the baseline factor, B is the pre-exponential factor, t_0 is the time offset, t is the time and τ is the lifetime.

Phosphorescence spectra were recorded using a pulsed UV Xenon FX-1102 flashlamp from Excelitas Technologies, each 41 ms a flash. Specimens were cooled down and measured at 77 K inside a specialized Dewar filled with liquid nitrogen. Parameters such as recording delay time, sample window time or counts per flash varied and are given next to the recorded spectra. Subsequently, triplet state determination carried out by using the software OriginPro 2023 (ver. 10.0.0.154) from OriginLab. The intersection of two linear fits marks the triplet state energy.

Organic elemental analysis (OEA). The determinations (wt%) of carbon, hydrogen, and nitrogen were performed with a FlashEA 1112 Series from Thermo Fisher Scientific. The amount of sample was weighed using a UMX-2 scale from METTLER TOLEDO, poured into a tin crucible and burned.

Differential thermoanalysis/thermogravimetry – mass spectrometry (DTA/TG-MS). Thermal properties were simultaneously determined regarding differential thermal analysis and thermogravimetry using a STA 409 PC coupled to a QMS 403 Aëolos Quadro mass spectrometer from NETZSCH. The sample (20–25 mg) was filled into a corundum crucible and heated up to 1000 °C with a heating rate of 5 °C min^{-1}. Argon (20 mL min^{-1}) was used as a protective gas and synthetic air (30 mL min^{-1}) as working gas. MS signals were recorded *via* the quasi-multiple ion detection method (QMID).

Conflicts of interest

There are no conflicts to declare.

Acknowledgements

This work is generously funded by the Deutsche Forschungsgemeinschaft (DFG) within the project MU-1562/13-1 within the priority program SPP-1928 “COORNETs”.

References

1 L. Mu, B. Liu, H. Liu, Y. Yang, C. Sun and G. Chen, *J. Mater. Chem.*, 2012, **22**, 12246.
2 D. Alezi, Y. Belmabkhout, M. Suyetin, P. M. Bhatt, L. J. Weseliński, V. Solovyeva, K. Adil, I. Spanopoulos, P. N. Trikalitis, A. H. Emwas and M. Eddaoudi, *J. Am. Chem. Soc.*, 2015, **137**, 13308–13318.
3 S. Denning, A. A. Majid, J. M. Lucero, J. M. Crawford, M. A. Carreon and C. A. Koh, *ACS Appl. Mater. Interfaces*, 2020, **12**, 53510–53518.

4 Z. He, Y. Dai, X. Li, D. Guo, Y. Liu, X. Huang, J. Jiang, S. Wang, G. Zhu, F. Zhang, L. Lin, J.-J. Zhu, G. Yu and X. Chen, *Small*, 2019, **15**, 1804131.

5 A. Wagner, Q. Liu, O. L. Rose, A. Eden, A. Vijay, Y. Rojanasakul and C. Z. Dinu, *Int. J. Nanomed.*, 2019, **14**, 7583–7591.

6 S. A. Ahmed, M. Nur Hasan, D. Bagchi, H. M. Altass, M. Morad, I. I. Althagafi, A. M. Hameed, A. Sayqal, A. E. R. S. Khder, B. H. Asghar, H. A. Katouah and S. K. Pal, *R. Soc. Open Sci.*, 2020, **7**, 200959.

7 R. Van Zeeland, X. Li, W. Huang and L. M. Stanley, *RSC Adv.*, 2016, **6**, 56330–56334.

8 A. Herbst, A. Khutia and C. Janiak, *Inorg. Chem.*, 2014, **53**, 7319–7333.

9 S. Aguado, J. Canivet and D. Farrusseng, *J. Mater. Chem.*, 2011, **21**, 7582.

10 A. D. Pournara, A. Margariti, G. D. Tarlas, A. Kourtelaris, V. Petkov, C. Kokkinos, A. Economou, G. S. Papaefstathiou and M. J. Manos, *J. Mater. Chem. A*, 2019, **7**, 15432–15443.

11 M. Wickenheisser, T. Paul and C. Janiak, *Microporous Mesoporous Mater.*, 2016, **220**, 258–269.

12 Z. Chen, P. Li, X. Zhang, P. Li, M. C. Wasson, T. Islamoglu, J. F. Stoddart and O. K. Farha, *J. Am. Chem. Soc.*, 2019, **141**, 2900–2905.

13 K. Müller-Buschbaum, F. Beuerle and C. Feldmann, *Microporous Mesoporous Mater.*, 2015, **216**, 171–199.

14 V. Chernikova, O. Yassine, O. Shekhah, M. Eddaoudi and K. N. Salama, *J. Mater. Chem. A*, 2018, **6**, 5550–5554.

15 L. J. Small, S. E. Henkelis, D. X. Rademacher, M. E. Schindelholz, J. L. Krumhansl, D. J. Vogel and T. M. Nenoff, *Adv. Funct. Mater.*, 2020, **30**, 2006598.

16 H. Yang, B. Liu, J. Bright, S. Kasani, J. Yang, X. Zhang and N. Wu, *ACS Appl. Energy Mater.*, 2020, **3**, 4007–4013.

17 S.-S. Liu, Z. Han, J.-S. Yang, S.-Z. Huang, X.-Y. Dong and S.-Q. Zang, *Inorg. Chem.*, 2020, **59**, 396–402.

18 Z. Wei, R. Maile, L. M. Riegger, M. Rohnke, K. Müller-Buschbaum and J. Janek, *Batteries Supercaps*, 2022, **5**(12), e202200318.

19 R. Freund, O. Zaremba, G. Arnauts, R. Ameloot, G. Skorupskii, M. Dincă, A. Bavykina, J. Gascon, A. Ejsmont, J. Goscianska, M. Kalmutzki, U. Lächelt, E. Ploetz, C. S. Diercks and S. Wuttke, *Angew. Chem., Int. Ed.*, 2021, **60**, 23975–24001.

20 L. V. Meyer, F. Schönfeld, A. Zurawski, M. Mai, C. Feldmann and K. Müller-Buschbaum, *Dalton Trans.*, 2015, **44**, 4070–4079.

21 K. Xu, F. Wang, S. Huang, Z. Yu, J. Zhang, J. Yu, H. Gao, Y. Fu, X. Li and Y. Zhao, *RSC Adv.*, 2016, **6**, 91741–91747.

22 K. Mandel, T. Granath, T. Wehner, M. Rey, W. Stracke, N. Vogel, G. Sextl and K. Müller-Buschbaum, *ACS Nano*, 2017, **11**, 779–787.

23 W. T. Carnall, in *Non-metallic Compounds – I*, 1979, vol. 3, pp. 171–208.

24 R. E. Whan and G. A. Crosby, *J. Mol. Spectrosc.*, 1962, **8**, 315–327.

25 S. I. Weissman, *J. Chem. Phys.*, 1942, **10**, 214–217.

26 F. Luo and S. R. Batten, *Dalton Trans.*, 2010, **39**, 4485.

27 T. N. Nguyen, S. V. Eliseeva, A. Gładysiak, S. Petoud and K. C. Stylianou, *J. Mater. Chem. A*, 2020, **8**, 10188–10192.

28 K. A. White, D. A. Chengelis, K. A. Gogick, J. Stehman, N. L. Rosi and S. Petoud, *J. Am. Chem. Soc.*, 2009, **131**, 18069–18071.

29 M. Naito, T. Yokoyama, K. Hosokawa and K. Nogi, in *Nanoparticle Technology Handbook*, Elsevier Science, 2018, pp. 3–44.

30 F. Martinez-Julian, A. Guerrero, M. Haro, J. Bisquert, D. Bresser, E. Paillard, S. Passerini and G. Garcia-Belmonte, *J. Phys. Chem. C*, 2014, **118**, 6069–6076.

31 S. S. El-Deen, A. M. Hashem, A. E. Abdel Ghany, S. Indris, H. Ehrenberg, A. Mauger and C. M. Julien, *Ionics*, 2018, **24**, 2925–2934.

32 D.-H. Ha, M. A. Islam and R. D. Robinson, *Nano Lett.*, 2012, **12**, 5122–5130.

33 Y. L. F. Musico, C. M. Santos, M. L. P. Dalida and D. F. Rodrigues, *ACS Sustain. Chem. Eng.*, 2014, **2**, 1559–1565.

34 W. Wanas, S. A. Abd El-Kaream, S. Ebrahim, M. Soliman and M. Karim, *Sci. Rep.*, 2023, **13**, 27.

35 G. Prencipe, S. M. Tabakman, K. Welsher, Z. Liu, A. P. Goodwin, L. Zhang, J. Henry and H. Dai, *J. Am. Chem. Soc.*, 2009, **131**, 4783–4787.

36 S. L. Pal, U. Jana, P. K. Manna, G. P. Mohanta and R. Manavalan, *J. Appl. Pharm. Sci.*, 2011, **1**, 228–234.

37 M. Naito, T. Yokoyama, K. Hosokawa and K. Nogi, in *Nanoparticle Technology Handbook*, Elsevier Science, 2018, pp. 49–105.

38 J. Andreo, R. Ettlinger, O. Zaremba, Q. Peña, U. Lächelt, R. F. De Luis, R. Freund, S. Canossa, E. Ploetz, W. Zhu, C. S. Diercks, H. Gröger and S. Wuttke, *J. Am. Chem. Soc.*, 2022, **144**, 7531–7550.

39 C. D. Ma, C. Wang, C. Acevedo-Vélez, S. H. Gellman and N. L. Abbott, *Nature*, 2015, **517**, 347–350.

40 X.-G. Wang, Q. Cheng, Y. Yu and X.-Z. Zhang, *Angew. Chem., Int. Ed.*, 2018, **57**, 7836–7840.

41 T. Kundu, S. Mitra, P. Patra, A. Goswami, D. Díaz Díaz and R. Banerjee, *Chem. – Eur. J.*, 2014, **20**, 10514–10518.

42 R. Nagarajan and E. Ruckenstein, *Langmuir*, 1991, **7**, 2934–2969.

43 X. Guo, G. Zhu, F. Sun, Z. Li, X. Zhao, X. Li, H. Wang and S. Qiu, *Inorg. Chem.*, 2006, **45**, 2581–2587.

44 I. Senkovska, F. Hoffmann, M. Fröba, J. Getzschmann, W. Böhlmann and S. Kaskel, *Microporous Mesoporous Mater.*, 2009, **122**, 93–98.

45 E. D. Bloch, D. Britt, C. Lee, C. J. Doonan, F. J. Uribe-Romo, H. Furukawa, J. R. Long and O. M. Yaghi, *J. Am. Chem. Soc.*, 2010, **132**, 14382–14384.

46 M. J. Neufeld, H. Winter, M. R. Landry, A. M. Goforth, S. Khan, G. Pratx and C. Sun, *ACS Appl. Mater. Interfaces*, 2020, **12**, 26943–26954.

47 X. Deng, J. Albero, L. Xu, H. García and Z. Li, *Inorg. Chem.*, 2018, **57**, 8276–8286.

48 S. Chhetri, N. Adak, P. Samanta, N. Murmu and T. Kuila, *J. Compos. Sci.*, 2018, **2**, 37.

49 Y. Yuan, W. Wang, L. Qiu, F. Peng, X. Jiang, A. Xie, Y. Shen, X. Tian and L. Zhang, *Mater. Chem. Phys.*, 2011, **131**, 358–361.
50 C. Wang, J. Kim, J. Tang, M. Kim, H. Lim, V. Malgras, J. You, Q. Xu, J. Li and Y. Yamauchi, *Chem*, 2020, **6**, 19–40.
51 X. Xia, J. Zeng, L. K. Oetjen, Q. Li and Y. Xia, *J. Am. Chem. Soc.*, 2012, **134**, 1793–1801.
52 Z. Haghi and S. M. Masoudpanah, *J. Sol-Gel Sci. Technol.*, 2019, **91**, 335–341.
53 Y. K. Du, P. Yang, Z. G. Mou, N. P. Hua and L. Jiang, *J. Appl. Polym. Sci.*, 2006, **99**, 23–26.
54 P. Horcajada, F. Salles, S. Wuttke, T. Devic, D. Heurtaux, G. Maurin, A. Vimont, M. Daturi, O. David, E. Magnier, N. Stock, Y. Filinchuk, D. Popov, C. Riekel, G. Férey and C. Serre, *J. Am. Chem. Soc.*, 2011, **133**, 17839–17847.
55 J. V Alemán, A. V Chadwick, J. He, M. Hess, K. Horie, R. G. Jones, P. Kratochvíl, I. Meisel, I. Mita, G. Moad, S. Penczek and R. F. T. Stepto, *Pure Appl. Chem.*, 2007, **79**, 1801–1829.
56 K. Binnemans, *Coord. Chem. Rev.*, 2015, **295**, 1–45.
57 P. A. Tanner, *Chem. Soc. Rev.*, 2013, **42**, 5090.
58 D. Y. Medina-Velazquez, U. Caldiño, A. Morales-Ramirez, J. Reyes-Miranda, R. E. Lopez, R. Escudero, R. Ruiz-Guerrero and M. F. Morales Perez, *Opt. Mater.*, 2019, **87**, 3–10.
59 M. Latva, H. Takalo, V.-M. Mukkala, C. Matachescu, J. C. Rodríguez-Ubis and J. Kankare, *J. Lumin.*, 1997, **75**, 149–169.
60 W. T. Carnall, P. R. Fields and K. Rajnak, *J. Chem. Phys.*, 1968, **49**, 4447–4449.
61 W. T. Carnall, P. R. Fields and K. Rajnak, *J. Chem. Phys.*, 1968, **49**, 4450–4455.
62 Y. Lu and B. Yan, *J. Mater. Chem. C*, 2014, **2**, 7411–7416.
63 A. E. Sedykh, M. Becker, M. T. Seuffert, D. Heuler, M. Maxeiner, D. G. Kurth, C. E. Housecroft, E. C. Constable and K. Müller-Buschbaum, *ChemPhotoChem*, 2023, **7**, e202200244.

3.2 NanoMOF-based Multi-Level Anti-Counterfeiting by a Combination of Visible and Invisible Photoluminescence and Conductivity

published in *Advanced Functional Materials*
as part of the “Special Issue Coordination Networks: Building Blocks for Functional Systems (COORNETs)”.

Moritz Maxeiner, Ruben Maile, Murat Cuvalli, Andreas Wolf, Ayisha Komal, Robert Oestreich, Christoph Janiak, Karl Mandel, Alexander Knebel, and Klaus Müller-Buschbaum

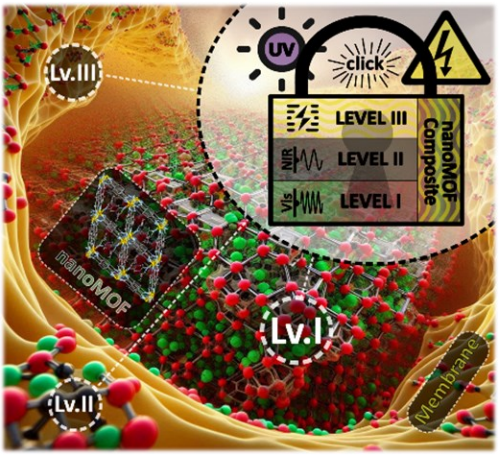

Supporting Information is available in
Appendix A – Supporting Information – Chapter 3.2.

Supporting video material is available online.

Reprinted with permission from *Adv. Funct. Mater.* **2025**, 2500794.

DOI: 10.1002/adfm.202500794

RESEARCH ARTICLE

ADVANCED FUNCTIONAL MATERIALS
www.afm-journal.de

NanoMOF-Based Multilevel Anti-Counterfeiting by a Combination of Visible and Invisible Photoluminescence and Conductivity

*Moritz Maxeiner, Ruben Maile, Murat Cuvalli, Andreas Wolf, Ayisha Komal, Robert Oestreich, Christoph Janiak, Karl Mandel, Alexander Knebel, and Klaus Müller-Buschbaum**

This study presents nanosized metal-organic framwork (nanoMOF)-based multifunctional mixed-matrix-membranes (MMMs) and composite powders as extremely sensitive responder materials for a responder-stimulus based multilevel anti-counterfeiting. The physicochemical properties of nanoMOF-based composites offer a wide operational range as anti-counterfeiting tags. Nine responder materials are presented, constituted of trivalent lanthanide-containing nanoMOFs ($[Ln_3(bdc)_{4.5}(H_2O)_3(dmf)_2]$ (nLn-bdc); bdc^{2-}=benzene-1,4-dicarboxylate; Ln=Eu, Tb, Yb) and polystyrene sulfonate, pyrolyzed resorcinol-formaldehyde and polysulfone as matrices. These materials inherit distinct properties, and their combination provides visible and near-infrared light emission and specific conductivity for multiple security level anti-counterfeiting. The additive and interdependent nature of security features in the developed anti-counterfeiting materials ensures that altering one feature will invariably affect others, thereby reinforcing the overall integrity and resilience of the security mechanism. Even the pitch-black composites of nLn-bdc and pyrolyzed resorcinol-formaldehyde show bright light emission to the near-infrared range, when stimulated by UV-light being suitable for black materials. This work also describes a matrix-based active contribution as security feature to an anti-counterfeiting tag, instead of being solely used as a carrier for the security feature-bearing nanoMOFs. The combination of multiple levels of security by different properties marks these multifunctional composites as anti-counterfeiting materials being complicated to copy including a proof-of-principle experiment.

1. Introduction

Product piracy, also known as counterfeiting or trademark infringement, refers to the illegal reproduction or imitation of goods, typically those protected by intellectual property laws such as trademarks, copyrights, or patents. Product piracy can occur in various industries including fashion, electronics, pharmaceuticals, automotive parts, luxury goods or banknotes. These actions lead to an estimated monetary loss of at least 119 billion EUR throughout all industries in the European Union alone in 2019 (and the estimated number of unreported cases is potentially much higher).[1] In order to protect and clearly identify trademarked products, a variety of different anti-counterfeiting tags have been developed using vast combinations of stimulus-responder pairs. Responder materials are made up by combinations of fillers and matrices such as carbon dots.[2–4] and inorganic materials.[5–7] The responder materials become stimulated by means of physical (e.g., light,[2–10] temperature,[8,11,12] magnetism[5,8,13]) or chemical (e.g., pH,[5,14,15] moisture[5,16,17]) stimuli, which in consequence provoke

M. Maxeiner, R. Maile, M. Cuvalli, K. Müller-Buschbaum
Institute of Inorganic and Analytical Chemistry
JustusLiebigUniversity Giessen
Heinrich-Buff-Ring 17, 35392 Giessen, Germany
E-mail: kmbac@uni-giessen.de

The ORCID identification number(s) for the author(s) of this article can be found under https://doi.org/10.1002/adfm.202500794

DOI: 10.1002/adfm.202500794

A. Wolf, K. Mandel
Department of Chemistry and Pharmacy
Friedrich-Alexander University Erlangen-Nürnberg
Egerlandstraße 1, 91058 Erlangen, Germany

A. Wolf, K. Mandel
Fraunhofer-Institute for Silicate Research ISC
Neunerplatz 2, 97082 Würzburg, Germany

A. Komal, A. Knebel
Otto Schott Institute of Materials Research
Friedrich-Schiller-University Jena
Fraunhoferstraße 6, 07743 Jena, Germany

R. Oestreich, C. Janiak
Institute of Inorganic Chemistry and Structural Chemistry
Heinrich-Heine-University Düsseldorf
Universitätsstraße 1, 40204 Düsseldorf, Germany

ADVANCED SCIENCE NEWS
www.advancedsciencenews.com

ADVANCED FUNCTIONAL MATERIALS
www.afm-journal.de

unique features of anti-counterfeiting tags by switching on/off or boost/diminish specific properties of the materials. The more complex the combination of properties, the more difficult the counterfeit is and, so, the more secure the trademarked good beneficially becomes.

Metal–organic frameworks (MOFs) as inorganic–organic hybrid materials open a vast field of possible compounds and properties by combining their inorganic building units (IBU) and bridging organic molecules (linkers) to 3D networks.[18–20] Their huge field of applications covers subjects as chemical sensing,[18,19,21,22] catalysis,[18,19,23] gas sorption[18,19,24–26] as well as biomedical implementation[18,27,28] or ionic conductors.[18,19,29] Especially, nanosized MOFs (nMOFs) are actively investigated in the past regarding their enhanced surface-to-volume ratio, inner surface accessibility and improved dispersibility compared to bulk MOFs.[30–32] Anti-counterfeiting tags made up by MOFs often make use of characteristic optical features in the visible (Vis) wavelength region.[33,34] With hidden security levels in the near-infrared (NIR) wavelength range[35] or proton conductivity[36] the counterfeiting can get even more complex. Specific intrinsic luminescence of MOFs can be provoked by the usage of trivalent lanthanides (Ln^{3+}) as IBUs or dopants, where for instance red and green emission is achieved by using Eu^{3+} and Tb^{3+}, respectively.[33,34] NIR emitters can also be obtained from the lanthanide series with Yb^{3+}, Nd^{3+}, or Er^{3+} and functionalized in MOFs as IBUs or dopants.[35,37] However, a direct excitation of Ln^{3+} ions is barely possible since their electromagnetic transitions are parity forbidden according to Laporte's rule[38] and 4f-orbitals electronically isolated.[39] The "antenna effect"[40] compensates this deficit by transferring energy which had been taken up by the linker (also called "sensitizer" in this context) received from a UV-light source. This sensitization process (see Scheme S1, Supporting Information) starts with the absorption of UV light by the linker as described, which results in the excitation of electrons to elevated energy levels (e.g., $S_{1,v}$). After relaxation to the vibrational ground state of the excited singlet level (e.g., $S_{1,0}$), an intersystem crossing (ISC) ensues, leading to an electron spin flip and the formation of a triplet state level (e.g., $T_{1,v}$) of the linker. Subsequently, after relaxation to the vibrational ground state (e.g., $T_{1,0}$), energy is transferred from the linker to the excited 4f-states of the Ln^{3+} (corresponding term symbol $^{2S+1}L_J^*$; with total quantum numbers for spin (S), orbital (L), and angular (J) momenta). The de-excitation of electrons to the non-excited energy levels $^{2S+1}L_J$ results in 4f–4f emissions that yield the characteristic color impressions observed for lanthanides. Furthermore, the nano character of nLn-MOFs was shown to improve the luminescence properties by providing an improved energy transfer due to a more efficient site occupancy for impregnated Ln^{3+} ions.[41]

Commonly, additives and fillers are deposited by methods such as printing, dip- and spin-coating or chemical binding onto a surface of a matrix which does not exhibit counterfeiting features.[33] A different approach is the use of polymer-filler mixed-matrix-membranes (MMMs).[42,43] In this case, the filler is embedded within a surrounding matrix with a certain vertical and lateral distribution.[44] This requires the filler to be highly dispersible in the matrix which offers a chemically protecting medium isolating the filler from environmental conditions.[45] Furthermore, a huge benefit of MMMs is the ability to combine features of two different materials by simple mixing of the components. For example, incorporating luminescent Ln-MOFs into flexible polymers combines light emission with increased physical and chemical stability, resulting in easy-to-handle luminescent MMMs[46] suitable for use as humidity sensors.[47] To the best of our knowledge, only one MOF-based MMM has been reported as anti-counterfeiting tag by Zhang et al. with Eu-MOF@PMMA (PMMA=poly methyl methacrylate) in 2021.[33,48]

In our work, we demonstrate nine composite materials made by combination of the nanoMOFs nLn-bdc (bdc^{2-}=benzene-1,4-dicarboxylate and Ln=Eu, Tb, Yb) and polystyrene sulfonate (PSS), pyrolyzed resorcinol-formaldehyde (pRF) as well as the polysulfone P-3500 from Udel (PSUd) as matrices. These composites are distinguishable in chemical composition, physical texture and processing procedure which establish a distinct set of properties for each composite. Furthermore, the responder materials were synthesized and designated as multilevel security anti-counterfeiting tags, with a proof-of-principle experiment shown for potential life-like scenarios. An overview of the additive properties and interdependent functions (level I, II, III) used in the development of the responder materials is presented in **Scheme 1**.

2. Results and Discussion

The nMOFs nLn-bdc ($[Ln_3(bdc)_{4.5}(H_2O)_3(dmf)_2]$,[49] Ln=Eu, Tb, Yb; bdc^{2-}=benzene-1,4-dicarboxylate) and another solvent-depending phase ($[Ln_2(bdc)_3(H_2O)_4]$)[50] were synthesized bottom-up with surfactant assisted methods, carrying the optical Vis/NIR features. PSS as well as pRF were selected as matrices showing conductivity as additional feature, while PSUd was used as nonconductive matrix to demonstrate differences between conductive and nonconductive composites in terms of conductivity and the impact of inserted nLn-bdc on the conductive properties of the composites. Schematic depictions and crystal structures of the materials used are shown in **Scheme 2**. In addition to MMMs obtained by the use of PSS as nLn-bdc@PSS and PSUd as nLn-bdc@PSUd, powder composites nLn-bdc@pRF using pRF were also synthesized – all composite materials are further referred to as responder materials. Notably, nonconductive PSUd was used as a representative of commonly used nonfeature-bearing matrices in anti-counterfeiting tags in order to emphasize the advantages of conductive matrices such as the investigated PSS and pRF. Responder material assignment and naming will henceforth be referenced, as shown in **Table 1**. Security levels are represented by luminescence in the Vis-region (level I) visible with the naked eye, while luminescence in the NIR-region (level II) as well as characteristic conductivities (level III) are hidden features invisible for the naked eye. Respective stimuli for the additive anti-counterfeiting are UV light for optical, as well as current and voltage for electrical features.

K. Müller-Buschbaum
Centre for Materials Research (LAMA)
Justus-Liebig-University Giessen
Heinrich-Buff-Ring 16, 35392 Giessen, Germany

ADVANCED SCIENCE NEWS
www.advancedsciencenews.com

ADVANCED FUNCTIONAL MATERIALS
www.afm-journal.de

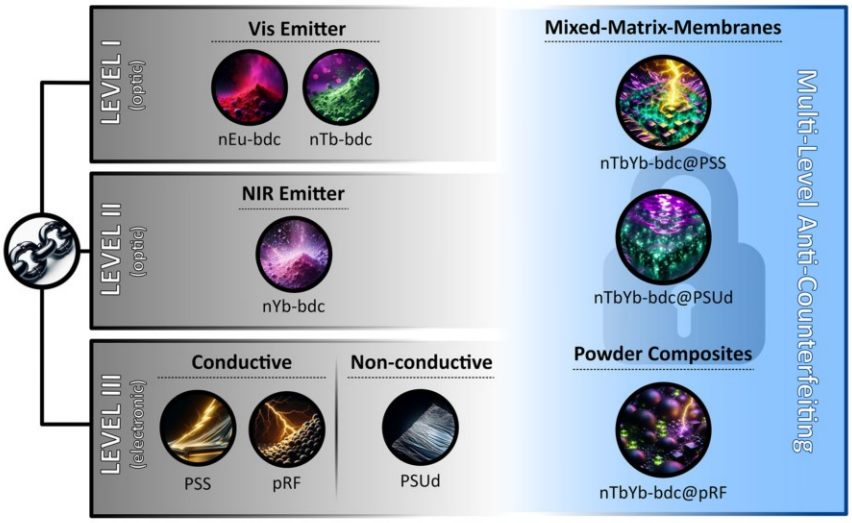

Scheme 1. Principle of the additive properties (Vis/NIR emission, conductivity) and interdependent functions (level I, II, III) of the used nMOFs nEu-bdc, nTb-bdc, and nYb-bdc (with bdc^{2-}=benzene-1,4-dicarboxylate) as well as matrices polystyrene sulfonate (PSS), pyrolyzed resorcinol-formaldehyde (pRF), polysulfone P-3500 from Udel (PSUd). The combination of feature-bearing components yields multilevel anti-counterfeiting mixed-matrix-membranes represented by nTbYb-bdc@PSS and nTbYb-bdc@PSUd as well as powder composites represented by nTbYb-bdc@pRF. The images within the black circles were generated using AI (DALL-E 3.0 engine). A more detailed view of the experiments conducted is given in Scheme S2 in the Supporting Information.

In this work the conductivity does not derive from the nMOFs nLn-bdc, which are insulators, but from the conductivity of PSS and pRF matrices, which is characteristically changed by nMOF incorporation. Furthermore, to replicate the conductivity property (level III), a common method involves incorporating black conductive carbon soot as an additive. However, this technique is inherently constrained, as the addition of black carbon soot alters the photophysical properties of the responsive materials in proportion to the amount used. This proves the interdependence of the security levels, rendering them non-counterfeitable through conventional means. The potential for combinations between nanoMOFs and matrices is vast, which renders these anti-counterfeiting tags more flexible and secure in use than conventional anti-counterfeiting tags where the matrix does not provide a standalone security feature.[2,5,8] Nevertheless, the nonconductive responder nLn-bdc@PSUd still shows level I

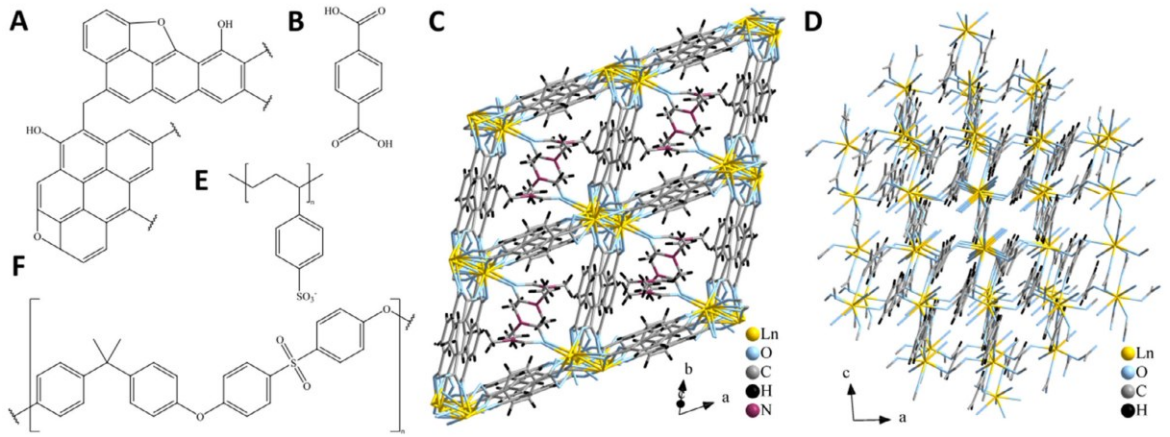

Scheme 2. A) pyrolyzed resorcinol-formaldehyde resin (pRF); B) benzene-1,4-dicarboxylic acid (H_2BDC); C) Phase I of nLn-bdc (Ln=Eu, Tb, Yb) reconstructed from single crystal data[49] representing the constitution $[Tb_3(bdc)_{4.5}(H_2O)_3(dmf)_2]$; D) Phase II of nLn-bdc (Ln=Eu, Tb, Yb) reconstructed from single crystal data[50] representing $[Tb_2(bdc)_3(H_2O)_4]$; E) polystyrene sulfonate (PSS); F) polysulfone Udel P-3500 (PSUd). Non-coordinated solvent molecules were omitted for clarity.

ADVANCED SCIENCE NEWS
www.advancedsciencenews.com

ADVANCED FUNCTIONAL MATERIALS
www.afm-journal.de

Table 1. Assignment and naming of the presented responder materials with respect to matrices and nLn-bdc (Ln=Eu, Tb, Yb).

Matrix	nLn-bdc / wt%			Responder material
	Tb	Eu	Yb	
PSS	9			nTb-bdc@PSS
	4.5	4.5		nTbEu-bdc@PSS
	4.5		4.5	nTbYb-bdc@PSS
PSUd	9			nTb-bdc@PSUd
	4.5	4.5		nTbEu-bdc@PSUd
	4.5		4.5	nTbYb-bdc@PSUd
pRF	20			nTb-bdc@pRF
	20[a)]	20[a)]		nTbEu-bdc@pRF
	10		10	nTbYb-bdc@pRF

[a)] Approach with 20 wt% of both nEu-bdc and nTb-bdc due to consecutive synthesis procedure (for more information see the Experimental Section).

and level II security features, depending on the Ln-cation, which makes it interesting for light responsive anti-counterfeiting applications.

2.1. Characterization

Characterization of the materials was conducted by using several methods including powder X-ray diffraction (PXRD), dynamic light scattering (DLS), scanning electron microscopy (SEM), energy-dispersive X-ray spectroscopy (EDS), and mapping, CHNS elemental analysis, Raman spectroscopy and N_2-physisorption (BET: Brunauer–Emmett–Teller).

2.1.1. Characterization of nLn-bdc (Ln=Eu, Tb, Yb)

The success of syntheses of nLn-bdc (Ln=Eu, Tb, Yb) was checked by PXRD to evaluate phase purity, crystallinity, and potential side phases as well as educt residues (Figure S12, Supporting Information). Furthermore, particle size and its distribution were investigated via DLS and SEM. PXRD results reveal products without reflections of additional phases. The patterns show broad reflections, which is an indicator for small particles and decreased crystallinity, which is typical for nMOFs.[41,51] The powder pattern of nLn-bdc fitting the simulated diffractogram of $[Tb_3(bdc)_{4.5}(H_2O)_3(dmf)_2]$ based on published single-crystal data.[49] As soon as nLn-bdc get soaked in H_2O during nLn-bdc@PSS syntheses, the constitution of the nMOF changes from $[Ln_3(bdc)_{4.5}(H_2O)_3(dmf)_2]$ to $[Ln_2(bdc)_3(H_2O)_4]$, as coordinated DMF exchanges with H_2O, while the stoichiometry between the IBU and the linker is retained. Such behavior was not observed during the exposition of nLn-bdc to ambient humidity. Here the crystal structure of $[Ln_3(bdc)_{4.5}(H_2O)_3(dmf)_2]$ did not undergo the respective transition but remained as-synthesized. A simulated diffractogram of the crystal structure of $[Tb_2(bdc)_3(H_2O)_4]$ obtained from published single crystal data[50] confirms this change to the structure for nLn-bdc@PSS (Figure S13, Supporting Information). Additionally, Figure S14 in the Supporting Information presents powder patterns of the matrices PSS, PSUd, and pRF as well as the responder materials nLn-bdc@PSS, nLn-bdc@PSUd and nLn-bdc@pRF, which are described in detail in the respective sections and corroborate this finding. Since the crystal structures of the nanoMOFs nLn-bdc with Ln=Eu, Tb, Yb are isotypic, the simulated diffractogram of $[Tb_3(bdc)_{4.5}(H_2O)_3(dmf)_2]$ is also valid for nEu-bdc and nYb-bdc.[38] Reflection intensities at $2\theta = 11°$ change between nLn-bdc with the highest intensity for nYb-bdc and weak intensity for nEu-bdc. Such difference can derive from anisotropic crystal growth as well as intercalations into the pore system, such as different amounts of solvent and is more prominent at smaller 2θ angles and different orientations of the crystallite in the X-ray beam. Both effects have previously been observed and assigned in literature for MOF-5.[52] Moreover, reflections are uniformly shifted to smaller 2θ for nLn-bdc@PSS, nLn-bdc@PSUd and nLn-bdc@pRF compared to the nanoMOFs nLn-bdc. Broad amorphous reflections recorded for PSS, PSUd, and pRF at 18°, 18°, and 22°, respectively, can also be seen in the corresponding responder materials and bring evidence for a successful transfer of nLn-bdc onto PSS and PSUd as well as into pRF, respectively. However, use of the Scherrer equation for determining an absolute crystallite size is not feasible due to the broad and unseparated reflections of nLn-bdc shown by PXRD and problems for non-spherical and porous materials.

DLS measures the hydrodynamic diameter of (spherical) particles in stable dispersions. It is important to note that these sizes are consistently larger than the actual sizes of the particles. Thanks to the nano character of the investigated nMOFs, the particles form the required stable dispersion without observed sedimentation for DLS analysis. Thus, DLS gives confident results of a homogeneous distribution of particle size and nano character of the investigated nLn-bdc with Ln=Eu: 190 ± 25 nm, Tb: 130 ± 40 nm, and Yb: 100 ± 30 nm, respectively. Additionally, electron images taken by SEM of nLn-bdc corroborate the DLS results and show particles homogenous in shape and size with dimensions of 20–90 nm for nEu-bdc, 20–50 nm for nTb-bdc and 30–90 nm for nYb-bdc, respectively (see **Figure 1**).

The results of the N_2 adsorption isotherms as well as the pore sizes are presented in the Supporting Information (Figures S5 and S6, Supporting Information). The BET surface area of the nanoMOF $[Tb_3(bdc)_{4.5}(H_2O)_3(dmf)_2]$ was calculated to be 147 $m^2\ g^{-1}$, while BET calculations for the bulk MOF $[Tb_3(bdc)_{4.5}(H_2O)_3(dmf)_2]$ gave a neglectable surface area. The same trend is observable for the nanoMOF $[Eu_3(bdc)_{4.5}(H_2O)_3(dmf)_2]$ and bulk MOF $[Eu_3(bdc)_{4.5}(H_2O)_3(dmf)_2]$. These results demonstrate that the nanoMOFs exhibit a higher surface area compared to the corresponding bulk MOFs. With the dimensions of the pore channels being 4 × 6 Å[49] and the coordinated DMF being located within these channels (see Scheme 2), a high surface area is not to be expected but also not required for the desired functions. Furthermore, the potential influence of residual surfactants on the comparison of bulk MOFs and nanoMOFs should be considered. The surfactants have the potential to obstruct the pore channels of the nanoMOFs, which could result in a reduction in the accessible surface area.

ADVANCED SCIENCE NEWS
www.advancedsciencenews.com

ADVANCED FUNCTIONAL MATERIALS
www.afm-journal.de

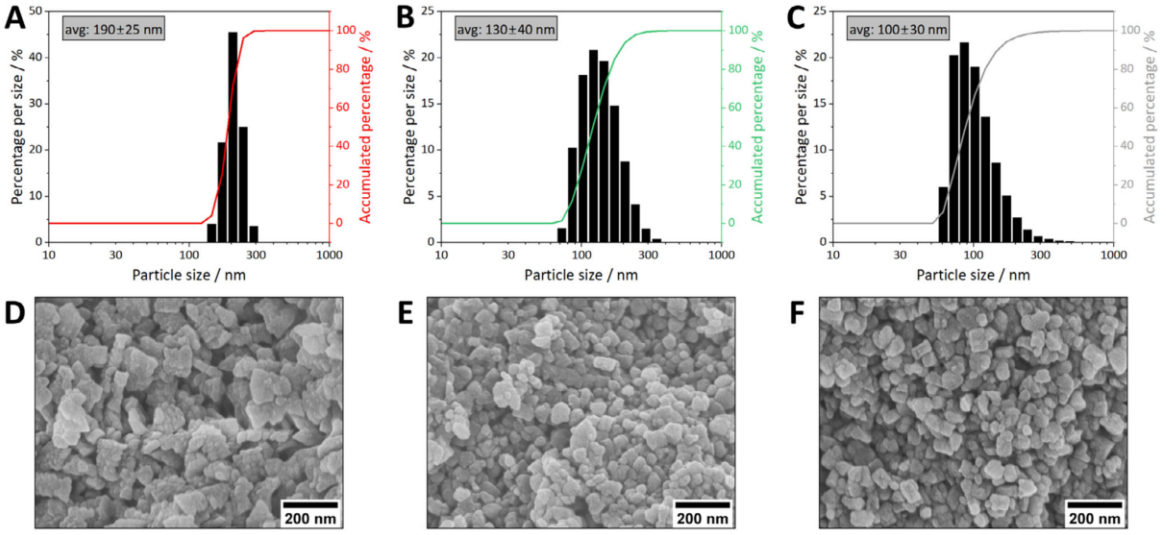

Figure 1. DLS results and SEM images of A,D) nEu-bdc, B,E) nTb-bdc, and C,F) nYb-bdc, respectively.

2.1.2. Characterization of PSS, PSUd, and pRF

In order to form MMMs and powdery composites, the polymers PSS, PSUd and the pyrolyzed resin pRF were investigated. They act as matrices for nLn-bdc (Ln=Eu, Tb, Yb) and are rather amorphous, as indicated by very broad, amorphous reflections in the diffractograms, as shown in Figure S12 in the Supporting Information. Pyrolysis of RF yielding pRF is validated by Raman spectroscopy, exhibiting two broad bands centered approximately at 1350 cm^{-1} (D band) and 1590 cm^{-1} (G band), which are characteristic for graphitic carbon (Figure S15, Supporting Information).[53–55] In addition, CHNS elemental analysis revealed 92.6% of carbon in the obtained powder (Table S1, Supporting Information), which indicates the presence of only few remaining organic functional groups.

The pRF was synthesized as powder and further analyzed with DLS revealing a particle size of 550 ± 190 nm with a homogenous size distribution (Figure S1, Supporting Information). Moreover, pRF particles turned out to be highly dispersible in solvents, such as DMF or EtOH as well as easily sprayable and abradable on air. SEM images show partially aggregated but distinct spheres with a smooth surface and particle sizes of 200–1000 nm (Figure S16C,F, Supporting Information).

In contrast to powdered pRF, the polymers PSS and PSUd were solution casted as membranes. The membranes of the neat polymers, PSS and PSUd, are given in the cross-section of the membranes in Figure S16A,D,B,E in the Supporting Information. Recorded SEM images show homogeneous PSS and PSUd membranes with a thickness of 40–50 and 140–150 µm. Additional SEM images of PSS, PSUd, and pRF are given in Figures S17–S19 (Supporting Information), respectively, to confirm the described properties throughout the whole materials of both PSS and PSUd membranes as well as powdery pRF.

2.1.3. Characterization of nLn-bdc@PSS, nLn-bdc@PSUd, and nLn-bdc@pRF

The responder materials nLn-bdc@PSS, nLn-bdc@PSUd, and nLn-bdc@pRF (Ln=Eu, Tb, Yb) were synthesized using several approaches according to the procedures described in the experimental section. Responder materials nLn-bdc@PSS and nLn-bdc@PSUd were synthesized as MMMs via solution casting, whereas powdery nLn-bdc@pRF were solvothermally synthesized in closed ampoules (under Ar atmosphere). Structure analysis via PXRD confirms the stability of nLn-bdc in nLn-bdc@PSUd and nLn-bdc@pRF as $[Ln_3(bdc)_{4.5}(H_2O)_3(dmf)_2]$, while the nanoMOFs nLn-bdc in nLn-bdc@PSS show a change in structure and constitution to $[Ln_2(bdc)_3(H_2O)_4]$ (see Figure S14, Supporting Information). In order to provide further evidence of the structure change from $[Ln_3(bdc)_{4.5}(H_2O)_3(dmf)_2]$ to $[Ln_2(bdc)_3(H_2O)_4]$, three different approaches were realized with nEu-bdc as a representative for nLn-bdc (Ln=Eu, Tb, Yb) and results are given in Figure S13 in the Supporting Information.

First, nEu-bdc was post-synthetically modified by soaking in H_2O for the addition of H_2O instead of DMF represents the difference between the synthesis procedures of nLn-bdc@PSS and nLn-bdc@PSUd/nLn-bdc@pRF, respectively. The H_2O soaking treatment provokes the structure change from $[Eu_3(bdc)_{4.5}(H_2O)_3(dmf)_2]$ to $[Eu_2(bdc)_3(H_2O)_4]$, as PXRD confirms.

Second, water soaked $[Eu_2(bdc)_3(H_2O)_4]$ was then utilized for the generation of an MMM nEu-bdc@PSS according to the procedure described in the experimental section. Powder diffractograms of nEu-bdc@PSS synthesized with both nEu-bdc and post-synthetically modified water soaked nEu-bdc, respectively, show identical PXRD patterns of reflection positions and intensities, especially, at $2\theta = 14°–16°$.

The third approach addresses the recovery of nEu-bdc from an existing MMM nEu-bdc@PSS. If the structure change

ADVANCED SCIENCE NEWS
www.advancedsciencenews.com

ADVANCED FUNCTIONAL MATERIALS
www.afm-journal.de

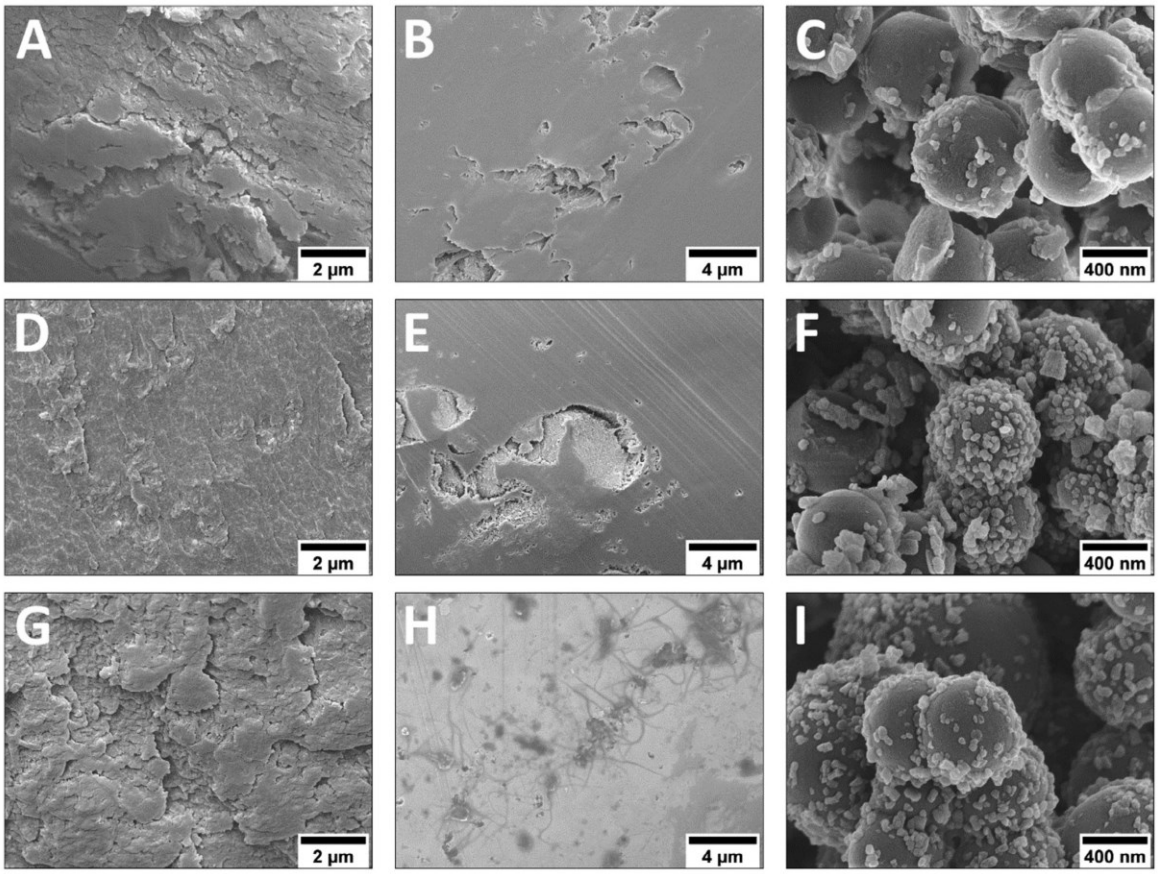

Figure 2. SEM images of responder materials show the distribution of the nLn-bdc as a cross-section in PSS and PSUd as well as onto the surface of pRF as detailed view. A) nTb-bdc@PSS, B) nTb-bdc@PSUd, C) nTb-bdc@pRF, D) nTbEu-bdc@PSS, E) nTbEu-bdc@PSUd, F) nTbEu-bdc@pRF, G) nTbYb-bdc@PSS, H) nTbYb-bdc@PSUd, and I) nTbYb-bdc@pRF.

happens during the embedding process, then the nEu-bdc should be still present as $[Eu_2(bdc)_3(H_2O)_4]$ after the recovery. Indeed, also the third approach is showing a powder pattern similar to the simulated powder pattern of $[Tb_2(bdc)_3(H_2O)_4]$ obtained from single crystal data, verifying this assumption.

Remarkably, the phase transition takes place in an aqueous mixture of dispersed nEu-bdc and diluted PSS which, as consequence, offers multiple coordination sites to the Eu^{3+}-ion. Someone may expect the Eu^{3+}-ion to establish new bonds with functional groups of PSS or the solvent H_2O, for instance, which would lead to either the decomposition of the nMOF or the formation of a different compound. Neither happens, which might be the consequence of the coverage with surfactants enclosing the nEu-bdc. PVP_{40000} and CTAB build some kind of dynamic shell surrounding the nEu-bdc, which allows smaller molecules like solvents to diffuse through the shell as described in a previous work.[41] This dynamic shell provides a confined space, which allows the observed phase transition to proceed undisturbed.

DLS data confirm the nano character with a homogenous particle size distribution maintained during the phase transition with particle sizes of 120 ± 50 nm (Figure S2, Supporting Information). SEM images of post-synthetically modified nEu-bdc corroborate with the particle size (50–100 nm) determined by DLS but also reveal a change in terms of particle shape to a more rod-like structure (Figure S21, Supporting Information) than in non-post-synthetically modified nEu-bdc (Figure 1). It is hypothesized that the treatment with H_2O is responsible for the structure and constitution change from $[Eu_3(bdc)_{4.5}(H_2O)_3(dmf)_2]$ to $[Eu_2(bdc)_3(H_2O)_4]$.

SEM is used to evaluate the vertical and lateral distribution of nLn-bdc in nLn-bdc@PSS and nLn-bdc@PSUd as well as the nLn-bdc distribution on the surface of nLn-bdc@pRF. SEM results are presented as detailed view in **Figure 2** and as overview in Figure S20 in the Supporting Information. Images reveal nLn-bdc spread over the whole cross-section of the composites due to the nanocharacter of the particles, which show the tendency to aggregate within the membrane in the case of nTb-bdc@PSS (Figure 2A) and nTbYb-bdc@PSS

ADVANCED SCIENCE NEWS
www.advancedsciencenews.com

ADVANCED FUNCTIONAL MATERIALS
www.afm-journal.de

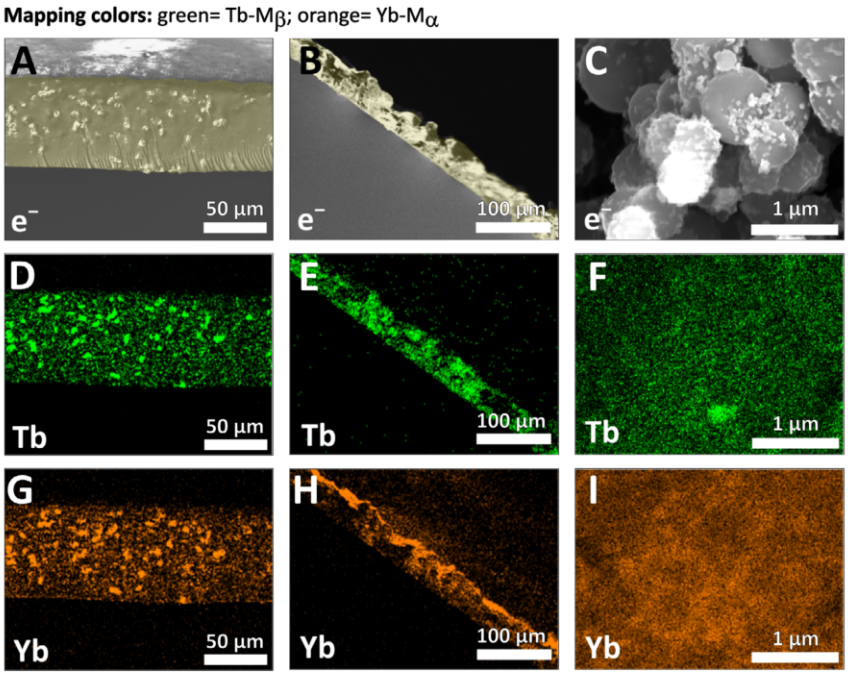

Figure 3. SEM images as well as EDS mappings for Tb and Yb of the responder materials A,D,G) nTbYb-bdc@PSS, B,E,H) nTbYb-bdc@PSUd, and C,F,I) nTbYb-bdc@pRF. The corresponding cross-sections of the membranes are highlighted in yellow for the sake of clarity.

(Figure 2G). Similar results can be observed for nTbEu-bdc@PSS (Figure 2D); however, the islands are even smaller leading to a better lateral and vertical distribution in the membrane compared to nTb-bdc@PSS. SEM images of the MMMs nLn-bdc@PSUd demonstrate the presence of nMOF particles encapsulated within the matrix PSUd (Figure 2B,E,H). However, it is notable that the nMOF particles exhibit a greater tendency to aggregate in nLn-bdc@PSUd than observed for nLn-bdc@PSS.

EDS results reveal Tb/Yb-containing particles in nTbYb-bdc@PSS (**Figure** 3A,D,G) and nTbYb-bdc@PSUd (Figure 3B,E,H) spreading over the membrane in cross-section. Mappings are congruent with observed particles in the respective SEM images and hence confirm the lateral and vertical distribution of the nanoMOFs nLn-bdc (Ln=Tb, Yb). EDS results of nTb-bdc@matrices and nTbEu-bdc@matrices are given in the Supporting Information in Figures S3 and S4, respectively. The SEM findings are confirmed by showing nTb-bdc and nEu-bdc homogenous spread over the membranes cross-sections for nTb-bdc@matrices and nTbEu-bdc@matrices, while nYb-bdc-containing materials tend to aggregate as shown in Figure 2. Instead of embedding into a membrane, nLn-bdc sticks to the surface of pRF spheres and forms nLn-bdc@pRF, while both nLn-bdc and pRF retain particle size and shape (Figure 2C,F,I). At this point, the nano-character of nLn-bdc is a crucial necessity to form stable composites with an extensive nLn-bdc distribution on the pRF surface. The order in which the different and multiple nLn-bdc are brought onto the surface of pRF is inconsequential and can be arranged either simultaneously, as in nTbYb-bdc@pRF, or consecutively, as in nTbEu-bdc@pRF, respectively. EDS mappings of Tb, Eu, and Yb affirm SEM results with the particles sticking onto the surface in all composites nLn-bdc@pRF (see Figure 3C,F,I; Figures S3 and S4, Supporting Information). Together with PXRD results, SEM and EDS analysis lead to the conclusion that the observed particles for all responder materials investigated are the original nMOFs nLn-bdc without decomposition.

2.2. Optical Security Features – Anti-Counterfeiting Levels I and II

Anti-counterfeiting technologies are essential in protecting trademarked products and intellectual property, with their effectiveness largely determined by the integration of multiple security features. As the number of security layers increases, so does the overall security of the system. In this study, the security properties employed are both optical (luminescence) and electronic (conductivity) in nature, encompassing characteristics visible and invisible to the naked eye. These properties are not only additive but also interdependent, meaning that altering one parameter directly affects the others. As a result, reproducing the composite materials nLn-bdc@PSS, nLn-bdc@PSUd, and nLn-bdc@pRF used in this work at an individual level becomes infeasible. This is going to be discussed in detail in the following sections.

This multilayered strategy enhances the complexity of the anti-counterfeiting measures and raises the barriers for

ADVANCED SCIENCE NEWS
www.advancedsciencenews.com

ADVANCED FUNCTIONAL MATERIALS
www.afm-journal.de

counterfeiting attempts. No single attribute can be replicated in isolation without influencing the others, thereby making the responder materials extremely difficult to duplicate. Effective anti-counterfeiting solutions rely on the inherent complexity of replication, combining both physical and chemical defenses. This integrated approach ensures that any attempt to counterfeit these materials becomes prohibitively expensive and labor-intensive. Counterfeiters are confronted with significant challenges in identifying and replicating the precise combination of properties required to produce a convincing counterfeit, further strengthening the protection of the developed composites nLn-bdc@PSS, nLn-bdc@PSUd, and nLn-bdc@pRF.

Optical security features were investigated with photoluminescence spectroscopy (PL), UV–vis–NIR absorption spectroscopy, diffuse reflectance spectroscopy (DRS), and fluorescence microscopy (FM).

2.2.1. Anti-Counterfeiting Level I – Vis-Light Emission

The first level of the additive anti-counterfeiting security features is constituted by a light emission in the visible part of the electromagnetic spectrum. Photoluminescence in the visible wavelength region (≈400–800 nm) is potentially visible with the naked eye and consequently easy to read-out but also simple to imitate. Yet, photoluminescence emission must be first provoked by excitation with light before it becomes visible, which recommends it as a first security level (level I) in anti-counterfeiting.

PL data (**Figure 4**) of vis-light emitting nLn-bdc (Ln=Eu, Tb) reveals a broad $\pi^*\leftarrow\pi$ excitation band at 280–320 nm, which refers to the π-system of the linker bdc^{2-} and illustrates light uptake as the first step of an "antenna effect."[40] By embedding nLn-bdc into PSS, the maximum of the $\pi^*\leftarrow\pi$ transition shifts bathochromically to 312 and 316 nm for nTb-bdc@PSS and nTbEu-bdc@PSS, respectively, compared to the $\pi^*\leftarrow\pi$ transition of nLn-bdc. The $\pi^*\leftarrow\pi$ excitation bands of nLn-bdc@PSUd are located at about the same energy as for nLn-bdc with maxima at 297 nm, while the bands appear to be sharper. A hypsochromic shift is observable for the $\pi^*\leftarrow\pi$ transition of nLn-bdc@PSUd at 297 nm compared to the $\pi^*\leftarrow\pi$ transition of the matrix PSUd with a maximum at 315 nm. The $\pi^*\leftarrow\pi$ band of pRF has an excitation maximum <280 nm, which causes the $\pi^*\leftarrow\pi$ transition of nLn-bdc@pRF to shift hypsochromically compared to nLn-bdc. Again, this is the result of the combination of properties of both, nLn-bdc and pRF. Prominent peaks are observable in the excitation spectra of nEu-bdc and less intense also in nTbEu-bdc@PSS as well as nTbEu-bdc@PSUd corresponding to the direct excitations $^5D_{1,2,4}$, $^5L_6\leftarrow{}^7F_0$, and $^5D_{1,3,4}\leftarrow{}^7F_1$ located at 525, 464, 392, 361 nm and 533, 414, 379 nm, respectively.[41] These transitions are weak due to the already described selection rules for electronic transitions between f–f orbitals and demonstrate the value of a sensitizer.[38,39] Barely visible are the direct excitation peaks of Tb^{3+} ions in nTb-bdc belonging to $^5D_{2,3,4}$, $^5L_{10}\leftarrow{}^7F_6$ at 352, 377, 485, and 369 nm, respectively, which are less intense than direct excitations of Eu^{3+} in nEu-bdc.[41] They appear partly also in nTbEu-bdc@PSS, nTbEu-bdc@PSUd, and nTbYb-bdc@PSUd along with the described excitations caused by nEu-bdc.

The nanoMOF nEu-bdc and the responder materials nTbEu-bdc@matrices show characteristic red emission at 580, 593, 616, 652, 700, 753, and 810 nm corresponding to the transitions $^5D_0\rightarrow{}^7F_J$ with J = 0–6. The shape and intensity of the signals are strongly dependent on the coordination environment of the lanthanide.[56,57] In a nonsymmetrically coordinated environment, the Stark levels of Eu^{3+} experience mixing due to a distorted electric ligand field, resulting in the formation of multiple electronic states that can be populated by electrons. Consequently, the emission from these multiple mixed electronic states leads to a broadening of the signals in the emission spectrum of Eu^{3+}.[58] Therefore, sharp signals for the transition $^5D_0\rightarrow{}^7F_2$ in nTbEu-bdc@PSS lead to the assumption of multiple similar electrostatic environments of Tb^{3+} and Eu^{3+} within PSS. Besides broadening, the intensity of the emission signals can be influenced by mixing different acceptors ions (i.e., Eu^{3+}, Tb^{3+}, or Yb^{3+}).[58]

After excitation, the second step of the "antenna effect" is the transfer of energy from the sensitizer donor state to an acceptor energy state. For this, the sensitizer has multiple options to transfer its energy onto the best energetic option in terms of energy levels. The emission spectra of nTbEu-bdc@matrices show for all three matrices PSS, PSUd, and pRF, that Eu^{3+} provides more suitable excited states than Tb^{3+}. In addition, an energy transfer from Tb^{3+} to Eu^{3+} is possible. This results in emission spectra different from a sum up of the emission spectra of nTb-bdc and nEu-bdc in terms of peak intensity ratios. The typical Tb^{3+} emission bands observable in nTb-bdc as well as in all Tb-containing responder materials at 489, 543, 584, 621, 647, 669, and 680 nm can be attributed to the transitions $^5D_4\rightarrow{}^7F_J$ with J = 6–0.[41] The energy transfer from the sensitizer onto excited states of the lanthanides is efficient in the case of nLn-bdc@PSS and nLn-bdc@pRF as indicated by no observable linker-based emission. If acceptor energy states of Ln^{3+} do not fit donor energy states of the sensitizer, no energy transfer would be present, and the energy uptake could end up in a prominent linker-based emission band along with nonradiative transitions.[41] This is observed to a minor degree in nLn-bdc@PSUd, where an emission band at 330–450 nm derives from PSUd fitting with the emission spectrum of neat PSUd. Interestingly, minor self-absorption takes place at 392 nm in nTbEu-bdc@PSUd and belongs to the $^5L_6\leftarrow{}^7F_0$ excitation of Eu^{3+}.

Remarkably, the pitch-black matrix pRF emits bright green light when excited by UV-light, if nTb-bdc was brought onto its surface to give nTb-bdc@pRF. Solid state UV–vis–NIR DRS confirms properties of a total absorber as pRF in the Vis-region with reflectance of <1.5%R, which is depicted in Figure 4. Moreover, the PL spectrum of pRF does not exhibit any emissive behavior under excitation with UV-light, excluding the involvement of pRF in the emission of visible light. As a total light absorber, one may expect that pRF suppresses the emission of light altogether. As plausible explanation for the light emission of nLn-bdc@pRF, nTb-bdc particles adhere to the surface rather than being encapsulated within pRF spheres. Consequently, light does not necessarily need to emanate from within the black pRF spheres, thereby preventing to some extent of the absorption by pRF. This behavior was also observed for other lanthanide ions in nLn-bdc@pRF (Ln=Tb/Eu: orange; Ln=Tb/Yb: green/NIR emission), which indicates their suitability as anti-counterfeiting

ADVANCED SCIENCE NEWS
www.advancedsciencenews.com

ADVANCED FUNCTIONAL MATERIALS
www.afm-journal.de

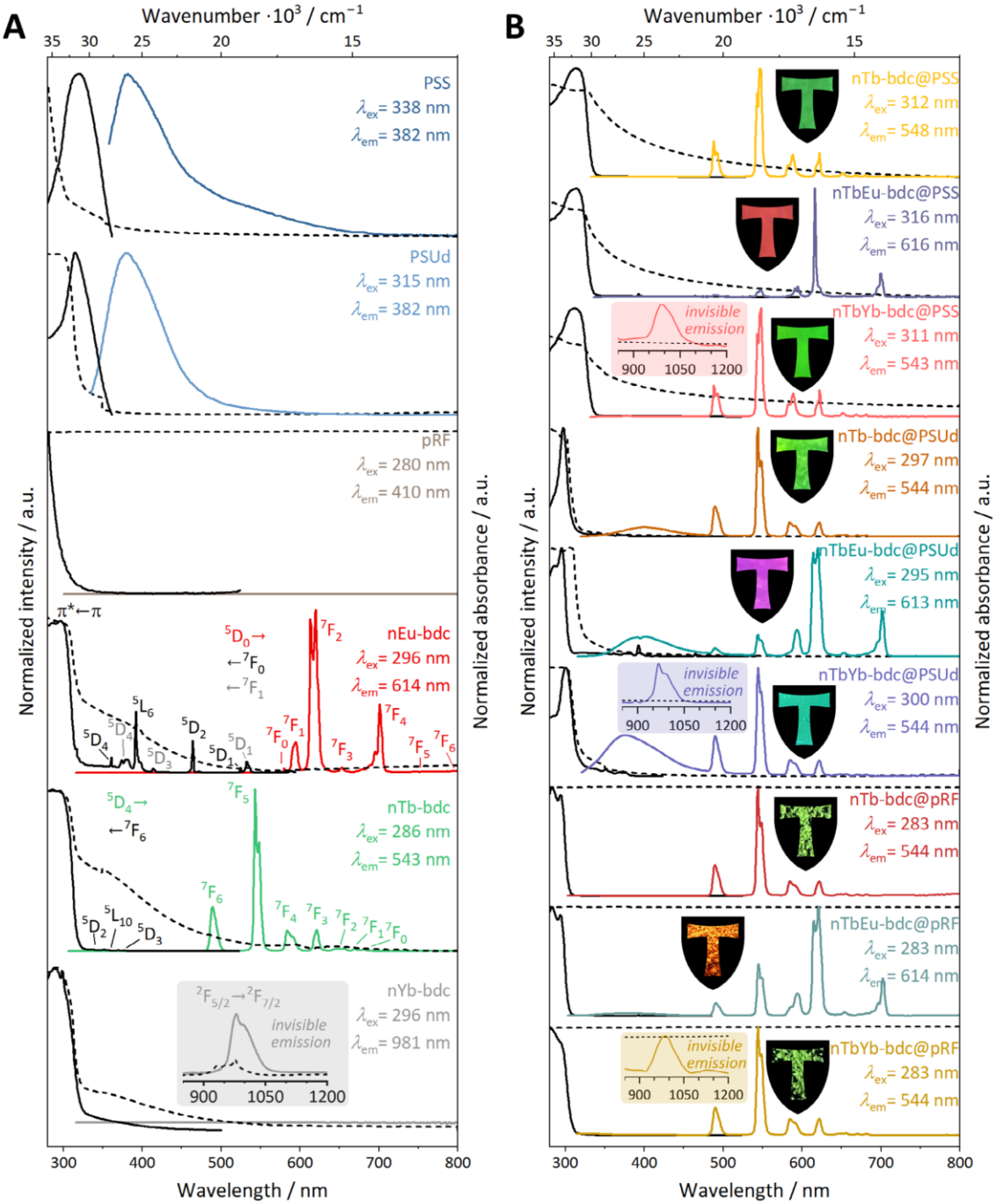

Figure 4. Normalized photoluminescence spectra of A) the nanoMOFs nLn-bdc (Ln=Eu, Tb, Yb) and the matrices PSS, PSUd, pRF as well as B) the MMMs nLn-bdc@PSS, nLn-bdc@PSUd and the powdery composite nLn-bdc@pRF. Insets show NIR emission spectra of nYb-bdc-containing materials indicating invisible emission. Moreover, UV–vis–NIR absorption spectra are given in normalized absorbance as dotted lines. Electronic states are exemplarily denoted for clarity as term symbols with the corresponding states in excitation and emission spectra. Photographs of the emission of the respective real responder materials are depicted in the shape of the official crest of the Justus-Liebig-University of Giessen and are inserted next to the corresponding emission spectrum.

ADVANCED SCIENCE NEWS
www.advancedsciencenews.com

ADVANCED FUNCTIONAL MATERIALS
www.afm-journal.de

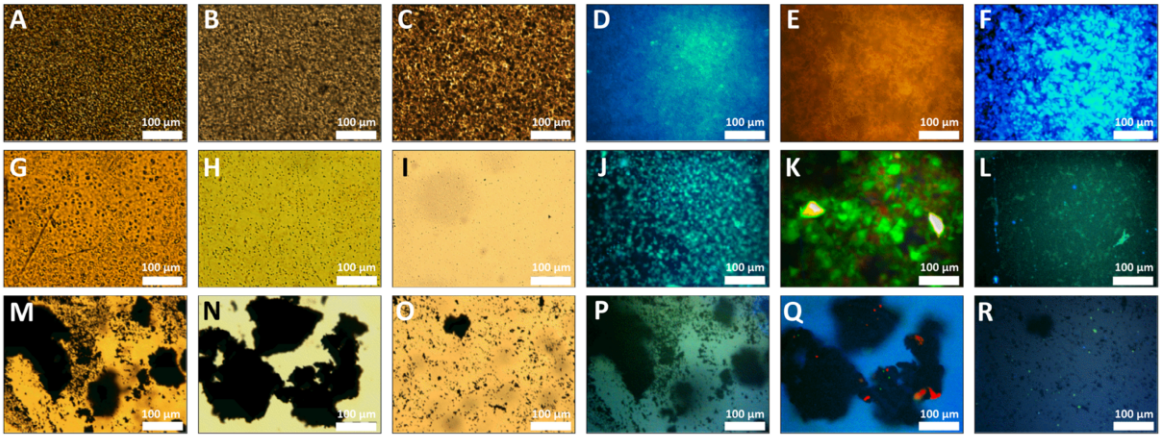

Figure 5. Fluorescence microscope images for white light (WL) and for 330 nm (UV) of nTb-bdc@PSS (A) WL, D) UV), nTbEu-bdc@PSS (B) WL, E) UV), nTbYb-bdc@PSS (C) WL, F) UV), nTb-bdc@PSUd (G) WL, J) UV), nTbEu-bdc@PSUd (H) WL, K) UV), nTbYb-bdc@PSUd (I) WL, L) UV), nTb-bdc@pRF (M) WL, P) UV), nTbEu-bdc@pRF (N) WL, Q) UV), and nTbYb-bdc@pRF (O) WL, R) UV).

materials due to their non-emissive properties under daylight, especially when used on black or dark goods (see Figure S7, also available as Video S1 in the Supporting Information).

Solid state UV–vis–NIR absorption and UV–vis–NIR DRS spectra shown in Figure 4 are in accordance with observed PL excitation spectra for all investigated materials showing large $\pi^*\leftarrow\pi$ bands below 300 nm. Furthermore, absorption peaks of Eu^{3+} are observable for nEu-bdc and correspond to the transitions $^5D_1\leftarrow{}^7F_0$, $^5D_2\leftarrow{}^7F_0$ and $^5L_6\leftarrow{}^7F_0$ at 525, 464, and 392 nm, respectively.

Additionally, fluorescence microscopy (FM) was used to record true-color depth-dependent photographs of the investigated responder materials. Unlike EDS mapping, where the depicted colors are selected at random for the elements under investigation, FM displays the emitted colors based on the wavelength emitted by the material after excitation. PL spectra were acquired for excitation with λ_{ex} = 330 nm to check which responder materials allows this kind of recording of true-color photographs (Figure S8, Supporting Information). Because nYb-bdc emits light in the NIR-region, only nEu-bdc and nTb-bdc are observable with FM due to their emission in the visible region of the electromagnetic spectrum. Since nYb-bdc emission is not observable by eye or other optical instruments, it can be considered as the key feature of anti-counterfeiting security level II (NIR emission) as explained in the following section.

Figure 5 shows composite materials with a homogenous particle distribution, which is recognizable by looking at unfocused structures appearing below and above the focal plane. Here, nLn-bdc@PSS membranes (Figure 5A–C) show a denser particle package than nLn-bdc@PSUd membranes (Figure 5G–I). All nTb-bdc@matrices show green glowing particles mixed with the above-described linker-based blue emission. The responder materials nTbEu-bdc@matrices gain a red color due to the addition of nEu-bdc, which results in an orange color of the emission of nTbEu-bdc@PSS (Figure 5E). The mixing of nTb-bdc and nEu-bdc in nTbEu-bdc@PSUd (Figure 5K) does not lead to an emitted violet color as presented in Figure 4 but separate green and red colors in different focal planes. Furthermore, the observed color impression depends on the magnification level, making particle size a crucial factor to consider. Light is emitted separately from nTb-bdc (green) and nEu-bdc (red), which on a microscopic level result in distinct color emissions for nTbEu-bdc@PSUd (Figure 5K). However, on a macroscopic level, visible to the naked eye, the nTb-bdc and nEu-bdc particles embedded in PSUd appear as a single emitting material, which leads to the observed violet color impression for nTbEu-bdc@PSUd (Figure 5K), resulting from the color mixing of green and red emissions, along with blue light emitted by the organic compounds of nTbEu-bdc@PSUd (Figure 5K). This microscopic effect is also observable in the emission color of nTbEu-bdc@pRF (Figure 5Q), where green and red spots are observable with an orange emission at the macroscopic level, as shown in Figure 4. As already described, because of the emission of nYb-bdc being in the infrared wavelength range, nYb-bdc does not lead to observable emission with FM, but photographs of nTbYb-bdc@matrices (Figure 5F,L,R) reveal particles reflecting the UV light giving them a blue glow.

Given the properties associated with the first security level, it might appear straightforward for counterfeiters to replicate the visible photoluminescence of the developed responder materials, namely nLn-bdc@PSS, nLn-bdc@PSUd, and nLn-bdc@pRF. This holds true for anti-counterfeiting measures based solely on visible light emission. However, the responder materials developed in this study incorporate two additional security levels – NIR-light emission and conductivity – both of which are affected by any modifications aimed at counterfeiting the visible photoluminescence. For example, using a material different from nTb-bdc to mimic the characteristic Tb^{3+} emission will alter the conductivity of the responder material differently (see Section 2.3.), thereby affecting the overall security functionality. This example illustrates the interdependency of the multilevel security structure, highlighting it as a

ADVANCED SCIENCE NEWS
www.advancedsciencenews.com

ADVANCED FUNCTIONAL MATERIALS
www.afm-journal.de

significant challenge for counterfeiters. The subsequent sections will provide additional evidence of the interdependence among the previously discussed properties by examining the other security levels employed.

2.2.2. Anti-Counterfeiting Level II – NIR-Light Emission

In order to divert potential counterfeiters and set them on a wrong track imitating a visible emission, an additional optical feature outside the Vis region was added, which is more difficult to discover and counterfeit, because it is an emission in the NIR region of the electromagnetic spectrum and thereby invisible to the naked eye. Mixing of vis-light emitters such as Tb^{3+} and Eu^{3+} is a suitable procedure (e.g., in MOF-based barcodes[59]), the principle of mixing two Ln^{3+} to achieve a mixed overall luminescence being demonstrated with the matrices used in this work shown in Figure 4. Although nEu-bdc and nTb-bdc were mixed 1:1, the resulting PL spectra show much more intense Eu^{3+} emission than Tb^{3+} emission due to metal-to-metal-energy transfer also recognizable in an overall emission color of orange instead of an expected yellow color by mixing red/green (additionally visualized in Figure S9 in the Supporting Information). That means; by adding distinct amounts of Ln^{3+}, characteristic emission peak ratios can be tuned by energy transfer to achieve more secure anti-counterfeiting tags by setting them in a specific ratio and yielding a characteristic emission pattern. For further improvement, instead of using a second vis-emitter, in this work the NIR-emitter nYb-bdc was mixed with nTb-bdc to achieve a feature invisible for the naked eye which is denoted as second anti-counterfeiting security level (level II, see also Scheme 1 and Scheme S2 in the Supporting Information).

Figure 4 shows the excitation spectra of Yb^{3+}-containing materials. The nanoMOF nYb-bdc shows $\pi^*\leftarrow\pi$ transition at 296 nm similar to those of nLn-bdc (Ln=Eu, Tb). Furthermore, $\pi^*\leftarrow\pi$ excitation for nTbYb-bdc@matrices give similar bands as already observed for nEu-bdc and nTb-bdc-containing responder materials. The characteristic Yb^{3+} NIR emission at 979 nm corresponding to the transition $^2F_{5/2}\rightarrow{}^2F_{7/2}$[60] is observable for nYb-bdc as well as for the composites nTbYb-bdc@PSS, nTbYb-bdc@PSUd, and nTbYb-bdc@pRF. Modifying the ratios of Tb^{3+}/Yb^{3+} emission peaks enable the fine-tuning of combined Vis/NIR photoluminescence, as in Eu^{3+}/Tb^{3+}-containing samples where the principle was showcased by a mixed visible color. Notably, despite an emission peak ratio adjustment for Tb^{3+}/Yb^{3+}, the observed color remains unchanged for the naked eye which holds the potential for enhanced security in anti-counterfeiting tags without changing the impression caught by eye (see insets in Figure 4 and Figure S9 in the Supporting Information). The observed results provide additional evidence supporting the interdependence of the properties. Complementary analysis was conducted by means of solid-state UV–vis–NIR DRS, revealing a broad peak in the reflectance spectrum of nYb-bdc with a maximum at 977 nm ($^2F_{5/2}\leftarrow{}^2F_{7/2}$) which is in accordance with literature[61,62] and the observed emission spectra. The $^2F_{5/2}\leftarrow{}^2F_{7/2}$ absorption is missing in corresponding absorption/reflectance spectra of the responder materials nTbYb-bdc@matrices.

Table 2. Calculated conductivity σ of the investigated materials with respect to the ohmic resistance R and the type of experimental setup (open sample chamber or closed sample chamber). The term "aged" refers to a period of four months during which the materials were stored at ambient conditions and temperature.

Material	Experimental setup	R [Ω]	σ [S cm^{-1}]
nEu-bdc	closed	∞	–
nTb-bdc	closed	∞	–
nYb-bdc	closed	∞	–
PSS	open	1×10^6	9.0×10^{-4}
pRF	closed	1 825	5.6×10^{-5}
PSUd	open	∞	–
nTb-bdc@PSS	open	1.2×10^6	7.5×10^{-4}
nTbEu-bdc@PSS	open	5×10^6	1.8×10^{-4}
nTbYb-bdc@PSS	open	4×10^6	2.3×10^{-4}
nTb-bdc@PSUd	open	∞	–
nTbEu-bdc@PSUd	open	∞	–
nTbYb-bdc@PSUd	open	∞	–
nTb-bdc@pRF	closed	9800	1.0×10^{-5}
nTb-bdc@pRF (aged)	closed	12 000	9.5×10^{-6}
nTbEu-bdc@pRF	closed	29 000	2.6×10^{-6}
nTbEu-bdc@pRF (aged)	closed	27 000	3.3×10^{-6}
nTbYb-bdc@pRF	closed	12 500	8.2×10^{-6}
nTbYb-bdc@pRF (aged)	closed	12 000	8.5×10^{-6}

2.3. Electronic Security Features – Anti-Counterfeiting Level III

Additional electronic security features were evaluated by potentiostatic electrochemical impedance spectroscopy (PEIS) with two different experimental setups for the determination of the conductivity for MMMs (open sample chamber, **Scheme 3**A–D) and powder responder materials (closed sample chamber, Scheme 3E–G), respectively.

Conductivity represents the third security level (level III) in the developed responder materials for anti-counterfeiting. In contrast to other publications, where only the security features of the MOFs are considered,[3,6–10] the nanoMOFs nLn-bdc (Ln=Eu, Tb, Yb) in this work provide optical security features, whereas additional conductive properties are provided by the matrices, as verified by PEIS. Electric voltage works as stimulus and conductivity can be used as another invisible security feature next to the NIR-emitter nYb-bdc. This feature originates solely from the matrices PSS and pRF. Impedance spectra of the responder materials nLn-bdc@PSS, nLn-bdc@pRF, and nLn-bdc@PSUd are given in Figure S10 (Supporting Information), while impedance spectra for the nanoMOFs nLn-bdc and matrices PSS, pRF and PSUd are shown in Figure S11 (Supporting Information). The impedance is given by Equation (1) and the observation of the impedance by variation of the angular frequency is given by Equation (2). In **Table 2**, conductivities σ are listed calculated according to Equations (3) and (4) (see Experimental Section) with respect to the experimental setup with an open and closed sample chamber (see Scheme 3), respectively, and the resistance R obtained from PEIS spectra. Subsequently, the results were evaluated by comparison to the non-conducting nLn-bdc@PSUd.

ADVANCED SCIENCE NEWS
www.advancedsciencenews.com

ADVANCED FUNCTIONAL MATERIALS
www.afm-journal.de

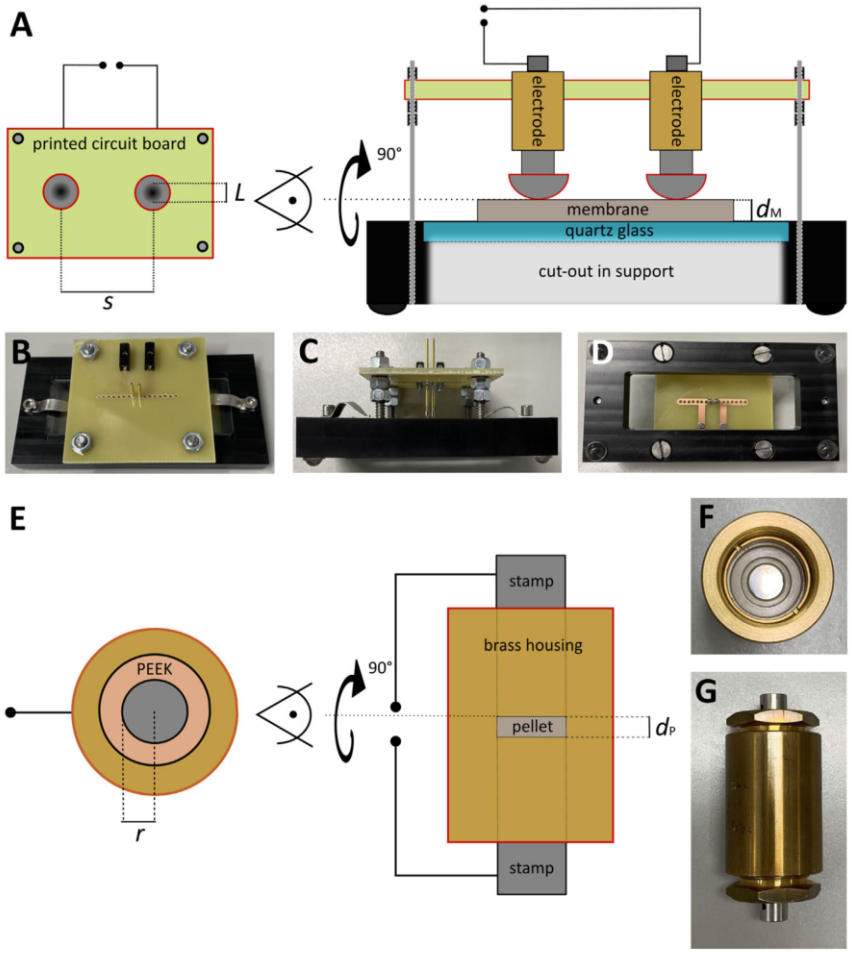

Scheme 3. Experimental PEIS setups (A–D) open sample chamber; E–G) closed sample chamber). Parameters which are needed for conductivity calculations are given together with photographs of the experimental setup with an open sample chamber from above (B), from the side (C), and from below (D), as well as photographs of the experimental setup with a closed sample chamber as a cross-section (F) and from the side (G).

Being inherently conductive, the neat matrices PSS (Figure S10D, Supporting Information) and pRF (Figure S10F, Supporting Information) show the highest conductivity of all investigated materials with 9.0×10^{-4} and 5.6×10^{-5} S cm^{-1}, respectively. Conductivity strongly depends on the ability of a material to transfer charges. For PSS synthesized as a membrane, molecular monomeric units are connected within a particular direction and therefore lead to a higher conductivity compared to pRF being a powder, loosely pressed between the stainless-steel stamps of the experimental setup with a closed sample chamber. Although PSUd is also synthesized as membrane, its molecular structure does not allow charge transfer.

Conductivity of the matrices is decreasing by the addition of nLn-bdc, because the synthesized nMOFs are insulators. An overview of the results is shown in Table 2. For instance, conductivity is reduced to 1.8×10^{-4} S cm^{-1} for nTbEu-bdc@PSS (Figure S11B, Supporting Information) with respect to neat PSS (Figure S10D, Supporting Information). The same trend is observed for pRF (Figure S10F, Supporting Information) and its nMOF composites (Figure S11G–I, Supporting Information), whereas insulation properties of nLn-bdc@PSUd (Figure S11D–F, Supporting Information) do not change after embedding nLn-bdc compared with their matrix PSUd (Figure S10E, Supporting Information). Altogether, the choice of lanthanide ions has almost no influence on the resulting conductivity.

However, it was observed that the difference in conductivity between the powder responder material nTbEu-bdc@pRF with 2.6×10^{-6} S cm^{-1} (Figure S11H, Supporting Information) and nTbYb-bdc@pRF with 8.2×10^{-6} S cm^{-1} (Figure S11I, Supporting Information) is strongly dependent on weight percent of nLn-bdc. In the case of nTbEu-bdc@pRF, 20 wt% of both nTb-bdc and nEu-bdc were brought onto the surface of pRF consecutively, which yields the responder material nTbEu-bdc@pRF with a coverage of 40 wt% of nMOFs. However, if the amount of nMOFs is

ADVANCED SCIENCE NEWS
www.advancedsciencenews.com

ADVANCED FUNCTIONAL MATERIALS
www.afm-journal.de

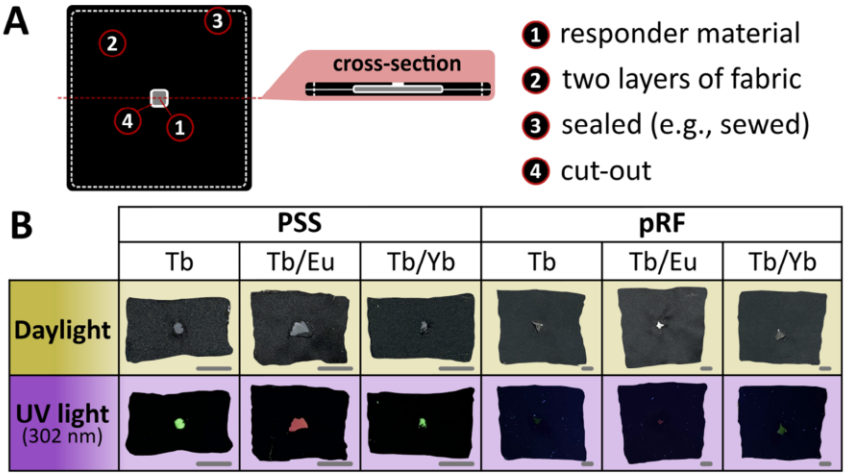

Figure 6. Proof-of-principle experiment for potential applications in fabric-made trademarked products using the developed anti-counterfeiting materials. The materials were aged for a period of four months under ambient atmosphere prior to the experiment to address long-term durability analysis. A) The schematic concept of the designed experiment is depicted, with the cross-section showing the position of the responder material and the cut-out. B) The photo series of the prepared fabrics containing the responder materials nLn-bdc@matrices (Ln=Eu, Tb, Yb; matrices = PSS, pRF) demonstrate the described photophysical (vis- and NIR-emission) and electrical properties (conductivity) by means of irradiation with UV light (302 nm). It is noteworthy that NIR emission and conductivity are not observable by the naked eye. The scale bars amount to 10 mm. Also available as Video S2 in the Supporting Information.

reduced as in nTbYb-bdc@pRF, where only 10 wt% of both nTb-bdc and nEu-bdc were simultaneously brought onto the surface of pRF, the conductivity rises. In consequence, conductivities calculated for the MMMs nTbEu-bdc@PSS (Figure S11B, Supporting Information) and nTbYb-bdc@PSS (Figure S11C, Supporting Information), with the same overall amount of nMOFs of 20 wt% as a mixture of nTb/nEu-bdc and nTb/nYb-bdc, respectively, show almost no difference. Hence, the decreasing conductivity is a consequence of the inserted amount of insulating nanoMOF nLn-bdc into PSS and onto pRF. Interestingly, it does not make a difference, whether nLn-bdc is enclosed into the molecular structure of the matrix as in nLn-bdc@PSS (Figure S11A–C, Supporting Information) or adsorbed onto a surface as in nLn-bdc@pRF (Figure S11G–I, Supporting Information) as shown by SEM – it leads in both cases to an insulating effect.

The obtained conductivities are characteristic and bear the potential to be a part of a new generation of advanced anti-counterfeiting tags in addition to the commonly used optical features provided by the nanoMOFs. As indicated in the preceding sections, the incorporation of black conductive carbon soot (or analogous materials) facilitates the precise adjustment of a material's conductivity. However, a composite material that exhibits both photoluminescence and conductivity, as demonstrated in this study, will experience not only a distinct alteration in conductivity but also a reduction in luminescent intensity. This reduction in intensity presents a significant disadvantage for counterfeiters, as it would be readily detectable to the naked eye. Overall, the properties of the anti-counterfeiting materials developed in this study are additive in nature, with an inevitable interdependence that further increases the security that counterfeiters must overcome to imitate the advanced responder materials nLn-bdc@PSS, nLn-bdc@PSUd, and nLn-bdc@pRF.

2.4. Anti-Counterfeiting Application – Proof-of-Concept

To address potential real-life applications, a proof-of-concept experiment is shown in **Figure 6** (also available as Video S2 in the Supporting Information) with selected responder materials. The developed responder materials are positioned between two layers of fabric and subsequently sealed along the edges; this is accomplished by adhering the edges together. In a commercial product, sewing may be employed for this purpose. To show the option of our responder materials to be black and work under conditions of total absorbers, we selected integration into black materials. The proof-of-principle experiment was conducted using aged responder materials stored for four months at ambient atmosphere, thereby offering additional insights regarding the long-term stability of the developed materials if subject to realistic environmental impacts. In order to show, what someone, who tries to put up a copy, would observe, a cut-out was added to one fabric layer, allowing for the detection of photoluminescence, as illustrated in Figure 6A. The MMMs nLn-bdc@PSS and the powder composites nLn-bdc@pRF (with Ln=Eu, Tb, Yb) were exposed to daylight and UV light (302 nm), as illustrated in Figure 6B. As evidenced by the photographic documentation, the NIR emission (level II) and the conductivity (level III) are not discernible to the naked eye, as illustrated for nTbYb-bdc@matrices in comparison to nTb-bdc@matrices, while the outcome of mixed visible luminescence (level I) is observable for nTbEu-bdc@matrices (with matrices = PSS and pRF). The anti-counterfeiting material provides limited information at first glance, which makes it even harder to decipher the combinatorial levels of anti-counterfeiting in a copy attempt. This is supposed to misdirect potential counterfeiters into focusing only on the visible properties.

ADVANCED SCIENCE NEWS
www.advancedsciencenews.com

ADVANCED FUNCTIONAL MATERIALS
www.afm-journal.de

The observed photoluminescence and mechanical stability of the investigated responder materials remained unchanged over time (four months) for the fabric adhered samples in the presence of atmospheric conditions and humidity, as evidenced by a comparison with the analysis of freshly prepared responder materials (refer to Figure 4; Figure S7 in the Supporting Information). This is also valid for the conductivity, which was also determined exemplarily for the four months aged powder composites nLn-bdc@pRF (refer to Table 2; Figure S11J–L, Supporting Information). The powder materials were additionally wrapped in a non-absorbing polymer foil (*STOE & Cie*), which ensures both the immobilization between the fabric and the recovery of the material for conductivity determination. The black appearance of nLn-bdc@pRF (Ln=Eu, Tb, Yb) serves to camouflage the materials in front of a black fabric, as proposed (refer also to Figure S7 and Video S1, Supporting Information). This approach bears resemblance to any application in which the developed anti-counterfeiting materials may be integrated into trademarked furnish, textiles, and apparel, or automotive interiors to name a few fabric-using industries.

3. Conclusion

Multi-functional nanoMOF-based composites were synthesized and studied as advanced multilevel anti-counterfeiting materials in combination with conductive and nonconductive polymers PSS and PSUd as nanoMOF mixed-matrix-membranes, and powder composites together with pRF. In order to protect goods from counterfeiting, the anti-counterfeiting materials have a characteristic light emission, mainly in the visible region of the electromagnetic spectrum. This emission is produced by the sensitized trivalent lanthanide ions Eu^{3+} and Tb^{3+} in the nanoMOFs nEu-bdc and nTb-bdc, respectively. In addition, Yb^{3+} ions of nYb-bdc-containing responder materials emit light in the NIR wavelength region, which is also specific but invisible to the naked eye. The matrices PSS and pRF provide additional invisible functionality by means of their conductivity. These properties were arranged to combine three levels of security: level I (Vis emission), level II (NIR emission), and level III (conductivity) with subsequent attribution to responder-stimuli mechanisms triggered by UV radiation and applied electric voltage. The levels demonstrate an additive character, which allows for the arbitrary combination of feature-bearing components to achieve multilevel counterfeiting. The integration of optical and electrical properties for the purpose of anti-counterfeiting in this manner is a subject that has scarcely been reported in extant literature. In particular, the invisible levels II and III contribute to the complexity of possible anti-counterfeiting since they are challenging to counterfeit in multifunctional composites. In combination with level I and its visible optical properties, an even higher level of security can be arranged, with the visible light emission masking the other anti-counterfeiting features. In addition to the advantage of incrementally adding security levels to achieve effective anti-counterfeiting, the interdependence among the multilevel properties creates an intrinsic linkage between these levels.

Altogether, we present comprehensive characterization of nine responder materials nLn-bdc@PSS, nLn-bdc@PSUd, and nLn-bdc@pRF (Ln=Eu, Tb, Yb) and a proof-of-concept to address life-like scenarios, such as integration into black fabrics. The syntheses of the responder materials benefit from the nanocharacter of the MOFs nLn-bdc in terms of particle distribution in the polymer membranes and the resulting MMMs nLn-bdc@PSS and nLn-bdc@PSUd. The nanosized MOFs improve connectivity of the components as well as the stability of the composite particles nLn-bdc@pRF. Sedimentation of the nMOFs in the polymer solutions and precursor solutions during the MMM synthesis was prevented because of the good colloidal stability of the dispersion of the nanoparticles in comparison to their bulk counterparts. It was further demonstrated how the mixing of Vis-light emitting nLn-bdc (Ln=Eu, Tb) impacts the overall luminescence and how this concept can be used to synthesis mixed Vis/NIR emitting responder materials nTbYb-bdc@PSS, nTbYb-bdc@PSUd, and nTbYb-bdc@pRF. Remarkably, it was possible to develop all-absorbing pitch-black responder materials nTb-bdc@pRF, nTbEu-bdc@pRF, and nTbYb-bdc@pRF under daylight which emit green, as well as mixed all-vis light (green/red) and green/NIR light, upon excitation by UV radiation. Thereby, responder materials comprising pRF are universally applicable to black materials, which typically do not allow emission due to their total light-absorbing properties. Furthermore, matrices (PSS and pRF) contribute a level III feature with their conductivities to the multilevel security MMM nTbYb-bdc@PSS and powder composite nTbYb-bdc@pRF, respectively, rather than solely serving as nonfunctional carriers for feature-bearing nMOFs.

The work presents different synthesis approaches to novel MMMs and powder responder materials, evaluates their pros and cons and classifies their interdependent features to achieve multiple levels of security demonstrated in a life-like scenario experiment of integration into black fabrics. This linkage ensures that any alteration at one security level will inevitably affect the others, thereby detecting and indicating any attempt at counterfeiting. Altogether, this work gives fundamental insights into a potential application by designing advanced nMOF-based multilevel anti-counterfeiting security tags with deliberate and steerable combinations of optical and electronic features provided by both, matrices and functional fillers/cover materials.

4. Experimental Section

All chemicals were used as purchased without further purification. Demineralized water (H_2O) was used throughout the synthesis, analysis, and product purification procedures. Poly(sodium-p-styrene sulfonate) (NaPSS, M_W: 70 000 g mol^{-1}) from *Thermo Scientific Chemicals*; ethanol (EtOH, ≥99.8% abs.) and triethylamine (TEA, 99% pur.) from *Fischer Scientific*; formaldehyde (≥37%, stabilized in methanol) and ammonia (4 mol L^{-1}) from *Carl Roth*; resorcinol (99%) from *Alfa Aesar*; polysulfone Udel P-3500 (PSUd, M_W: 82 000 g mol^{-1}) from *Solvay*; *N*,*N*-dimethylformamide (DMF, 99% pur. purchased from *Grüssing*); nitric acid (HNO_3, tech. qual.) was purchased from *STOCKMEIER Chemie*; polytetrafluoroethylene (PTFE, 1 µm particle size), the surfactants cetyltrimethylammonium bromide (CTAB, ≥96% pur.) and poly(1-ethenylpyrrolidin-2-one) ($PVP_{40\,000}$, M_W: 40 000 g mol^{-1}, MQ: 200) from *Sigma-Aldrich* (*Merck*); $Eu(NO_3)_3{\cdot}6H_2O$ (99.9% pur.), $Tb(NO_3)_3{\cdot}6H_2O$ (99.9% pur.), $Yb(NO_3)_3{\cdot}5H_2O$ (99.9% pur.), and the organic linker benzene-1,4-dicarboxylic acid (H_2BDC, 98% pur.) from *abcr*.

Synthesis of bulk Eu-bdc and bulk Tb-bdc: The synthesis procedure was modified from the literature.[49] It began by mixing $Eu(NO_3)_3{\cdot}6H_2O$ (80 mg, 0.179 mmol) or $Tb(NO_3)_3{\cdot}6H_2O$ (80 mg, 0.177 mmol) with

ADVANCED SCIENCE NEWS
www.advancedsciencenews.com

ADVANCED FUNCTIONAL MATERIALS
www.afm-journal.de

H_2BDC (32 mg, 0.193 mmol) in a 30 mL snap-on cap glass vial. The mixture was then diluted with DMF (20 mL), absolute EtOH (4 mL), and H_2O (4 mL), forming a colorless, transparent solution. After adding TEA (four drops), the solution turned opaque. Shaking for 60 s followed by the addition of HNO_3 (five drops, 6 M) rendered the dispersion transparent again. The vial was sealed with a lid and Parafilm, then placed in an autoclave (*Heraeus*) at 55 °C for 7 d. The resulting colorless precipitate was washed sequentially with 10 mL each of DMF and EtOH and centrifuged at 10 565·g (rcf) for 10 min after each wash step.

Bulk Eu-bdc: Drying under vacuum gave 38 mg of a colorless powder.

Bulk Tb-bdc: Drying under vacuum gave 48 mg of a colorless powder.

Synthesis of nLn-bdc (with Ln═Eu, Tb, Yb): The synthesis was performed according to the procedure described in previous work[41] by the dissolution of either $Eu(NO_3)_3{\cdot}6H_2O$ (280 mg, 0.628 mmol), $Tb(NO_3)_3{\cdot}6H_2O$ (280 mg, 0.618 mmol) or $Yb(NO_3)_3{\cdot}5H_2O$ (280 mg, 0.623 mmol). Simultaneously, $PVP_{40\,000}$ (4220 mg, 29.90 mmol) was dissolved in DMF (40 mL) while H_2BDC (190 mg, 1.14 mmol) and CTAB (3220 mg, 8.78 mmol) were dissolved in DMF (200 mL) in a 500 mL three-necked round-bottomed flask equipped with a reflux condenser and stirred vigorously at 55 °C for 60 min. Subsequently, the previously prepared Ln^{3+}-salt solutions were added gradually, followed by the addition of TEA (200 µL). The reaction mixture became slightly opaque and was continuously stirred for an additional 60 min at 55 °C. Further heating at 90 °C for 6 h resulted in a thick, opaque, pale yellowish dispersion. This dispersion was subjected to washing with DMF (10 mL, 1×) and EtOH (10 mL, 2×), consecutively. After each washing step, the dispersion was centrifuged at 17 855·g rcf (UniCen MR, *Herolab*) for 10 min. Due to the surfactant content, yield calculation was not feasible. For the postsynthetic modification of nEu-bdc, synthesized nEu-bdc (50 mg) was used and soaked in H_2O (5 mL) for 10 min in an ultrasonic bath. After centrifugation (10 min, 17 855·g rcf) the supernatant was decanted.

nEu-bdc: Vacuum drying yielded 181 mg of a light yellowish powder.

post-syn. mod. nEu-bdc: Vacuum drying yielded 38 mg of a light yellowish powder.

nTb-bdc: Vacuum drying yielded 121 mg of a light yellowish powder.

nYb-bdc: Vacuum drying yielded 83 mg of a light yellowish powder.

Synthesis of resorcinol-formaldehyde resin polymer spheres (pRF): The pRF spheres were produced according to a previously reported Stöber-like approach.[63–65] H_2O (8000 mmol, 144 g), resorcinol (8 mmol, 881 mg), and ammonia (4 mmol, 1085 mg of 4 mol L^{-1} solution) were stirred at 25 °C for 30 min. Formaldehyde (16 mmol, 1299 g of a 37% solution) was added and stirred for 4 h. Subsequently, stirring was turned off and the dispersion rested for 20 h. The supernatant was decanted, and the sediment washed 3x via centrifugation (*Hermle* Z236K, 12 000 rpm, 15 min) in a H_2O/EtOH mixture (1/1 v/v). The product was obtained as whitish powder after drying in a vacuum oven (VO29, *Memmert*) at 50 °C and 30 mbar for 4 h. For pyrolysis, the RF spheres were filled in corundum crucibles and placed in a *Nabertherm* B180 tube furnace. The furnace was flushed with N_2 (standard purity 5.0) for 2 h (6 L h^{-1} gas flow). Subsequently, the N_2 gas flow was reduced to 2 L h^{-1}, the furnace heated to 600 °C at 5 K min^{-1} and held at 600 °C for 2 h. After cooling, the weight loss was determined gravimetrically to 47 wt%. Elemental analysis (found, (%): C, 92.6; H, 1.8; N, 0.4).

Synthesis of MMMs nLn-bdc@PSS and nLn-bdc@PSUd: Responder materials were synthesized as MMMs according to the following procedures.

nLn-bdc@PSS: NaPSS (100 mg, 0.423 mmol) were dissolved in H_2O (5 mL) in a 15 mL Falcon tube until the mixture turned yellowish and transparent. Subsequently, nLn-bdc (Ln═Eu, Tb, Yb; 10 mg, 9 wt%) was added to the solution and homogenized by sonication (Sonorex DL, *Bandelin*) for 10 min. Finally, the dispersion was poured into a glass support and left at room temperature for 12 h. The same procedure was applied to synthesize nEu-bdc@PSS with post-synthetically modified nEu-bdc. This procedure yielded yellowish foils.

nLn-bdc@PSUd: PSUd (100 mg, 0.23 mmol) were dissolved in DMF (3 mL) under stirring at 50 °C in a beaker for 4 h. Simultaneously, nLn-bdc (Ln═Eu, Tb, Yb; 10 mg, 9 wt%) was dispersed in DMF (2 mL) inside a Falcon tube and homogenized by sonication (Sonorex DL, *Bandelin*) for 10 min. Subsequently, the dispersion was added to the PSUd solution and further stirred for 4 h at 50 °C. Finally, the mixture was poured into a glass support and left at 50 °C for 12 h. This procedure yielded colorless foils.

PSS and PSUd: Neat matrices PSS and PSUd were synthesized according to the above-described procedure except for the addition of nLn-bdc, yielding yellowish and colorless transparent membranes, respectively.

Synthesis of powdered nLn-bdc@pRF: Different quantities pRF with nLn-bdc (Ln═Eu, Tb, Yb; 10 wt%) were weighed and both filled into a glass ampule. The used funnel was rinsed with DMF (0.8 mL) into the glass ampule and a magnetic stirring bar was added. Afterward, the ampule was closed with a Young Schlenk-Quickfit. Subsequently, the mixture was frozen out by liquid N_2, evacuated by applying reduced pressure (1×10^{-3} mbar) followed by flushing the ampule with Ar (standard purity 5.0) and thawing at room temperature (RT) for 5 min. This procedure was repeated three times. Afterward, the ampule was closed using an oxygen/natural gas burner under constant cooling with liquid N_2. The closed ampule was sonicated for 15 min (Sonorex DL, *Bandelin*) placed in a *Büchi* B-585 glass oven which in turn was placed on top of a magnet stirrer. The mixture was heated at 90 °C for 48 h under constant stirring. Afterward, the ampule was let cool down to RT and then cracked open. Finally, the mixture was poured into a Falcon tube and purified with DMF (2 mL) and EtOH (2 mL), respectively. The product was separated by centrifugation (10565· g (rcf), 10 min, UniCen MR, *Herolab*). Instead of mixing two nLn-bdc (each 10 wt%) with pRF simultaneously, in the case of nTbEu-bdc@pRF, the nTb-bdc@pRF was synthesized first with nTb-bdc (20 wt%). Then, nTb-bdc@pRF was dispersed in DMF (0.8 mL) with nEu-bdc (20 wt%), relative to the initially used amount of pRF.

nTb-bdc@pRF: Vacuum drying yielded 129 mg of pitch-black powder.

nTbEu-bdc@pRF: Vacuum drying yielded 59 mg of pitch-black powder.

nTbYb-bdc@pRF: Vacuum drying yielded 45 mg of pitch-black powder.

Conductivity determination via Potentiostatic Electrochemical Impedance Spectroscopy (PEIS): Conductivity determinations were carried out at RT by means of PEIS with two different experimental setups shown in Scheme 3.

PSS, PSUd, and related responder materials: Conductivity determination using the experimental setup with an open sample chamber, starting with fixing the materials between the quartz glass, which is embedded in the support, and the two electrodes soldered on a printed circuit board. The socket together with the safety nuts ensured that the electrodes always put the same pressure on the materials during the data acquisition. Connections to the power source were plugged into sockets, also soldered to the printed circuit board. The thickness of investigated membranes d_M was determined by SEM with $d_M = 40$ µm for PSS. For PSUd did not show conductivity, thickness determination is hardly accessible via SEM. After obtaining the ohmic resistance R from a Nyquist plot conductivities were calculated using Equation (3).

pRF, and related responder materials: Conductivity determinations using the experimental setup with a closed sample chamber were done as follows: quantities of the sample were weighed and put between two circular stainless-steel stamps (radius $r_S = 5$ mm) inside a support made of polyether ether ketone (PEEK) surrounded by a brass housing and an aluminum scaffolding. The stamps were fastened with 4 Nm to assure constant pressure for the PEIS analysis. The thickness of the pellet d_P was determined by subtracting the length of the stamps with sample from the length without the sample in between. After obtaining the ohmic resistance R from a Nyquist plot, conductivities were calculated using Equation (4).

Impedance spectra were recorded (3× each) and analyzed by a Potentiostat SP-300 and the associated EC-Lab software (ver. V11.46) from *Bio-Logic* with the following parameters

i. frequency range from $f_i = 3$ MHz to $f_f = 1$ Hz with $N_d = 10$ points per decade in logarithmic spacing
ii. sinus amplitude $V_a = 10$ mV
iii. wait for $p_w = 0.6$ period before each frequency
iv. average $N_a = 6$ measures per frequency

ADVANCED SCIENCE NEWS
www.advancedsciencenews.com

ADVANCED FUNCTIONAL MATERIALS
www.afm-journal.de

The impedance $Z(t)$ is described by the ratio of an applied perturbating alternating voltage $E(t)$ and the resulting current density $j(t)$ over time t as follows

$$Z(t) = \frac{E(t)}{j(t)} \tag{1}$$

Since both $E(t)$ and $j(t)$ contain information about magnitude and phase they must be written as complex numbers. Consequently, $Z(t)$ is also represented as a complex number by the sum of a real part $\mathrm{Re}(Z(t))$ and an imaginary part $\mathrm{Im}(Z(t))$. Particularly, PEIS allows the observation of processes on varying timescales by means of modulating the angular frequency ω, resulting in $Z(\omega)$ and leads to the following correlation

$$|Z(\omega)| = \sqrt{\mathrm{Re}(Z(\omega))^2 + \mathrm{Im}(Z(\omega))^2} \tag{2}$$

Based on Equation (2), a Nyquist-plot ($-\mathrm{Im}(Z)$ vs. $\mathrm{Re}(Z)$) is commonly used to describe and illustrate the impedance. The resulting spectrum can be modelled as an electric circle consisting of capacitors ($-\mathrm{Im}(Z)$) and resistors ($\mathrm{Re}(Z)$) in parallel.[66] Hence, PEIS allows the determination of the ohmic resistance R by looking at the terminating part of the semicircle in the Nyquist-plot where $-\mathrm{Im}(Z) = 0\ \Omega$.

The conductivity σ is calculated by using R and specific setup related quantities as follows:[67] The experimental setup with an open sample chamber refers to

$$\sigma = \frac{s}{R \cdot A} = \frac{s}{R \cdot (d_M \cdot L)} \tag{3}$$

with the fixed distance between the electrodes s = 1.8 mm, the area A which becomes penetrated by electricity, thickness of the membranes d_M = 40 µm and the length of the interface electrode/membrane L = 0.5 mm. The experimental setup with a closed sample chamber refers to

$$\sigma = \frac{d_p}{R \cdot A} = \frac{d_p}{R \cdot \pi \cdot r^2} \tag{4}$$

with the thickness of the pellets d_p, the area A which becomes penetrated by electricity and the radius r of the stainless-steel stamps.

Dynamic Light Scattering (DLS): Particle size and distribution were analyzed using a StabiSizer PMX 200CS provided by *Particle Metrix*. Data acquisition was conducted using Microtrac FLEX Application Software (ver. 10.5.4.) from *Microtrac*. To prepare the samples, snap-on cap glass vials were filled with EtOH up to half of their volume after thorough rinsing. A spatula tip of a sample was then added to one vial, followed by sonication at 30 °C for 10 min (Sonorex DL, *Bandelin*). After confirming the dispersion's stability by eye, data acquisition took place, initially for the blank (EtOH only) and subsequently for the dispersion. For enhanced statistical accuracy, the measurement was repeated three times, each lasting 120 s. The particle size distribution plots presented in this study represent the average of these three measurements and were illustrated using OriginPro 2024 (ver. 10.1.0.178, *OriginLab*). Additionally, the average particle size value is indicated with $\pm 2\sigma$.

Photoluminescence Spectroscopy (PL): Photoluminescence (PL) excitation and emission spectra were acquired using a Jobin Yvon Fluorolog 3 spectrometer, coupled with the FluorEssenceTM for Windows software (ver. 3.9.0.1) provided by *HORIBA*. The excitation source utilized a xenon short-arc lamp (*USHIO*) in combination with a double-grated monochromator at the excitation site. Simultaneously, another monochromator was employed in tandem with a photomultiplier tube R928P (*HAMAMATSU PHOTONICS K.K.*) at the emission site to capture the spectral data. For recording NIR emission, an R5509-73 detector was used. The monochromators and detectors underwent mathematical corrections, as per the manufacturer's recommendations. The spectral profile of the lamp was characterized by means of a reference detector (R signal) and corrected on-site. To obtain complete spectral information, long-pass edge filters with a cutoff at wavelengths of 495 nm, 550 nm (*Newport*) and 830 nm (*Reichmann Optics*) were inserted into the optical pathway between the sample and the detector. The excitation and emission spectra were recorded separately and subsequently combined in a unified graphical representation using OriginPro 2024 software (ver. 10.0.0.178) from *OriginLab*.

PSS, PSUd, and related responder materials: Samples were fixed onto a flat black sample holder and positioned as described above with the membrane towards the incoming beam.

pRF, and related responder materials: Samples were filled into a cylindrical cuvette constructed from synthetic quartz glass (*proQuarz*) and positioned precisely at the focal point of the incident light beam.

Raman Spectroscopy: Raman spectroscopy was conducted with a LabRAM Amiris (*HORIBA*) confocal Raman microscope equipped with an automated XYZ table (*Märzhäuser*) and a laser spot size of approximately 1 µm (100x objective, NA = 0.90). The spectrometer was calibrated to the frequency of diamond (1332 cm^{-1}). The measurement was performed using an excitation wavelength of 532 nm, D2 filter (incident laser energy approximately 0.21 mW), acquisition times of 5 s and two accumulations with a grating of 1800 $g{\cdot}mm^{-1}$.

UV-Vis-NIR Absorption Spectroscopy and Diffuse Reflection Spectroscopy (DRS): Spectra were obtained using a Cary 5000 UV–vis–NIR Spectrophotometer and the Cary WinUV Scan Application software (ver. 6.3.0.1595) by *Agilent Technologies*. The instrument was run in double beam mode with reduced slit height. Two different setups were used corresponding to the physical texture of the material.

PSS, PSUd, and related responder materials: The instrument was run in transmission mode equipped with a double-head foil-support from *Agilent Technology*. The MMMs were placed in the "sample" beam, the "reference" beam was left empty. Raw data is presented in absorbance units (abs). The absorbance spectrum was recorded and corrected based on the following operation: $\mathrm{abs_{sample}}^{\mathrm{corr}} = \mathrm{abs_{sample}}^{\mathrm{raw}} / \mathrm{abs_{atmosphere}}^{\mathrm{raw}}$.

pRF, and related responder materials: The instrument used a Praying Mantis Diffuse Reflectance Accessory from *Harrick Scientific Products*. Raw data is presented in reflectance units (%R). Given the relative nature of this method, PTFE was selected as reference material. The reference was ground and loaded into a DRP-SAP macro sample cup from *Harrick Scientific Products*, then flattened with a spatula. The powdery sample was poured into the DRP-SAP micro sample cup from *Harrick Scientific Products*. Subsequently, the reflectance spectrum was recorded and corrected based on the following operation: $\%\mathrm{R_{sample}}^{\mathrm{corr}} = \%\mathrm{R_{sample}}^{\mathrm{raw}} / \%\mathrm{R_{PTFE}}^{\mathrm{raw}}$.

Powder X-Ray Diffractometry (PXRD): Different setups with either Bragg-Brentano geometry (reflection) or Debye–Scherrer geometry (transmission) were used.

PSS, pRF, and related responder materials: Structural characterization was conducted employing an X'Pert Pro MPD with Data Collector (ver. 5.4.0.90) software from *PANalytical*. The analysis involved the use of an Empyrean Cu LFF X-ray tube ($\lambda_{\mathrm{Cu\text{-}K}\alpha}$ = 154.06 pm) operating at 40 kV and 40 mA to produce the X-ray beam. The incident beam underwent collimation by Soller slits (0.04 rad), a beam mask (10 mm), and a fixed anti-scatter slit (1°) before interacting with a planar material positioned on a silicon wafer, which diffracted the beam. The diffracted beam subsequently traversed an angled anti-scatter slit (0.5°), Soller slits (0.04 rad), and a Nickel Beta-filter, directed towards an X'Celerator equipped with a FASS detector. The analysis was carried out in the Bragg-Brentano (reflection) geometry within a 2θ range of 3.5° to 60° using a PW3050/60 goniometer at room temperature and under ambient atmospheric conditions.

PSUd, and related responder materials: Diffraction data were collected using a STOE Stadi P powder X-ray diffractometer (*STOE & Cie*), which is equipped with a focusing Ge(111) monochromator and a MYTHEN1 K strip detector (angular range 12.5° in 2θ). The measurements were performed in a Debye–Scherrer (transmission) geometry with Cu-K_α X-ray radiation. Data was acquired with STOE Win XPOW software (ver. 3.05, *STOE & Cie*) covering a 2θ range from 3.5° to 60°, with a step size of 0.015° and an integration time of 30 s per step.

Regardless of which setup diffractograms were obtained, they underwent background correction using DIFFRAC.EVA (ver. 5.2.0.5, *Bruker*) and were visualized through plotting by OriginPro 2024 (ver. 10.0.0.178, *OriginLab*).

Scanning Electron Microscopy (SEM) and Energy-dispersive X-Ray Spectroscopy (EDS): Examinations via SEM were conducted with a

GeminiSEM 560 microscope, using the SMART SEM software (ver. 7.04) provided by *Carl Zeiss NTS*. Ground samples were gently placed onto an adhesive carbon pad affixed to an aluminum carrier. 90° angle carriers were used to investigate cross-sections of membranes, whereas surface examinations were done using horizontal orientated carriers. For analysis, meticulous cleaning was carried out by removing any loose material using pressurized air to prevent contamination within the vacuum chamber of the instrument. Samples exhibiting electrostatic charging of their surfaces were sputtered with 4 nm platinum to enhance their surface conductivity, thereby facilitating the acquisition of higher-resolution images. Electron images were captured using a 7.5 µm aperture and an acceleration voltage of 3 kV, with a working distance of 3 mm, employing a Schottky field emitter as electron source. Additionally, an SE-InLens detector was utilized to acquire images of secondary electrons. Scale bars were added afterward using ImageJ (ver. 1.53f51), a software tool from the *National Institute of Health*. EDS data was acquired using the same setup as described above except for the InLens-detector which was changed to the UltimMax (*Oxford Instruments*). The working distance was set to 8.5 mm with an acceleration voltage of 10 keV and a 60 µm aperture. Data were processed by the software Aztec (ver. 6.1, *Oxford Instruments*) and the following elements were analyzed (X-ray emission lines): Eu ($M\alpha_1$, 1.131 keV; $L\alpha_1$, 5.846 keV; $L\alpha_2$, 5.817 keV; $L\beta_1$, 6.456 keV; $L\beta_2$, 6.843 keV; $L\gamma_1$, 7.480 keV), Tb ($M\alpha_1$, 1.240 keV; $L\alpha_1$, 6.273 keV; $L\alpha_2$, 6.238 keV; $L\beta_1$, 6.978 keV; $L\beta_2$, 7.367 keV; $L\gamma_1$, 8.102 keV), Yb ($M\alpha_1$, 1.521 keV; $L\alpha_1$, 7.416 keV; $L\alpha_2$, 7.367 keV; $L\beta_1$, 8.402 keV; $L\beta_2$, 8.759 keV; $L\gamma_1$, 9.780 keV).[68]

Fluorescence Microscopy (FM): True-color images were recorded with a fluorescence transmitted-light microscope BX-41 from *Olympus* (now: *Evident*). The images were recorded with a CC12 camera (*Soft Imaging System*) at 20x magnification (UMPlanFl, 20x/0.46, BD, Japan, *Olympus*) and the software Cell_F (*Olympus*). Samples were excited by a U-LH100HG mercury vapor lamp coupled to a U-RFL-T controller from *Olympus* utilizing a U-MWU-2 filter cube (UV broadband 330–385 nm, *Olympus*). Additional PL spectra were recorded of all responder materials matching the excitation wavelengths of the U-MWU-2 filter cube.

N_2 adsorption experiments: N_2 adsorption experiments were done on the BELSorp-max II (*MicrotracBEL Corporation*) after activation under vacuum at 150 °C overnight.

CHNS elemental analysis: Results are given in Table S1 in the Supporting Information.

pRF: Elemental analysis was performed using a Euro EA 3000 (*Euro Vector*), with oxygen serving as the carrier gas.

All other materials: Elemental analysis was performed using Unicube (*Elementar*).

Schemes were self-sketched using the free and open-source vector graphics editor software Inkscape (ver. 1.2.2) from *Inkscape Developers*. All instances where artificial intelligence was employed have been duly identified.

Supporting Information

Supporting Information is available from the Wiley Online Library or from the author.

Acknowledgements

This work was generously funded by the Deutsche Forschungsgemeinschaft (DFG) within the projects MU-1562/13-1, RE-3044/8-1, and JA-466/31-1 of the priority program SPP-1928/2 (project no. 434440165) "COORNETs".

Furthermore, the authors are grateful for the passionate support of our in-house electronics and precision engineering workshops in the development of our experimental setup with an open sample chamber for PEIS analysis.

Open access funding enabled and organized by Projekt DEAL.

Conflict of Interest

The authors declare no conflict of interest.

Data Availability Statement

The data that support the findings of this study are available in the supplementary material of this article.

Keywords

anti-counterfeiting, conductivity, mixed-matrix-membranes, nanoMOFs, photoluminescence

Received: January 9, 2025
Revised: March 6, 2025
Published online:

[1] EUIPO & Europol, Intellectual Property Crime Threat Assessment **2022**, Publications Office of the European Union, Luxembourg.
[2] R. Simões, J. Rodrigues, V. Neto, T. Monteiro, G. Gonçalves, *Small* **2024**, *20*, 2311526.
[3] W. Li, Y. Han, L. Wang, G. S. Selopal, X. Wang, H. Zhao, *RSC Adv.* **2024**, *14*, 83.
[4] A. Verhagen, A. Kelarakis, *Nanomaterials* **2020**, *10*, 1535.
[5] H. Huang, X. Wang, X. Li, Y. Li, G. Liu, L. Zhou, J. Shao, *Dyes Pigments* **2024**, *221*, 111802.
[6] L. Xu, J. Chen, J. Song, J. Li, J. Xue, Y. Dong, B. Cai, Q. Shan, B. Han, H. Zeng, *ACS Appl. Mater. Interfaces* **2017**, *9*, 26556.
[7] X. Yu, L. Wu, D. Yang, M. Cao, X. Fan, H. Lin, Q. Zhong, Y. Xu, Q. Zhang, *Angew. Chem., Int. Ed. Engl.* **2020**, *59*, 14527.
[8] Y. Shen, X. Le, Y. Wu, T. Chen, *Chem. Soc. Rev.* **2024**, *53*, 606.
[9] M. Babazadeh-Mamaqani, S. Alipour-Fakhri, M. Mohammadi-Jorjafki, H. Roghani-Mamaqani, H. Mardani, A. Babaie, *J. Mater. Chem. C* **2024**, *12*, 545.
[10] Y. Weng, Y. Hong, J. Deng, S. Cao, L.-J. Fan, *J. Colloid Interface Sci.* **2024**, *655*, 622.
[11] X. Wen, J. Zhang, J. Li, Y. Li, Y. Shi, X. Lu, S. Yang, J. Yu, *Adv. Funct. Mater.* **2024**, *34*, 2308973.
[12] H.-Q. Wang, Y. Tang, Z.-Y. Huang, F.-Z. Wang, P.-F. Qiu, X. Zhang, C.-H. Li, Q. Li, *Angew. Chem., Int. Ed. Engl.* **2023**, *62*, 202313728.
[13] B. Ding, P. Zeng, Z. Huang, L. Dai, T. Lan, H. Xu, Y. Pan, Y. Luo, Q. Yu, H.-M. Cheng, B. Liu, *Nat. Commun.* **2022**, *13*, 1212.
[14] E. Hendrick, M. Frey, E. Herz, U. Wiesner, *J. Eng. Fiber. Fabr.* **2010**, *5*, 155892501000500.
[15] H. Sha, B. Yan, *J. Mater. Chem. C* **2022**, *10*, 7633.
[16] V. Maritano, P. Barge, A. Biglia, L. Comba, D. Ricauda Aimonino, C. Tortia, P. Gay, *J. Food Prot.* **2024**, *87*, 100251.
[17] X. Zhang, Y. Cheng, J. You, J. Zhang, Y. Wang, J. Zhang, *ACS Appl. Mater. Interfaces* **2022**, *14*, 16582.
[18] R. Freund, O. Zaremba, G. Arnauts, R. Ameloot, G. Skorupskii, M. Dincă, A. Bavykina, J. Gascon, A. Ejsmont, J. Goscianska, M. Kalmutzki, U. Lächelt, E. Ploetz, C. S. Diercks, S. Wuttke, *Angew. Chem., Int. Ed. Engl.* **2021**, *60*, 23975.
[19] H. Furukawa, K. E. Cordova, M. O'Keeffe, O. M. Yaghi, *Science* **2013**, *1979*, 341.
[20] P. Falcaro, R. Ricco, C. M. Doherty, K. Liang, A. J. Hill, M. J. Styles, *Chem. Soc. Rev.* **2014**, *43*, 5513.
[21] T. Kasper, M. Pavan, K. Müller-Buschbaum, *J. Mater. Chem. A* **2024**, *12*, 769.

[22] T. Burger, M. V. Hernández, C. Carbonell, J. Rattenberger, H. Wiltsche, P. Falcaro, C. Slugovc, S. M. Borisov, A. C. S. Appl, *Nano Mater.* **2023**, *6*, 248.
[23] S. Yang, L. Peng, S. Bulut, W. L. Queen, *Chem.-Eur. J.* **2019**, *25*, 2161.
[24] A. Justin, J. Espín, M. J. Pougin, D. Stoian, T. Schertenleib, M. Mensi, I. Kochetygov, A. Ortega-Guerrero, W. L. Queen, *Adv. Funct. Mater.* **2024**, *34*, 2307430.
[25] B. Hosseini Monjezi, B. Sapotta, S. Moulai, J. Zhang, R. Oestreich, B. P. Ladewig, K. Müller-Buschbaum, C. Janiak, T. Hashem, A. Knebel, *Chem. Ing. Tech.* **2022**, *94*, 135.
[26] B. Chen, D. Fan, R. V. Pinto, I. Dovgaliuk, S. Nandi, D. Chakraborty, N. García-Moncada, A. Vimont, C. J. McMonagle, M. Bordonhos, A. Al Mohtar, I. Cornu, P. Florian, N. Heymans, M. Daturi, G. De Weireld, M. Pinto, F. Nouar, G. Maurin, G. Mouchaham, C. Serre, *Adv. Sci.* **2024**, *11*, 2401070.
[27] A. Wang, M. Walden, R. Ettlinger, F. Kiessling, J. J. Gassensmith, T. Lammers, S. Wuttke, Q. Peña, *Adv. Funct. Mater.* **2023**, *34*, 2308589.
[28] M. J. de Velásquez-Hernández, M. Linares-Moreau, E. Astria, F. Carraro, M. Z. Alyami, N. M. Khashab, C. J. Sumby, C. J. Doonan, P. Falcaro, *Coord. Chem. Rev.* **2021**, *429*, 213651.
[29] Z. Wei, R. Maile, L. M. Riegger, M. Rohnke, K. Müller-Buschbaum, J. Janek, *Batteries Supercaps* **2022**, *5*, 202200318.
[30] J. Andreo, R. Ettlinger, O. Zaremba, Q. Peña, U. Lächelt, R. F. De Luis, R. Freund, S. Canossa, E. Ploetz, W. Zhu, C. S. Diercks, H. Gröger, S. Wuttke, *J. Am. Chem. Soc.* **2022**, *144*, 7531.
[31] X. Cai, Z. Xie, D. Li, M. Kassymova, S.-Q. Zang, H.-L. Jiang, *Coord. Chem. Rev.* **2020**, *417*, 213366.
[32] S. Dai, C. Simms, G. Patriarche, M. Daturi, A. Tissot, T. N. Parac-Vogt, C. Serre, *Nat. Commun.* **2024**, *15*, 3434.
[33] H. Zhou, J. Han, J. Cuan, Y. Zhou, *J. Chem. Eng.* **2022**, *431*, 134170.
[34] X. He, H. Li, J. Wang, Y. Li, M. Su, Z. Xu, *Cryst. Growth Des.* **2021**, *21*, 1625.
[35] J. I. Deneff, K. S. Butler, L. E. S. Rohwer, C. J. Pearce, N. R. Valdez, M. A. Rodriguez, T. S. Luk, D. F. Sava Gallis, *Angew. Chem., Int. Ed. Engl.* **2021**, *60*, 1203.
[36] K.-J. Li, Y. Shen, S.-L. Li, X.-M. Zhang, *Dyes Pigm.* **2024**, *224*, 112033.
[37] M. Runowski, D. Marcinkowski, K. Soler-Carracedo, A. Gorczyński, E. Ewert, P. Woźny, I. R. Martín, *ACS Appl. Mater. Interfaces* **2023**, *15*, 3244.
[38] W. T. Carnall, in *Non-metallic Compounds – I*, **1979**, Elsevier, Amsterdam, *3*, pp. 171–208.
[39] R. E. Whan, G. A. Crosby, *J. Mol. Spectrosc.* **1962**, *8*, 315.
[40] S. I. Weissman, *J. Chem. Phys.* **1942**, *10*, 214.
[41] M. Maxeiner, L. Wittig, A. E. Sedykh, T. Kasper, K. Müller-Buschbaum, *J. Mater. Chem. A* **2023**, *11*, 22478.
[42] J. Dechnik, J. Gascon, C. J. Doonan, C. Janiak, C. J. Sumby, *Angew. Chem., Int. Ed. Engl.* **2017**, *56*, 9292.
[43] Y. Cheng, Y. Ying, S. Japip, S. Jiang, T. Chung, S. Zhang, D. Zhao, *Adv. Mater.* **2018**, *30*, 1802401.
[44] A. Knebel, J. Caro, *Nat. Nanotechnol.* **2022**, *17*, 911.
[45] A. Knebel, A. Bavykina, S. J. Datta, L. Sundermann, L. Garzon-Tovar, Y. Lebedev, S. Durini, R. Ahmad, S. M. Kozlov, G. Shterk, M. Karunakaran, I. D. Carja, D. Simic, I. Weilert, M. Klüppel, U. Giese, L. Cavallo, M. Rueping, M. Eddaoudi, J. Caro, J. Gascon, *Nat. Mater.* **2020**, *19*, 1346.
[46] J. Dechnik, F. Mühlbach, D. Dietrich, T. Wehner, M. Gutmann, T. Lühmann, L. Meinel, C. Janiak, K. Müller-Buschbaum, *Eur. J. Inorg. Chem.* **2016**, 4408.
[47] J. M. Stangl, D. Dietrich, A. E. Sedykh, C. Janiak, K. Müller-Buschbaum, *J. Mater. Chem. C* **2018**, *6*, 9248.
[48] J.-P. Gao, R.-X. Yao, X.-H. Chen, H.-H. Li, C. Zhang, F.-Q. Zhang, X.-M. Zhang, *Dalton Trans.* **2021**, *50*, 1690.
[49] X. Guo, G. Zhu, F. Sun, Z. Li, X. Zhao, X. Li, H. Wang, S. Qiu, *Inorg. Chem.* **2006**, *45*, 2581.
[50] T. M. Reineke, M. Eddaoudi, M. Fehr, D. Kelley, O. M. Yaghi, *J. Am. Chem. Soc.* **1999**, *121*, 1651.
[51] M. J. Neufeld, H. Winter, M. R. Landry, A. M. Goforth, S. Khan, G. Pratx, C. Sun, *ACS Appl. Mater. Interfaces* **2020**, *12*, 26943.
[52] J. Hafizovic, M. Bjørgen, U. Olsbye, P. D. C. Dietzel, S. Bordiga, C. Prestipino, C. Lamberti, K. P. Lillerud, *J. Am. Chem. Soc.* **2007**, *129*, 3612.
[53] M. V. Galaburda, V. M. Bogatyrov, J. Skubiszewska-Zięba, O. I. Oranska, D. Sternik, V. M. Gunko, *Appl. Surf. Sci.* **2016**, *360*, 722.
[54] X. Zhao, M. Zhang, X. Sun, X. Li, J. Li, *Appl. Surf. Sci.* **2020**, *506*, 144591.
[55] P. Staciwa, D. Sibera, I. Pełech, U. Narkiewicz, D. Moszyński, *J. Environ. Chem. Eng.* **2024**, *12*, 111735.
[56] W. T. Carnall, P. R. Fields, K. Rajnak, *J. Chem. Phys.* **1968**, *49*, 4447.
[57] W. T. Carnall, P. R. Fields, K. Rajnak, *J. Chem. Phys.* **1968**, *49*, 4450.
[58] K. Binnemans, *Coord. Chem. Rev.* **2015**, *295*, 1.
[59] Y. Lu, B. Yan, *J. Mater. Chem. C* **2014**, *2*, 7411.
[60] A. E. Sedykh, D. G. Kurth, K. Müller-Buschbaum, *Eur. J. Inorg. Chem.* **2019**, *2019*, 4564.
[61] M. A. Zhernakov, A. E. Sedykh, J. Becker, M. Maxeiner, K. Müller-Buschbaum, V. G. Shtyrlin, *Z. Anorg. Allg. Chem.* **2022**, *648*, 202200230.
[62] Y. Xie, G. Sun, G. A. Mandl, S. L. Maurizio, J. Chen, J. A. Capobianco, L. Sun, *Angew. Chem., Int. Ed. Engl.* **2023**, *62*, 202216269.
[63] V. G. Pol, L. K. Shrestha, K. Ariga, *ACS Appl. Mater. Interfaces* **2014**, *6*, 10649.
[64] T. Li, M. Cao, J. Liang, X. Xie, G. Du, *Polymers (Basel)* **2017**, *9*, 426.
[65] J. Liu, S. Z. Qiao, H. Liu, J. Chen, A. Orpe, D. Zhao, G. Qing, M Lu, *Angew. Chem., Int. Ed. Engl.* **2011**, *123*, 6069.
[66] P. Vadhva, J. Hu, M. J. Johnson, R. Stocker, M. Braglia, D. J. L. Brett, A. J. E. Rettie, *ChemElectroChem* **2021**, *8*, 1930.
[67] Y. Hu, A. Ruud, V. Miikkulainen, T. Norby, O. Nilsen, H. Fjellvåg, *RSC Adv.* **2016**, *6*, 60479.
[68] A. Thompson, D. Vaughan, in *X-Ray Data Booklet* (Eds.: J. Kirz, D. Attwood, E. Gullikson, M. Howells, K.-J. Kim, J. Kortright, I. Lindau, P. Pianetta, A. Robinson, J. Underwood, G. Williams, H. Winick), 2nd ed., Lawrence Berkeley National Laboratory, Berkeley **2001**.

3.3 Biodegradable and Recyclable Luminescent Mixed-Matrix-Membranes, Hydrogels and Cryogels based on Nanoscale Metal-Organic Frameworks and Biopolymers

published in *Advanced Functional Materials*
as part of the “Special Issue Coordination Networks: Building Blocks for Functional Systems (COORNETs)”.

Moritz Maxeiner, Julian Burkhart, Kateryna Borysova, Chiara Mazzariol, and Klaus Müller-Buschbaum

Supporting Information is available in
Appendix A – Supporting Information – Chapter 3.3.

Supporting video material is available online.

Reprinted with permission from *Adv. Funct. Mater.* **2025**, 2506570.

DOI: 10.1002/adfm.202506570

RESEARCH ARTICLE

ADVANCED FUNCTIONAL MATERIALS
www.afm-journal.de

Biodegradable and Recyclable Luminescent Mixed-Matrix-Membranes, Hydrogels, and Cryogels based on Nanoscale Metal-Organic Frameworks and Biopolymers

*Moritz Maxeiner, Julian Burkhart, Kateryna Borysova, Chiara Mazzariol, and Klaus Müller-Buschbaum**

This study presents the development of biodegradable and recyclable mixed-matrix-membranes (MMMs), hydrogels, and freeze-dried cryogels based on luminescent nanoscale metal-organic frameworks (nMOFs) and biopolymers agar and gelatine. Modified synthesis routes provide alternatives to membranes, particularly luminescent hydrogels and cryogels. Nanoscale MOFs are integrated to form stable composite materials keeping the matrix functional while the nMOF ($[Eu_2(bdc)_3(H_2O)_4]$: nEu-bdc, with bdc^{2-} = benzene-1,4-dicarboxylate) functions as a luminescent optical probe indicating the status of the hybrid material (bio-nMOF-MMMs). This research focuses on sustainability by utilizing biopolymers, such as agar and gelatine, instead of anthropogenic polymers to get bio-nMOF-MMMs. Analysis of two red luminescent bio-nMOF-MMMs, nEu-bdc@agar and nEu-bdc@gelatine, allow for synthesis and handling in non-inert and even aqueous environments, including characterization in terms of the constitution, photophysical properties, and recyclability. In response to a range of environmental stresses, the materials demonstrate a high capacity for regeneration and the capability to minimize waste in membrane technology, supporting circular economic principles. The bio-nMOF MMMs remain stable over multiple regeneration cycles of high-quality recycling leading back to the original bio-nMOF-MMMs. Altogether, luminescent bio-nMOF-MMM films, hydrogels, and cryogels offer alternatives to conventional membranes, with an inherent function to detect changes in the material's condition.

1. Introduction

Mixed-matrix-membranes (MMMs) are advanced materials that combine polymer matrices with dispersed inorganic or organic compounds and constituents to enhance the properties of traditional polymer membranes. Designed to improve gas separation, pervaporation, and other filtration processes, MMMs offer numerous benefits.[1–6] By incorporating fillers, they achieve improved selectivity and permeability, enhancing separation performance through additional pathways or selective adsorption sites for specific molecules. Developing MMMs presents challenges, such as ensuring uniform dispersion of fillers, compatibility between the polymer and filler, and maintaining consistent performance under operational conditions.[5,6] Despite these challenges, MMMs represent a promising direction in membrane technology, offering significant advantages over conventional membranes. Metal-organic frameworks (MOFs) represent a promising material as a potential filler, comprising inorganic building units (IBUs) of metals interconnected by organic linkers.[7–9] MOF properties derive mainly from their 3D structure[10,11] and can be combined with MMM features for tailoring specific applications, such as CO_2 capture,[2,5,6] hydrogen purification,[2,5] organic solvent nanofiltration,[6,12] or other functional composites.[13,14] In previous publications,[15–20] the impressive benefits of nanosized luminescent lanthanide MOFs (nLn-MOFs) over bulk Ln-MOFs were highlighted, specifically in terms of improved dispersibility and enhanced luminescence. The reduced particle size and improved luminescence properties of nLn-MOFs provide a distinctive advantage over their bulk counterparts, rendering them optimal fillers for luminescent nMOF-MMMs. Additionally, the photoluminescence of the nLn-MOFs has potential applications in probe-based optical detection of changes in the status of hybrid materials associated with chemical or physical changes. Biodegradable MOF-MMMs (bio-MOF-MMMs) represent a step forward from conventional polymer-based MOF-MMMs, aligning with the

M. Maxeiner, J. Burkhart, K. Borysova, C. Mazzariol, K. Müller-Buschbaum
Institute of Inorganic and Analytical Chemistry
Justus-Liebig-University Giessen
Heinrich-Buff-Ring 17, 35392 Giessen, Germany
E-mail: kmbac@uni-giessen.de
K. Müller-Buschbaum
Centre for Materials Research (LAMA)
Justus-Liebig-University Giessen
Heinrich-Buff-Ring 16, 35392 Giessen, Germany

The ORCID identification number(s) for the author(s) of this article can be found under https://doi.org/10.1002/adfm.202506570

DOI: 10.1002/adfm.202506570

ADVANCED SCIENCE NEWS
www.advancedsciencenews.com

ADVANCED FUNCTIONAL MATERIALS
www.afm-journal.de

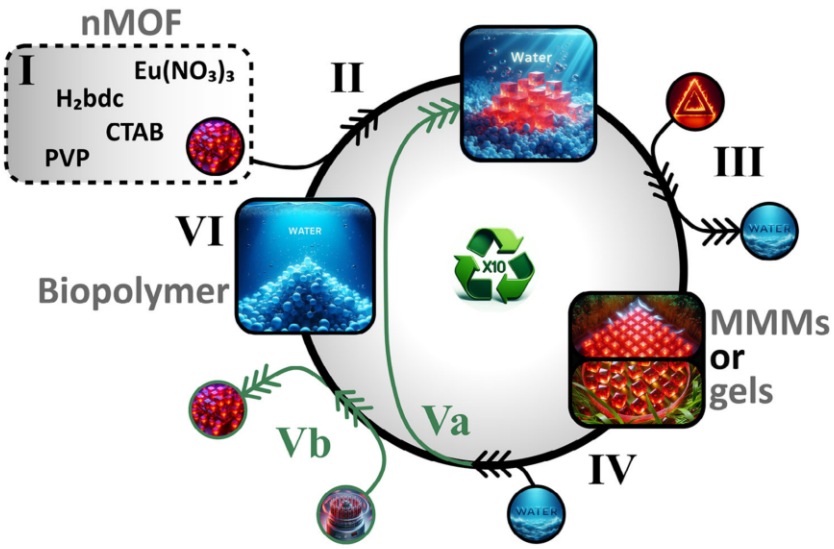

Scheme 1. A sketched experimental procedure of the high-quality recycling process was developed. Synthesis of a luminescent nMOF $[Eu_2(bdc)_3(H_2O)_4]$ (nEu-bdc, where bdc^{2-} = benzene-1,4-dicarboxylate) from $Eu(NO_3)_3$ and terephthalic acid (H_2bdc) in a surfactant-assisted approach with CTAB (cetyltrimethylammonium bromide) and PVP (polyvinyl pyrrolidone) (I). Bio-nMOF-MMMs or gels were formed by incorporating nEu-bdc into the biopolymers agar and gelatine (nEu-bdc@agar and nEu-bdc@gelatine) through aqueous dispersion (II) and water evaporation (III). After characterization, the bio-nMOF-MMMs were redispersed in water (IV) and processed either by high-quality recycling of the bio-nMOF-MMMs (Va) or by separating nEu-bdc via centrifugation (Vb) allowing the separate reuse of biopolymer (VI) and nEu-bdc. Durability and recyclability were evaluated by repeating the high-quality recycling (Va) up to ten times. The scheme was created with the support of AI (DALL·E 3 engine).

growing demand for sustainable materials[21–24] and fulfill similar roles to conventional MMMs, such as gas separation[25–27] or water treatment,[28,29] but with the added benefit of being environmentally friendly.

Green chemistry, as part of the concept of sustainability, is defined as the design, development, and implementation of chemical processes and products that minimize environmental impact, reduce resource consumption, and enhance societal benefits without compromising the ability of future generations to meet their needs.[30] Especially the chemical industry encounters sustainability on a daily basis for it is a driver of climate change by emitting 7.4% of global greenhouse gas emissions, for instance.[31] To mitigate greenhouse gas emissions, enhancing the recycling of materials in place of synthesizing new compounds represents a key factor for improvement. The term 'circular economy' refers to a sustainable economic model in which used materials are reintegrated into the production cycle to create new products. High-quality recycling refers to a recycling process that restores the original material's properties and reduces the need for virgin resources thereby supporting a circular economy.[32] Polymers are a significant component within this approach, yet in 2022, the global recycling rate for polymers remained at just 9% (35.5 million tons).[33] Over the past decade, there has been a growing interest in nature-derived biopolymers as these materials can naturally decompose without causing environmental harm.[34–36] Typical biopolymers in use are agar,[37–39] pectin,[40–42] gelatine[43–45] or chitosan.[46–48]

This study focuses on the biodegradability, recyclability, and development of advanced nMOF@biopolymer composites, including materials beyond membranes to hydrogels and cryogels. Biodegradable bio-nMOF-MMMs with a luminescent nMOF as an optical probe (nEu-bdc, where bdc^{2-} = benzene-1,4-dicarboxylate) were successfully generated as luminescent films, hydrogels, and freeze-dried cryogels.

2. Results and Discussion

The goal of this work was to achieve biopolymers as mixed-matrix-membranes together with an MOF as an optical probe for a status analysis of polymer vs. chemical and physical influences as well as an indicator for recyclability. Altogether, luminescent and biodegradable bio-nMOF-MMMs were successfully generated, combining the biopolymers agar and gelatine with the red luminescent europium-containing nanoMOF nEu-bdc (nMOF, bdc^{2-} = benzene-1,4-dicarboxylate) including the synthesis as luminescent films, hydrogels and freeze-dried cryogels suitable for high-quality recycling.

Scheme 1 illustrates the experimental procedure of the synthesis and high-quality recycling process developed for nEu-bdc@biopolymer, which is described in detail in the following section. The red luminescent nMOF $[Eu_2(bdc)_3(H_2O)_4]$ (referred to as nEu-bdc, where bdc^{2-} = benzene-1,4-dicarboxylate) was synthesized using a surfactant-assisted method (I), as described in a recent publication[15] and subsequently altered as outlined in the Experimental Section. With regard to the nMOF, it should be noted that its synthesis is not part of the recycling process; the nEu-bdc is only required to be synthesized once in the preliminary step (I). Nevertheless, the synthesis must be critically evaluated in the context of environmental concerns.

ADVANCED SCIENCE NEWS
www.advancedsciencenews.com

ADVANCED FUNCTIONAL MATERIALS
www.afm-journal.de

Dimethylformamide (DMF) is a widely employed solvent in the synthesis of MOFs,[8] yet its detrimental impact on the environment cannot be denied.[49] Therefore, the DMF-free composition $[Eu_2(bdc)_3(H_2O)_4]$ was selected for this study, which limits DMF to the formation of initial nEu-bdc $[Eu_3(bdc)_{4.5}(dmf)_2(H_2O)_3]$, then being replaced with water in a controlled way, as described in a recent publication.[50] The transformation to the DMF-free form of nEu-bdc allows the recovery of the applied DMF through a process involving centrifugation to separate nEu-bdc from dissolved reactants and subsequent vacuum distillation to precipitate dissolved reactants to gain purified DMF. Consequently, this approach minimizes the potential environmental impact of DMF, thereby reducing concerns regarding ecological sustainability. The role of reagents and surfactants is evaluated concerning their sustainability later in this article. Bio-nMOF-MMMs consisting of nEu-bdc incorporated into the biopolymer matrices agar and gelatine (nEu-bdc@agar and nEu-bdc@gelatine) were prepared by dispersing nEu-bdc in aqueous solutions of the respective biopolymer (II), followed by water evaporation at varying temperatures (III). After characterization, the bio-nMOF-MMMs were redispersed in water (IV), providing two options for further processing: (Va) a high-quality recycling without adding new nMOF or new biopolymer and continuing with step (III) in the depicted process, or (Vb) the separation of nEu-bdc from the biopolymer matrix via centrifugation for a potentially separate use of the two components. This recovery method, in conjunction with other strategies for the urban mining of critical resources,[51] contributes to the reutilization of these valuable materials (i.e., including europium), supporting the advancement toward a circular economy. In pathway (VI), the separated biopolymer could be reused with freshly synthesized nEu-bdc, if intended. To evaluate the durability and recyclability of the developed bio-nMOF-MMMs, the high-quality recycling (Va) was repeated ten times, which allowed for the assessment of the material's resistance to environmental stresses and overall recyclability.

2.1. Characterization of nEu-bdc

Fundamental characterization of the nMOF nEu-bdc was performed using powder X-ray diffraction (PXRD) in Bragg-Brentano geometry, alongside simultaneous differential thermal analysis/thermogravimetry coupled with mass spectrometry (DTA/TG-MS). Particle analysis, including aspect ratio, size, and size distribution, was conducted using dynamic light scattering (DLS) and scanning electron microscopy (SEM). Optical properties were characterized via qualitative photoluminescence spectroscopy, UV–vis diffuse reflectance spectroscopy (UV–vis-DRS), quantum yield determination, and luminescence decay time determinations. Additionally, the pore system characteristics of nEu-bdc were determined via N_2 adsorption isotherms (BET = Brunauer–Emmett–Teller).

2.1.1. Powder X-Ray Diffraction Analysis of nEu-bdc

The diffraction patterns shown in **Figure 1** confirm the successful synthesis of nEu-bdc as $[Eu_2(bdc)_3(H_2O)_4]$, for it aligns with

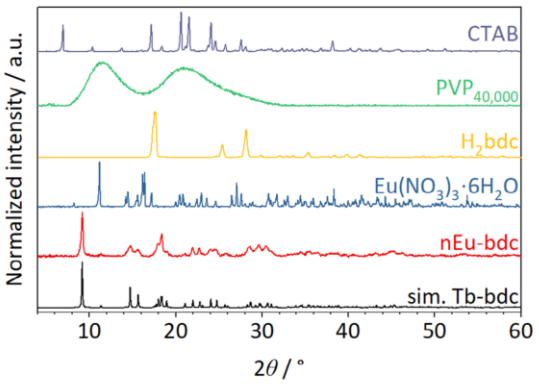

Figure 1. Diffractograms of the nMOF nEu-bdc as $[Eu_2(bdc)_3(H_2O)_4]$ (red), the educts H_2bdc (yellow) and $Eu(NO_3)_3{\cdot}6H_2O$ (blue), the surfactants CTAB (violet) and $PVP_{40,000}$ (green) as well as the simulated diffractogram of Tb-bdc as $[Tb_2(bdc)_3(H_2O)_4]$ (black) obtained from single-crystal data.[52]

the simulated pattern derived from the single-crystal data of Tb-bdc.[52] **Scheme 2A** shows the structure of the linker bdc^{2-} while the 3D structure of $[Eu_2(bdc)_3(H_2O)_4]$ is illustrated in Scheme 2B. Due to the close structural proximity, the single-crystal data of Tb-bdc is applicable to nEu-bdc. Additionally, the analysis of the diffractograms reveals no presence of the educts or alternative MOF modifications. However, a broadening of the reflections is observed for the powder pattern of nEu-bdc, which can be attributed to a reduction in crystallinity, likely resulting from a decrease in particle size and the coverage with the amorphous surfactants polyvinyl pyrrolidone (PVP) and cetyltrimethylammonium bromide (CTAB). Similar phenomena have been reported for related nMOFs.[15,53] Thus, the application of the Scherrer equation for crystallite size determination is not feasible in this case. N_2 adsorption isotherm (Figure S16, Supporting Information), pore size distribution (Figure S17, Supporting Information) as well as the calculated specific surface area, pore size, and pore volume of nEu-bdc (Table S3, Supporting Information) are given in the Supporting Information. For the surfactants that are still present on the surface of nEu-bdc, an effect of surfactants on the BET calculations needs to be considered evaluating the results that are hard to quantify.

2.1.2. Thermal Properties of nEu-bdc

In order to determine the thermal properties including thermal decomposition, nEu-bdc was analyzed using DTA/TG-MS. To also simulate environmental conditions, the decomposition of nEu-bdc was performed using synthetic air, resulting in material breakdown via oxidation. As shown in **Figure 2**, the release of H_2O trapped within the pores of nEu-bdc begins at ≈150 °C, as evidenced by the MS signal of H_2O and a corresponding mass loss of 4%. Oxidation of the surfactants, CTAB and $PVP_{40,000}$, starts at ≈250 °C, indicated by the detection of NO and CO_2 gases. The decomposition of nEu-bdc starts at ≈350 °C, accompanied by CO_2 emission, typical for carbohydrate oxidation. Subsequently, a further 50% reduction in mass is observed,

ADVANCED SCIENCE NEWS
www.advancedsciencenews.com

ADVANCED FUNCTIONAL MATERIALS
www.afm-journal.de

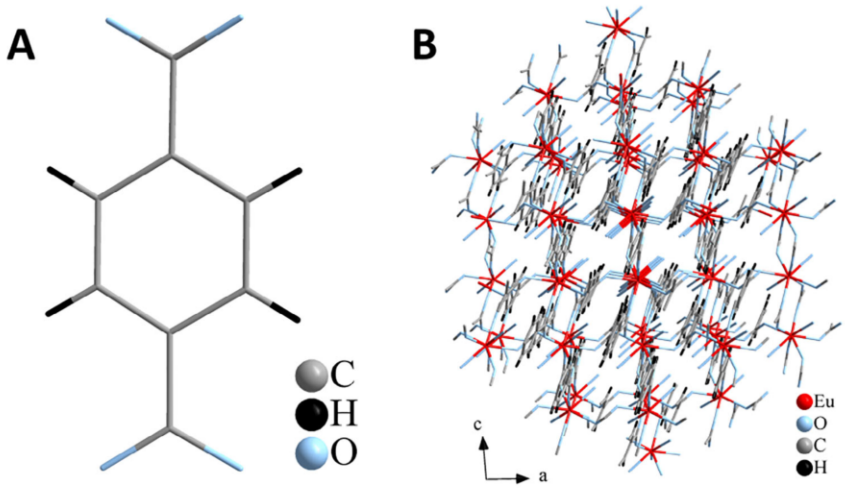

Scheme 2. A) Molecular structure of the deprotonated linker bdc^{2-} and B) the crystal structure of nMOF nEu-bdc as $[Eu_2(bdc)_3(H_2O)_4]$. The color code is depicted next to the corresponding structure.

concluding at ≈700 °C without any further loss in mass up to 1000 °C. The abrupt decrease of the exothermic signal observed by DTA indicates the complete oxidation of the organic moieties of nEu-bdc. PXRD analysis confirms the formation of Eu_2O_3 (see Figure S4, Supporting Information).

2.1.3. Particle and Particle Size Distribution Analysis of nEu-bdc

The particle size and its distribution are presented in **Figure 3A** for nEu-bdc. DLS analysis indicates an average particle size of 160±60 nm, with a homogeneous particle size distribution characterized by a prominent global maximum and minimal tailing. It is important to note that DLS measures the hydrodynamic radius, which accounts for both the particle and the coordinated solvent molecules. As a result, the observed particle size is larger than the actual core particle size. Hence, the SEM image presented in Figure 3B, shows the investigated nEu-bdc particles revealing their partially aggregated, rod-like morphology with smaller particle sizes ranging from 25 to 100 nm. The narrow particle size distribution detected by DLS is corroborated by SEM observations.

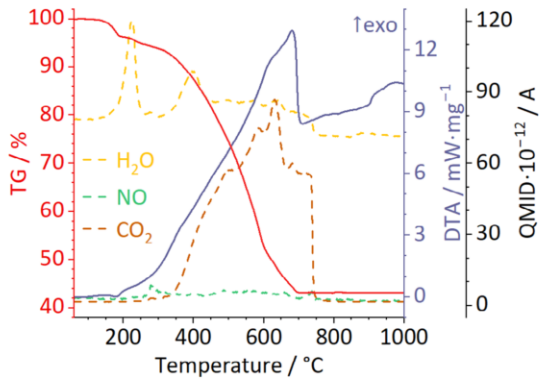

Figure 2. The DTA/TG-MS analysis of nEu-bdc identified as $[Eu_2(bdc)_3(H_2O)_4]$ with residual surfactants and conducted using synthetic air. The dashed lines in the MS spectra correspond to the mass signals of H_2O (m/z = 18, yellow) and CO_2 (m/z = 40, brown), with their intensities plotted against a scale of QMID·10^{-12} A (black axis). Whereas the signal of NO (m/z = 30, green) is displayed with QMID·10^{-13} A.

2.1.4. Photophysical Properties of nEu-bdc

Photoluminescence excitation and emission spectra of nEu-bdc were measured at both room temperature (RT, see **Figure 4**) and 77 K (see Figure S6, Supporting Information). The results align with previously reported data for bulk Eu-bdc.[15,54,55] This includes the broad band between 280 and 330 nm and the weak f-f transitions[56] in the excitation spectrum of nEu-bdc, corresponding to the $\pi^*\leftarrow\pi$ transition of the linker and the transitions of Eu^{3+} ($^5L_6$,^5D_J (J = 0–4)←$^7F_0$ and ^5D_J (J = 0–4)←$^7F_1$), respectively. The results emphasize the role of the organic linker as a sensitizer, facilitating an energy transfer to Eu^{3+}. Upon excitation, Eu^{3+} emits light via its characteristic $^5D_0\rightarrow{}^7F_J$ (J = 0–6) transitions. The hyperfine structure[56] of the peaks serves as a distinctive fingerprint for a specific coordination environment of Eu^{3+} and facilitates the assessment of changes in coordination through the entire recycling cycle. The luminescence decay of the transition $^5D_0\rightarrow{}^7F_2$ at 617 nm shows characteristic lifetimes of τ_1 = 1.02(4) ms and τ_2 = 0.3895(2) ms with quantum yields of 11.9(2)%. For a highly water-containing MOF, this is a proper efficiency enabling the MOF for its probe role in this study.

Additionally, UV–vis-DRS was applied to investigate the absorption behavior of nEu-bdc. Figure 4 reveals a broad absorption band at 280–320 nm, which can be attributed to the $\pi^*\leftarrow\pi$ transition of the organic linker and fits the recorded excitation

ADVANCED SCIENCE NEWS
www.advancedsciencenews.com

ADVANCED FUNCTIONAL MATERIALS
www.afm-journal.de

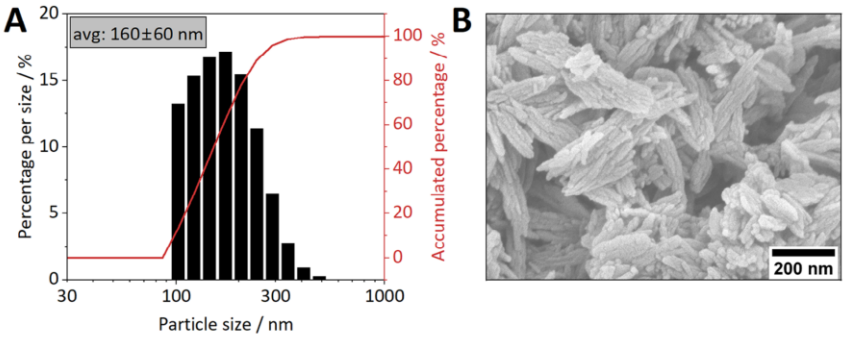

Figure 3. A) Particle size distribution of nEu-bdc with the average particle size ±2σ given in the gray box and B) SEM image of nEu-bdc particles.

spectrum of nEu-bdc. Furthermore, the absorption spectrum of nEu-bdc shows three peaks, low in intensity, at 394, 465, and 535 nm corresponding to the transitions $^5L_6 \leftarrow ^7F_0$, $^5D_2 \leftarrow ^7F_0$ and $^5D_1 \leftarrow ^7F_1$.

2.1.5. Resilience of nEu-bdc for Varying pH Levels

The pH value plays a critical role in biocompatibility and biodegradability.[24] Consequently, the stability of the nMOF nEu-bdc was experimentally assessed by introducing three droplets of nEu-bdc dispersed in H_2O (pH 5.3) into aqueous solutions spanning pH 0–14 at $T = 22.7$ °C. **Figure 5** illustrates the results of the stability test of nEu-bdc across different pH values (also available as a Video S1, Supporting Information). The nEu-bdc remains stable between pH 3 and pH 11 indicated by the typical red luminescence of the Eu^{3+}-containing MOF, with the most stable dispersions observed in solutions with pH values of 8 and 9. The aqueous nEu-bdc dispersion, with an initial pH of 5.3, shows similar stability at pH 6 and 7 due to the sensitivity of proton concentration near neutral pH. It is less stable at pH 5–7 compared to the more stable conditions at pH 4 or pH 8–10.

Below pH 3 the linker bdc^{2-} gets protonated which opens the chelating coordination Eu-O and consequently leads to degradation of nEu-bdc visualized by the diminished red photoluminescence.[57,58] The emerging terephthalic acid is not detrimental to the environment and has been attested to a low order of toxicity to organisms,[59] which allows its usage as a food supplement.[24] The same can be said of the surfactant PVP.[60] CTAB is insoluble in aqueous solutions if it is not ionically bound. Despite its use in several pharmaceutical products, CTAB is controversial and discussed by means of safety concerns.[61] At pH values exceeding 11, the Eu^{3+} interacts with OH^- resulting in the formation of amorphous hydroxides of Eu^{3+}, as shown in the literature.[62–64] Trivalent europium ions, as obtained after the degradation of nEu-bdc, were assessed as low-toxic with good biocompatibility in the solution. Albeit aqueous solutions of trivalent europium, the chemical composition ($[Eu^{3+}X_n]$, with $X = O^{2-}$, Cl^-, OH^-, ...) as well as particle size (e.g., macroparticles, nanoparticles, ...) of possible solid-state compounds need to be taken into account for hazard assessments.[65]

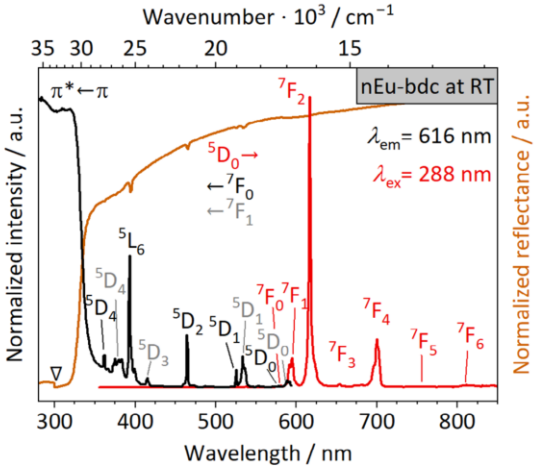

Figure 4. Normalized photoluminescence excitation (black) and emission (red) spectra, and the UV–vis-DRS (brown) of nEu-bdc at RT. The observed transitions are denoted with the respective term symbols. ∇ marks the position of the source changeover of the UV–vis spectrophotometer, resulting in a systematic artifact not related to nEu-bdc.

2.2. Characterization of the Bio-nMOF-MMMs nEu-bdc@agar and nEu-bdc@gelatine

The bio-nMOF-MMMs were characterized by PXRD (transmission), qualitative photoluminescence spectroscopy, UV–vis absorption spectroscopy, SEM, and energy-dispersive X-ray spectroscopy (EDS).

Agar and gelatine are classified as biopolymers, indicating that they are naturally derived macromolecules produced by living organisms. Their excellent water-solubility is fundamental to environmentally friendly synthesis routes and enables the resignation of harmful chemicals.[66,67] Water solubility further benefits their biodegradability over time, which is a plus compared to anthropogenic polymers.

Agar is available on a commercial scale through hot water extraction from the cell walls of the red algae *Gracilaria* (family: Rhodophyceae), which is easy to cultivate. Despite the energy-consuming extraction process, red algae are part of the "protist" clade, which are neither animals nor plants.[68]

ADVANCED SCIENCE NEWS
www.advancedsciencenews.com

ADVANCED FUNCTIONAL MATERIALS
www.afm-journal.de

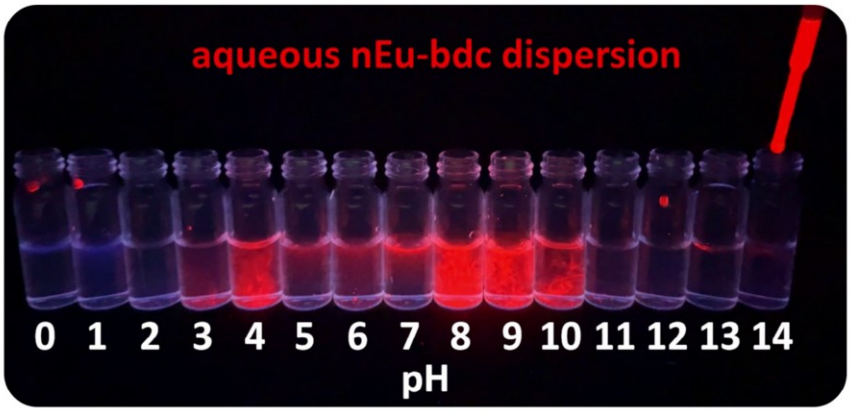

Figure 5. pH-dependent stability test of red luminescent nEu-bdc against aqueous solutions with pH values of 0–14. The aqueous nEu-bdc dispersion was added to each vial containing an aqueous solution with a certain pH (e.g., a vial labeled 0 indicated pH = 0). This image represents the moment after the last droplet was added to the vial with pH = 14. Also, available as Video S1 (Supporting Information) in the Supporting Information.

This makes their use considered to be eco-friendly, while the extraction methods become greener as recent literature shows.[69,70] Agar consists primarily of two components: agarose (composed of β-D-galactose and 3,6-anhydro-α-L-galactose) and agaropectin (similar to agarose, but with the hydroxyl groups of 3,6-anhydro-α-L-galactose substituted by methoxy, pyruvate, or sulfoxy groups).[39,66] Its polymer structure is given in **Scheme 3**A. Agar achieves its characteristic reversible hydrogel form when a hot aqueous solution of agar is allowed to cool to RT.[38,71] However, the formation of hydrogel capsules and sponge-like cryogels is also feasible via a modification of the synthesis pathway.

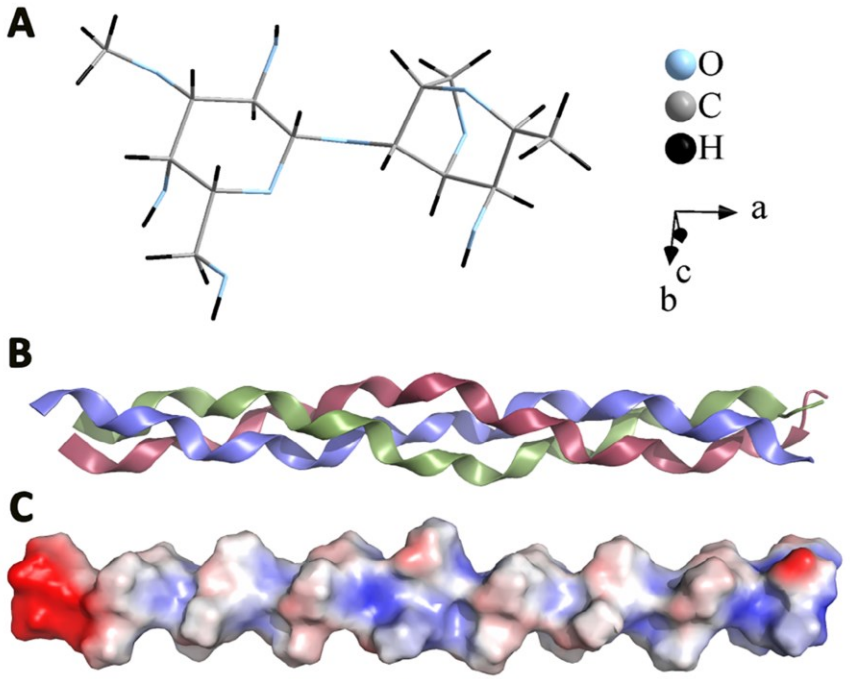

Scheme 3. Illustration of (A) the polysaccharide molecular unit of agar,[39] B) the tertiary structure of associated α-helices of the protein collagen as the main component of gelatine[75] (PDB code: 1cag), and C) the simulation of the charge density distribution in the protein collagen (software: PyMOL, ver. 3.1.0, *Schrödinger LLC*). Each α-helix subunit is depicted in a distinct color for clarity. In (C) the color code indicates the positively (blue) charged N-terminus and the negatively (red) charged C-terminus as well as neutral (white) amino acid residues of collagen.

ADVANCED SCIENCE NEWS
www.advancedsciencenews.com

ADVANCED FUNCTIONAL MATERIALS
www.afm-journal.de

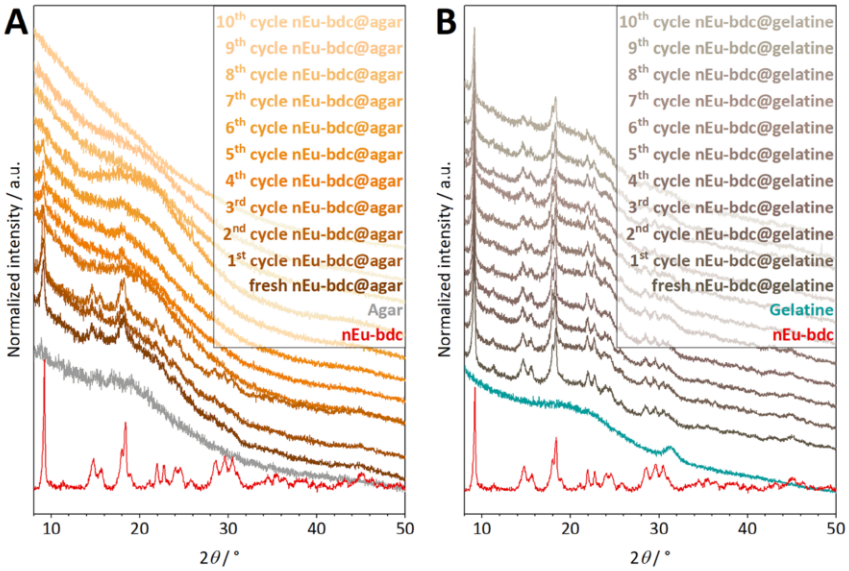

Figure 6. Powder patterns of A) nEu-bdc@agar and B) nEu-bdc@gelatine (both with 10 wt.% nEu-bdc), the pure biopolymers agar and gelatine as well as the pure nMOF nEu-bdc prior to inserting into the biopolymer.

Gelatine is commercially derived from animal skin or bones, which are by-products from the meat industry. The extraction process is a time-consuming, multi-step process. However, there are greener alternatives that are ready to be adopted in order to make extraction processes more environmentally friendly.[72,73] Gelatine is mainly composed of a mixture of multiple short polypeptide sequences derived from the hydrolytic breakdown of collagen.[45,74] Each polypeptide string is folded as α-helix and associated by intermolecular hydrogen bond interactions as a triplet strand (see Scheme 3B).[75] The charge density distribution calculated from single crystal X-ray data of collagen[75] using the software PyMOL (ver. 3.1.0, *Schrödinger LLC*) is depicted in Scheme 3C. The red (negatively charged), blue (positively charged) and white (neutral) color code clearly emphasizes interactions of the hydrophobic amino acid residues with the surfactants PVP and CTAB (Scheme S1, Supporting Information), which enclose the nEu-bdc nanoparticles.

In the following sections of this article, when referring to nEu-bdc@agar and nEu-bdc@gelatine in equal measure, they will be collectively referred to as nEu-bdc@biopolymer.

2.2.1. Structural Properties of nEu-bdc@biopolymer

A 10 wt.% loading of nEu-bdc for nEu-bdc@biopolymer was needed to produce a sufficiently strong diffraction signal during PXRD analysis over the entire recycling cycle (**Figure 6**). Experiments with 5 wt.% nEu-bdc were also conducted for greater sustainability and improved nEu-bdc@biopolymer stability (Figure S5, Supporting Information).

In Figure 6, the powder patterns of nEu-bdc@biopolymer show reflections similar in position as for nEu-bdc hereby confirming an intact crystal structure without potential side phases or decomposition. For high-quality recycling never reaches 100% efficiency, a natural overall mass loss after each cycle is apparent for nEu-bdc@biopolymer but to a different extent. The diffractograms show that nEu-bdc reflections fade in both nEu-bdc@agar and nEu-bdc@gelatine throughout the recycling cycle, with the fading being stronger for nEu-bdc@agar. The broad background is caused by the amorphous character of agar and gelatine which also undergo a decrease in intensity, as observed at $2\theta = 18°$ and 32°, respectively. Additionally, reduced intensity of the red emission along with particle aggregation and a loss of physical stability in nEu-bdc@agar (**Figure 7A**; Figure S3A, Supporting Information for 5 wt.% nEu-bdc) support the previously drawn conclusion. In contrast, nEu-bdc@gelatine shows a constant red emission with retaining physical integrity (Figure 7B; Figure S3B, Supporting Information for 5 wt.% nEu-bdc). Given that these observations are easily detectable by the naked eye, nEu-bdc luminescence is capable of imparting a red emission color to the bio-nMOF-MMMs and hence is able to function as a status probe for the materials state even in aqueous media. Consequently, changes in the material's condition can provoke a corresponding alteration, e.g., in the luminescence intensity of the material. Agar provides fewer proper conditions for a stable nEu-bdc/agar dispersion, which then results in sedimentation processes, where a small amount of nEu-bdc is lost along with a small amount of agar at each recycling step due to a less homogeneous dispersion compared to nEu-bdc@gelatine. Still, multiple high-quality recycling steps are possible for nEu-bdc@agar, The observations lead to the conclusion that nEu-bdc@gelatine is more durable over time and recycling cycles in terms of physical stability than nEu-bdc@agar and underline the crucial balance between the membrane integrity and its performance defined by the amount of filler used.

ADVANCED SCIENCE NEWS
www.advancedsciencenews.com

ADVANCED FUNCTIONAL MATERIALS
www.afm-journal.de

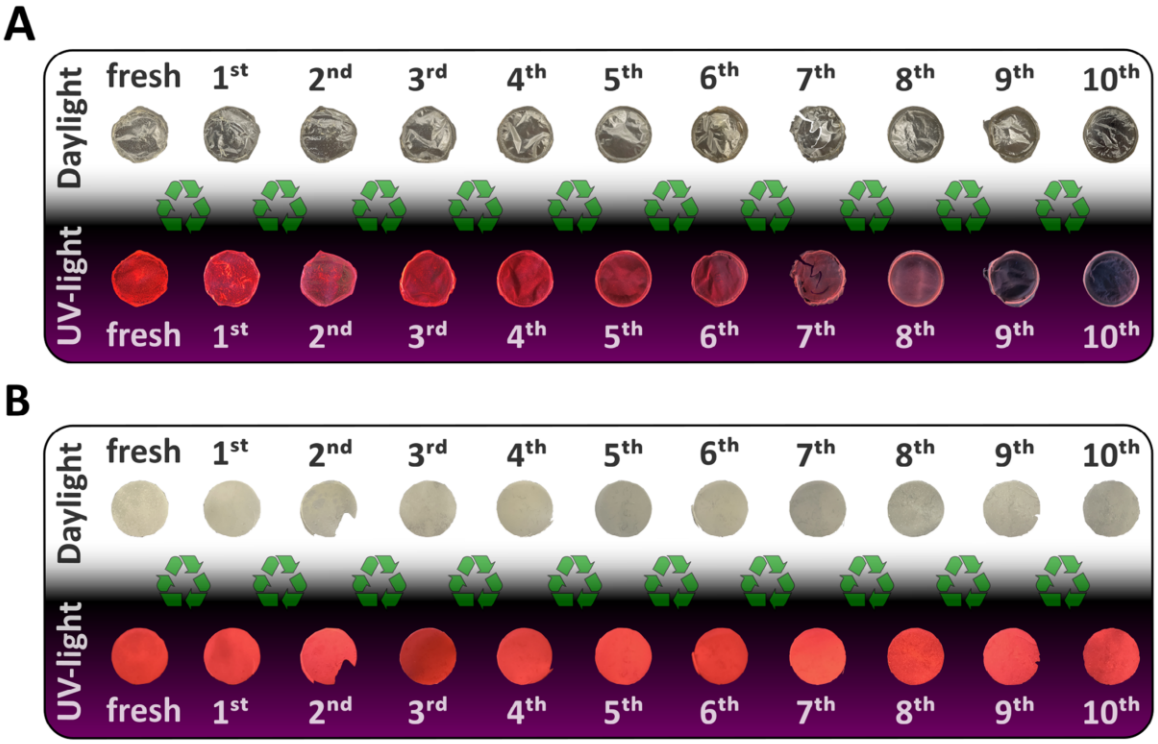

Figure 7. Photographs of A) nEu-bdc@agar and B) nEu-bdc@gelatine (both with 10 wt.% nEu-bdc) beginning with a freshly synthesized bio-nMOF-MMM and continuing through each subsequent recycling step. Imaging was conducted under both daylight and UV light (302 nm), focusing on circular cutouts. Color impressions always must be evaluated together with qualitative photoluminescence spectra and chromaticity.

2.2.2. Photophysical Properties of nEu-bdc@biopolymer

Qualitative photoluminescence spectroscopy provides the excitation and emission spectra of nEu-bdc@biopolymer shown in **Figure 8** for 10 wt.% nEu-bdc (see Figure S7, Supporting Information for 5 wt.% nEu-bdc). Furthermore, the corresponding UV–vis absorption spectra are presented in Figure S12 (Supporting Information). Additionally, the photoluminescence spectra and UV–vis absorption spectra of pure agar and gelatine are shown in Figures S8 and S11 (Supporting Information), respectively.

In Figure 8, the excitation and emission spectra of the linker bdc^{2-} clearly differ in shape and location of the peak maxima from those of nEu-bdc@biopolymer. This evidence suggests that an efficient energy transfer to the Eu^{3+} occurs, thereby providing further support for the hypothesis that the crystal structure of nEu-bdc is maintained throughout the entire recycling cycle.

The excitation spectra of nEu-bdc@agar and nEu-bdc@gelatine exhibit disparate shapes when compared. However, there are only minor discrepancies in intensity, and the Eu^{3+} transition $^5L_6 \leftarrow {}^7F_0$ is discernible at 394 nm between the fresh and tenfold high-quality cycled membranes. The comparison with nEu-bdc shows no significant difference in the excitation spectra of nEu-bdc@biopolymer, except for the tenfold cycled nEu-bdc@agar, which can be attributed to the minimal amount of nEu-bdc present in the agar.

A broad peak in the emission spectrum of nEu-bdc@agar with a maximum at 420 nm corresponds to an agar-based emission, which becomes more prominent throughout the recycling cycles. This development gives reason for the more bluish appearance of tenfold cycled nEu-bdc@agar as presented in Figure 7. However, an emission based on gelatine has not been observed in nEu-bdc@gelatine. The emission spectra of nEu-bdc@gelatine reveal congruent fingerprint areas for freshly synthesized nEu-bdc@gelatine and ten times cycled nEu-bdc@gelatine proving a retained nEu-bdc crystal structure (compare also to Figure 4). However, the transition $^5D_0 \rightarrow {}^7F_2$ in ten times cycled nEu-bdc@agar undergoes a weak Stark splitting in response to a changing chemical environment. Nevertheless, the characteristic emission spectrum of Eu^{3+} in nEu-bdc@agar confirms the presence of nEu-bdc. Characteristic decay lifetimes in the millisecond for the nEu-bdc range support reported findings and are in accordance with the literature.[76] As presented in Figures S13–S15 (Supporting Information), the influence of the polymer materials, hydroxy groups in nEu-bdc@agar and amine groups in nEu-bdc@gelatine cause the lifetime of the emitting europium states to decrease to one-tenth of nEu-bdc. The effect of amine groups and hydroxy groups is also observed in the quantum yield, where the original 11.9(2)% of nEu-bdc slightly decreased to 7.4(2)%

ADVANCED SCIENCE NEWS
www.advancedsciencenews.com

ADVANCED FUNCTIONAL MATERIALS
www.afm-journal.de

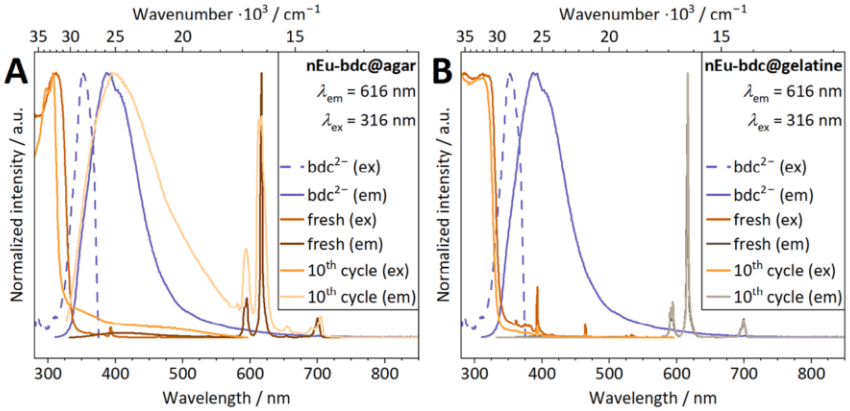

Figure 8. Normalized excitation (ex) and emission (em) spectra of (A) nEu-bdc@agar and (B) nEu-bdc@gelatine, both containing 10 wt.% nEu-bdc. The freshly synthesized nEu-bdc@biopolymer and the sample from the 10th recycling cycle represent the initial and final bio-nMOF-MMM in a ten-cycle recycling process. The excitation and emission spectrum of the linker bdc^{2-} is also given for the evaluation of the stability of nEu-bdc (λ_{ex} = 350 nm, λ_{em} = 395 nm).

and 9.1(2)% for nEu-bdc@agar and nEu-bdc@gelatine, respectively.

The overall loss of material throughout the high-quality recycling cycles is accompanied by a decline in the emission intensity of nEu-bdc. Therefore, a semi-quantitative estimation of the correlation between the mass loss of nEu-bdc and its luminescence intensity was calculated with the results given in Table S1 and Figure S2 (Supporting Information). The mass-luminescence correlation is calculated as the ratio of the loss of emission intensity (of the most intense transition $^5D_0 \rightarrow {}^7F_2$ at 616 nm) per mass loss from fresh nEu-bdc@biopolymer through a tenfold recycling process. The calculations demonstrate that nEu-bdc@agar exhibits a loss of ≈1100 cps mg^{-1} $cycle^{-1}$ (equal to 0.1% mg^{-1} $cycle^{-1}$), whereas nEu-bdc@gelatine displays only a loss of ≈300 cps mg^{-1} $cycle^{-1}$ (equal to 0.04% mg^{-1} $cycle^{-1}$). The data indicate that the observed loss of intensity is correlated with a mass loss of nEu-bdc rather than the decomposition of nEu-bdc. Otherwise, the calculated loss of intensity per cycle and mass would be significantly higher.

Further validation of the stability of nEu-bdc is provided by the asymmetry ratio of the Eu^{3+} emissions $^5D_0 \rightarrow {}^7F_1$ and $^5D_0 \rightarrow {}^7F_2$ based on their distinct sensitivity to a changing coordination environment.[77] Hence, the ratio of the sensitive $^5D_0 \rightarrow {}^7F_2$ transition to the non-sensitive $^5D_0 \rightarrow {}^7F_1$ transition indicates the changing interactions of Eu^{3+} with its chemical environment. The calculated asymmetry ratios are given in **Table 1** (integrated peaks are shown in Figure S1, Supporting Information). Asymmetry ratios of 5.5 for the freshly synthesized nEu-bdc@agar and 4.5 for the nEu-bdc@agar after ten recycling cycles suggest certain changes in the local environment, most likely caused by the overall loss of material and therefore a more pronounced agar-based emission. With asymmetry ratios of 4.1 and 4.0 for the freshly synthesized nEu-bdc@gelatine and the ten times cycled nEu-bdc@gelatine to be similar, a remaining local environment of nEu-bdc is confirmed and leads to the conclusion that nEu-bdc@gelatine represents a more stable bio-nMOF-MMM than nEu-bdc@agar. Altogether, these findings indicate that the MOF containing trivalent europium exhibits remarkable recyclability, thereby validating it as an environmentally sustainable optical probe for determining the status of the material under investigation.

Table 1. Calculated asymmetry ratios of nEu-bdc@agar and nEu-bdc@gelatine.

	Agar		Gelatine	
	5 wt.%	10 wt.%	5 wt.%	10 wt.%
fresh	5.4	5.5	4.2	4.1
10th cycle	4.8	4.5	4.1	4.0

2.2.3. Physical Texture and Constitution of nEu-bdc@biopolymer

SEM and EDS give information about the physical texture of the biopolymers agar and gelatine as well as the distribution of nEu-bdc nanoparticles within both biopolymers.

Figure 9 shows the recorded SEM images and elemental mappings (C:K$\alpha_{1,2}$-edge, Eu Mβ-edge) of nEu-bdc@biopolymers cross-sections with 10 wt.% nEu-bdc loading (see Figure S9, Supporting Information for 5 wt.% nEu-bdc). Both bio-nMOF-MMMs nEu-bdc@agar and nEu-bdc@gelatine consist of smooth surfaces sprinkled with nEu-bdc nanoparticles embedded in the biopolymer. The nEu-bdc is homogeneously distributed in nEu-bdc@gelatine while the particle distribution in nEu-bdc@agar is less uniform (Figure 9C,F,I,L). Previous MOF@gelatine composites have been reported with only surface-attached particles due to the sequential formation of a gelatine film followed by the addition of MOF.[78] However, in this study, the water-resistant nEu-bdc allows the addition of nMOF directly during the formation of the gelatine membrane, which results in nMOF particles distributed throughout the entire volume of the membrane. The distribution hugely benefits from the increased

ADVANCED SCIENCE NEWS
www.advancedsciencenews.com

ADVANCED FUNCTIONAL MATERIALS
www.afm-journal.de

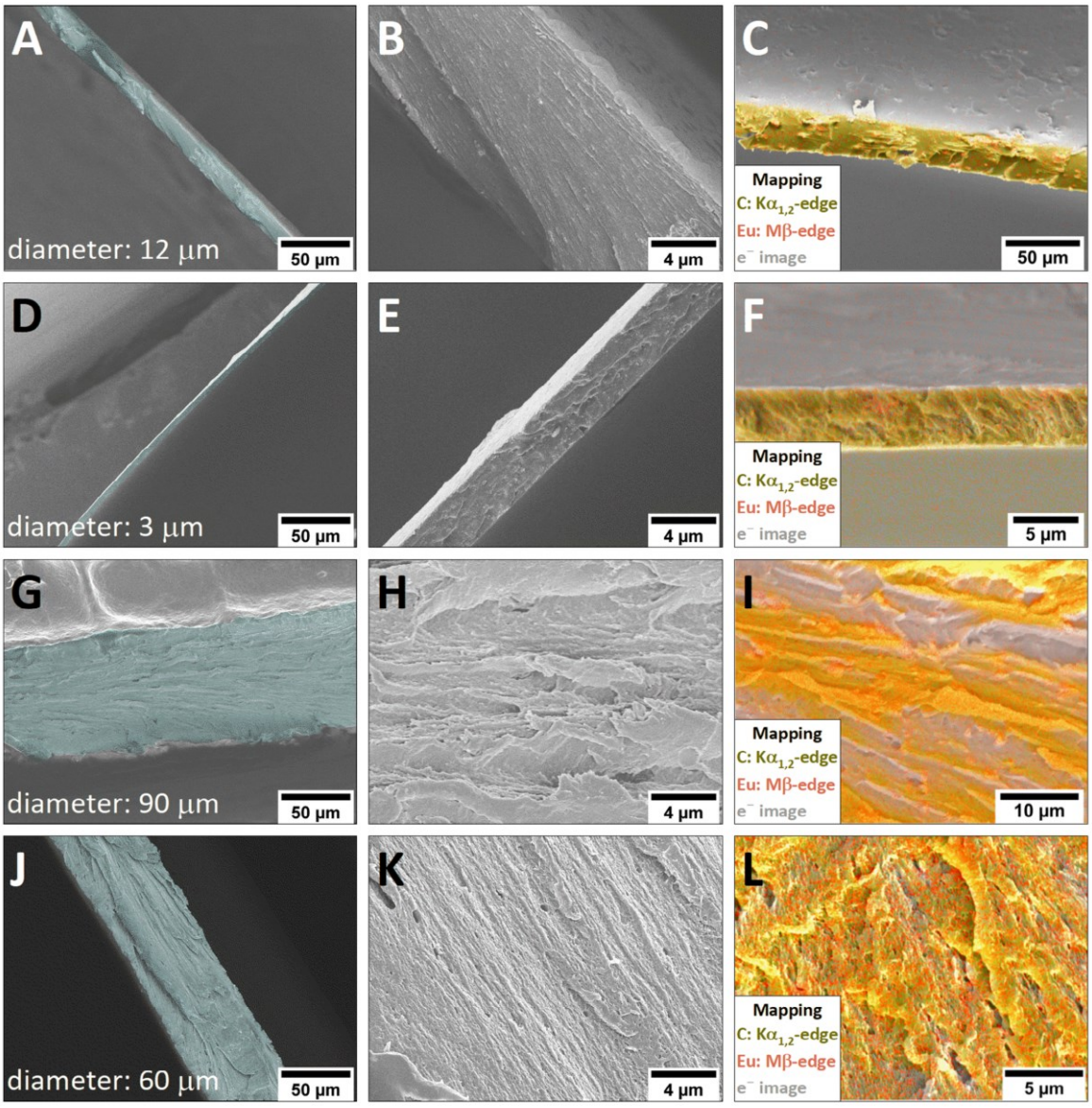

Figure 9. SEM images and elemental mappings (carbon: yellow, europium: red) of fresh nEu-bdc@agar (A,B,C), 10th cycle nEu-bdc@agar (D,E,F), fresh nEu-bdc@gelatine (G,H,I) and 10th cycle nEu-bdc@gelatine (J,K,L) with each 10 wt.% nEu-bdc at different magnifications. Cross-sections of the membranes are highlighted in light blue for clarity with denoted cross-section diameters.

dispersibility of nMOF compared to its bulk counterparts. Besides, the potential altogether mass loss of nEu-bdc@biopolymer is supported by SEM images. A decrease in thickness is observable after the ten-time high-quality recycling for bio-nMOF-MMMs. Figure 9A,B shows a freshly synthesized nEu-bdc@agar membrane with a thickness of 12 µm while Figure 9D,E reveals ten times cycled nEu-bdc@agar membrane with only ≈25% of the thickness of the freshly synthesized nEu-bdc@agar. Additionally, but to a lesser extent, the fresh nEu-bdc@gelatine (Figure 9G,H) and the ten times cycled nEu-bdc@gelatine (Figure 9J,K) demonstrate a reduction in membrane thickness of only 30 µm, which corresponds to a deficit in thickness of 30%. These findings are in accordance with the observed decreasing mechanical stability of nEu-bdc@agar.

In conclusion, nEu-bdc@gelatine forms more sustainable bio-nMOF-MMMs than nEu-bdc@agar. This is due to the fact that the latter loses more material during each recycling cycle, with a less uniform particle distribution and,

ADVANCED SCIENCE NEWS
www.advancedsciencenews.com

ADVANCED FUNCTIONAL MATERIALS
www.afm-journal.de

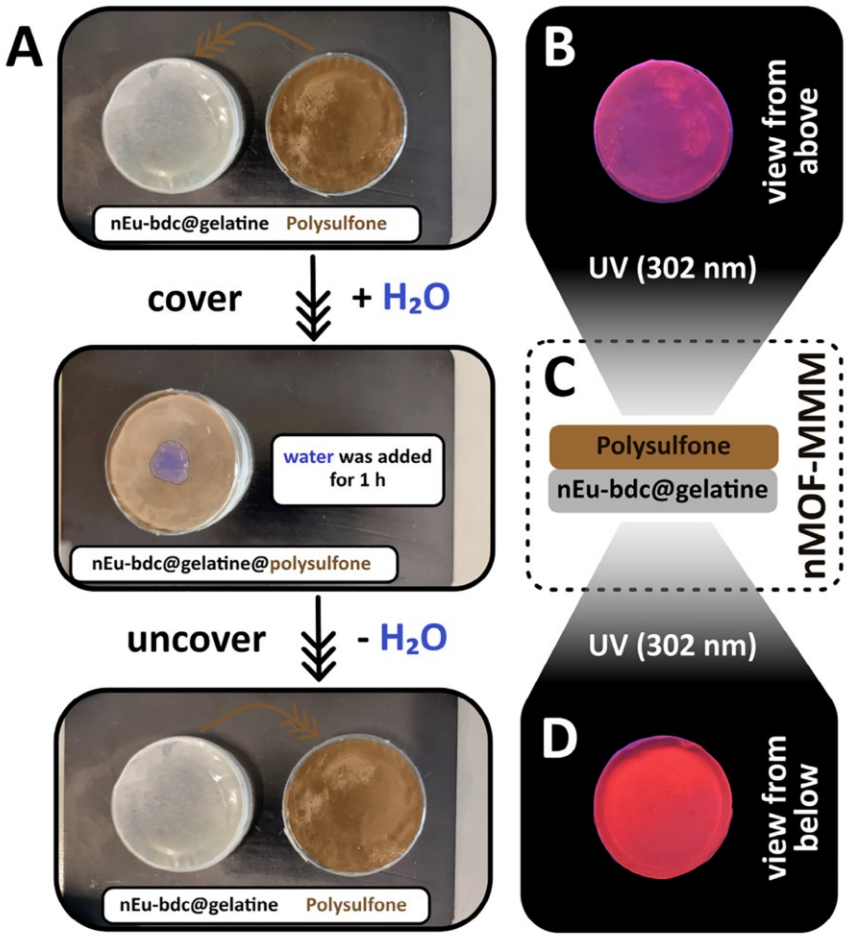

Figure 10. A) The photograph series demonstrates the protective value of polysulfone (PSU) on nEu-bdc@gelatine (also available as Video S2, Supporting Information). B) The violet emission is visible when viewed from the side covered with PSU (top). C) A simplified model of polysulfone protecting nEu-bdc@gelatine. D) The red luminescence is visible when viewed from the side with nEu-bdc@gelatine (bottom).

consequently, a more significant impact on the performance of the material.

2.3. Functionalization of nEu-bdc@biopolymer as Bio-nMOF-MMMs, Hydrogels and Cryogels

This section explores three potential customizations, providing examples of how the bio-nMOF-MMMs nEu-bdc@agar and nEu-bdc@gelatine can be further functionalized. One approach entails the incorporation of an additional component into nEu-bdc@gelatine. In contrast, the other two approaches involve modifications of the nEu-bdc@agar synthesis route, with the aim of producing luminescent hydrogels and cryogels with a series of new properties compared to bio-nMOF-MMMs, using the same components. In contrast to other publications,[78,79] the formation of membranes, hydrogels, and cryogels does not require additional cross-linking agents.

2.3.1. Polysulfone Protective Layer Covers for nEu-bdc@gelatine

While agar shows a high resistance against degradation in water at RT, gelatine starts to dissolve at RT already. Hence, prior to the synthesis of nEu-bdc@gelatine, an additional membrane insoluble in aqueous environments was synthesized as a protective layer. Here, a polysulfone (PSU) membrane serves as a protective layer by covering nEu-bdc@gelatine (nEu-bdc@gelatine@PSU). After the drying process of the PSU membrane, the aqueous dispersion of nEu-bdc and gelatine was poured onto the synthesized PSU membrane. **Figure 10**A shows the nEu-bdc@gelatine covered with PSU and also uncovered nEu-bdc@gelatine (10 wt.% nEu-bdc) at Vis-light (also available as Video S2, Supporting Information in the Supporting Information). The PSU membrane and the bio-nMOF-MMM nEu-bdc@gelatine are easy to separate and reassemble, which allows separate recycling procedures for the sake of sustainability. The PSU membrane maintains the functionality of nEu-bdc@gelatine after exposure to water. The

ADVANCED SCIENCE NEWS
www.advancedsciencenews.com

ADVANCED FUNCTIONAL MATERIALS
www.afm-journal.de

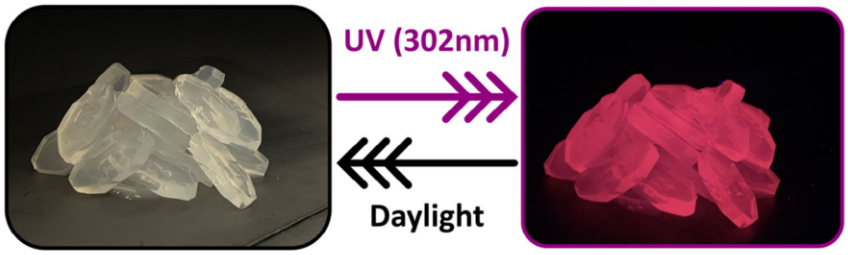

Figure 11. Hydrogels of nEu-bdc@agar (10 wt.% nEu-bdc) shaped as pills in daylight and under UV radiation (302 nm).

effect of PSU on the photophysical properties of nEu-bdc@gelatine under UV light (302 nm) during protection is also shown in Figure 10B,D. When viewed from the side with PSU (from above, B), a more violet emission is discernible to the naked eye. Conversely, when viewed from the side with nEu-bdc@gelatine (from below, D), the characteristic red luminescence is evident. The assembled three-component system nEu-bdc@gelatine@PSU was observed under UV light as simplified and shown in Figure 10C.

2.3.2. Modification of nEu-bdc@agar as Hydrogels

A hydrogel offers distinct properties compared to a film, such as dynamic modulation or increased flexibility,[80] enabling the production of, for example, nEu-bdc@agar-based pills that retain their shape when removed from the support (see **Figure 11**). But also, other shapes are possible, such as agar slices, reported for bulk MOF composites working as sensors via luminescence quenching processes.[81] For hydrogel formation, the dispersion was allowed to cool at RT during evaporation in a water vapor-saturated atmosphere (see Experimental Section for further details). Only a minor adjustment in temperature during the solvent evaporation allows nEu-bdc@agar to form hydrogels instead of films, which demonstrates impressively the variability of agar as a matrix for nMOF composites.

2.3.3. Modification of nEu-bdc@agar as Freeze-Dried Cryogels

The synthesis of cryogels commences with the formation of nEu-bdc@agar (10 wt.% nEu-bdc) hydrogels, which are subsequently subjected to freeze-drying, resulting in the production of cryogels (see Experimental Section for further details). Cryogels are known as sponge-like porous materials with pores at micrometer scale and are used mainly in biomedical applications such as drug delivery or tissue engineering.[82] The freeze-drying process induces a swelling of the hydrogel while imparting sponge-like properties. The cryogel nEu-bdc@agar is compressible without losing its original shape after releasing the pressure, as shown in **Figure 12A** (also available as Video S3, Supporting Information). Since nEu-bdc is present, its typical red luminescence can be observed in Figure 12B. Furthermore, Figure 12C shows an SEM image of nEu-bdc@agar as cryogel, revealing a cell-like, rigid material webbed by filament-like particle-carrying structures (see Figure S10 (Supporting Information) as a comparison to pure freeze-dried agar). Despite the publication of studies on MOF cryogels,[83] the formation of web-like structures resulting from the presence of surfactants has not been observed until now. Elemental mapping via EDS reveals the presence of europium embedded in both the cell-like structures and the filament-like structures (Figure 12D). Figure S10 (Supporting Information) does not show those filaments in pure freeze-dried agar, the surfactants covering the nEu-bdc must play a key role in the formation of these filament-like structures.

Freeze-dried agar alone is considered a promising biodegradable packaging material,[84] as its properties resemble those of conventional packaging materials. When combined with luminescent nMOFs, additional functional properties, such as those of nMOFs as described in the introduction, are conferred. This enhancement of nEu-bdc@agar as cryogels presents a smart and environmentally friendly alternative for conventional sponge-like, microporous materials, offering tunable features derived from MOFs. In particular, luminescent cryogels with embedded lanthanide ions in the lanthanide-based MOFs do not possess a functional secondary porous structure with even smaller pores than in agar cryogels.[85]

2.4. Comparison of Bio-nMOF-MMMs, Hydrogels and Cryogels of nEu-bdc@biopolymer

This section gives a brief comparison of nEu-bdc@biopolymer for the different forms of bio-nMOF-MMMs, hydrogels, and cryogels while highlighting the unique properties of each physical condition.

In order to facilitate a comparative analysis of the stability of the different forms of nEu-bdc@biopolymer, freshly prepared bio-nMOF-MMMs, hydrogels, and cryogels of nEu-bdc@agar were investigated regarding their dissolution in water from room temperature up to boiling water ($T = 100$ °C). It is noteworthy that actual literature typically addresses the water-solubility test of Eu-bdc composites only at or close to RT.[76] The inherent red luminescence of nEu-bdc was employed as an optical probe to monitor the dissolution process (**Figure 13**, and available as Video S4, Supporting Information). At RT, all forms stay perfectly stable in water, neither the bio-nMOF-MMM, nor the hydrogel, nor the cryogel dissolve, which is a significant advantage for potential applications. This follows the stability of agar in water at atmospheric conditions and temperature.[39,66] In boiling water, it takes 1:40 (min:s) for the bio-nMOF-MMM to completely dissolve into agar hydrate and dispersion of nEu-bdc in water. The hydrogel and

ADVANCED SCIENCE NEWS
www.advancedsciencenews.com

ADVANCED FUNCTIONAL MATERIALS
www.afm-journal.de

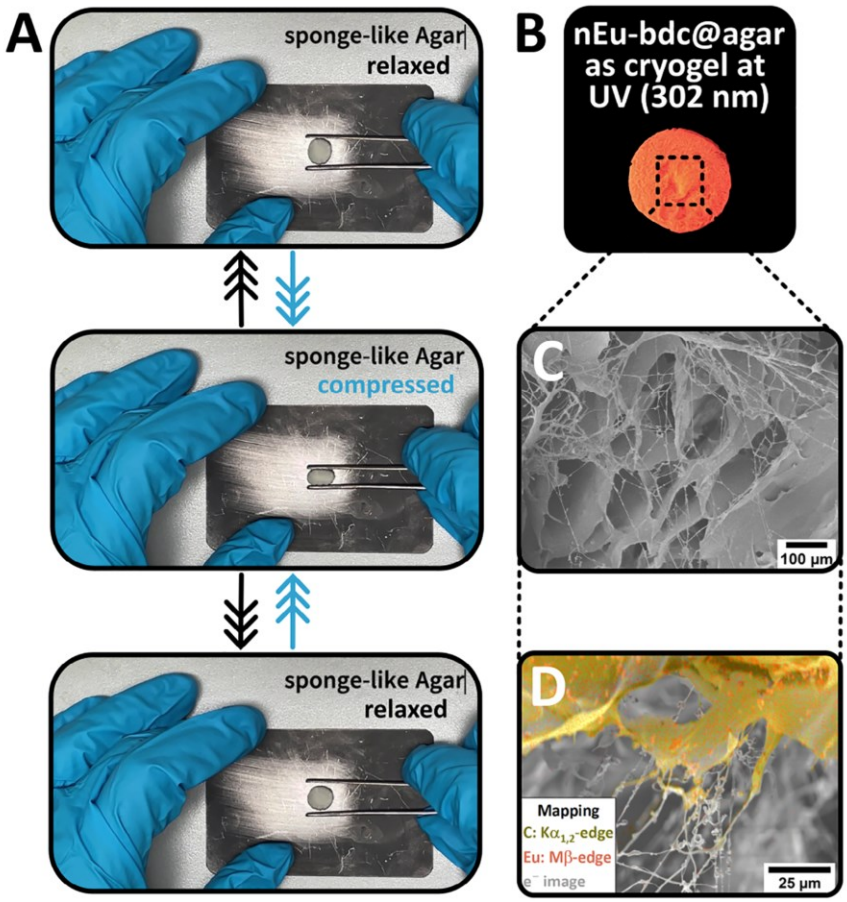

Figure 12. Photographs of nEu-bdc@agar (10 wt.% nEu-bdc) as cryogel. A) The photograph series demonstrates the squeezing properties of the sponge-like cryogel which retains its shape after deformation under pressure (available as Video S3, Supporting Information). B) Photoluminescence of nEu-bdc@agar as cryogel under UV light (302 nm). C) SEM images and D) elemental mappings (carbon: yellow, europium: red) of nEu-bdc@agar as cryogel.

cryogel start to dissolve simultaneously after 2:20 (min:s) being completed after 3:50 (min:s), again forming a dispersion of nEu-bdc in water. It is noteworthy that the nMOF nEu-bdc itself incorporated in MMM, hydrogel and cryogel demonstrate stability in boiling water, as evidenced by the red luminescence. In terms of the mechanical stability of bio-nMOF MMMs, the more difficult it is to get the bio-nMOF MMM back into a nEu-bdc/biopolymer dispersion, the less homogeneous the dispersion will be. A less homogeneous dispersion will result in sedimentation processes of nEu-bdc particles and biopolymer agglomerates, eventually leading to loss of mechanical integrity over several recycling steps as observed in Figure 6A.

In order to address the biodegradability of the developed materials in real water bodies, an experiment was conducted in controlled artificial seawater, as used in marine biology research. This experiment was similar to the one described in demineralized water. The characteristics of the artificial seawater provided by the Marine Holobiomics Lab of the JLU Giessen are listed in Table S2 (Supporting Information) and are similar to real seawater. Additionally, pure nEu-bdc and the bio-nMOF-MMM nEu-bdc@gelatine were also exposed to the same artificial seawater. The experiment yielded no significant differences in comparison to the results obtained in demineralized water. This is noteworthy, as the salinity of seawater (i.e., the amount of dissolved salt ions; expressed as $m_{salt}\ m_{water}{}^{-1}$, with [salinity] = g kg^{-1}) is 35‰, which is 35 times higher than in freshwater bodies. In contrast, demineralized water has a salinity of 0‰. The pH of the artificial water was found to be 8.12, which is significantly higher than the pH of demineralized water, which was 5.3. These results indicate that the composite materials remain consistent over a wide range of parameters, enabling precise predictions of their potential behavior once exposed to the environment.

Altogether, the experiment evaluates the resilience of the bio-nMOF-MMM, hydrogel, and cryogel in an aqueous environment. In addition, it shows the remarkable stability of the nanoMOF nEu-bdc in boiling water. Once dissolved, the nEu-bdc-agar dispersions can be re-used for the synthesis of fresh bio-nMOF-MMMs, hydrogels, or cryogels, regardless of the shape they had

ADVANCED SCIENCE NEWS
www.advancedsciencenews.com

ADVANCED FUNCTIONAL MATERIALS
www.afm-journal.de

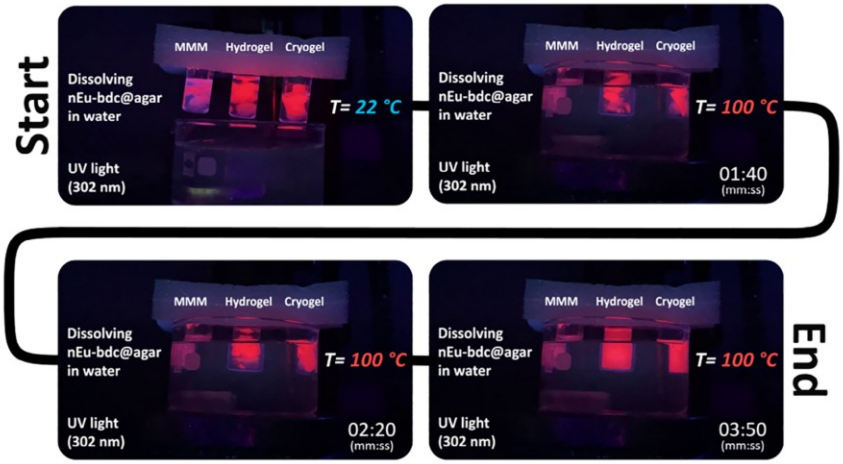

Figure 13. Demonstration of the dissolving behavior of bio-nMOF-MMMs, hydrogels, and cryogels of nEu-bdc@agar (10 wt.% nEu-bdc) in water (at $T = 100$ °C) over time. The pictures were captured from the corresponding Video S4 (Supporting Information) at $t = 0$, 1:40, 2:20, and 03:50 min. The process was followed by the intrinsic red Eu luminescence of nEu-bdc@agar upon irradiation with UV light (302 nm).

prior to dissolution, e.g., a bio-nMOF-MMM can be synthesized as a cryogel in the next cycle.

The investigation of hydrogels and cryogels has been performed exemplarily, using the same methods as for bio-nMOF-MMMs. **Figure** 14A shows powder patterns of fresh and once-recycled hydrogels and cryogels. Neither hydrogels nor cryogels show any changes in their powder diffractograms compared to the membranes and predominantly retain the reflections of nEu-bdc. Furthermore, excitation and emission spectra shown in Figure 14B, indicate unchanged luminescence properties for both nEu-bdc@agar hydrogels and cryogels after high-quality recycling. The congruent emission spectra confirm the stability of nEu-bdc as thoroughly discussed in the previous sections.

Furthermore, the chromaticity of the luminescence of the bio-nMOF-MMMs, hydrogels, and cryogels as well as for pure nEu-bdc and the pure biopolymers agar and gelatine were investigated, as illustrated in **Figure** 15. The intense red luminescence of pure nEu-bdc (M) remains in the same chromaticity region when embedded in gelatine, regardless of the concentration of nEu-bdc (I-L). When nEu-bdc is embedded in agar (B-G), the emission is hypsochromically shifted progressively toward a more bluish emission compared to nEu-bdc after ten times of high-quality recycling (C, E)–the characteristic bluish luminescence of pure agar (A). This trend is also evident, albeit to a lesser extent, in nEu-bdc@gelatine (J, L), where the luminescence exhibits a bluish component attributable to the properties of pure gelatine (H). The freeze-dried nEu-bdc@agar cryogel (G)

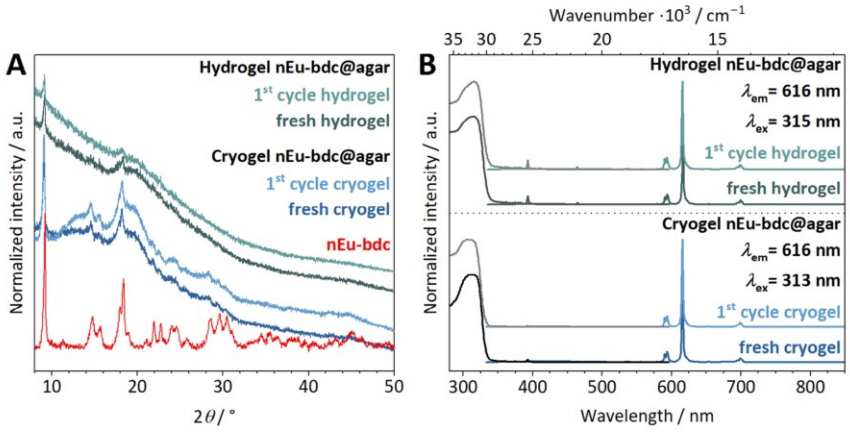

Figure 14. A) Powder diffractograms of hydrogels (green) and cryogels (blue) of nEu-bdc@agar as freshly synthesized materials and after one cycle of high-quality recycling, and the powder diffractogram of nEu-bdc (red). B) Photoluminescence spectra of hydrogels and cryogels of nEu-bdc@agar as freshly synthesized material and after one cycle of high-quality recycling.

ADVANCED SCIENCE NEWS
www.advancedsciencenews.com

ADVANCED FUNCTIONAL MATERIALS
www.afm-journal.de

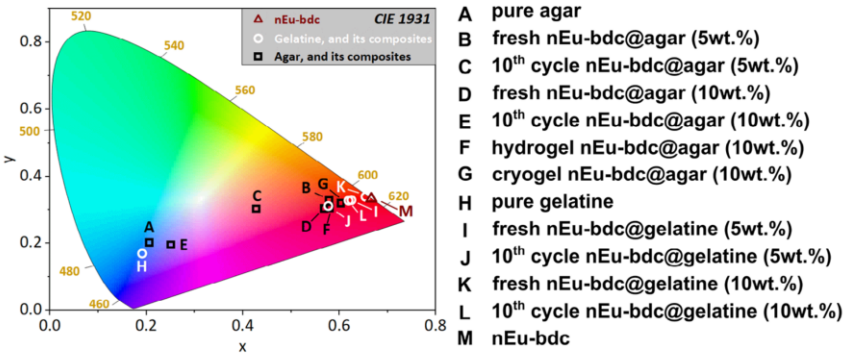

Figure 15. Illustrated chromaticity of nEu-bdc, biopolymers, and nEu-bdc@biopolymer by means of a CIE 1931 plot. A key is presented next to the CIE 1931 diagram.

demonstrates a more reddish luminescence in comparison to its bio-nMOF-MMM (D). Literature indicates that the characteristic luminescence of Eu is quenched by the presence of humidity within its coordination environment, leading to a more bluish emission based on the emission of the agar matrix, which is apparent in the hydrogel (F).[86] Consequently, the enhanced red shift of the emission observed in nEu-bdc@agar cryogels (G) may be attributed to the lower amount of water present compared to hydrogels or bio-nMOF-MMMs. These observations are consistent with the already mentioned photophysical characteristics of nEu-bdc@biopolymer.

3. Conclusion

In conclusion, this study demonstrates the successful development of biodegradable and recyclable bio-nMOF-MMMs together with the luminescent nanoMOF nEu-bdc suitable for multi-cycle high-quality recycling, as well as the deliberate formation of hydrogels and cryogels based on nEu-bdc and the biopolymers agar and gelatine.

Within the mixed-matrix-membranes, nEu-bdc acts as a probe to evaluate the physical and chemical state of the bio-nMOF-MMMs, hydrogels, and cryogels through its luminescence, as changes in the status of the hybrid materials can be monitored by changes in the luminescence intensity and chromaticity. The resilience of nEu-bdc to environmental conditions was investigated by applying a series of environmental stressors, including pH variations, stability in aqueous environment, and temperature. The results demonstrate that the selected nanoMOF nEu-bdc itself exhibits good performance in a range of common environmental conditions.

Investigations on the durability as well as recyclability of the new bio-nMOF-MMMs suggest that nEu-bdc@gelatine is mechanically more stable than nEu-bdc@agar, as it retains better luminosity and physical integrity even after ten recycling cycles. In fact, this also allows for monitoring "on the fly" by the naked eye, which confirms that the luminescence of nEu-bdc functions as a probe for the status of the materials. In addition, electron microscopy and elemental mapping with EDS showed a more uniform distribution of nEu-bdc particles in gelatine than in agar, resulting in more stable bio-nMOF-MMMs and more suitable for repeated high-quality recycling.

nEu-bdc was observed to remain intact in both the nEu-bdc@agar and nEu-bdc@gelatine samples, as evidenced by only minimal differences in the hyperfine structure of the europium emissions and comparable asymmetry ratios. Moreover, the mass-luminescence correlation demonstrated a higher loss of intensity per mass and cycle of nEu-bdc@agar in comparison to nEu-bdc@gelatine. This was evidenced by the diminished emission intensities following tenfold high-quality recycling, which was attributed to the inherent overall loss of material.

Further functionalization of the developed bio-nMOF-MMMs as multi-component systems (nEu-bdc@gelatine@PSU) or modification of the synthesis routes led to the observation of a variety of new properties through the formation of hydrogels and cryogels of nEu-bdc@agar. Both, hydrogels and cryogels are stable in aqueous environments at room temperature. It is noteworthy that nEu-bdc exhibits an exceptional degree of stability even in boiling water, an uncommon stability, particularly for nanoscale MOFs. The potential for transformation is exemplified by the ability to transfer a film into a hydrogel, or a hydrogel into a cryogel ad libitum using high-quality recycling techniques.

Altogether, the study advances the field of sustainable nMOF-composite materials by creating luminescent, biodegradable, and recyclable bio-nMOF-MMMs, and alternative hydrogels, as well as cryogels, which are both multifunctional and environmentally friendly. Luminescence serves a dual purpose: it is both a visible feature and a probe for assessing the condition of the materials. Furthermore, the bio-nMOF-MMM's recyclability is consistent with the tenets of a circular economy and the reduction of reliance on non-biodegradable polymers.

4. Experimental Section

In this work, demineralized water was used solely and is referred to as water. All chemicals were used as purchased without further purification. The rare-earth nitrate $Eu(NO_3)_3 \cdot 6H_2O$ (99.9% pur.) and the organic linker benzene-1,4-dicarboxylic acid (H_2bdc, 98% pur.) were supplied from *abcr*. In addition, the surfactants *N,N,N*-trimethylhexadecan-1-ammonium bromide (CTAB, ≥96% pur.) and 1-ethenylpyrrolidin-2-one ($PVP_{40,000}$, avg. mol. wt. 40,000; MQ: 200), the biopolymer agar (ash 2.0%–4.5%) and

ADVANCED SCIENCE NEWS
www.advancedsciencenews.com

ADVANCED FUNCTIONAL MATERIALS
www.afm-journal.de

gelatine (powder from bovine skin, Type B), polytetrafluoroethylene (PTFE, 1 µm particle size) were purchased from Sigma–Aldrich (Merck), and the polysulfone Udel P-3500 (PSU, M_w: 82,000) from Solvay. The solvents *N,N*-dimethylformamide (DMF, 99% pur.) were purchased from Grüssing and triethylamine (TEA, 99% pur.) from Fischer Scientific.

Synthesis Procedures—Synthesis of the nEu-bdc: The synthetic procedure was based on the previous work,[15] but modified at specific steps. Initially, $Eu(NO_3)_3{\cdot}6H_2O$ (280 mg, 0.628 mmol) and PVP (4220 mg, 29.90 mmol; M_w: 40,000) were separately dissolved in DMF (40 mL) under vigorous stirring. In parallel, H_2bdc (190 mg, 1.14 mmol) and CTAB (3220 mg, 8.78 mmol) were dissolved in DMF (200 mL) within a three-necked round-bottom flask (500 mL) equipped with a reflux condenser. This mixture was stirred vigorously at 55 °C for 60 min. Subsequently, the previously prepared solutions were added gradually, followed by the addition of TEA (200 µL). The reaction mixture turned slightly opaque and was further stirred for an additional 60 min at 55 °C. The mixture was then heated at 90 °C for 6 h, resulting in a thick, opaque, pale-yellow dispersion. The product was washed sequentially with DMF (10 mL) and H_2O (10 mL), each time centrifuging at 17,855·g for 15 min. Finally, the material was dried under vacuum, yielding 211 mg of colorless powder. Elemental Analysis: found (%): C 34.8, H 3.2, N 0.9.

Synthesis Procedures—Synthesis of the nEu-bdc@agar and nEu-bdc@gelatine: A solution was prepared by dissolving agar (80 mg) and gelatine (100 mg), respectively, in water (4 mL). The mixture was agitated in a glass vial equipped with a lid at 110 °C until complete dissolution was achieved. Subsequently, nEu-bdc (either 5 wt.% or 10 wt.%) was dispersed in water (1 mL) in an Eppendorf vial and sonicated for 10 min at 30 °C. After sonication, the dispersion was combined with the biopolymer solution and mixed thoroughly for an additional 5 min at 110 °C. The nEu-bdc@agar dispersion was then poured into a Petri dish and left to rest in a drying cabinet set at 120 °C until complete solvent evaporation. Since stability issues occurred with nEu-bdc@agar with 5 wt.% nEu-bdc, the amount of agar used for nEu-bdc@agar with 5 wt.% nEu-bdc was increased to 160 mg. Conversely, the nEu-bdc@gelatine dispersion was poured into a polypropylene container and allowed to rest at room temperature until the solvent evaporated. Both nEu-bdc@agar and nEu-bdc@gelatine were synthesized as flexible, transparent membranes.

Synthesis Procedures—Synthesis of nEu-bdc@gelatine@polysulfone: A polysulfone (Udel P-3500, PSU) membrane was prepared by dissolving PSU (100 mg, 0.23 mmol; M_w: 82,000) in DMF (5 mL) and stirring the mixture for 30 min at 110 °C. The resulting hot solution was then poured into a Petri dish, where DMF was allowed to evaporate at 80 °C. Once the PSU membrane was fully dried, a hot dispersion of nEu-bdc and gelatine (see subhead "Synthesis of the nEu-bdc@agar and nEu-bdc@gelatine" under Experimental Section) was poured onto the surface of the PSU membrane within the same Petri dish. Allowing the solvent to evaporate at room temperature resulted in the formation of a three-component system, designated as nEu-bdc@gelatine@PSU. This configuration facilitated the easy separation and reassembly of the PSU membrane and the bio-nMOF-MMM nEu-bdc@gelatine.

Synthesis Procedures—Synthesis of nEu-bdc@agar as Hydrogel: The synthesis started with the dispersion of nEu-bdc (10 wt.% with respect to the mass of agar) in water (1 mL) and subsequent sonication at 30 °C for 10 min. Meanwhile, agar (100 mg) was solved in water (10 mL) at 110 °C in a snap-on glass vial until a clear solution. Both, the solution of agar and the dispersion of nEu-bdc were mixed under stirring at 110 °C for 5 min. Subsequently, the mixture was transferred by means of Eppendorf pipettes into silicon support at RT and stayed in a saturated water vapor atmosphere until the hydrogel was formed. After the pills were reamed from the support, twenty-four nEu-bdc@agar hydrogels were collected.

Synthesis Procedures—Synthesis of Freeze-Dried nEu-bdc@agar as Cryogel: The synthesis started with the dispersion of nEu-bdc (10 wt.% with respect to the mass of agar) in water (1 mL) and subsequent sonication at 30 °C for 10 min. Meanwhile, agar (100 mL) was solved in water (5 mL) at 110 °C in a snap-on glass vial until the solution became clear. Both, the solution of agar and the dispersion of nEu-bdc were mixed under stirring at 110 °C for 5 min. Afterward, the mixture was poured into a test tube and stayed at −79 °C for 24 h. Finally, the test tube was removed and the frozen nEu-bdc@agar thawed at RT under vacuum to remove excess water while defrosting. This yielded freeze-dried nEu-bdc@agar as cryogel, which was cut in slices.

Analytical Methods—Differential Thermoanalysis/Thermogravimetry–Mass Spectrometry (DTA/TG-MS): Thermal properties were analyzed using simultaneous thermal analysis (STA) consisting of differential thermal analysis (DTA) and thermogravimetry (TG) with a STA 409 PC system coupled to a QMS 403 Aëolos Quadro mass spectrometer (NETZSCH). 20–25 mg of the samples were placed in a corundum crucible and heated to 1000 °C at a constant rate of 5 °C min^{-1}. Argon was supplied at a flow rate of 20 mL min^{-1} as a protective gas, while synthetic air (30 mL min^{-1}) was used as the reactive working gas. Mass spectrometry (MS) signals were monitored using the quasi-multiple ion detection (QMID) method to track the release of gaseous species during the thermal degradation process.

Analytical Methods—Dynamic Light Scattering (DLS): Particle size and distribution were analyzed using a StabiSizer PMX 200CS provided by Particle Metrix. Data acquisition was conducted using Microtrac FLEX Application Software (ver. 10.5.4) from Microtrac. To prepare the samples, snap-on cap glass vials were filled with EtOH up to half of their volume after thorough rinsing. A spatula tip of the sample was then added to one vial, followed by sonication at 30 °C for 10 min. After confirming the dispersion's stability, data acquisition took place, initially for the blank (EtOH only) and subsequently for the dispersion. For enhanced statistical accuracy, the measurement was repeated three times, each lasting 120 s. The particle size distribution plots presented in this study represent the average of these three measurements and were generated using OriginPro 2024 (ver. 10.1.0.178, OriginLab). Additionally, the average particle size value is indicated with $\pm 2\sigma$.

Analytical Methods—Methods for the Determination of Photophysical Properties: Photoluminescence (PL) excitation and emission spectra were acquired using a Jobin Yvon Fluorolog 3 spectrometer, coupled with the FluorEssence for Windows software (ver. 3.9.0.1) provided by HORIBA. The excitation source utilized a xenon short-arc lamp (USHIO) in combination with a double-grated monochromator at the excitation site. Simultaneously, another monochromator was employed in tandem with a photomultiplier tube R928P (HAMAMATSU PHOTONICS K.K.) at the emission site to capture the spectral data. The monochromators and detectors underwent mathematical corrections, as per the manufacturer's recommendations. The spectral profile of the lamp was characterized by means of a reference detector (R signal) and corrected on-site. To obtain complete spectral information, a long-pass edge filter with a cutoff wavelength of 550 nm (Newport) was inserted into the optical path between the sample and the detector. The excitation and emission spectra were recorded separately and subsequently combined in a unified graphical representation using OriginPro 2024 software (ver. 10.1.0.178) from OriginLab.

Investigations of Powders: Samples were filled into a cylindrical cuvette constructed from synthetic quartz glass (proQuarz) and positioned precisely at the focal point of the incident light beam. For spectra recording at 77 K, prior to measurement, a transparent dewar was placed into the beam and filled with liquid nitrogen. As soon as the dewar was cooled down completely, a cuvette carrying the sample was placed inside the dewar and adjusted to the focal point of the excitation beam.

Investigations of Membranes: Membranes were fixed in a solid sample holder (#5500001933, HORIBA) and subsequently placed together in the focal point of the excitation beam.

Luminescence lifetime determinations were carried out by recording the overall luminescence decay times (τ) using a Jobin Yvon Fluorolog 3 with the Data Station (ver. 2.7.4) software for data acquisition and the Decay Analysis Software (ver. 6.8.16) for raw data fitting, respectively, from HORIBA. For this purpose, the instrument was upgraded with a TCSPC (time-correlated single photon counting) and UV Xenon FX 1102 flashlamp from Excelitas Technologies. Moreover, for this method, the sample powder samples were filled into a cylindrical synthetic-quartz glass cuvette (proQuarz), while the membranes were fixed in a solid sample holder (#5500001933, HORIBA), and placed in the focus of the beam.

ADVANCED SCIENCE NEWS
www.advancedsciencenews.com

ADVANCED FUNCTIONAL MATERIALS
www.afm-journal.de

Subsequently, after recording the overall emission decay, the lifetime was calculated by exponentially fitting the data with:

$$I(t) = A + B_1 \cdot e^{-(t-t_0/\tau_1)} + B_2 \cdot e^{-(t-t_0/\tau_2)} \quad (1)$$

where $I(t)$ is the emission intensity depending on time, A is the baseline factor, B is the pre-exponential factor, t_0 is the time offset, t is the time and τ is the lifetime. Results were graphically represented using OriginPro 2024 software (ver. 10.1.0.178) from OriginLab.

Quantum yield determinations were performed using a Jobin Yvon Fluorolog 3 with the FluorEssenceTM for Windows (ver. 3.9.0.1) software equipped with a Quanta-φ Integrating Sphere F-3029 from HORIBA. Reference material and samples, respectively, were filled into a microcell cuvette 18-F/ST/C/Q/10 from StarnaGmbH. The membranes were cut into pieces and evenly filled into cuvettes. MgO was utilized as additional reference material. Each sample was measured four times and related to the reference material with subsequent calculation of quantum yield value (an average value) and standard deviation estimation that represents the measurement error. A long-pass edge filter of 395 nm was used to acquire a full spectrum of Eu emission. Experimental parameters for investigated samples: λ_{ex} = 320 nm, λ_{em} = 575–720 nm. Additionally, photoluminescence standards were measured to verify the calibration of the Quanta-φ Integrating Sphere (measured/literature value): $[Eu_4(OAc)_{12}(phenylterpyridine)_2]$ (69.9(8)/63%) λ_{ex} = 310 nm, λ_{em} = 570–720 nm and (59.3(7)/58%), λ_{ex} = 355 nm, λ_{em} = 570–720 nm; $[Tb_4(OAc)_{12}(phenylterpyridine)_2]$ (49.9(1.2)/46%), λ_{ex} = 355 nm, λ_{em} = 450–690 nm.[87]

Analytical Methods—Physisorption BET (Brunauer–Emmett–Teller): Adsorption isotherms were measured on an Autosorb AS-1MP (Quantachrome), with the data subsequently analyzed using AS1win software (ver. 2.11). The nEu-bdc was utilized with the implementation of an additional outgas step at the device (T = 100 °C, $p = 1{\cdot}10^{-3}$ mbar). Nitrogen dioxide (N_2, Nippon Gases, 5.0) was employed as the adsorbate, and the temperature was adjusted to 77 K. The saturated vapor pressure of the adsorbate (p_0) was dynamically ascertained in a reference gas cell.

Analytical Methods—Powder X-Ray Diffraction (PXRD): Different setups were utilized for the X-ray diffraction analysis. Powders were investigated using the Bragg–Brentano geometry, while the examination of films, hydrogels, and cryogels was carried out using a transmission setup.

Bragg–Brentano geometry: Structural characterization was conducted employing an X'Pert Pro MPD with Data Collector (ver. 5.4.0.90) software from PANalytical. The analysis involved the utilization of an Empyrean Cu LFF X-ray tube ($\lambda_{Cu\text{-}K\alpha}$ = 154.06 pm) operating at 40 kV and 40 mA. The incident beam underwent collimation by Soller slits (0.04 rad), a beam mask (10 mm), and a fixed anti-scatter slit (1°) before interacting with a planar sample positioned on a silicon wafer. The diffracted beam subsequently traversed an angled anti-scatter slit (0.5°), Soller slits (0.04 rad), and a Nickel Beta-filter, directed toward an X'Celerator equipped with a FASS detector. The analysis was conducted in the Bragg–Brentano geometry within a 2θ range of 8° to 50° using a PW3050/60 goniometer at room temperature and under ambient atmospheric conditions.

Transmission: Powder X-ray diffraction data were acquired using a Stadi P diffractometer with WinXPOW software (ver. 3.0.2.5) from STOE & Cie equipped with a Ge(111) focusing monochromator and a MYTHEN 1 K strip detector, operating within an angular range of 12.5° in 2θ. The measurements were conducted in transmission utilizing Cu-Kα radiation ($\lambda_{Cu\text{-}K}\alpha$ = 154.06 pm) at room temperature and ambient atmosphere. The data were collected over a 2θ range of 8°–50° with a step increment of 0.015° and an integration time of 60 s per step. For hydrogels and cryogels a zero scattering foil provided by STOE & Cie was used to fix the samples in position.

The obtained diffractograms of both the Bragg-Brentano geometry setup and transmission setup underwent background correction using DIFFRAC.EVA (ver. 5.2.0.5, Bruker) and were visualized through plotting using OriginPro 2024 (ver. 10.1.0.178, OriginLab).

Analytical Methods—Scanning Electron Microscopy (SEM) and Energy-Dispersive X-Ray Spectroscopy (EDS): Examinations on MMM homogeneity were conducted with a GeminiSEM 560 microscope, using the SMART SEM software (ver. 6.08) provided by Carl Zeiss NTS. Ground samples were gently placed onto an adhesive carbon pad affixed to an aluminum carrier. Prior to analysis, meticulous cleaning was conducted by removing any loose material using pressurized air to prevent contamination within the vacuum chamber of the instrument. Additionally, all samples were sputtered with 4 nm Pt to enhance conductivity. Electron images were captured using a 7.5 µm aperture and an acceleration voltage of 3 kV, with a working distance of 3 mm, employing a Schottky field emitter as the electron source. Additionally, a SE-InLens detector was utilized to acquire images of secondary electrons. Scale bars were added using ImageJ (ver. 1.53f51), a software tool from the National Institute of Health. EDS data was acquired using the same setup as described above except for the InLens-detector, which was changed to the UltimMax (Oxford Instruments). The working distance was set to 8.5 mm with an acceleration voltage of 10 keV and a 60 µm aperture. Data were processed by the software Aztec (ver. 6.1, Oxford Instruments) and the following Eu X-ray emissions were analyzed (X-ray emission energy): $M\alpha_1$ (1.131 keV), $L\alpha_1$ (5.846 keV), $L\alpha_2$ (5.817 keV), $L\beta_1$ (6.456 keV), $L\beta_2$ (6.843 keV) and $L\gamma_1$ (7.480 keV).

Analytical Methods—UV–Vis Diffuse Reflectance Spectroscopy and UV–Vis Absorption Spectroscopy: Spectra were obtained using a Cary 5000 UV–vis–NIR Spectrophotometer and the Cary WinUV Scan Application software (ver. 6.3.0.1595) by Agilent Technologies. The instrument was run with different setups with respect to the physical texture of the material.

Investigations of Powders: A Praying Mantis Diffuse Reflectance Accessory from Harrick Scientific Products was utilized for the reflectance measurements. Raw data was presented in reflectance units (%R). Due to the relative nature of this measurement technique, polytetrafluoroethylene (PTFE) was chosen as the reference material. PTFE was ground and placed into a DRP-SAP macro sample cup from Harrick Scientific Products, where it was flattened using a spatula. The powder sample was then transferred into the DRP-SAP micro sample cup, also from Harrick Scientific Products. Following this, the reflectance spectrum was recorded and corrected according to the formula:

$$\%R_{sample}{}^{corr} = \%R_{sample}{}^{raw} / \%R_{PTFE}{}^{raw} \quad (2)$$

Investigations of Membranes: The instrument was operated in transmission mode, utilizing double-head foil support from Agilent Technologies. The membranes were positioned in the 'sample' beam, while the 'reference' beam was left empty. Raw data was presented in absorbance units (*abs*). The absorbance spectrum was recorded and subsequently corrected using the following formula:

$$abs_{sample}{}^{corr} = abs_{sample}{}^{raw} / abs_{atmosphere}{}^{raw} \quad (3)$$

Supporting Information

Supporting Information is available from the Wiley Online Library or from the author.

Acknowledgements

This work was generously funded by the Deutsche Forschungsgemeinschaft (DFG) in the project MU-1562/13-1 within the priority program SPP-1928/2 (project no. 434440165) "COORNETs". Furthermore, the authors gratefully acknowledge the Justus-Liebig-University Giessen for start-up financing of this research. The authors would also like to express our sincere gratitude to the Marine Holobiomics Lab of the Justus-Liebig-University Giessen, under the direction of Professor Maren Ziegler, for generously providing artificial seawater.

Conflict of Interest

The authors declare no conflict of interest.

ADVANCED SCIENCE NEWS
www.advancedsciencenews.com

ADVANCED FUNCTIONAL MATERIALS
www.afm-journal.de

Data Availability Statement

The data that support the findings of this study are available in the supplementary material of this article.

Keywords

biodegradable, biopolymers, cryogels, hydrogels, mixed-matrix-membranes, nMOFs, recyclability

Received: March 13, 2025
Revised: April 29, 2025
Published online:

[1] A. Knebel, A. Bavykina, S. J. Datta, L. Sundermann, L. Garzon-Tovar, Y. Lebedev, S. Durini, R. Ahmad, S. M. Kozlov, G. Shterk, M. Karunakaran, I. D. Carja, D. Simic, I. Weilert, M. Klüppel, U. Giese, L. Cavallo, M. Rueping, M. Eddaoudi, J. Caro, J. Gascon, *Nat. Mater.* **2020**, *19*, 1346.
[2] A. Knebel, J. Caro, *Nat. Nanotechnol.* **2022**, *17*, 911.
[3] J. M. Stangl, D. Dietrich, A. E. Sedykh, C. Janiak, K. Müller-Buschbaum, *J. Mater. Chem. C* **2018**, *6*, 9248.
[4] J. Dechnik, F. Mühlbach, D. Dietrich, T. Wehner, M. Gutmann, T. Lühmann, L. Meinel, C. Janiak, K. Müller-Buschbaum, *Eur. J. Inorg. Chem.* **2016**, *2016*, 4408.
[5] J. Dechnik, J. Gascon, C. J. Doonan, C. Janiak, C. J. Sumby, *Angew. Chem., Int. Ed.* **2017**, *56*, 9292.
[6] Y. Cheng, Y. Ying, S. Japip, S. Jiang, T. Chung, S. Zhang, D. Zhao, *Adv. Mater.* **2018**, *30*, 1802401.
[7] R. Freund, O. Zaremba, G. Arnauts, R. Ameloot, G. Skorupskii, M. Dincă, A. Bavykina, J. Gascon, A. Ejsmont, J. Goscianska, M. Kalmutzki, U. Lächelt, E. Ploetz, C. S. Diercks, S. Wuttke, *Angew. Chem., Int. Ed.* **2021**, *60*, 23975.
[8] J. Andreo, R. Ettlinger, O. Zaremba, Q. Peña, U. Lächelt, R. F. De Luis, R. Freund, S. Canossa, E. Ploetz, W. Zhu, C. S. Diercks, H. Gröger, S. Wuttke, *J. Am. Chem. Soc.* **2022**, *144*, 7531.
[9] H. Furukawa, K. E. Cordova, M. O'Keeffe, O. M. Yaghi, *Science* **2013**, *341*, 1230444.
[10] S. Yang, L. Peng, S. Bulut, W. L. Queen, *Chem. - Eur. J.* **2019**, *25*, 2161.
[11] A. Justin, J. Espín, M. J. Pougin, D. Stoian, T. Schertenleib, M. Mensi, I. Kochetygov, A. Ortega-Guerrero, W. L. Queen, *Adv. Funct. Mater.* **2024**, *34*, 2307430.
[12] B. Hosseini Monjezi, B. Sapotta, S. Moulai, J. Zhang, R. Oestreich, B. P. Ladewig, K. Müller-Buschbaum, C. Janiak, T. Hashem, A. Knebel, *Chem. Ing. Tech.* **2022**, *94*, 135.
[13] R. Bo, M. Taheri, H. Chen, J. Bradford, N. Motta, S. Surve, T. Tran-Phu, P. Garg, T. Tsuzuki, P. Falcaro, A. Tricoli, *Adv. Funct. Mater.* **2022**, *32*, 2100351.
[14] C. Carbonell, M. Linares-Moreau, S. M. Borisov, P. Falcaro, *Adv. Mater.* **2024**, *36*, 2408770.
[15] M. Maxeiner, L. Wittig, A. E. Sedykh, T. Kasper, K. Müller-Buschbaum, *J. Mater. Chem. A* **2023**, *11*, 22478.
[16] E.-L. Wang, L. Li, J.-Y. Zou, C. Hong, L. Zhang, S.-Y. You, *ACS Appl. Nano Mater.* **2024**, *7*, 17748.
[17] L. Wang, Y. Chen, *ACS Appl. Mater. Interfaces* **2020**, *12*, 8351.
[18] X. Wang, K. Batra, G. Clavier, G. Maurin, B. Ding, A. Tissot, C. Serre, *Chem. - Eur. J.* **2023**, *29*, 202203136.
[19] T. Simon-Yarza, A. Mielcarek, P. Couvreur, C. Serre, *Adv. Mater.* **2018**, *30*, 1707365.
[20] T. Burger, M. V. Hernández, C. Carbonell, J. Rattenberger, H. Wiltsche, P. Falcaro, C. Slugovc, S. M. Borisov, *ACS Appl. Nano Mater.* **2023**, *6*, 248.
[21] N. Rabiee, R. Sharma, S. Foorginezhad, M. Jouyandeh, M. Asadnia, M. Rabiee, O. Akhavan, E. C. Lima, K. Formela, M. Ashrafizadeh, Z. Fallah, M. Hassanpour, A. Mohammadi, M. R. Saeb, *Environ. Res.* **2023**, *231*, 116133.
[22] S. El Hankari, M. Bousmina, A. El Kadib, *Prog. Mater. Sci.* **2019**, *106*, 100579.
[23] F. Galiano, K. Briceño, T. Marino, A. Molino, K. V. Christensen, A. Figoli, *J. Membr. Sci.* **2018**, *564*, 562.
[24] N. Singh, S. Qutub, N. M. Khashab, *J. Mater. Chem. B* **2021**, *9*, 5925.
[25] F. Russo, F. Galiano, A. Iulianelli, A. Basile, A. Figoli, *Fuel Process. Technol.* **2021**, *213*, 106643.
[26] G. B. D'Souza, M. M. Sanjay, M. Swathi, U. Thummar, H. Yoon, S. K. Nataraj, *Sep. Purif. Technol.* **2024**, *347*, 127426.
[27] P. Tignol, V. Pimenta, A. Dupont, S. Carvalho, A. Al Mohtar, M. Inês Severino, F. Nouar, M. L. Pinto, C. Serre, B. Lavédrine, *Small Methods* **2024**, *8*, 2301343.
[28] H. Kolya, C.-W. Kang, *Polymers* **2023**, *15*, 3421.
[29] F. Yang, P. Yang, *Macromol. Rapid Commun.* **2022**, *43*, 2100669.
[30] P. T. Anastas, J. C. Warner, in *Green Chemistry: Theory and Practice*, Oxford University Press, Oxford, UK, **2000**.
[31] I. A. Bashmakov, L. J. Nilsson, A. Acquaye, C. Bataille, J. M. Cullen, S. de la Rue du Can, M. Fischedick, Y. Geng, K. Tanaka, in *Climate Change 2022 - Mitigation of Climate Change*, Cambridge University Press, Cambridge, UK, **2023**, pp. 1161–1244.
[32] A. Grant, M. Cordle, E. Bridgwater, in *Quality of Recycling - Towards an Operational Definition*, (Eds.: P. Canfora, M. Dri, I. Antonopoulos, P. Gaudillat), Publications Office of the European Union, Luxembourg, **2020**.
[33] Plastics Europe AISBL, in *Plastics - The Fast Facts 2023*, Plastics Europe, Bruxelles, Belgium, **2023**.
[34] S. Nanda, B. R. Patra, R. Patel, J. Bakos, A. K. Dalai, *Environ. Chem. Lett.* **2022**, *20*, 379.
[35] A. Das, T. Ringu, S. Ghosh, N. Pramanik, *Polym. Bull.* **2023**, *80*, 7247.
[36] A. George, M. R. Sanjay, R. Srisuk, J. Parameswaranpillai, S. Siengchin, *Int. J. Biol. Macromol.* **2020**, *154*, 329.
[37] R. Zhang, Q. Wang, H. Shen, Y. Yang, P. Liu, Y. Dong, *Algal Res.* **2024**, *78*, 103384.
[38] W.-K. Lee, Y.-Y. Lim, A. T.-C. Leow, P. Namasivayam, J. Ong Abdullah, C.-L. Ho, *Carbohydr. Polym.* **2017**, *164*, 23.
[39] X. Chen, X. Fu, L. Huang, J. Xu, X. Gao, *Carbohydr. Polym.* **2021**, *265*, 118076.
[40] C. M. P. Freitas, J. S. R. Coimbra, V. G. L. Souza, R. C. S. Sousa, *Coatings* **2021**, *11*, 922.
[41] J. Chen, W. Liu, C.-M. Liu, T. Li, R.-H. Liang, S.-J. Luo, *Crit. Rev. Food Sci. Nutr.* **2015**, *55*, 1684.
[42] Z. Yang, Y. Zhang, G. Jin, D. Lei, Y. Liu, *Int. J. Biol. Macromol.* **2024**, *261*, 129851.
[43] Y. Lu, Q. Luo, Y. Chu, N. Tao, S. Deng, L. Wang, L. Li, *Polymers* **2022**, *14*, 436.
[44] H. Nagahama, H. Maeda, T. Kashiki, R. Jayakumar, T. Furuike, H. Tamura, *Carbohydr. Polym.* **2009**, *76*, 255.
[45] J.-Y. Lai, P.-K. Lin, G.-H. Hsiue, H.-Y. Cheng, S.-J. Huang, Y.-T. Li, *Biomacromolecules* **2009**, *10*, 310.
[46] B. Sun, S. F. Wan Muhamad Hatta, N. Soin, M. F. Z. B. A. Kadir, F. A. Md Rezali, S. N. Aidit, L. Y. Ma, Q. Ma, *ACS Appl. Electron. Mater.* **2024**, *6*, 2336.
[47] Q. Long, Z. Zhang, G. Qi, Z. Wang, Y. Chen, Z.-Q. Liu, *ACS Sustainable Chem. Eng.* **2020**, *8*, 2512.
[48] S. S. Vedula, G. D. Yadav, *J. Indian Chem. Soc.* **2021**, *98*, 100017.
[49] Environmental Criteria and Assessment Office, in *Health and Environmental Effects Profile for N,N-Dimethylformamide*, Environmental Criteria and Assessment Office, Cincinnati, Ohio, **1986**.

[50] M. Maxeiner, R. Maile, M. Cuvalli, A. Wolf, A. Komal, R. Oestreich, C. Janiak, K. Mandel, A. Knebel, K. Müller-Buschbaum, *Adv. Funct. Mater.* **2025**, https://doi.org/10.1002/adfm.202500794.
[51] A. E. Sedykh, J. J. Pflug, T. C. Schäfer, R. Bissert, D. G. Kurth, K. Müller-Buschbaum, *ACS Sustain. Chem. Eng.* **2022**, *10*, 5101.
[52] T. M. Reineke, M. Eddaoudi, M. Fehr, D. Kelley, O. M. Yaghi, *J. Am. Chem. Soc.* **1999**, *121*, 1651.
[53] M. J. Neufeld, H. Winter, M. R. Landry, A. M. Goforth, S. Khan, G. Pratx, C. Sun, *ACS Appl. Mater. Interfaces* **2020**, *12*, 26943.
[54] X. Zhang, X. Kang, W. Cui, Q. Zhang, Z. Zheng, X. Cui, *New J. Chem.* **2019**, *43*, 8363.
[55] A. Cadiau, C. D. S. Brites, P. M. F. J. Costa, R. A. S. Ferreira, J. Rocha, L. D. Carlos, *ACS Nano* **2013**, *7*, 7213.
[56] W. T. Carnall, P. R. Fields, K. Rajnak, *J. Chem. Phys.* **1968**, *49*, 4450.
[57] L. Rozenberga, W. Skinner, D. G. Lancaster, W. M. Bloch, A. Blencowe, M. Krasowska, D. A. Beattie, *Sci. Rep.* **2022**, *12*, 11982.
[58] W. Donghan, K. Han, W. Xinrui, Z. Wei, *J. Solid State Chem.* **2024**, *333*, 124635.
[59] G. L. Ball, C. J. McLellan, V. S. Bhat, *Crit. Rev. Toxicol.* **2012**, *42*, 28.
[60] V. Bühler, in *Polyvinylpyrrolidone Excipients for Pharmaceuticals*, Springer, Berlin, Germany, **2005**, pp. 5–124.
[61] J. M. Pollard, A. J. Shi, K. E. Göklen, *J. Chem. Eng. Data* **2006**, *51*, 230.
[62] H. Zheng, K. Zhu, A. Onda, K. Yanagisawa, *Nanomaterials* **2021**, *11*, 529.
[63] D. Elenkova, Y. Dimitrova, M. Tsvetkov, B. Morgenstern, M. Milanova, D. Todorovsky, J. Zaharieva, *Molecules* **2024**, *29*, 3713.
[64] N. Patel, P. Shukla, P. Lama, S. Das, T. K. Pal, *Cryst. Growth Des.* **2022**, *22*, 3518.
[65] L. Wu, F. Yang, Y. Xue, R. Gu, H. Liu, D. Xia, Y. Liu, *Mater. Today Bio* **2023**, *19*, 100595.
[66] M. Shah, A. Hameed, M. Kashif, N. Majeed, J. Muhammad, N. Shah, T. Rehan, A. Khan, J. Uddin, A. Khan, H. Kashtoh, *Carbohydr. Polym.* **2024**, *346*, 122619.
[67] J. Alipal, N. A. S. Mohd Pu'ad, T. C. Lee, N. H. M. Nayan, N. Sahari, H. Basri, M. I. Idris, H. Z. Abdullah, *Mater. Today Proc.* **2021**, *42*, 240.
[68] X. Ji, X. Bai, Z. Li, S. Wang, Z. Guan, X. Lu, *Appl. Microbiol. Biotechnol.* **2013**, *97*, 7317.
[69] B. Deepika, P. Ganesan, B. Sivaraman, N. Neethiselvan, P. Padmavathy, *Algal Res.* **2024**, *82*, 103618.
[70] S. G. Pereira, J. S. Gomes-Dias, R. N. Pereira, J. A. Teixeira, C. M. R. Rocha, *Innov. Food Sci. Emerg. Technol.* **2023**, *84*, 103306.
[71] M. M. Jayakody, M. P. G. Vanniarachchy, I. Wijesekara, *J. Food Meas. Charact.* **2022**, *16*, 1195.
[72] M. Usman, A. Ishaq, J. Mac Regenstein, A. Sahar, R. M. Aadil, A. Sameen, M. I. Khan, A. Alam, *Biomass Conv. Bioref.* **2023**, *11*, 1.
[73] N. Q. I. M. Noor, R. S. Razali, N. K. Ismail, R. A. Ramli, U. H. M. Razali, A. R. Bahauddin, N. Zaharudin, A. Rozzamri, J. Bakar, S. Md. Shaarani, *Processes* **2021**, *9*, 2227.
[74] O. V. Mikhailov, *Int. J. Mol. Sci.* **2023**, *24*, 3583.
[75] J. Bella, M. Eaton, B. Brodsky, H. M. Berman, *Science* **1994**, *266*, 75.
[76] Q. Zheng, L. Xiong, L. Yu, D. Wu, C. Yang, Y. Xiao, *J. Lumin.* **2021**, *236*, 118076.
[77] P. A. Tanner, *Chem. Soc. Rev.* **2013**, *42*, 5090.
[78] W. Yang, J. Wang, Y. Han, X. Luo, W. Tang, T. Yue, Z. Li, *Food Control* **2021**, *130*, 108409.
[79] R. Li, S. Wang, P. Lan, X. Luo, D. Zhuang, J. Zhu, *Int. J. Biol. Macromol.* **2025**, *296*, 139699.
[80] Y. S. Zhang, A. Khademhosseini, *Science* **2017**, *356*, aaf3627.
[81] J. Song, B. Zhao, Y. Wang, X. Liu, Z. Cheng, X. Zhang, X. Feng, *Food Chem.* **2024**, *437*, 137883.
[82] H. Omidian, S. Dey Chowdhury, N. Babanejad, *Pharmaceutics* **2023**, *15*, 1836.
[83] R. He, J. He, J. Shen, H. Fu, Y. Zhang, B. Wang, *Soft Sci.* **2024**, *4*, 37.
[84] S. Tiwari (Sharma), A. Chakkaravarthi, S. Bhattacharya, *J. Food Eng.* **2015**, *165*, 60.
[85] V. Kaplin, A. Kopylov, A. Koryakovtseva, N. Minaev, E. Epifanov, A. Gulin, N. Aksenova, P. Timashev, A. Kuryanova, I. Shershnev, A. Solovieva, *Gels* **2022**, *8*, 617.
[86] T. Xia, W. Cao, Y. Cui, Y. Yang, G. Qian, *Opto-Electron. Adv.* **2021**, *4*, 200063.
[87] A. E. Sedykh, M. Becker, M. T. Seuffert, D. Heuler, M. Maxeiner, D. G. Kurth, C. E. Housecroft, E. C. Constable, K. Müller-Buschbaum, *ChemPhotoChem* **2023**, *7*, 202200244.

4 Results and Interpretation

This chapter will discuss and interpret the results obtained from the published scientific contributions presented in **Chapter 3**. It also provides a link between the chapters to show how they relate to the main theme of luminescent and conductive hybrid materials.

In order to achieve the objective of creating new hybrid materials, it was necessary to surmount the described disadvantages inherent in the archetypal bulk MOFs Ln^{3+}-BDC (Ln^{3+}= Eu^{3+}, Tb^{3+}), DUT-5(Al) and MOF-253(Al). **Chapter 3.1** addresses the size-related properties with the successful bottom-up synthesis approach using the surfactants CTAB and PVP. This approach allowed the synthesis of the aforementioned MOFs with homogenous particle size distributions, analysed by dynamic light scattering (DLS), with particle sizes down to a few nanometres for nDUT-5(Al) – a mere 21 times smaller with only one percent of the original particle size distribution of bulk DUT-5(Al). The homogeneity of the particle size distribution is congruent with electron images obtained *via* scanning electron microscopy (SEM). The trivalent lanthanides Eu^{3+} and Tb^{3+} were either incorporated as luminescent species during the synthesis of nLn^{3+}-BDC or post-synthetically *via* impregnation as nDUT-5(Al):Ln^{3+} and nMOF-253(Al):Ln^{3+}. Thermogravimetric analysis (DTA/TG-MS) clearly demonstrates the presence of a few percent of residual surfactants still encapsulating the nanoMOFs, which effectively reduces the MOF's surface energy and hence prevents particle agglomeration and aggregation in dispersion. It is notable that the Ln^{3+} ions are capable of diffusing through the remaining layer of surfactants as microwave-induced plasma atomic emission spectroscopy (MP-AES) confirmed the presence of Ln^{3+} in the nanoMOFs after post-synthetic modification, while the nanoMOFs retain their particle size. This observation emphasises that the enclosure by surfactants is rather a dynamic process than a stationary condition. It further states the efficacy of the surfactant approach and accomplishes aimed bottom-up downsizing of bulk MOFs.

In accordance with the empirical rule of *Latva*, it was found that an energy transfer from the linker to Tb^{3+} is not preferred in nDUT-5(Al):Tb^{3+} and nMOF-253(Al):Tb^{3+}, as well as their bulk counterparts. However, doping the same bulk MOFs and nanoMOFs with Eu^{3+} yielded an energy transfer that was more efficient in nDUT-5(Al):Eu^{3+} and nMOF-253(Al):Eu^{3+} than in their bulk versions. This phenomenon is related to the crystallite size of the MOFs used, with the inner pores of a three-dimensional MOF crystal structure being less accessible, the larger the crystallite size (hence, the longer the pore channels) of the MOF is. An ion (*i.e.*, Eu^{3+}) traversing the pore channels of a MOF encounters *van der Waals* and/or *Coulomb* interactions, consequently leading to its capture within an outer pore along its pathway. This effectively obstructs the pore channels for incoming ions, resulting in unoccupied inner pores. Consequently, the linkers forming the unoccupied inner pores are unable to provide Eu^{3+} with the energy required to trigger red emission. Nevertheless, the energy of the linkers is dissipated

through the process of mostly bluish fluorescence linker-based emission. However, by employing nanoMOFs, the pore channels become shorter and the average pathway of Eu^{3+} is reduced, thereby increasing the probability of inner pore occupation and consequently leading to a more efficient energy transfer. This, in turn, enhances the number of emitting Eu^{3+} ions and less prominent linker-based emissions. Bathochromic shifts revealed by PL spectroscopy yield more reddish luminescent nDUT-5(Al):Eu^{3+} and nMOF-253(Al):Eu^{3+} in comparison to their bulk counterparts and are supported by these statements. Despite the coverage of surfactants, nTb^{3+}-BDC showed particularly excellent PLQY in the solid-state. The discrepancy in reported PLQY between the investigated nanoMOFs and their bulk counterparts is likely attributable to the presence of surfactants, as evidenced by UV-Vis absorption spectroscopy, which revealed absorption bands of CTAB and PVP in the lower Vis wavelength region. The full range of chromaticity exhibited by developed nanoMOFs is also showcased in a recorded video.

In summary, this chapter introduced three nanoscale variants of the archetypal bulk MOFs Ln^{3+}-BDC, DUT-5(Al) and MOF-253(Al), along with novel insights into the impact of particle size on the photophysical and morphological properties of nanoMOFs, and the function of surfactants. Together with the synthetic and post-synthetic modifications, a total of eight novel nanoMOF materials have been added to literature. From an environmental point of view, the enhanced photophysical properties of nanoMOFs enable the utilisation of reduced material quantities to attain equivalent outcomes to those achieved by conventional bulk MOFs.

As homogenously dispersed particles and stable dispersions of the additives are key parameters for well-manufactured hybrid materials, the previously presented nanoMOFs nLn^{3+}-BDC were used for the development of luminescent and conductive nLn^{3+}-BDC@polymer multi-functional hybrid materials as stated in **Chapter 3.2**. For a comprehensive overview of the essential criteria that must be met in order to facilitate the utilisation of electric current in MOF@polymer hybrid materials, please refer to Chapter 1.4. Briefly: MOFs are usually behaving like insulators; therefore, the polymer moiety has to be able to conduct electricity. A luminescent nLn^{3+}-BDC (Ln^{3+}= Eu^{3+}, Tb^{3+}, Yb^{3+}) was added to the conductive polymer matrices polystyrene sulfonate (PSS) and pyrolyzed resorcinol-formaldehyde (pRF), as well as to the non-conductive polysulfone (Udel® P-3500, PSUd) to create an interconnected multi-level anti-counterfeiting mechanism. The objective of implementing conductive polymers in hybrid materials was successfully met by utilising PSS and the pitch-black pRF. In order to emphasise the conductive properties of PSS and pRF, a MMM using a PSUd was developed as well. The conductivity of the materials under discussion was determined by means of EIS using two different setups, one of which was newly developed specifically for the purpose as part of this work. Combining features that are visible and invisible to the naked eye is one of the most effective ways to prevent counterfeiting. As invisible features require specialised instrumentation for identification, visible features mask those that are not visible to the naked eye. While the modular design approach of hybrid materials imparts an additive character to the

features, the interdependence of features establishes an intrinsic link between the levels. It is essential to note that a change in one property of the multi-level structure will invariably result in an alteration to at least one other property, with the result of a hard-to-copy anti-counterfeiting mechanism. The multi-level structure comprises visible and invisible PL, designated as Level I (= Vis light emission) and Level II (= NIR emission), respectively, as well as conductivity designated as Level III. While Level I is characterised by the visible PL of nLn^{3+}-BDC (Ln^{3+}= Eu^{3+}, Tb^{3+}), Level II is defined by the invisible PL of nYb^{3+}-BDC. The conductivity provided by the PSS and the pRF, which is also invisible to the naked eye, has been specified as Level III.

A homogenous lateral and vertical distribution of nLn^{3+}-BDC within the matrices was confirmed by SEM and cross-sectional energy-dispersive X-ray spectroscopy (EDS). The investigations revealed that the small particle size of nLn^{3+}-BDC offers two key benefits that are not available using the bulk analogues. Firstly, it provides enhanced nLn^{3+}-BDC particle distribution within the MMMs nLn^{3+}-BDC@PSS and nLn^{3+}-BDC@PSUd. Secondly, the potential to apply nLn^{3+}-BDC onto the surface of larger particles, with sizes as large as a couple of hundred nanometres, is demonstrated by nLn^{3+}-BDC@pRF. Furthermore, it has been demonstrated the principle of mixed visible PL by incorporating both red-emitting nEu^{3+}-BDC and green-emitting nTb^{3+}-BDC into the same polymer as $nEu^{3+}Tb^{3+}$-BDC@polymer, resulting in an orange luminescence checked *via* PL spectroscopy and fluorescence microscopy.

The pitch-black $nTb^{3+}Yb^{3+}$-BDC@pRF and $nTb^{3+}Eu^{3+}$-BDC@pRF hybrid materials are particularly interesting because they appear black in daylight but emit intense green and orange light under UV irradiation, respectively, as can be seen in a video sequence recorded as part of this work. The nLn^{3+}-BDC located on the surface of the pRF enables the bright emission; if nLn^{3+}-BDC were embedded in the pRF particles, the emission would be expected to be weaker or even completely quenched. It can thus be concluded that the light does not trespass through the pRF spheres; rather, it is emitted by nLn^{3+}-BDC from the pRF surface. Such an intense emission from a black body, normally characterised by its ability to absorb all light, has not been described in literature so far. The pitch-black powder material $nTb^{3+}Yb^{3+}$-BDC@pRF is especially well-suited for use in tagging black goods and achieves, together with the MMM $nTb^{3+}Yb^{3+}$-BDC@PSS the objective of providing three-level anti-counterfeiting solutions. The developed multi-level anti-counterfeiting mechanism was demonstrated in a proof-of-concept experiment, where the MMMs nLn^{3+}-BDC@PSS and the powders nLn^{3+}-BDC@pRF were put between two black fabrics, sealed and subsequently irradiated with UV light. This real-life scenario was presented in both a photo series and a video; it shows how the anti-counterfeiting materials can be used in various branded products, including furniture, textiles and apparel.

In conclusion, the present chapter has combined luminescent nLn^{3+}-BDC (Ln^{3+}= Eu^{3+}, Tb^{3+}, Yb^{3+}) with two conductive polymers (PSS, pRF) and one non-conductive polymer (PSUd) to contribute six novel MMMs and three novel powder materials to the extant literature on advanced anti-counterfeiting measures. An interdependent multi-level anti-counterfeiting mechanism comprising visible and invisible PL as well as

conductivity was developed, which achieved the set objective. Given that the majority of polymers do not contribute properties other than chemical resistance, mechanical stability or plasticity (*cf.*, Chapter 1.4), a more advanced approach to make use of polymers in hybrid materials has been established by introducing conductivity. Moreover, the effectiveness of these hybrid materials was evaluated through a proof-of-concept experiment, similar to potential real-world applications.

Chapter 3.3 reported the successful synthesis of sustainable and biodegradable hybrid materials nEu^{3+}-BDC@agar and nEu^{3+}-BDC@gelatine as bio-nMOF-MMMs. In addition, hydrogels and cryogels (the latter belonging to the class of aerogels[113] obtained from freeze-drying) were obtained from nEu^{3+}-BDC@agar after modifying the synthesis procedure of bio-nMOF-MMMs. These objectives have been achieved by leveraging the expertise gained from the development of nanoMOF nEu^{3+}-BDC and the anti-counterfeiting MMMs, which involved the development of membrane fabrication techniques. It is noteworthy that all bio-based hybrid materials have been synthesised in an aqueous environment using only water as solvent, which met the set objective of greener synthesis.

Agar and gelatine have been chosen due to their natural abundancy and good commercial availability.[114,115] The polysaccharide agar is composed of two primary components: agarose, which is composed of 3,6-anhydro-α-L-galactose and β-D-galactose, and agaropectin, which is similar to agarose, but with the hydroxyl groups of 3,6-anhydro-α-L-galactose substituted by methoxy, pyruvate, or sulfoxy groups.[115] Gelatine, on the other hand, consists mainly of a mixture of several short polypeptide sequences derived from the hydrolytic breakdown of collagen. Three polypeptides are arranged as triple-helix structure with a mostly apolar surface.[114] Once dispersed in water, nEu^{3+}-BDC changed its modification from the as-synthesised DMF-containing modification $^{\infty}_{3}[Eu_3(bdc)_{4.5}(dmf)_2(H_2O)_3]$ to an only water-containing modification $^{\infty}_{3}[Eu_2(bdc)_3(H_2O)_4]$. It is noteworthy that this phase transition occurs in the presence of surrounding surfactants, namely CTAB and PVP, as confirmed by DTA/TG-MS. Furthermore, the $^{\infty}_{3}[Eu_2(bdc)_3(H_2O)_4]$ modification persists from freezing temperatures, such as those present during the cryogel formation, up to several hundred degrees Celsius. Moreover, stability tests of nEu^{3+}-BDC at varying pH units of aqueous solutions reveal an intact crystal structure over almost the entire pH range, also demonstrated in a video.

The work further addressed sustainability criteria by implementing a ten-times HQ recycling process to assess the viability of the developed bio-based hybrid materials. In this instance, red luminescence from the nEu^{3+}-BDC was used as “on-the-fly”-status probe to indicate the material’s condition, with the result clearly visible to the naked eye. Should there be a compromise in the material’s physical or chemical integrity (*e.g.*, loss of mechanical stability), outcomes may include a change of the nEu^{3+}-BDC luminescence properties, such as a shift in the emission colour, amongst other possible outcomes. For the bio-nMOF-MMM nEu^{3+}-BDC@gelatine showing no change in the chemical environment of Eu^{3+}, the calculated asymmetry ratio of the characteristic Eu^{3+} emissions $^5D_0 \rightarrow {}^7F_1$ and $^5D_0 \rightarrow {}^7F_2$ remained unchanged, while the

asymmetry ratio of nEu^{3+}-BDC@agar slightly decreased due to the increasing linker-based PL. Taken together the asymmetry ratio and the calculated loss of PL intensity per mass, which was more than twice as high for nEu^{3+}-BDC@agar as for nEu^{3+}-BDC@gelatine, the superior stability of the gelatine-based hybrid materials compared to their agar counterpart has been attested. Following ten cycles of HQ recycling, X-ray diffractometry confirmed the intact crystal structure of nEu^{3+}-BDC in both agar and gelatine materials, which is noteworthy for MOFs considering the aqueous environment.

To examine the potential of the gelation properties of agar, hydrogels and freeze-dried cryogels of nEu^{3+}-BDC@agar were successfully synthesised by modifying the gelation process. The physical texture of agar changes from a membrane to a hydrogel to a cryogel as the temperature is lowered towards freezing to remove excess water. At temperatures below zero degrees Celsius, the frozen water must be sublimated using vacuum drying, resulting in macroporous cryogels. Both hydrogel and cryogel were subject of an exemplarily HQ recycling demonstrated excellent recyclability of nEu^{3+}-BDC@agar under retained photophysical properties, structural integrity and mechanical stability. Notwithstanding the nature of the bio-based hybrid material, whether it be bio-nMOF-MMM, hydrogel or cryogel, it is possible to reclaim the nEu^{3+}-BDC through the process of centrifugation, subsequent to the dispersal of the material in water. A further step towards greener chemistry and the objective of more sustainability that has been set for this work. Bio-based hybrid materials of nEu^{3+}-BDC@agar show excellent stability in aqueous solutions below the boiling point of water, whereas the water-soluble nEu^{3+}-BDC@gelatine needs the formation of an additional water-proof layer to ensure water-resistance, as shown by a video. Moreover, evidence has been presented in the form of a video demonstrating the water stability of nEu^{3+}-BDC@agar as bio-nMOF-MMM, hydrogel and cryogel at elevated temperatures. The results emphasis that both the hydrogel and cryogel exhibited twice the stability of the bio-nMOF-MMM of nEu^{3+}-BDC@agar in boiling water. In addition, the experiment demonstrated the notable stability of nEu^{3+}-BDC, as evidenced by the red colour emission. To address real-life scenarios, the exposition of nEu^{3+}-BDC, nEu^{3+}-BDC@agar and nEu^{3+}-BDC@gelatine to seawater, with defined parameters resembling real-world conditions, yielded the same results as observed for the experiment with demineralized water usually used in laboratories. Together with hazard assessments obtained from literature for the individual components (Eu^{3+} ions, BDC^{2-}, PVP, CTAB, agar, gelatine), stability experiments in artificial seawater allow an accurate prediction of consequences after intended or unintended exposition to the environment.

The properties exhibited by hydrogels and cryogels differ from those of bio-nMOF-MMMs, thereby providing access to a range of different shapes and physical textures. For instance, the synthesis of hydrogels in virtually any shape is enabled by their gel-like properties, demonstrated by the synthesis of red luminescent pill-like nEu^{3+}-BDC@agar gels. Conversely, freeze-dried cryogels exhibit sponge-like characteristics, enabling reversible compression without compromising their original structure.[113]

The effect was also demonstrated in a video. The cell-like structure of cryogels on the microscopic level enables squeezing behaviour and provides a macroporous framework for physical and chemical interactions with guest molecules or ions. In combination with nEu^{3+}-BDC, this work introduced a hybrid material providing a macroporous and a mesoporous pore system within one material at the same time – an impressive demonstration of one of the biggest advantages of hybrid materials: additive properties.

Taking all achievements into consideration, this work successfully produced four sustainable and biodegradable hybrid materials as membranes, hydrogels and cryogels of nEu^{3+}-BDC@agar and nEu^{3+}-BDC@gelatine. These novel bio-based hybrid materials are less harmful to nature than hybrid materials that make use of APs as matrices. In addition, the successful HQ recycling further reduces their environmental impact, especially by using water as a solvent, and aligns with the principle of a circular economy. Moreover, the Eu^{3+} PL provides the developed bio-based hybrid materials with an “on-the-fly”-status probe for the material’s condition, opening the field for potential sensor-related applications.

5 Summary and Outlook

As outlined in **Chapter 4** and summarised in **Figure 8**, the objectives set for this PhD thesis have all been successfully accomplished, with a total of 21 novel nanoMOF or nanoMOF-based hybrid materials developed.

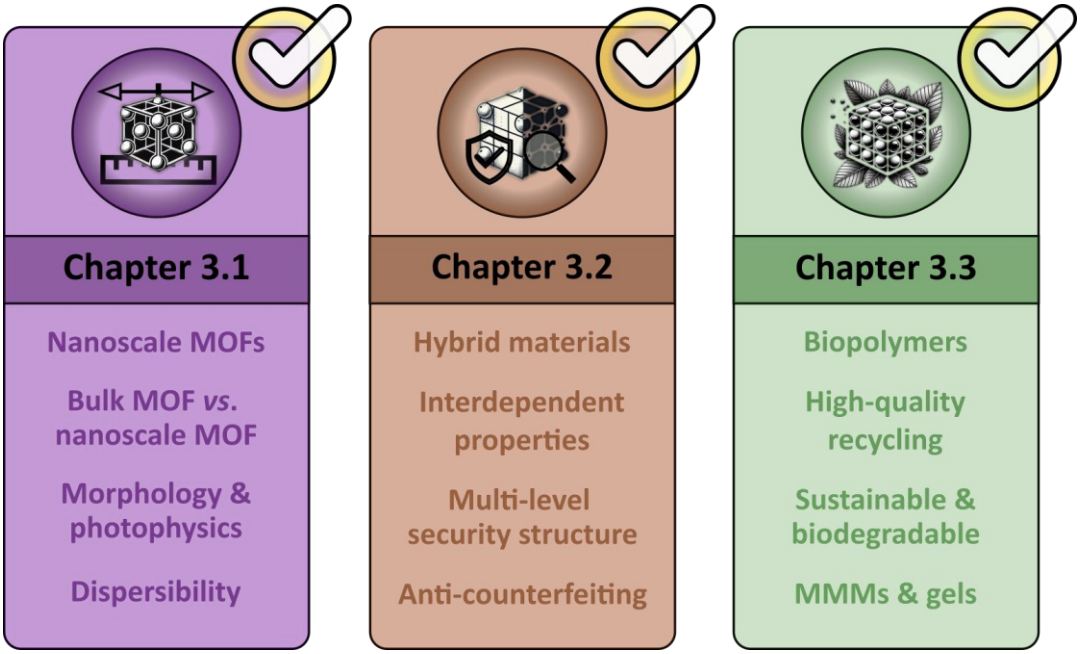

Figure 8. Chapter-wise overview of the accomplished research objectives. Keywords are defined as the most significant aspects related to the research conducted within the designated chapter, without excluding other aspects investigated.

Luminescent nLn^{3+}-BDC (in two different modifications), nDUT-5(Al):Ln^{3+} and nMOF-253(Al):Ln^{3+} have been synthesised and thoroughly investigated regarding their photophysical and morphological properties as well as thermal stability. A comparison was made between the properties of the nanoMOFs and their bulk MOF counterparts. This comparison revealed distinct differences, suggesting that nanoMOFs are well-suited and better applicable as their bulk analogues for further applications, in particular for incorporation into (bio)polymer matrices.

The utilisation of nLn^{3+}-BDC resulted in the successful development of multi-level anti-counterfeiting nMOF-MMMs, nLn^{3+}-BDC@PSS and nLn^{3+}-BDC@PSUd, as well as a multi-level anti-counterfeiting powder material nLn^{3+}-BDC@pRF. The multi-level anti-counterfeiting mechanism is composed of interconnected properties, including visible (Level I, exposed) and invisible (Level II, concealed) photoluminescence, as well as conductivity (Level III, concealed). Alteration of one property invariably entails modification of at least one other property. This renders the mechanism difficult to reproduce. Furthermore, a proof-of-concept experiment demonstrated the ease with which the developed hybrid materials can be incorporated into trademarked goods.

The development of hybrid materials in the context of greener chemistry has been advanced through the utilisation of biopolymers agar and gelatine, in conjunction with

the red luminescent DMF-free nEu^{3+}-BDC modification. The fabrication of sustainable and biodegradable hybrid materials nEu^{3+}-BDC@agar and nEu^{3+}-BDC@gelatine as bio-nMOF-MMMs was successful. In addition, nEu^{3+}-BDC@agar was also synthesised as a semi-solid gel-like hydrogel and a macroporous sponge-like cryogel. All novel bio-based hybrid materials developed in this PhD thesis demonstrated potential for multiple HQ-recycling, thus aligning with the principles of a circular economy. Furthermore, the bio-based hybrid materials demonstrated exceptional stability when subjected to environmental stressors such as humidity, pH, temperature and high ion concentrations as existing in artificial seawater. As the HQ-recycling process occurred within an entirely aqueous environment, the nEu^{3+}-BDC@agar and nEu^{3+}-BDC@gelatine materials exhibited a sustainable characteristic, facilitated by the inherent "on-the-fly"-status probe functionality of the nEu^{3+}-BDC, allowing the evaluation of the material's condition.

Looking forward, it may be fruitful to initiate research that pertains to the advancement of certain steps or approaches developed in the three aforementioned works. The successful bottom-up nanoparticle synthesis could be used to synthesise nano versions of other known archetype MOFs. In lieu of PL, properties such as sorption behaviour may prove to be of interest, given that the inner surface of nanoMOFs are better accessible. In this context, further functionalisation *via* the MOF's pore system is promising (*e.g.*, loading dyes or gases). With regard to the interconnected multi-level security mechanism in hybrid materials, the presence of a distinct emission can be qualitatively analysed by means of a semi-professional spectrometer setup. However, a quantitative ratiometric approach could be developed. In addition to the qualitative approach – the presence or absence of the emission – the ratio of nTb^{3+}-BDC to nYb^{3+}-BDC could be modified, which would make it even more difficult to ascertain the precise composition of the anti-counterfeiting material. As the matrix structure on the molecular level is crucial for conductivity, matrices exhibiting preferred orientations could be produced through methodologies such as electrospinning. In terms of the environmental impact and sustainability of nanoMOF-based hybrid material design, the use of other nMOF@biopolymer combinations has the potential to yield even more sustainable alternatives. Specifically, components that are as multi-functionable as agar but more stable could offer a greener solution in the field of hybrid material technology.

6 References

[1] N. G. Connelly, T. Damhus, R. M. Hartshorn, A. T. Hutton, In *Nomenclature of Inorganic Chemistry (IUPAC Recommendations 2005)*, RSC Publishing, **2005**, pp. 51–52.

[2] US Department of Energy, *Notice of Final Determination on 2023 DOE Critical Materials List*, **2023**.

[3] S. Carrara, S. Bobba, D. Blagoeva, P. Alves Dias, A. Cavalli, K. Georgitzikis, M. Grohol, A. Itul, T. Kuzov, C. Latunussa, L. Lyons, G. Malano, T. Maury, A. Prior Arce, J. Somers, T. Telsnig, C. Veeh, D. Wittmer, C. Black, D. Pennington, M. Christou, *Supply chain analysis and material demand forecast in strategic technologies and sectors in the EU – a foresight study*, Publications Office of the European Union, Luxembourg, **2023**.

[4] J. Gambogi, In *Rare Earth Elements: Sustainable Recovery, Processing, and Purification, Special Publications 79* (Eds.: Karamalidis, A. K.; Eggert, R. G.), John Wiley & Sons, Inc., Hoboken, NJ, USA, **2024**, pp. 1–25.

[5] H. Höppe, In *Rare-Earth Elements*, De Gruyter, Berlin, **2024**, pp. 11–16.

[6] H. Höppe, In *Rare-Earth Elements*, De Gruyter, Berlin, **2024**, pp. 97–116.

[7] H. Höppe, In *Rare-Earth Elements*, De Gruyter, Berlin, **2024**, pp. 50–94.

[8] H. Höppe, In *Rare-Earth Elements*, De Gruyter, Berlin, **2024**, pp. 17–35.

[9] F. Ortu, *Chem. Rev.* **2022**, *122*, 6040.

[10] G. N. Lewis, *Valence and the Structure of Atoms and Molecules*, Chemical Catalog Company, Incorporated, **1923**.

[11] R. G. Pearson, *J. Am. Chem. Soc.* **1963**, *85*, 3533.

[12] A. M. Hamisu, A. Ariffin, A. C. Wibowo, *Inorg. Chim. Acta* **2020**, *511*, 119801.

[13] K. O. Kirlikovali, S. L. Hanna, F. A. Son, O. K. Farha, *ACS Nanosci. Au* **2023**, *3*, 37.

[14] E. Condon, *Phys. Rev.* **1926**, *28*, 1182.

[15] J. Franck, E. G. Dymond, *Trans. Faraday Soc.* **1926**, *21*, 536.

[16] F. Hund, *Z. Phys.* **1925**, *33*, 855.

[17] H. N. Russell, F. A. Saunders, *Astrophys. J.* **1925**, *61*, 38.

[18] O. Laporte, W. F. Meggers, *J. Opt. Soc. Am.* **1925**, *11*, 459.

[19] H. Höppe, In *Rare-Earth Elements*, De Gruyter, Berlin, **2024**, pp. 117–173.

[20] K. Binnemans, *Coord. Chem. Rev.* **2015**, *295*, 1.

[21] G. S. Ofelt, *J. Chem. Phys.* **1962**, *37*, 511.

[22] B. R. Judd, *Phys. Rev.* **1962**, *127*, 750.

[23] Chr. K. Jørgensen, In *Progress in Inorganic Chemistry* (Ed.: Cotton, A. F.), John Wiley & Sons, Inc., **1962**, pp. 73–124.

[24] J.-C. G. Bünzli, C. Piguet, *Chem. Soc. Rev.* **2005**, *34*, 1048.

[25] S. V. Eliseeva, J.-C. G. Bünzli, *Chem. Soc. Rev.* **2010**, *39*, 189.

[26] A. K. Singh, *Chem. Soc. Rev.* **2022**, *455*, 214365.

[27] G. H. Dieke, *Spectra and Energy Levels of Rare Earth Ions in Crystals* (Eds.: Crosswhite, H.; Crosswhite, H.), John Wiley & Sons Inc, New York, **1968**.

[28] M. Latva, H. Takalo, V.-M. Mukkala, C. Matachescu, J. C. Rodríguez-Ubis, J. Kankare, *J. Lumin.* **1997**, *75*, 149.

[29] D. L. Dexter, *J. Chem. Phys.* **1953**, *21*, 836.

[30] H. H. Jaffe, A. L. Miller, *J. Chem. Educ.* **1966**, *43*, 469.

[31] D. C. Harris, M. D. Bertolucci, *Symmetry and Spectroscopy: An Introduction to Vibrational and Electronic Spectroscopy*, Dover Publications, New York, **1989**.

[32] J. R. Lakowicz, *Principles of Fluorescence Spectroscopy* (Ed.: Lakowicz, J. R.), Springer US, Boston, MA, **2006**.

[33] O. M. Yaghi, M. O'Keeffe, N. W. Ockwig, H. K. Chae, M. Eddaoudi, J. Kim, *Nature* **2003**, *423*, 705.

[34] X. Guo, G. Zhu, F. Sun, Z. Li, X. Zhao, X. Li, H. Wang, S. Qiu, *Inorg. Chem.* **2006**, *45*, 2581.

[35] R. Freund, O. Zaremba, G. Arnauts, R. Ameloot, G. Skorupskii, M. Dincă, A. Bavykina, J. Gascon, A. Ejsmont, J. Goscianska, M. Kalmutzki, U. Lächelt, E. Ploetz, C. S. Diercks, S. Wuttke, *Angew. Chem. Int. Ed.* **2021**, *60*, 23975.

[36] Z. Lin, J. J. Richardson, J. Zhou, F. Caruso, *Nat. Rev. Chem.* **2023**, *7*, 273.

[37] N. Stock, S. Biswas, *Chem. Rev.* **2012**, *112*, 933.

[38] O. M. Yaghi, H. Li, *J. Am. Chem. Soc.* **1995**, *117*, 10401.

[39] J. Rouquerol, D. Avnir, C. W. Fairbridge, D. H. Everett, J. M. Haynes, N. Pernicone, J. D. F. Ramsay, K. S. W. Sing, K. K. Unger, *Pure Appl. Chem.* **1994**, *66*, 1739.

[40] L. Qiu, T. Xu, Z. Li, W. Wang, Y. Wu, X. Jiang, X. Tian, L. Zhang, *Angew. Chem. Int. Ed.* **2008**, *47*, 9487.

[41] B. Achenbach, A. Yurdusen, N. Stock, G. Maurin, C. Serre, *Adv. Mater.* **2025**.

[42] C. Burda, X. Chen, R. Narayanan, M. A. El-Sayed, *Chem. Rev.* **2005**, *105*, 1025.

[43] T. Kiyonaga, M. Higuchi, T. Kajiwara, Y. Takashima, J. Duan, K. Nagashima, S. Kitagawa, *Chem. Commun.* **2015**, *51*, 2728.

[44] Y. Qi, Y. Luan, J. Yu, X. Peng, G. Wang, *Chem. Eur. J.* **2015**, *21*, 1589.

[45] J. Łuczak, M. Kroczewska, M. Baluk, J. Sowik, P. Mazierski, A. Zaleska-Medynska, *Adv. Colloid Interface Sci.* **2023**, *314*, 102864.

[46] S. Wang, Y. Lv, Y. Yao, H. Yu, G. Lu, *Inorg. Chem. Commun.* **2018**, *93*, 56.

[47] E. A. Flügel, A. Ranft, F. Haase, B. V. Lotsch, *J. Mater. Chem.* **2012**, *22*, 10119.

[48] I. Senkovska, F. Hoffmann, M. Fröba, J. Getzschmann, W. Böhlmann, S. Kaskel, *Microporous Mesoporous Mater.* **2009**, *122*, 93.

[49] E. D. Bloch, D. Britt, C. Lee, C. J. Doonan, F. J. Uribe-Romo, H. Furukawa, J. R. Long, O. M. Yaghi, *J. Am. Chem. Soc.* **2010**, *132*, 14382.

[50] W. P. Mounfield, K. S. Walton, *J. Colloid Interface Sci.* **2015**, *447*, 33.

[51] T. M. Reineke, M. Eddaoudi, M. Fehr, D. Kelley, O. M. Yaghi, *J. Am. Chem. Soc.* **1999**, *121*, 1651.

[52] Y. Zhang, S. Yuan, G. Day, X. Wang, X. Yang, H.-C. Zhou, *Coord. Chem. Rev.* **2018**, *354*, 28.

[53] X. Wang, Y. Jiang, A. Tissot, C. Serre, *Coord. Chem. Rev.* **2023**, *497*, 215454.

[54] S. Sun, Y. Zhao, J. Wang, R. Pei, *J. Mater. Chem. B* **2022**, *10*, 9535.

[55] H. Zhou, J. Han, J. Cuan, Y. Zhou, *Chemical Engineering Journal* **2022**, *431*, 134170.

[56] P. P. Mondal, M. Neem, R. Chand, A. Pandit, S. Neogi, *Chem. Mater.* **2024**, *36*, 10451.

[57] G. Férey, C. Serre, *Chem. Soc. Rev.* **2009**, *38*, 1380.

[58] J. Yang, Y. Yang, *Small* **2020**, *16*.

[59] M. Al Sharabati, R. Sabouni, G. A. Husseini, *Nanomaterials* **2022**, *12*, 277.

[60] Y. Absalan, M. Gholizadeh, E.-B. Kim, S. Ameen, Y. Wang, Y. Wang, H. He, *Coord. Chem. Rev.* **2024**, *515*, 215972.

[61] A. J. Rieth, A. M. Wright, M. Dincă, *Nat. Rev. Mater.* **2019**, *4*, 708.

[62] A. Knebel, J. Caro, *Nat. Nanotechnol.* **2022**, *17*, 911.

[63] A. Ebadi Amooghin, H. Sanaeepur, M. Ghomi, R. Luque, H. Garcia, B. Chen, *Coord. Chem. Rev.* **2024**, *505*, 215660.

[64] S. Ma, W. Han, W. Han, F. Dong, Z. Tang, *J. Mater. Chem. A* **2023**, *11*, 3315.

[65] Y. Lin, C. Kong, Q. Zhang, L. Chen, *Adv. Energy Mater.* **2017**, *7*.

[66] C. Liu, C. Tian, J. Guo, X. Zhang, L. Wu, L. Zhu, B. Du, *ACS Appl. Mater. Interfaces* **2024**, *16*, 43156.

[67] A. Fick, *Lond.Edinb.Dubl.Phil.Mag* **1855**, *10*, 30.

[68] M. von Smoluchowski, *Ann. Phys.* **1906**, *326*, 756.

[69] A. Einstein, *Ann. Phys.* **1905**, *322*, 549.

[70] S. Xing, C. Janiak, *Chem. Commun.* **2020**, *56*, 12290.

[71] M. Teixeira, R. A. Maia, S. Shanmugam, B. Louis, S. A. Baudron, *Microporous Mesoporous Mater.* **2022**, *343*, 112148.

[72] K. Binnemans, *Chem. Rev.* **2009**, *109*, 4283.

[73] W.-B. Sun, P.-F. Yan, G.-M. Li, H. Xu, J.-W. Zhang, *J. Solid State Chem.* **2009**, *182*, 381.

[74] N. Kerbellec, D. Kustaryono, V. Haquin, M. Etienne, C. Daiguebonne, O. Guillou, *Inorg. Chem.* **2009**, *48*, 2837.

[75] G. E. Gomez, R. Marin, A. N. Carneiro Neto, A. M. P. Botas, J. Ovens, A. A. Kitos, M. C. Bernini, L. D. Carlos, G. J. A. A. Soler-Illia, M. Murugesu, *Chem. Mater.* **2020**, *32*, 7458.

[76] L. Zhao, X. Song, X. Ren, D. Fan, Q. Wei, D. Wu, *Anal. Chem.* **2021**, *93*, 8613.

[77] X. Yu, A. A. Ryadun, D. I. Pavlov, T. Y. Guselnikova, A. S. Potapov, V. P. Fedin, *Angew. Chem. Int. Ed.* **2023**, *62*.

[78] B. Chen, Y. Yang, F. Zapata, G. Qian, Y. Luo, J. Zhang, E. B. Lobkovsky, *Inorg. Chem.* **2006**, *45*, 8882.

[79] H. Xu, R. Jin, C. Wu, Y. Yang, G. Qian, *Spectrosc. Spectral Anal.* **2008**, *28*, 1734.

[80] D. B. Kanzariya, M. Y. Chaudhary, T. K. Pal, *Dalton Trans.* **2023**, *52*, 7383.

[81] N. Riehl, *Physik und technische Anwendungen der Lumineszenz*, Springer Berlin Heidelberg, Berlin, Heidelberg, **1941**.

[82] S. Liu, W. Liu, Y. Sun, W. Liu, *Inorg. Chem.* **2023**, *62*, 9781.

[83] E. Bourgeat-Lami, V. de Zea Bermudez, L. A. D. Carlos, S. Hayakawa, W. Caseri, N. Hüsing, H. A. Currie, G. Kickelbick, D. A. Loy, P. Roach, A. Osaka, R. A. Sa Ferreira, S. V. Patwardhan, N. J. Shirtcliffe, C. C. Perry, M. D. Soucek, J. E. Ritchie, K. Tsuru, C. A. Wilkie, J. Zhu, *Hybrid Materials* (Ed.: Kickelbick, G.), Wiley, **2006**.

[84] J. Dechnik, J. Gascon, C. J. Doonan, C. Janiak, C. J. Sumby, *Angew. Chem. Int. Ed.* **2017**, *56*, 9292.

[85] O. Smirnova, S. Ojha, A. De, A. Schneemann, F. Haase, A. Knebel, *Adv. Funct. Mater.* **2024**, *34*.

[86] A. Knebel, J. Caro, *Nat. Nanotechnol.* **2022**, *17*, 911.

[87] J. M. Stangl, D. Dietrich, A. E. Sedykh, C. Janiak, K. Müller-Buschbaum, *J. Mater. Chem. C* **2018**, *6*, 9248.

[88] J.-X. Wang, J. Yin, O. Shekhah, O. M. Bakr, M. Eddaoudi, O. F. Mohammed, *ACS Appl. Mater. Interfaces* **2022**, *14*, 9970.

[89] H. Zhou, J. Han, J. Cuan, Y. Zhou, *Chem. Eng. J.* **2022**, *431*, 134170.

[90] W.-J. Li, J.-F. Feng, Z.-J. Lin, Y.-L. Yang, Y. Yang, X.-S. Wang, S.-Y. Gao, R. Cao, *Chem. Commun.* **2016**, *52*, 3951.

[91] V. Baglio, A. S. Arico, A. Di Blasi, P. L. Antonucci, F. Nannetti, V. Tricoli, V. Antonucci, *J. Appl. Electrochem.* **2005**, *35*, 207.

[92] J. Escorihuela, R. Narducci, V. Compañ, F. Costantino, *Adv. Mater. Interfaces* **2019**, *6*.

[93] B. J. A. Tarboush, D. Rana, T. Matsuura, H. A. Arafat, R. M. Narbaitz, *J. Membr. Sci.* **2008**, *325*, 166.

[94] X. Zheng, Z. Yang, G. Zeng, Q. Lin, X. Chen, Y. Xiang, Y.-H. Chiao, R. R. Gonzales, Z.-X. Low, J. Luo, *Chem. Eng. J.* **2025**, *505*, 159865.

[95] T. F. Otero, *Conducting Polymers*, Royal Society of Chemistry, Cambridge, **2015**.

[96] N. K, C. S. Rout, *RSC Adv.* **2021**, *11*, 5659.

[97] S. Bedi, K. Bharti, D. Banerjee, K. Biradha, *Small* **2024**, *20*.

[98] M. Gosh, A. Barman, A. K. Meikap, S. K. De, S. Chatterjee, *Phys. Lett. A* **1999**, *260*, 138.

[99] N. F. Mott, E. A. Davis, *Electronic Processes in Non-Crystalline Materials*, Oxford University Press, Incorporated, Oxford, UNITED KINGDOM, **2012**.

[100] Nobel Prize Outreach AB 2025, *Advanced Information - The Nobel Prize in Chemistry 2000*, **2000**.

[101] Y. Hu, A. Ruud, V. Miikkulainen, T. Norby, O. Nilsen, H. Fjellvåg, *RSC Adv.* **2016**, *6*, 60479.

[102] C. A. Gross, T. A. Roppel, *Fundamentals of Electrical Engineering*, CRC Press, **2012**.

[103] Y.-L. Hong, L.-L. Kang, B. Li, Z.-Q. Shi, Z. Li, G. Li, *Microporous Mesoporous Mater.* **2025**, *381*, 113342.

[104] C. Wang, C. Liu, J. Li, X. Sun, J. Shen, W. Han, L. Wang, *Chem. Commun.* **2017**, *53*, 1751.

[105] A. Grant, M. Cordle, E. Bridgwater, *Quality of Recycling - Towards an operational definition* (Eds.: Canfora, P.; Dri, M.; Antonopoulos, I.; Gaudillat, P.), Publications Office of the European Union, Luxembourg, **2020**.

[106] H.-W. Li, J.-L. Zhang, R. Xue, Z.-W. An, W. Wu, Y. Liu, G.-H. Hu, H. Zhao, *Sep. Purif. Technol.* **2023**, *320*, 124145.

[107] Plastics Europe AISBL, *Plastics - the fast Facts 2023*, **2023**.

[108] United Nations Environment Programme, Secretariat of the Basel Rotterdam and Stockholm Conventions, *Chemicals in plastics: a technical report*, Geneva, **2023**.

[109] S. El Hankari, M. Bousmina, A. El Kadib, *Prog. Mater. Sci.* **2019**, *106*, 100579.

[110] R. M. Abdelhameed, H. Abdel-Gawad, M. Elshahat, H. E. Emam, *RSC Adv.* **2016**, *6*, 42324.

[111] M. Pooresmaeil, R. Safarpour, H. Namazi, *J. Polym. Environ.* **2025**.

[112] J. Huo, J. Aguilera-Sigalat, S. El-Hankari, D. Bradshaw, *Chem. Sci.* **2015**, *6*, 1938.

[113] J. V. Alemán, A. V. Chadwick, J. He, M. Hess, K. Horie, R. G. Jones, P. Kratochvíl, I. Meisel, I. Mita, G. Moad, S. Penczek, R. F. T. Stepto, *Pure Appl. Chem.* **2007**, *79*, 1801.

[114] M. Usman, A. Ishaq, J. Mac Regenstein, A. Sahar, R. M. Aadil, A. Sameen, M. I. Khan, A. Alam, *Biomass Conv. Bioref.* **2023**.

[115] X. Ji, X. Bai, Z. Li, S. Wang, Z. Guan, X. Lu, *Appl. Microbiol. Biotechnol.* **2013**, *97*, 7317.

7 Appendix A

7.1 Supporting Information – Chapter 3.1

SUPPLEMENTARY INFORMATION

Nano vs. Bulk – Surfactant-controlled Photophysical and Morphological Features of Luminescent Lanthanide MOFs

Moritz Maxeiner, Lea Wittig, Alexander E. Sedykh, Thomas Kasper and
Klaus Müller-Buschbaum*

Journal of Materials Chemistry A

CONTENTS

Crystal Structures

Eu^{3+}-bdc and Tb^{3+}-bdc

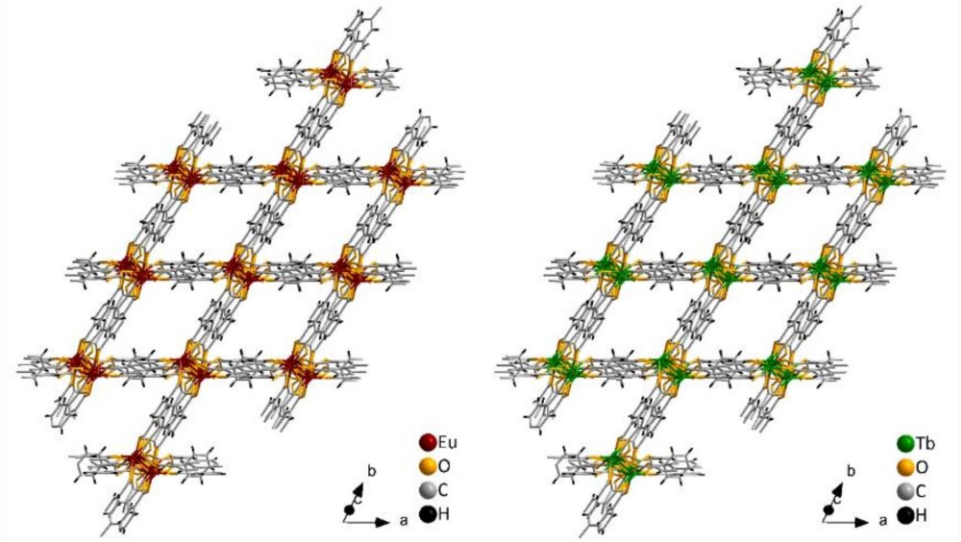

Figure SI 1 Illustrated excerpt from the crystal structure of Eu^{3+} bdc (left) and Tb^{3+}-bdc (right). Atom colour code: Europium (red), Terbium (green), Oxygen (orange), Carbon (grey) and Hydrogen (black). Solvent molecules have been omitted for clarity.[1]

DUT-5 and MOF-253

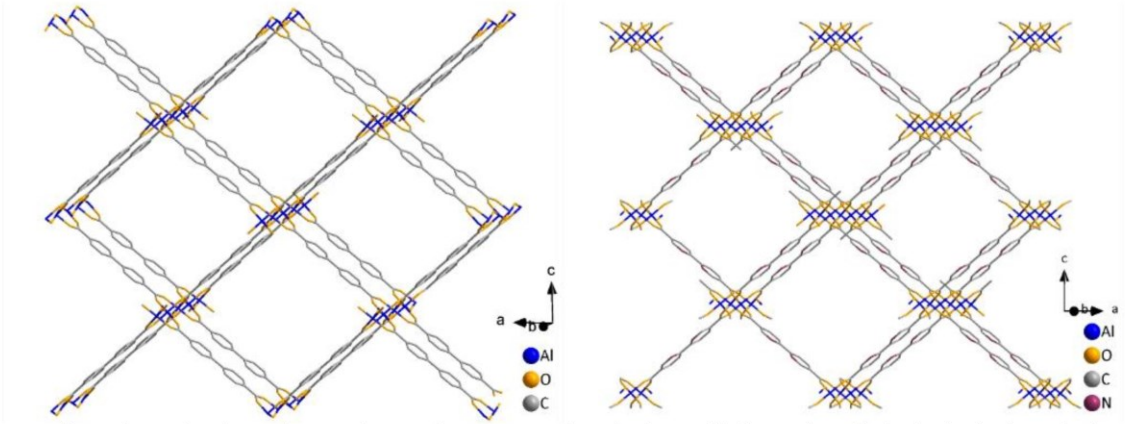

Figure SI 2 Illustrated excerpt from the crystal structure of DUT-5 and MOF-253. Atom colour code: Aluminium (blue), Oxygen (orange) and Carbon (grey). Solvent molecules and hydrogen atoms have been omitted for clarity.[2,3]

Powder X-Ray Diffractometry

PXRD patterns of Tb^{3+}-bdc, nTb^{3+}-bdc, reagents and surfactants

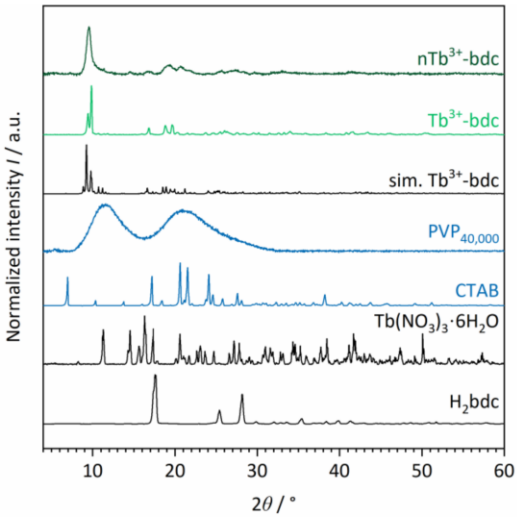

Figure SI 3 Simulated (sim.) PXRD pattern for single-crystal data of Tb^{3+}-bdc (black) and recorded PXRD patterns of Tb^{3+}-bdc (dark green), nTb^{3+}-bdc (pale green), surfactants (blue) and educts (black).

PXRD patterns of Eu^{3+}-bdc, nEu^{3+}-bdc, educts and surfactants

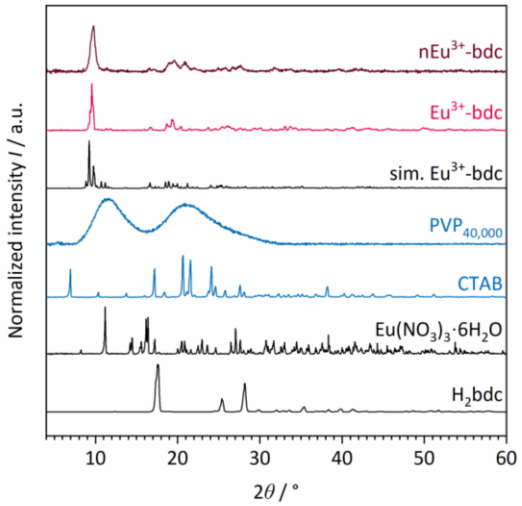

Figure SI 4 Simulated (sim.) PXRD pattern for single-crystal data of Eu^{3+}-bdc (black) and recorded PXRD patterns of Eu^{3+}-bdc (dark red), nEu^{3+}-bdc (pale red), surfactants (blue) and educts (black).

PXRD patterns of DUT-5, nDUT-5, educts and surfactants

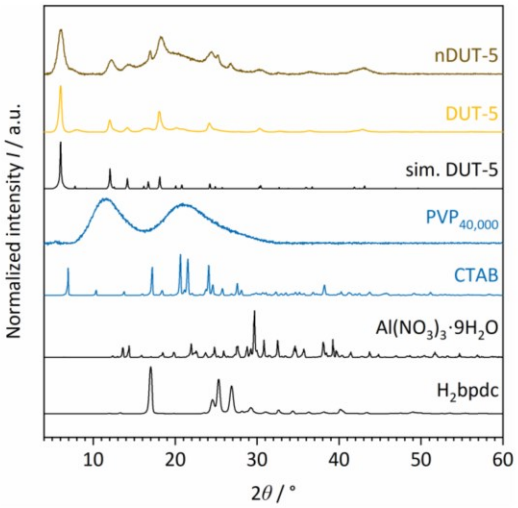

Figure SI 5 Simulated (sim.) PXRD pattern for single-crystal data of DUT-5 (black) and recorded PXRD patterns of DUT-5 (dark yellow), nDUT-5 (pale yellow), surfactants (blue) and educts (black).

PXRD patterns of MOF-253, nMOF-253, educts and surfactants

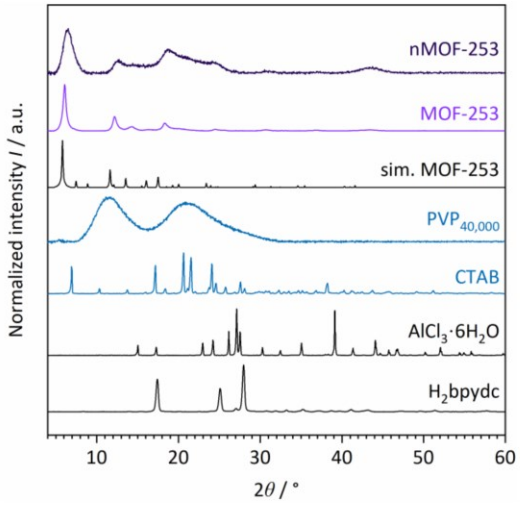

Figure SI 6 Simulated (sim.) PXRD pattern for single-crystal data of MOF-253 (black) and recorded PXRD patterns of MOF-253 (dark violet), nMOF-253 (pale violet), surfactants (blue) and educts (black).

PXRD patterns of post-synthetic modified DUT-5:Ln^{3+} and nDUT-5:Ln^{3+} with Ln^{3+}= Eu^{3+}, Tb^{3+}

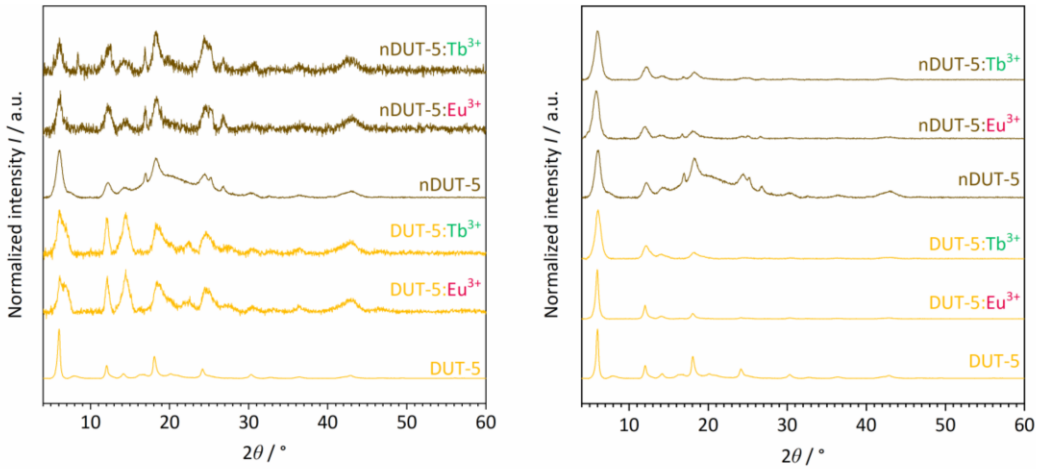

Figure SI 7 Powder diffractograms of post-synthetic modified DUT-5:Ln^{3+} (pale yellow) and nDUT-5:Ln^{3+} (dark yellow) with Ln^{3+}= Eu^{3+}, Tb^{3+} in EtOH (left) and MeCN (right).

PXRD patterns of post-synthetic modified MOF-253:Ln^{3+} and nMOF-253:Ln^{3+} with Ln^{3+}= Eu^{3+}, Tb^{3+}

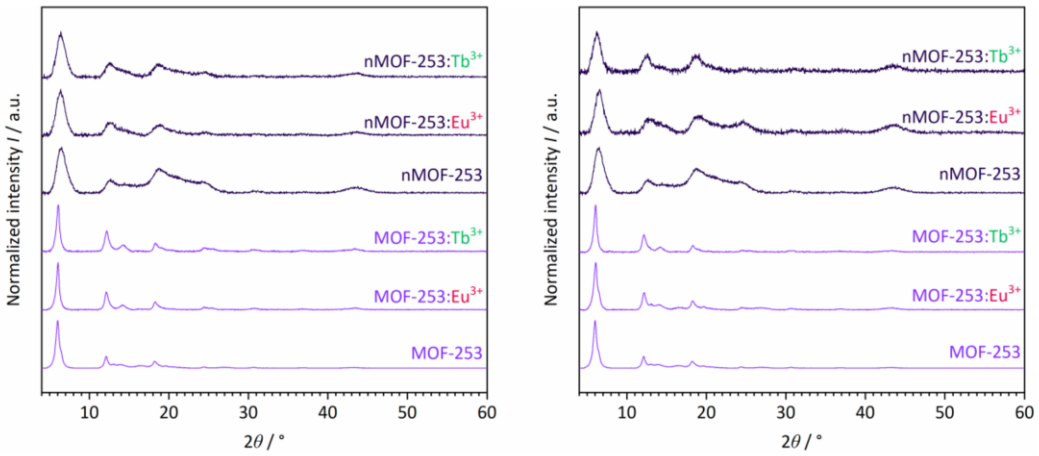

Figure SI 8 Powder diffractograms of post-synthetic modified MOF-253:Ln^{3+} (pale violet) and nMOF-253:Ln^{3+} (dark violet) with Ln^{3+}= Eu^{3+}, Tb^{3+} in EtOH (left) and MeCN (right).

Oxidation products of DUT-5, nDUT-5, MOF-253 and nMOF-253 (=Al_2O_3) as well as Tb^{3+}-bdc and nTb^{3+}-bdc (=Tb_4O_7)

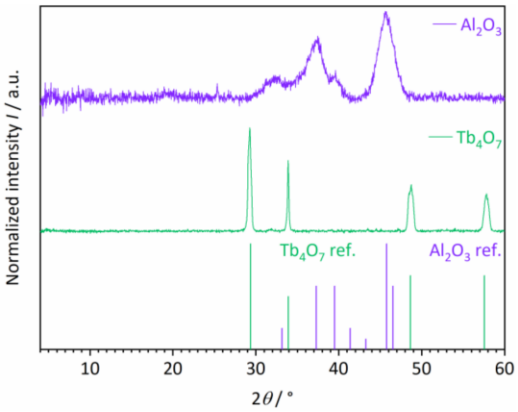

Figure SI 9 Powder diffractograms of the investigated oxidation products ofDUT-5, nDUT-5, MOF-253 and nMOF-253 (=Al_2O_3, violet) as well as Tb^{3+}-bdc and nTb^{3+}-bdc (=Tb_4O_7, green) and corresponding reference (ref.) angles in 2θ for Al_2O_3 (JCPDS 00-047-1308) and Tb_4O_7 (JCPDS 00-013-0387).

Scanning Electron Microscopy and Dynamic Light Scattering

SEM images and DLS results of Eu^{3+}-bdc, Tb^{3+}-bdc, DUT-5 and MOF-253

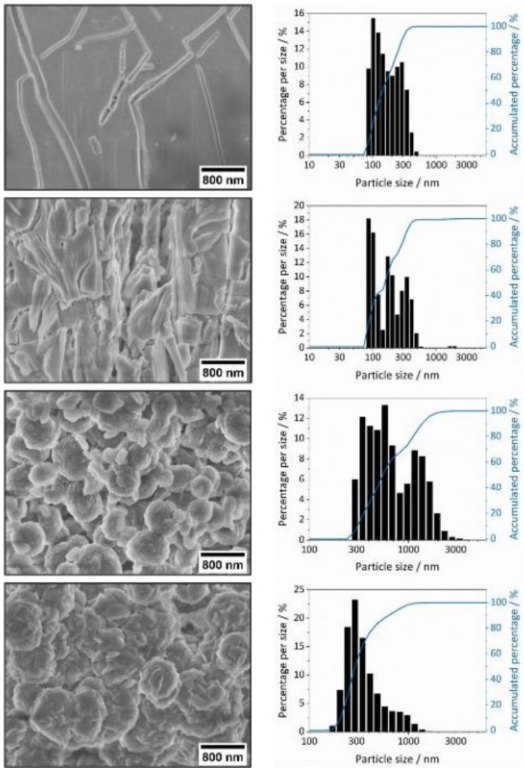

Figure SI 10 SEM images (25k magnification, left) and particle size distributions (right) of Eu^{3+}-bdc, Tb^{3+}-bdc, DUT-5 and MOF-253 (top to bottom).

SEM images and DLS results of nDUT-5:Ln^{3+} and nMOF-253:Ln^{3+} with Ln^{3+}= Eu^{3+}, Tb^{3+}

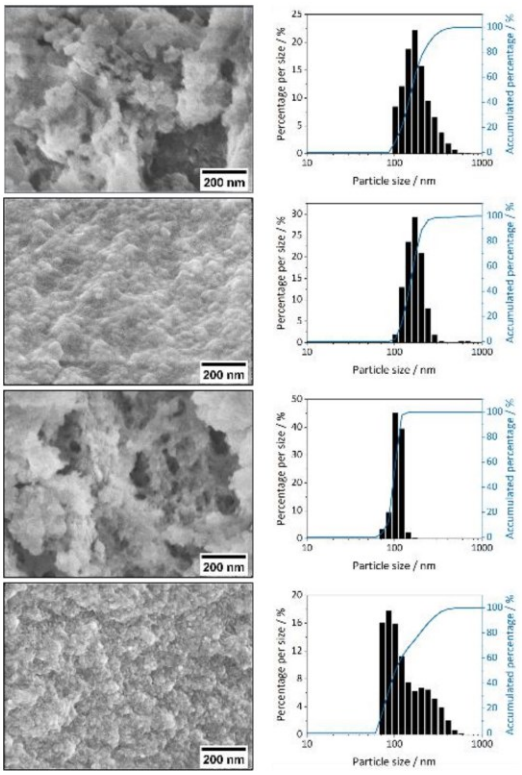

Figure SI 11 SEM images (100k magnification, left) and particle size distributions (right) of nDUT-5:Eu^{3+}, nDUT-5:Tb^{3+}, nMOF-253:Eu^{3+} and nMOF-253:Tb^{3+} (top to bottom).

SEM images of Eu^{3+}-bdc, DUT-5:Eu^{3+} and MOF-253:Eu^{3+}

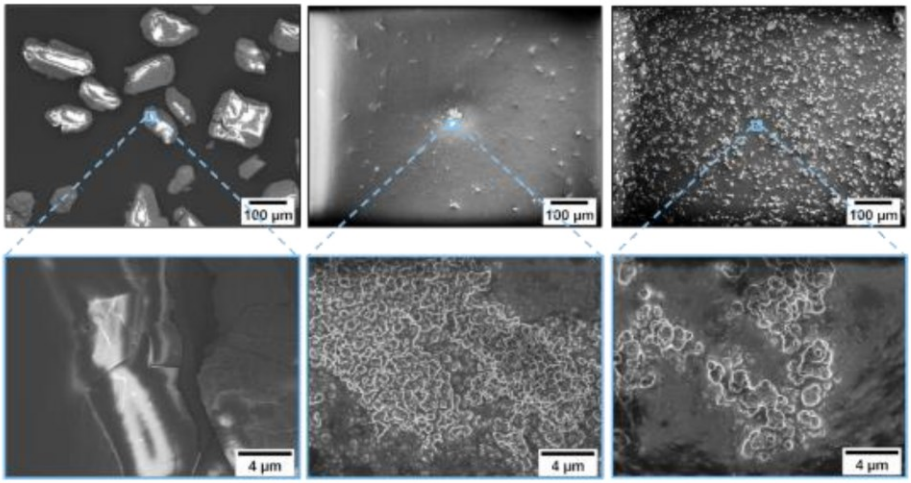

Figure SI 12 SEM images (150 magnification, top) with blue enlarged sectors (5k magnification, bottom) of Eu^{3+}-bdc (left), DUT-5:Eu^{3+} (mid) and MOF-253:Eu^{3+} (right).

SEM images of Tb^{3+}-bdc, DUT-5:Tb^{3+} and MOF-253:Tb^{3+}

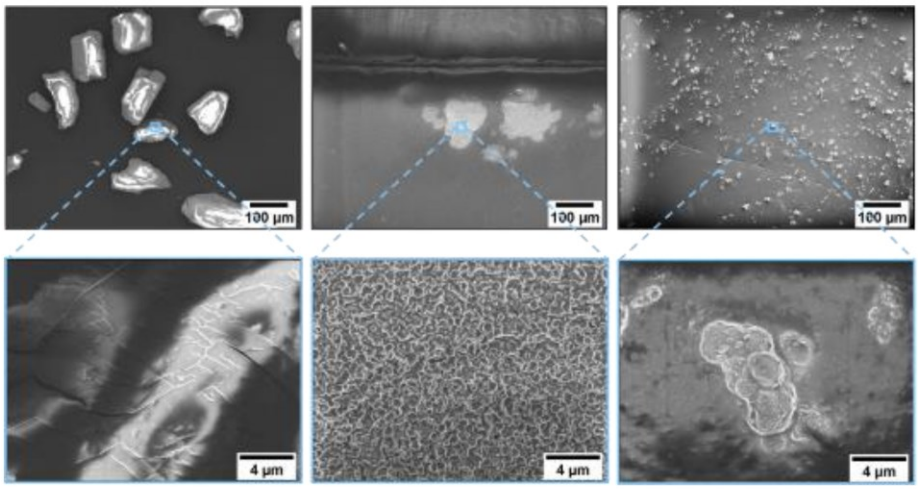

Figure SI 13 SEM images (150 magnification, top) and blue enlarged sectors (5k magnification, bottom) of Tb^{3+} bdc (left), DUT 5:Tb^{3+} (mid) and MOF 253:Tb^{3+} (right).

Differential Thermal Analysis/Thermogravimetric-Mass Spectrometry

Tb^{3+}-bdc and nTb^{3+}-bdc

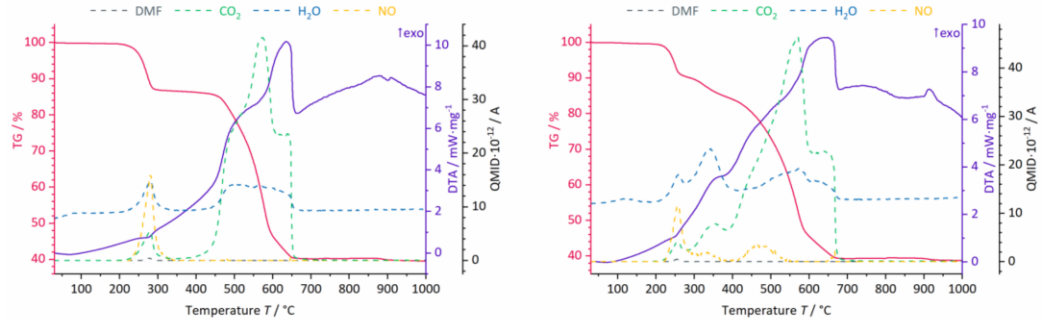

Figure SI 14 DTA/TG-MS results of Tb^{3+}-bdc (left) and nTb^{3+}-bdc (right) for a constant stream of synthetic air as working gas. NO signal (yellow) is given in QMID·10^{-12} A for a more detailed insight.

DUT-5 and nDUT-5

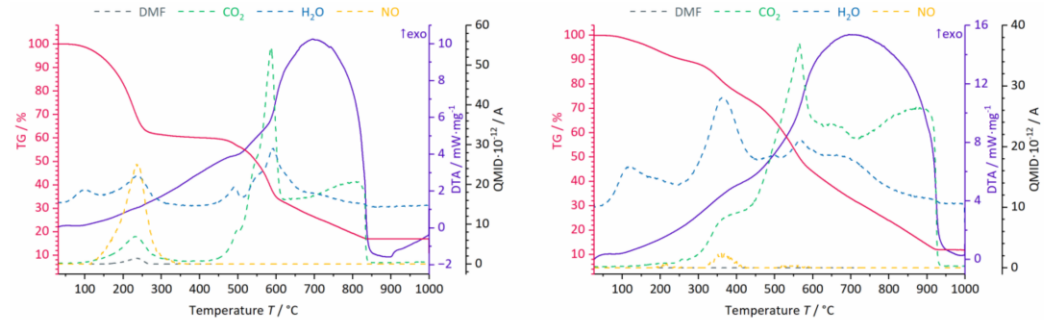

Figure SI 15 DTA/TG-MS results of DUT-5 (left) and nDUT-5 (right) for a constant stream of synthetic air as working gas. NO signal (yellow) is given in QMID·10^{-12} A for a more detailed insight.

MOF-253 and nMOF-253

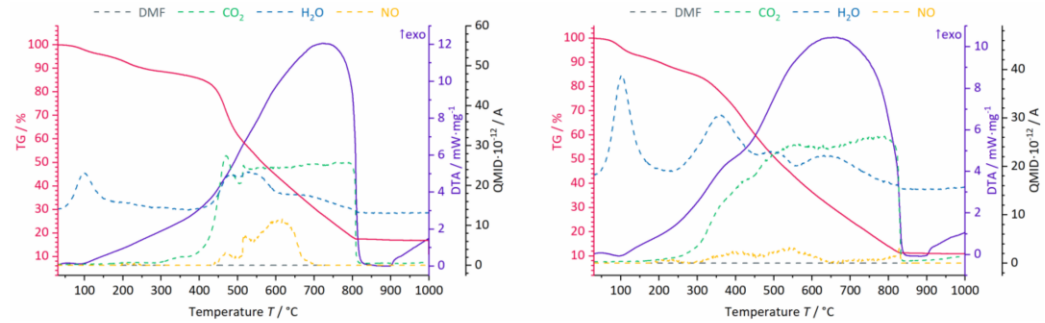

Figure SI 16 DTA/TG-MS results of MOF-253 (left) and nMOF-253 (right) for a constant stream of synthetic air as working gas. NO signal (yellow) is given in QMID·10^{-12} A for a more detailed insight.

UV-Vis-Diffuse Reflectance Spectroscopy

Eu^{3+}-bdc and nEu^{3+}-bdc

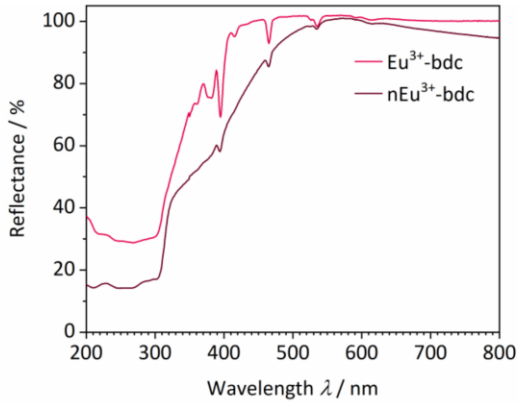

Figure SI 17 UV-Vis diffuse reflectance spectra of Eu^{3+}-bdc (pale red) and nEu^{3+}-bdc (dark red).

Tb^{3+}-bdc and nTb^{3+}-bdc

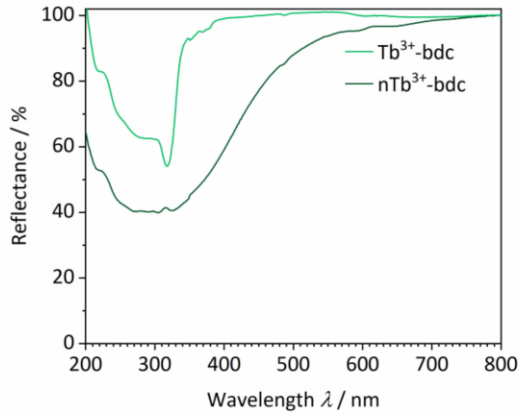

Figure SI 18 UV-Vis diffuse reflectance spectra of Tb^{3+}-bdc (pale green) and nTb^{3+}-bdc (dark green).

DUT-5 and nDUT-5

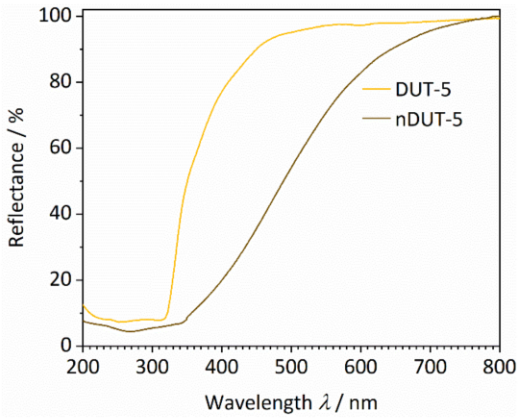

Figure SI 19 UV-Vis diffuse reflectance spectra of DUT-5 (pale yellow) and nDUT-5 (dark yellow).

MOF-253 and nMOF-253

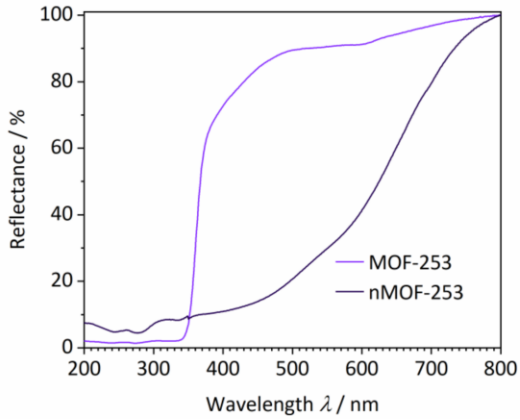

Figure SI 20 UV-Vis diffuse reflectance spectra of MOF-253 (pale violet) and nMOF-253 (dark violet).

Photoluminescence Spectra

DUT-5:Tb^{3+} and nDUT-5:Tb^{3+}

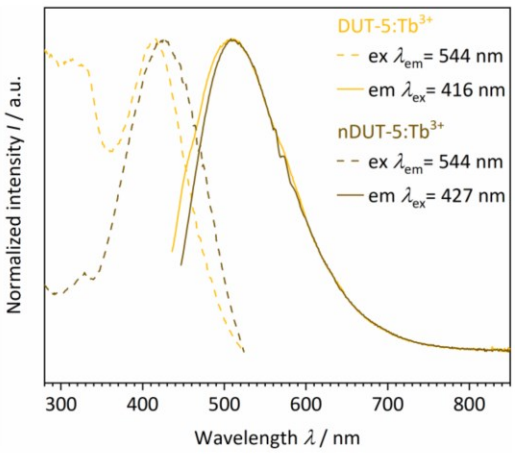

Figure SI 21 Excitation and emission photoluminescence spectra of DUT-5:Tb^{3+} (pale yellow) and nDUT-5:Tb^{3+} (dark yellow).

MOF-253:Tb^{3+} and nMOF-253:Tb^{3+}

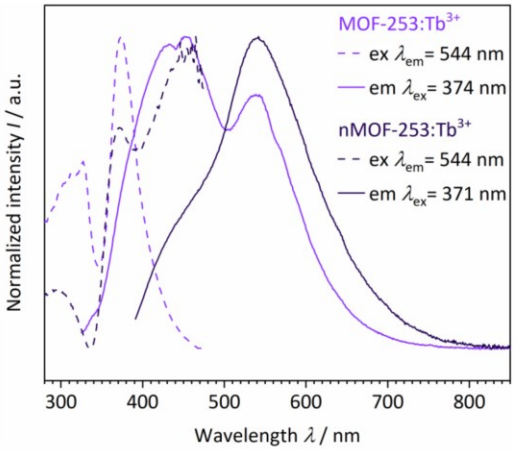

Figure SI 22 Excitation and emission photoluminescence spectra of MOF-253:Tb^{3+} (pale violet) and nMOF-253:Tb^{3+} (dark violet).

Triplet State Determinations

Gd^{3+}-bdc

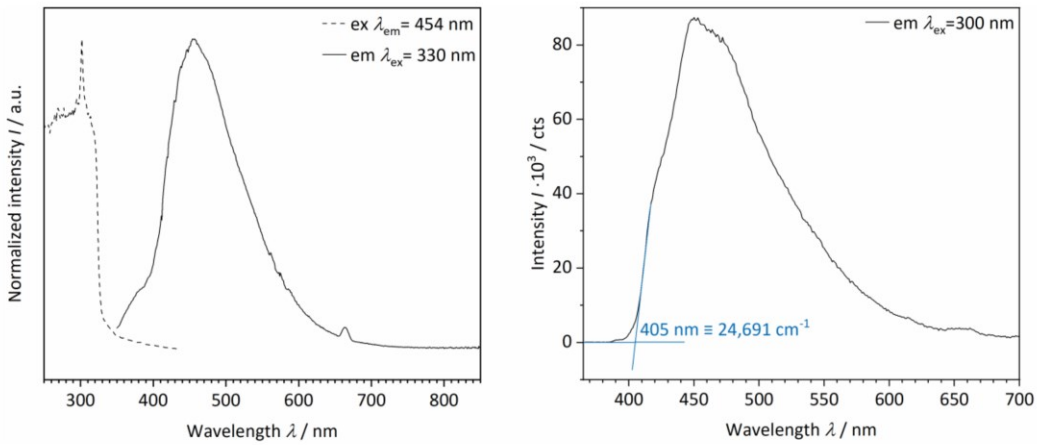

Figure SI 23 Photoluminescence spectra (left) and triplet state phosphorescence spectrum (right) of Gd^{3+}-bdc. Recording delay time: 0.2 ms, sample window time: 2 ms, and counts per flash: 30.

DUT-5:Gd^{3+}

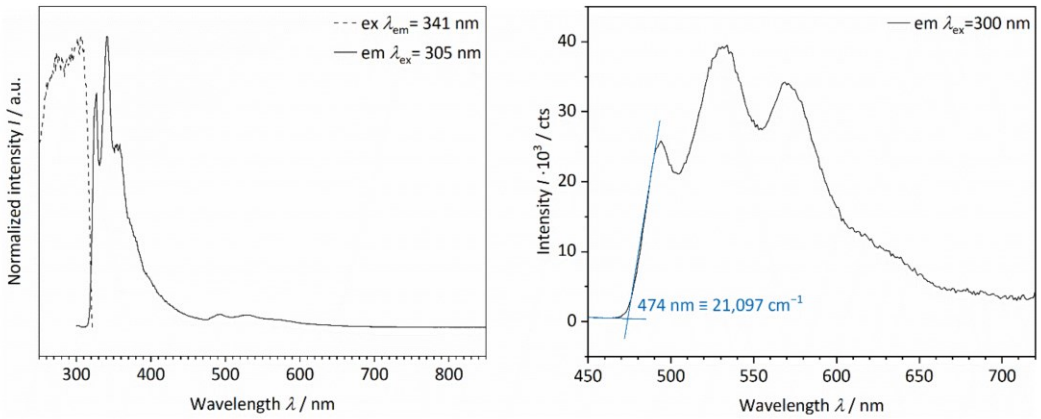

Figure SI 24 Photoluminescence spectra (left) and triplet state phosphorescence spectrum (right) of DUT-5:Gd^{3+}. Recording delay time: 0.1 ms, sample window time: 1 ms, and counts per flash: 50.

MOF-253:Gd^{3+}

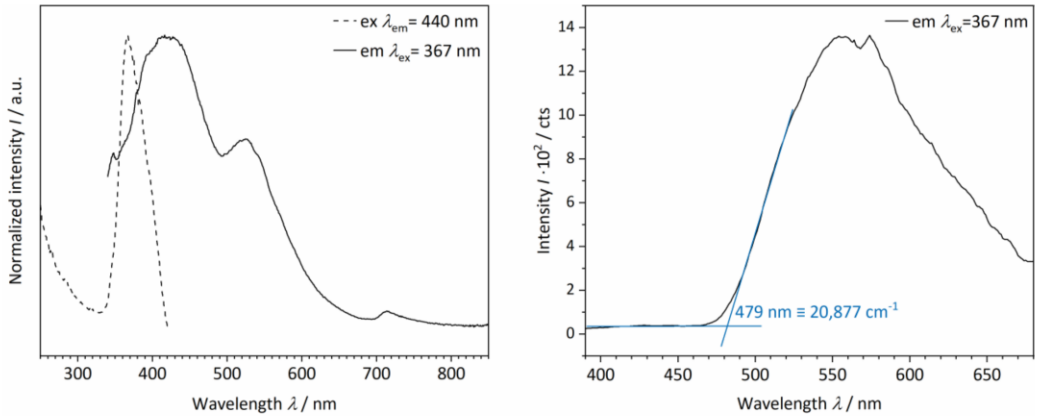

Figure SI 25 Photoluminescence spectra (left) and triplet state phosphorescence spectrum (right) of MOF-253:Gd^{3+}. Recording delay time: 0.1 ms, sample window time: 0.5 ms, and counts per flash: 50.

Luminescence Decay Measurements

Eu^{3+}-bdc and nEu^{3+}-bdc

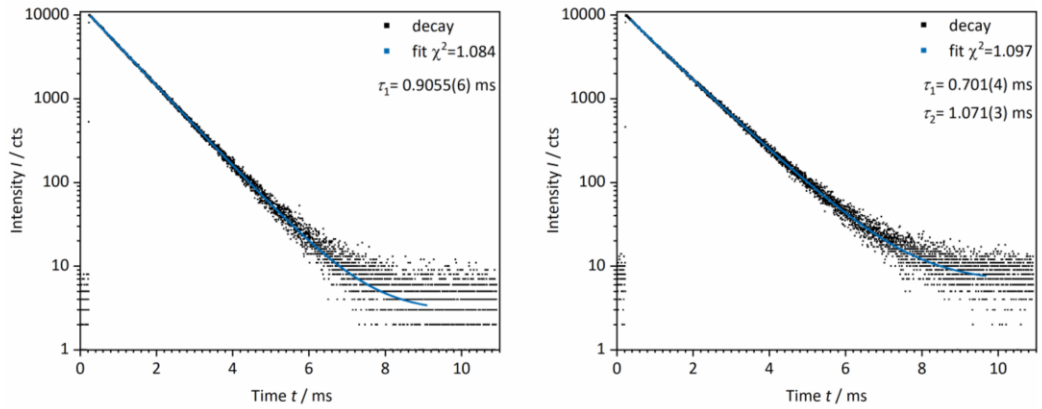

Figure SI 26 Luminescence decay measurement of Eu^{3+}-bdc (left, λ_{ex}=288 nm, λ_{em}=614 nm) and nEu^{3+}-bdc (right, λ_{ex}=296 nm, λ_{em}=614 nm).

Tb^{3+}-bdc and nTb^{3+}-bdc

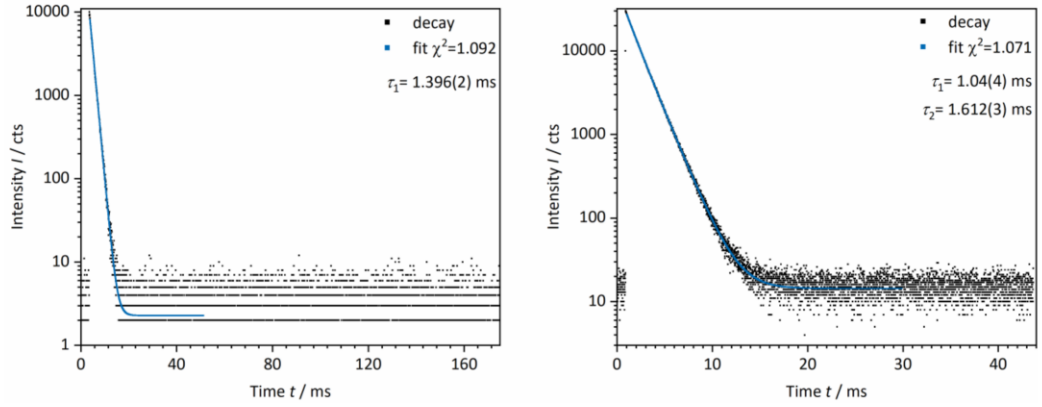

Figure SI 27 Luminescence decay measurement of Tb^{3+}-bdc (left, λ_{ex}=300 nm, λ_{em}=544 nm) and nTb^{3+}-bdc (right, λ_{ex}=286 nm, λ_{em}=543 nm).

DUT-5 and nDUT-5

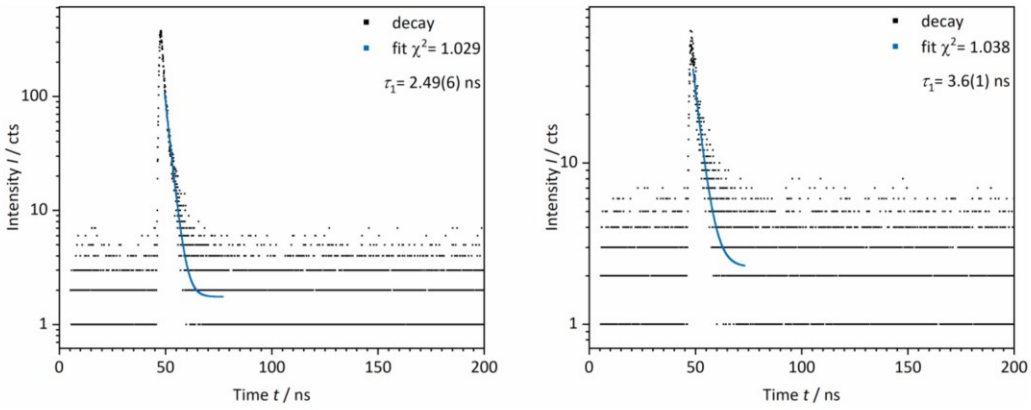

Figure SI 28 Luminescence decay measurement of DUT-5 (left, λ_{ex}=287 nm, λ_{em}=378 nm) and nDUT-5 (right, λ_{ex}=287 nm, λ_{em}=378 nm).

MOF-253 and nMOF-253

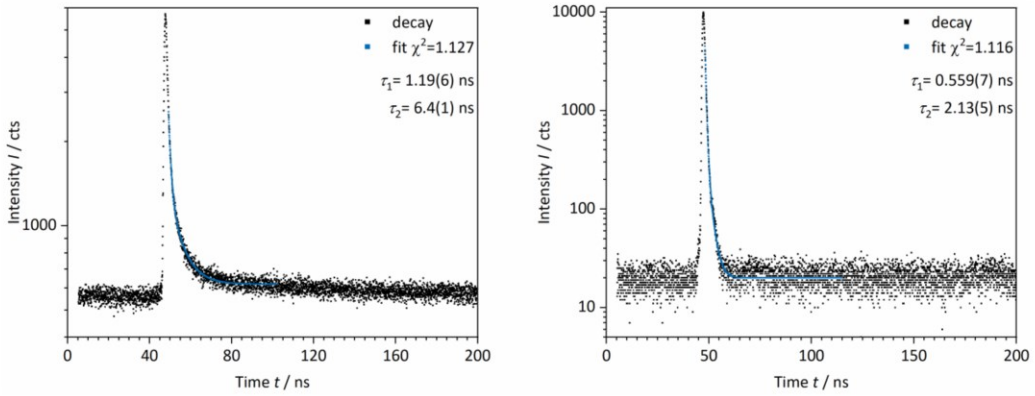

Figure SI 29 Luminescence decay measurement of MOF-253 (left, λ_{ex}=287 nm, λ_{em}=536 nm) and nMOF-253 (right, λ_{ex}=287 nm, λ_{em}=536 nm).

DUT-5:Eu^{3} and nDUT-5:Eu^{3+}

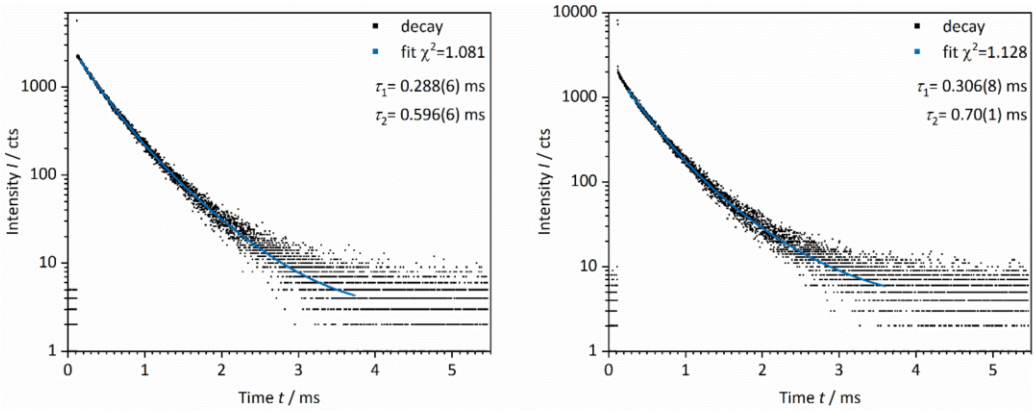

Figure SI 30 Luminescence decay measurement of DUT-5:Eu^{3+} (left, λ_{ex}=298 nm, λ_{em}=616 nm) and nDUT-5:Eu^{3+} (right, λ_{ex}=295 nm, λ_{em}=616 nm).

MOF-253:Eu^{3+} and nMOF-253:Eu^{3+}

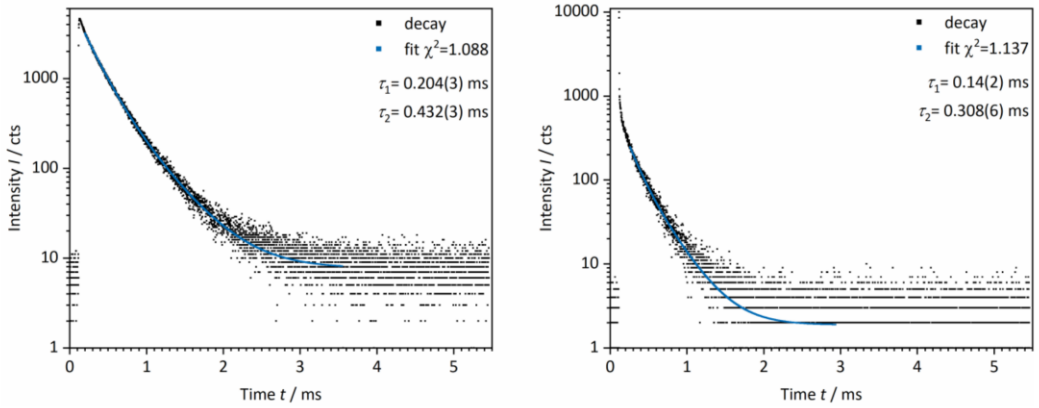

Figure SI 31 Luminescence decay measurement of MOF-253:Eu^{3+} (left, λ_{ex}=327 nm, λ_{em}=617 nm) and nMOF-253:Eu^{3+} (right, λ_{ex}=310 nm, λ_{em}=616 nm).

External Calibration of Microwave Plasma - Atomic Emission Spectroscopy Measurements

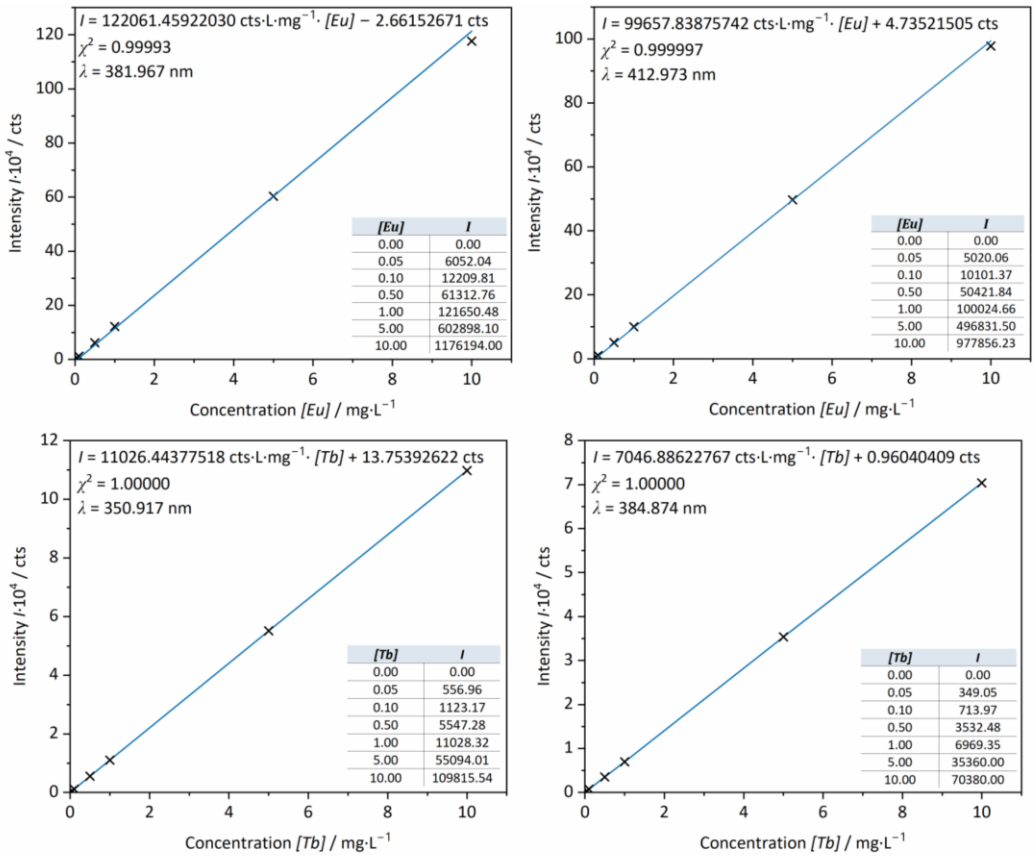

Figure SI 32 External calibration of microwave plasma - atomic emission spectrometry for characteristic Eu (top) and Tb (bottom) emission lines. The table insets show the data points marked in the graph. Fitting parameters of the blue linear fit are also given at the top of the graph.

Investigated MOFs exposed to Vis-light and UV-light

Figure SI33 is also available as video download.

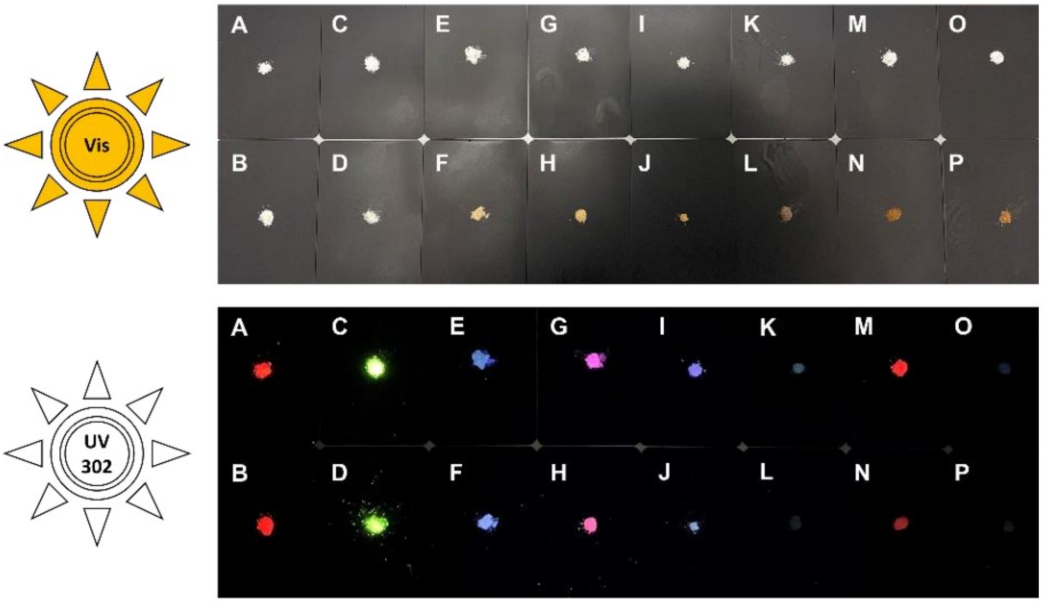

Figure SI 33 Photographs of powders of investigated bulk MOFs and nMOFs exposed to Vis-light (top) and UV-light (302 nm, bottom). A= Eu^{3+}-bdc, B= nEu^{3+}-bdc, C= Tb^{3+}-bdc, D= nTb^{3+}-bdc, E= DUT-5, F= nDUT-5, G= DUT-5:Eu^{3+}, H= nDUT-5:Eu^{3+}, I= DUT-5:Tb^{3+}, J= nDUT-5:Tb^{3+}, K= MOF-253, L= nMOF-253, M= MOF-253:Eu^{3+}, N= nMOF-253:Eu^{3+}, O= MOF-253:Tb^{3+}, P= nMOF-253:Tb^{3+}.

References

1 X. Guo, G. Zhu, F. Sun, Z. Li, X. Zhao, X. Li, H. Wang and S. Qiu, *Inorg. Chem.*, 2006, **45**, 2581–2587.

2 I. Senkovska, F. Hoffmann, M. Fröba, J. Getzschmann, W. Böhlmann and S. Kaskel, *Microporous Mesoporous Mater.*, 2009, **122**, 93–98.

3 E. D. Bloch, D. Britt, C. Lee, C. J. Doonan, F. J. Uribe-Romo, H. Furukawa, J. R. Long and O. M. Yaghi, *J. Am. Chem. Soc.*, 2010, **132**, 14382–14384.

7.2 Supporting Information – Chapter 3.2

ADVANCED FUNCTIONAL MATERIALS

– Supporting Information –

NanoMOF-based Multi-Level Anti-Counterfeiting by a Combination of Visible & Invisible Photoluminescence and Conductivity

*Moritz Maxeiner, Ruben Maile, Murat Cuvalli, Andreas Wolf, Ayisha Komal, Robert Oestreich, Christoph Janiak, Karl Mandel, Alexander Knebel, and Klaus Müller-Buschbaum**

List of Content

WILEY-VCH

Supporting Information

List of Figures

Supporting Information

List of Tables

List of Schemes

WILEY-VCH

Supporting Information

1 CHNS elemental analysis

Table S1. Results of CHNS elemental analysis of the investigated materials.

Material	C / %	H / %	N / %	S / %
Bulk Eu-bdc	37.9	3.0	4.0	-
nEu-bdc	37.2	3.3	2.5	-
Post-syn. mod. nEu-bdc	34.8	3.2	0.9	-
Bulk Tb-bdc	37.4	3.0	3.5	-
nTb-bdc	41.2	4.5	4.1	-
nYb-bdc	36.2	3.1	2.4	-
PSS	35.4	4.2	0.1	13.4
nTb-bdc@PSS	36.2	4.2	0.1	11.9
Post-syn. mod. nEu-bdc@PSS	34.0	4.1	0.1	7.6
nTbEu-bdc@PSS	34.1	4.2	0.1	11.9
nTbYb-bdc@PSS	35.0	4.1	0.2	12.1
PSUd	77.0	5.7	0.8	7.3
nTb-bdc@PSUd	72.4	5.4	0.7	6.8
nTbEu-bdc@PSUd	69.0	5.3	1.3	6.3
nTbYb-bdc@PSUd	67.1	5.1	1.0	5.8
pRF	92.6	1.8	0.4	-
nTb-bdc@pRF	77.7	3.0	2.7	-
nTbEu-bdc@pRF	70.7	3.0	2.9	-
nTbYb-bdc@pRF	75.4	3.0	2.3	-

2 Dynamic Light Scattering (DLS)

2.1 DLS result of pyrolyzed resorcinol-formaldehyde (pRF)

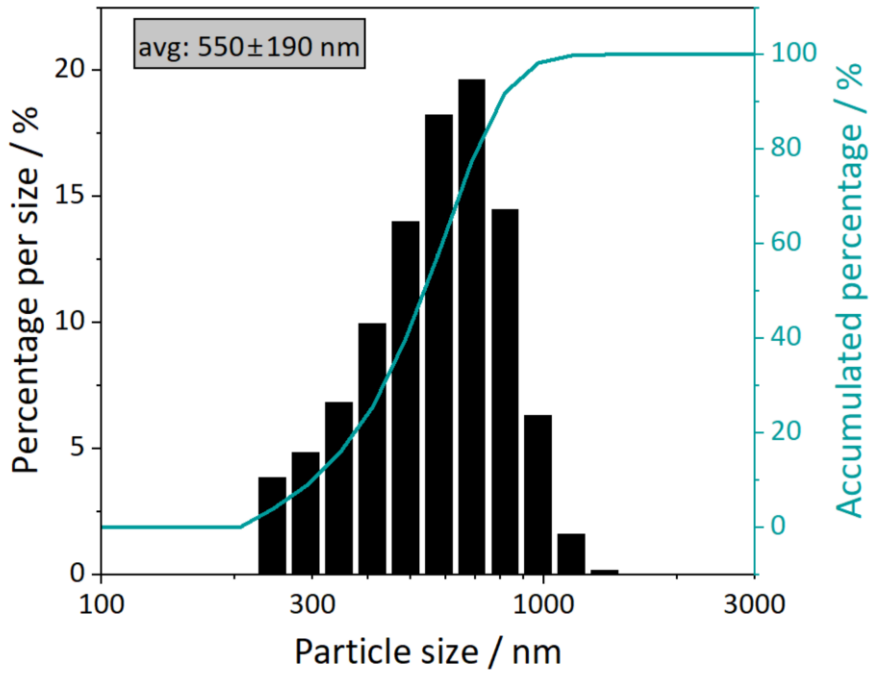

Figure S1. DLS result of pyrolyzed resorcinol-formaldehyde resin (pRF).

2.2 DLS result of post-synthetically modified water soaked nEu-bdc as $[Eu_2(bdc)_3(H_2O)_4]$

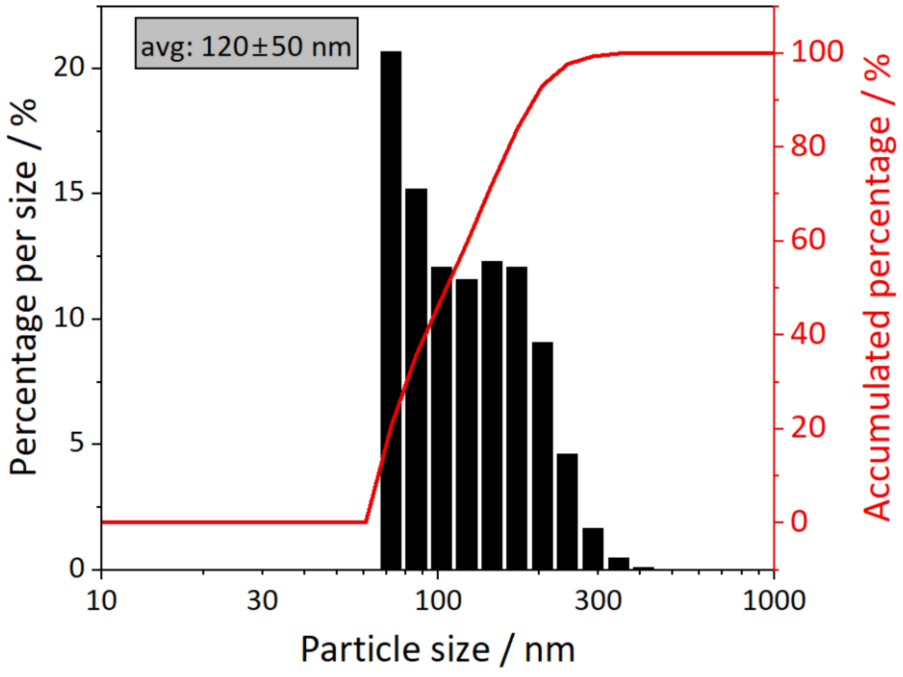

Figure S2. DLS result of post-synthetically modified water soaked nEu-bdc as $[Eu_2(bdc)_3(H_2O)_4]$.

WILEY-VCH

Supporting Information

3 Energy-dispersive X-ray Spectroscopy (EDS)

3.1 EDS results of nTb-bdc@PSS, nTb-bdc@PSUd and nTb-bdc@pRF

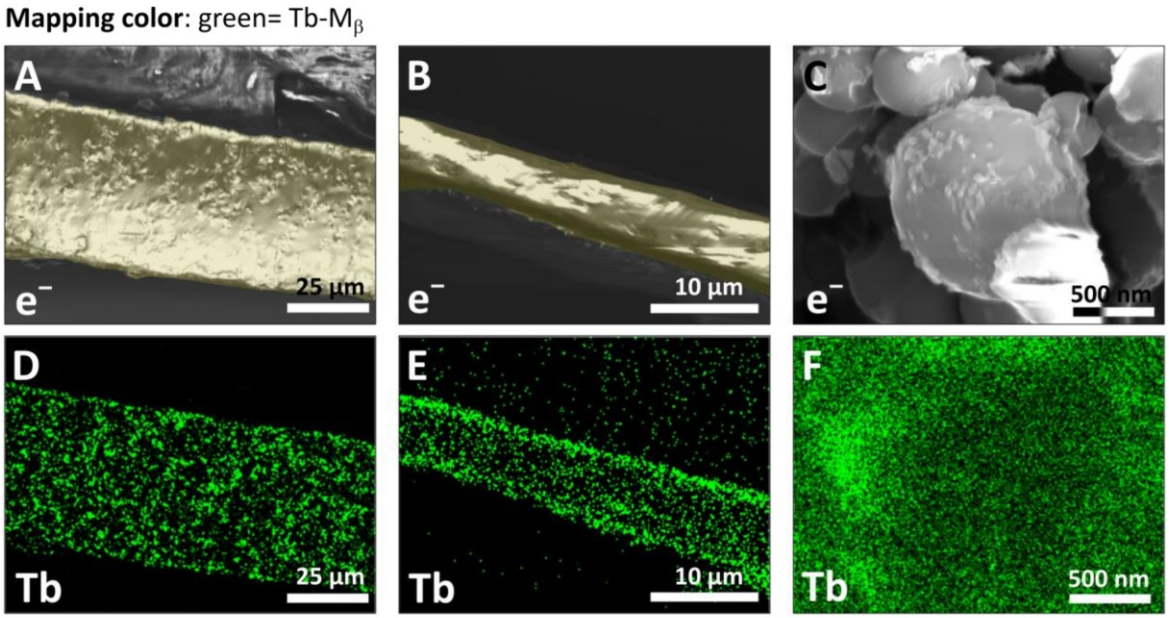

Figure S3. Scanning electron microscopy images and EDS mapping of Tb of the responder materials nTb-bdc@PSS (A, D), nTb-bdc@PSUd (B, E) and nTb-bdc@pRF (C, F). The corresponding cross-sections of the membranes are highlighted in yellow for the sake of clarity.

3.2 EDS results of nTbEu-bdc@PSS, nTbEu-bdc@PSUd and nTbEu-bdc@pRF

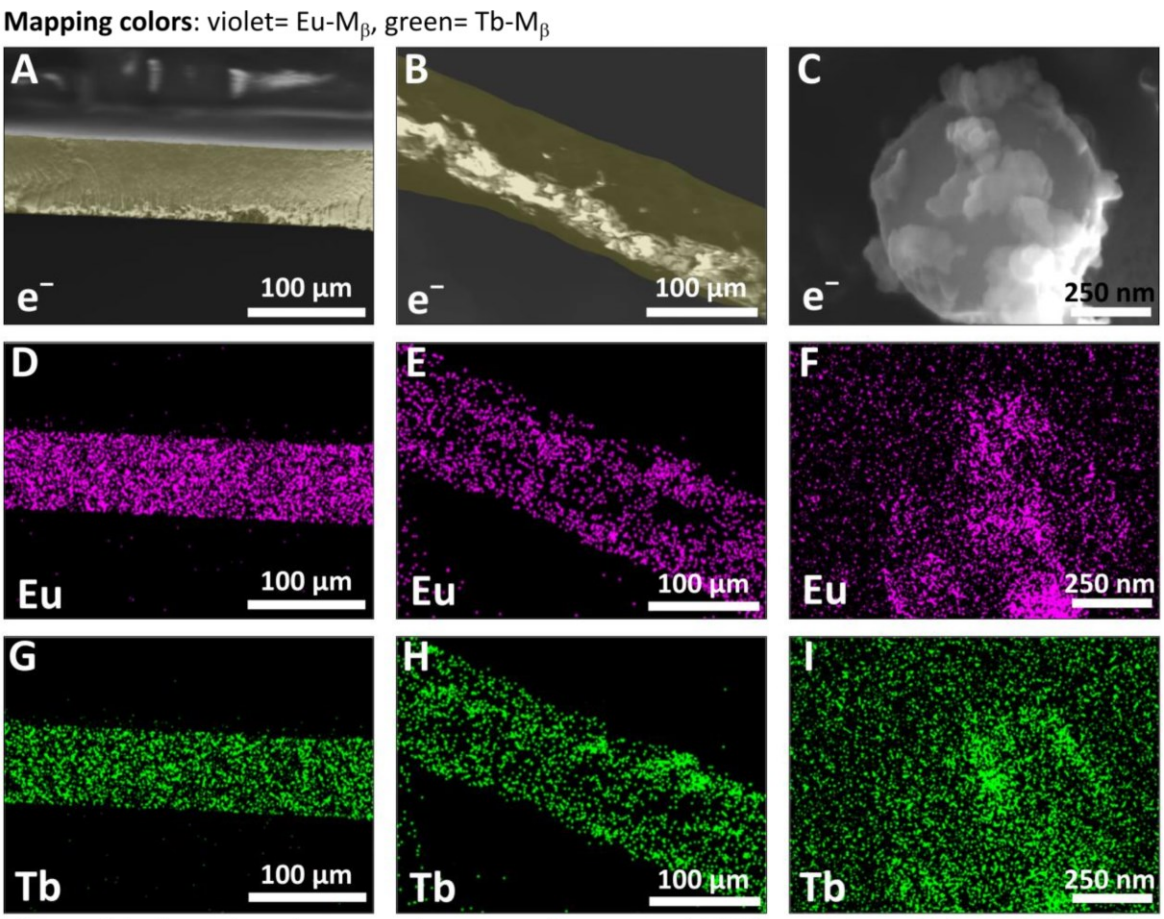

Figure S4. Scanning electron microscopy images and EDS mapping of Tb and Eu of the responder materials nTbEu-bdc@PSS (A, D, G), nTbEu-bdc@PSUd (B, E, H and nTbEu-bdc@pRF (C, F, I). The corresponding cross-sections of the membranes are highlighted in yellow for the sake of clarity.

WILEY-VCH

Supporting Information

4 Gas Adsorption Experiments

N_2 adsorption experiments were done exemplarily for bulk Ln-bdc and nLn-bdc (Ln= Eu, Tb) after activation according to the experimental section (**Figure S5** and **Figure S6**).

The N_2 sorption isotherms for nTb-bdc show Type IV behavior, with a microporous and mesoporous part in adsorption and a small H1 hysteresis. The BET surface area was calculated to be 147 $m^2 \cdot g^{-1}$ (C constant= 1927; correlation coefficient r= 0.9998), while BET calculations for bulk Tb-bdc gave a surface area of 9 $m^2 \cdot g^{-1}$ (C= 776, r= 0.9994). NLDFT calculations for nTb-bdc, using Tikhonov-regularization to fit the adsorption isotherm, show a distinct main peak of the pore size distribution around a diameter of 1 nm and smaller peaks around 2 nm to 3 nm. Peaks appearing at larger sizes, especially at 37 nm, could be caused by interparticle condensation, also fitting with the H1 hysteresis. The calculated micropore volume was 0.07 $cm^3 \cdot g^{-1}$ out of a total pore volume of 0.33 $cm^3 \cdot g^{-1}$.

For nEu-bdc a similar isotherm shape was found, but with a less microporous character and only a very small hysteresis. BET calculations gave a surface area of 57 $m^2 \cdot g^{-1}$ (C= 220, r= 0.9994), while BET calculations for bulk Eu-bdc yielded a surface area of 17 $m^2 \cdot g^{-1}$ (C= 476, r= 0.9964). NLDFT calculations for nEu-bdc, using Tikhonov-regularization to fit the adsorption isotherm, show a broad main peak centered at a diameter of 2-3 nm and smaller peaks at larger diameters. Most likely these are also caused by interparticle condensation. The calculated micropore volume was 0.008 $cm^3 \cdot g^{-1}$ out of a total pore volume of 0.38 $cm^3 \cdot g^{-1}$.

4.1 Sorption isotherms and pore diameter of nLn-bdc (Ln= Eu, Tb)

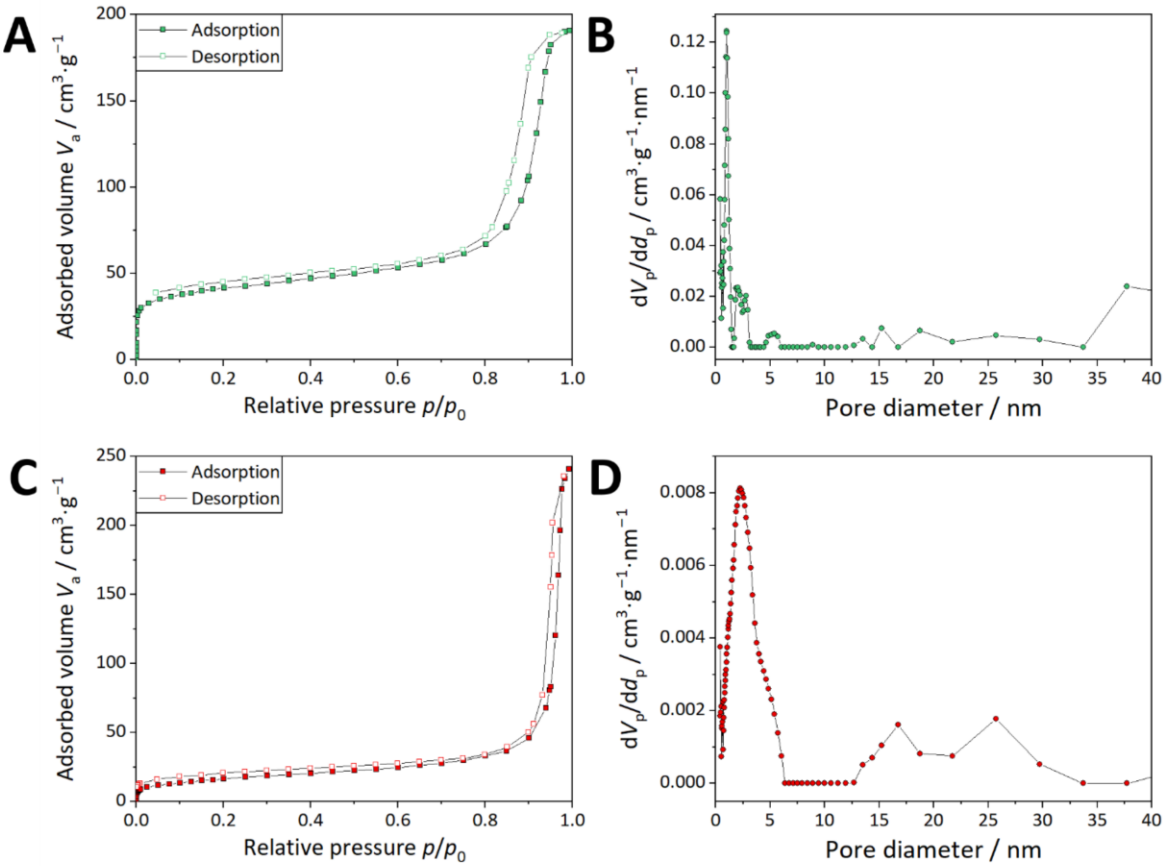

Figure S5. N_2 Sorption isotherms and pore diameters of nTb-bdc (A, B) and nEu-bdc (C, D).

Supporting Information

4.2 Sorption isotherms and pore diameter of bulk Ln-bdc (Ln= Eu, Tb)

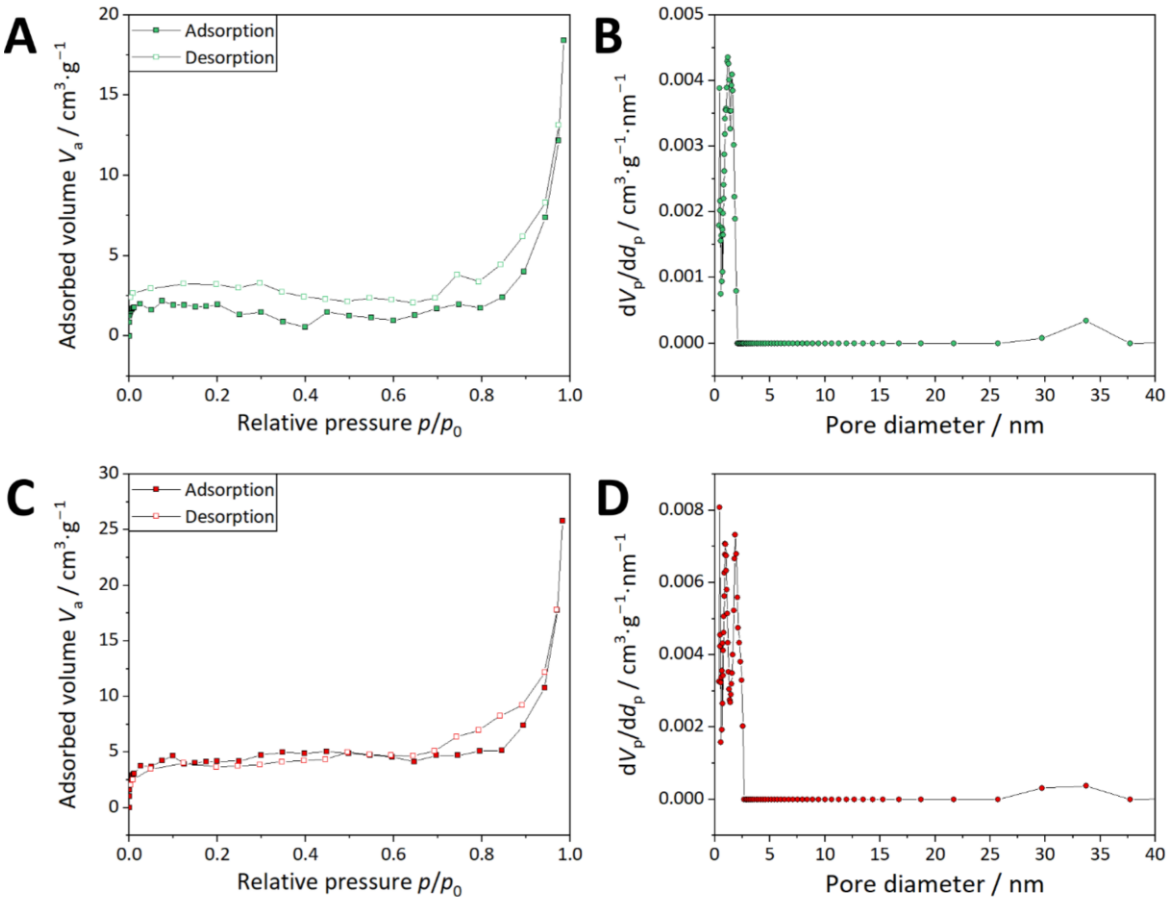

Figure S6. N_2 Sorption isotherms and pore diameters of bulk Tb-bdc (A, B) and bulk Eu-bdc (C, D). The corrugated isotherm curvatures are due to the very low adsorption capacity of the bulk MOF materials which largely correspond to the outer surface of a fine powder.

5 Photographs of Photoluminescence

5.1 Responder materials nTb-bdc@pRF, nTbEu-bdc@pRF and nTbYb-bdc@pRF

Photograph series are also available as video (**Video S1**).

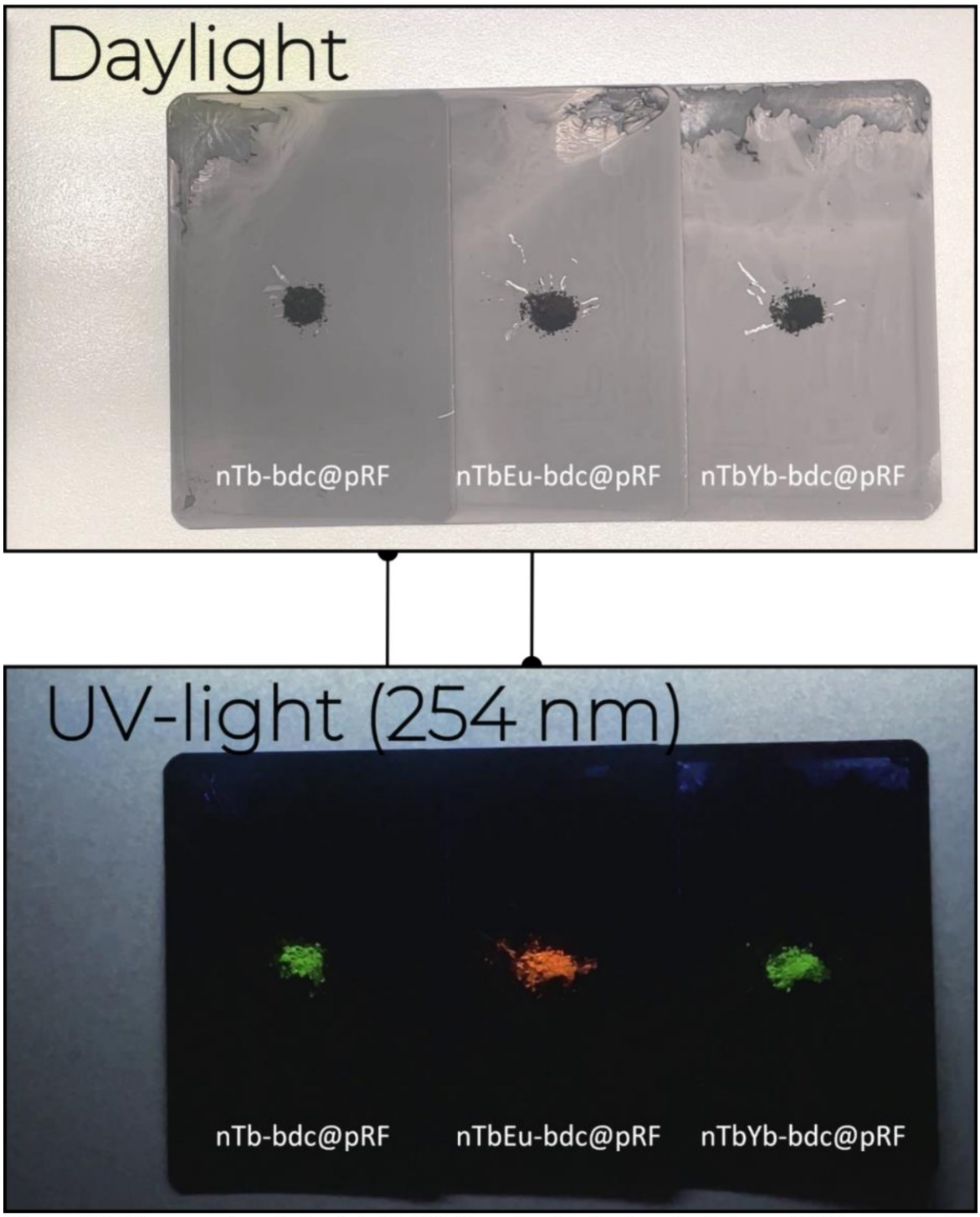

Figure S7. Photographs of nLn-bdc@pRF (Ln= Eu, Tb, Yb) at daylight and 254 nm and also available as Video S1.

Supporting Information

6 Photoluminescence Spectroscopy

6.1 Excitation and emission spectra of nLn-bdc@PSS, nLn-bdc@PSUd and nLn-bdc@pRF (Ln= Eu, Tb, Yb) with λ_{ex} = 330 nm

Fluorescence microscopy is primarily used in biological studies, for instance, the analysis of green-fluorescence-protein (GFP) marked tissues,[3] therefore, method limitations exist for the investigation of lanthanides such as the small stokes-shift in biological samples compared to the distinct shift of excitation and emission processes of lanthanides. Despite the limitations originating from sample properties, the optical components of the microscope do not allow wavelengths <330 nm to transmit, hence, materials can be excited only at 330 nm and above (**Figure S8**).

In **Figure 5** (see Article), FM photographs exhibit a yellowish background at white light, which does not derive from the materials investigated but from the light source. In contrast, photographs taken with a mercury vapor arc lamp and a UV broadband filter cube (330-380 nm) show a blueish background. In the case of nLn-bdc@PSS and nLn-bdc@PSUd, a ligand-based emission is observable at 350-450 nm contributing to the blue color at λ_{ex}= 330 nm.

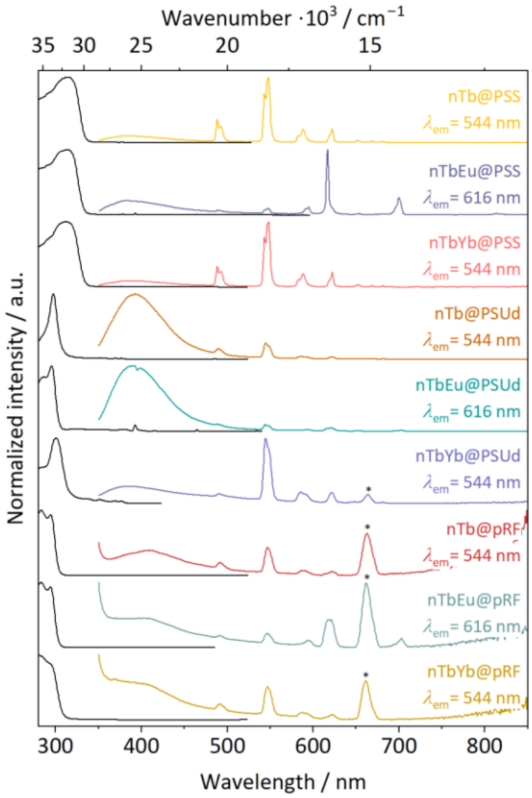

Figure S8. Photoluminescence excitation and emission spectra of nLn-bdc@PSS, nLn-bdc@PSUd and nLn-bdc@pRF (Ln= Eu, Tb, Yb) with λ_{ex} = 330 nm to check the suitability for FM photograph recording. For FM does not allow the observation of emission processes beyond the visible electromagnetic spectrum, no emission spectra >800 nm were recorded. Signals marked with an asterisk are artifacts of the measurement and do not belong to the emission spectra. They originate from lighting source and are located at 660 nm making double of the excitation wavelength of λ_{ex}= 330 nm not cut off by an edge filter due to the low overall emission intensity of nLn-bdc@pRF at λ_{ex}= 330 nm.

Supporting Information

WILEY-VCH

6.2 CIE diagram of investigated materials

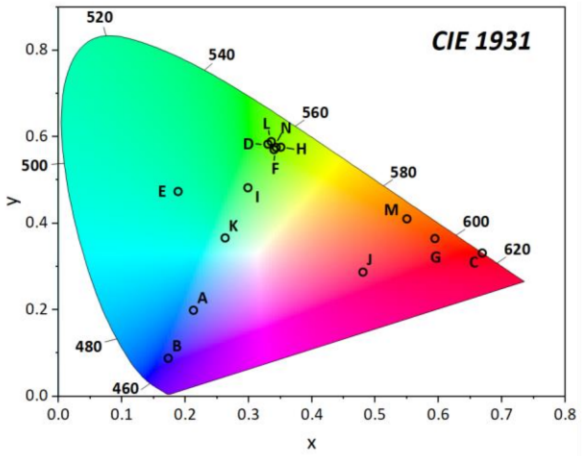

A	PSS	**H**	nTbYb-bdc@PSS
B	PSUd	**I**	nTb-bdc@PSUd
C	nEu-bdc	**J**	nTbEu-bdc@PSUd
D	nTb-bdc	**K**	nTbYb-bdc@PSUd
E	nYb-bdc	**L**	nTb-bdc@pRF
F	nTb-bdc@PSS	**M**	nTbEu-bdc@pRF
G	nTbEu-bdc@PSS	**N**	nTbYb-bdc@pRF

Figure S9. CIE diagram of investigated materials calculated from PL data. The pRF is an all-visible light absorbing material, which is why it is not shown in this diagram.

6.3 Sensitization mechanism of lanthanide photoluminescence

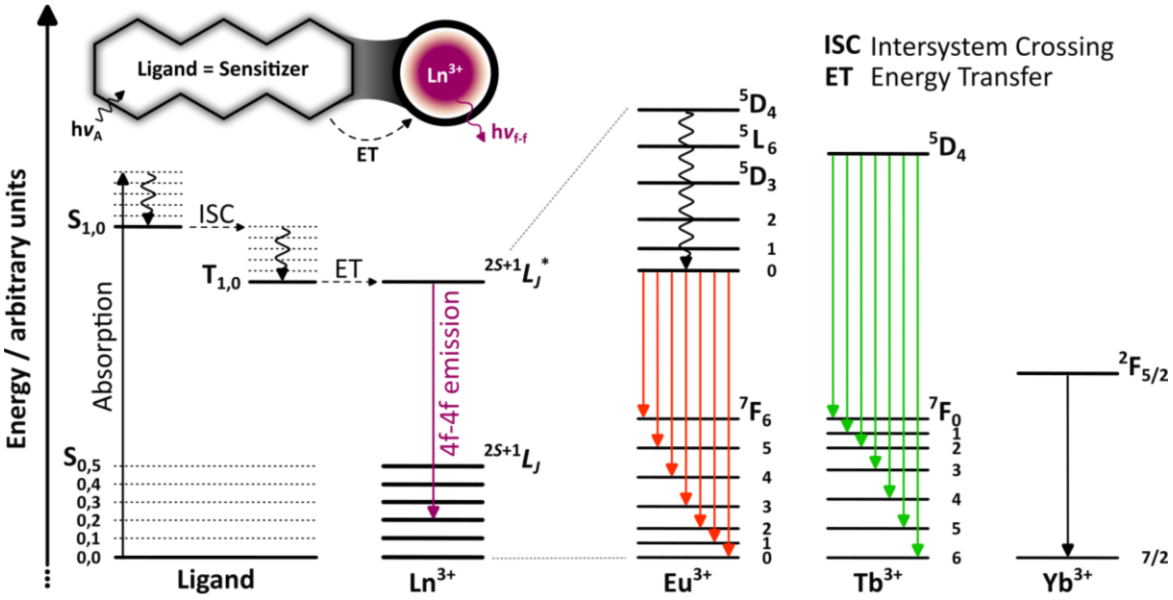

Scheme S1. A Jablonski diagram is visualizing the mechanism underlying the sensitization process of Ln^{3+}, which results in the characteristic emission colors observed. In this example, the emission colors correspond to Eu^{3+} (red), Tb^{3+} (green), and Yb^{3+} (black: NIR emission). The diagram exclusively depicts relevant processes to enhance clarity, while excluding emission processes of the linker, weak direct 4f-4f excitations, and non-relevant non-radiative processes. The singlet states ($S_{e,v}$) and triplet states ($T_{e,v}$) of the linker are defined as the state of an electron level (e) and a vibrational level (v), while the 4f-4f energy states are defined by means of the term symbol $^{2S+1}L_J$ (with the total quantum numbers for spin (S), orbital (L), and angular (J) momenta). The simplified schematic inset illustrates the sensitization process, which initiates with the absorption of UV-light ($h\nu_A$) and culminates in the 4f-4f emission ($h\nu_{f\text{-}f}$).

Supporting Information

7 Potentiostatic Electrochemical Impedance Spectroscopy (PEIS)

7.1 Impedance spectra of nLn-bdc (Ln= Eu, Tb, Yb), PSS, PSUd and pRF

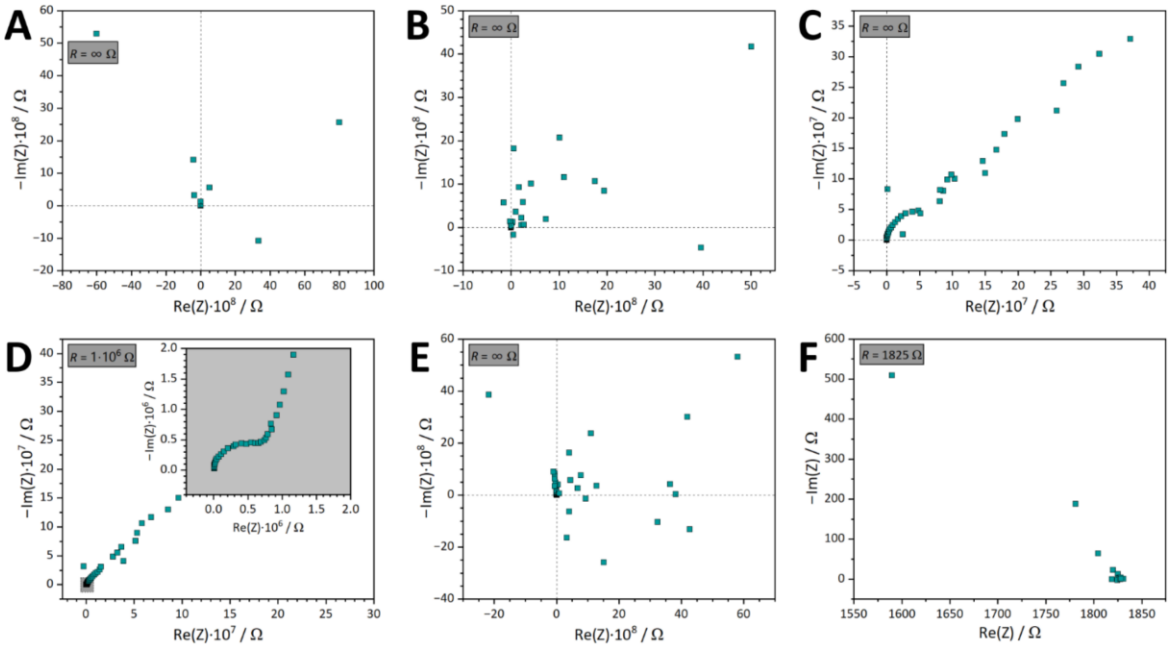

Figure S10. PEIS spectra of the nEu-bdc (A), nTb-bdc (B) and nYb-bdc (C) as well as the matrices PSS (D), PSUd (E) and pRF (F).

WILEY-VCH

Supporting Information

7.2 Impedance spectra of responder materials

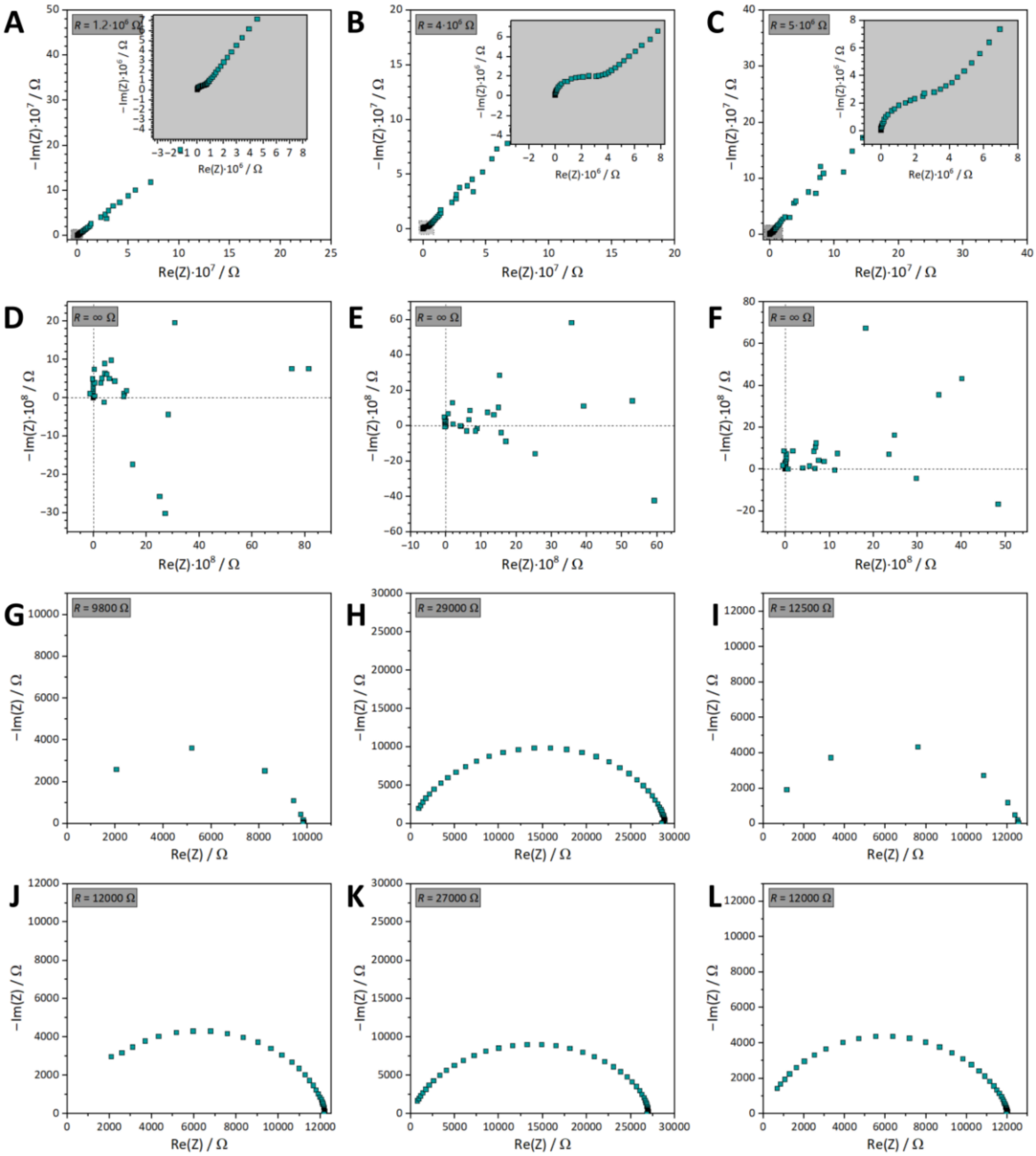

Figure S11. PEIS spectra of the responder materials nTb-bdc@PSS (A), nTb-bdc@PSUd (D), nTb-bdc@pRF (G), aged nTb-bdc@pRF (J), nTbEu-bdc@PSS (B), nTbEu-bdc@PSUd (E), nTbEu-bdc@pRF (H), aged nTbEu-bdc@pRF (K), nTbYb-bdc@PSS (C), nTbYb-bdc@PSUd (F), nTbYb-bdc@pRF (I) and aged nTbYb-bdc@pRF (L). Inserts in the gray boxes show relevant sections of the measurements for the determination of the resistance *R* listed in Table 2 (see Article).

8 Powder X-Ray Diffractometry (PXRD)

8.1 Characterization of nLn-bdc (Ln= Eu, Tb, Yb)

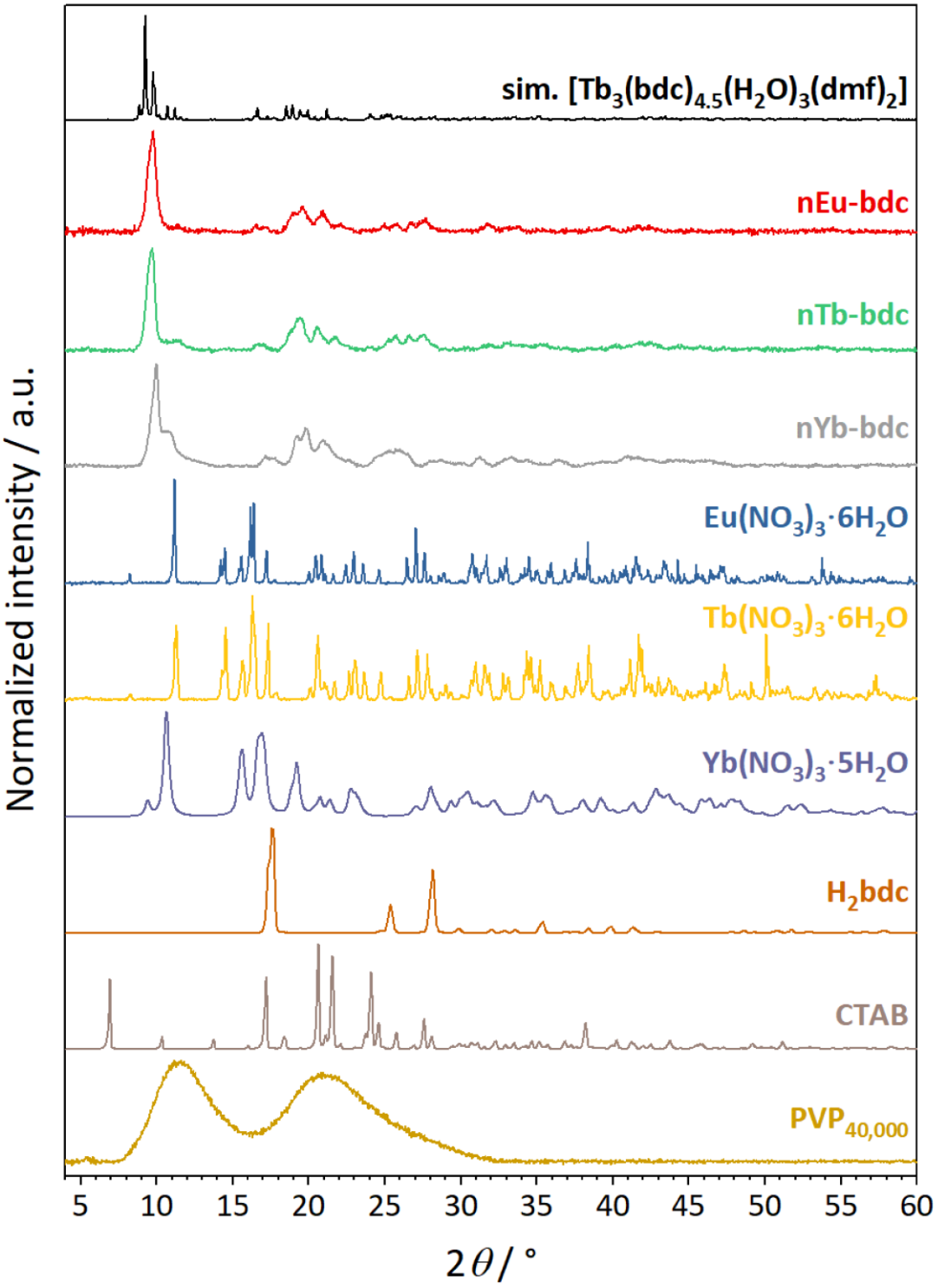

Figure S12. Powder X-ray diffractograms of the reagents $Ln(NO_3)_3{\cdot}6H_2O$ (Ln= Eu, Tb), $Yb(NO_3)_3{\cdot}5H_2O$ and H_2bdc, the surfactants $PVP_{40,000}$ and CTAB as well as nLn-bdc (Ln= Eu, Tb, Yb), and a simulated diffractogram based on the single-crystal data of $[Tb_3(bdc)_{4.5}(H_2O)_3(dmf)_2]$.[1]

8.2 Characterization of the phase $[Eu_2(bdc)_3(H_2O)_4]$

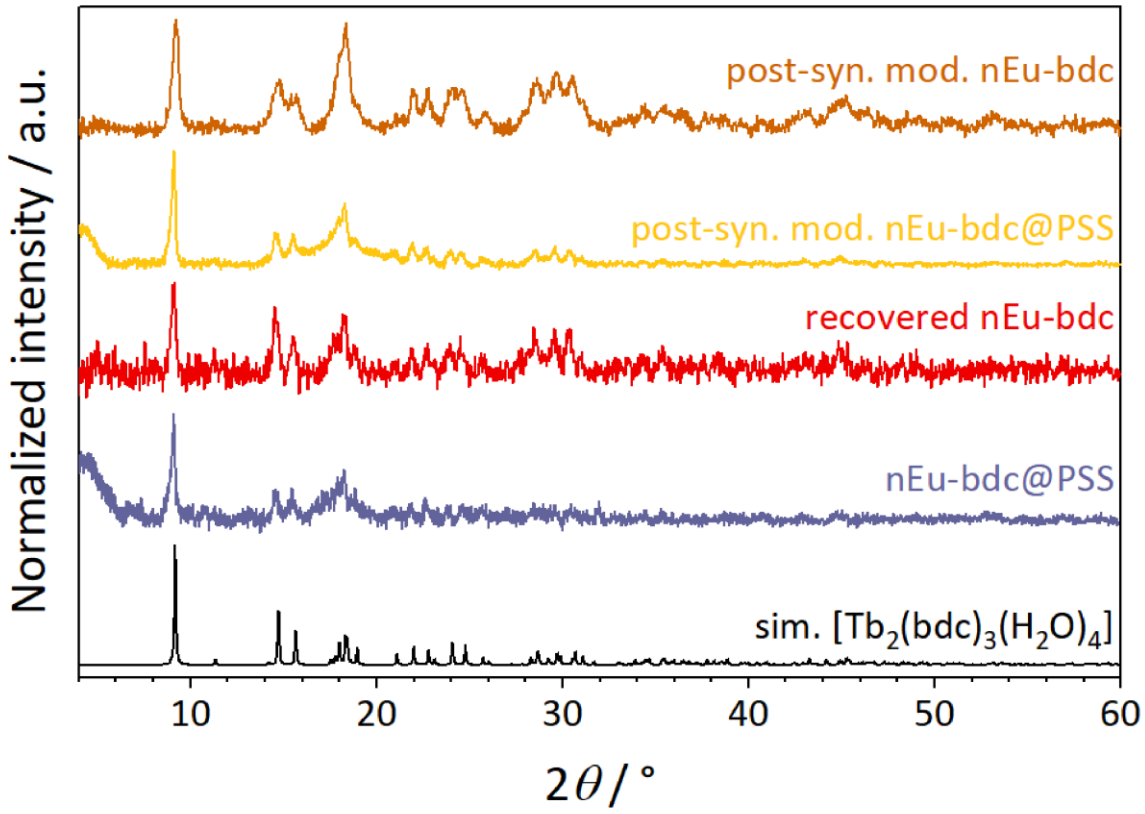

Figure S13. Powder X-ray diffractograms of the post-synthetically modified nEu-bdc after soaked in H_2O, the recovered nEu-bdc from nEu-bdc@PSS, the nEu-bdc@PSS synthesized with the post-synthetically modified nEu-bdc, the nEu-bdc@PSS synthesized with as syn. nEu-bdc and the simulated diffractogram based on the single crystal data of $[Tb_2(bdc)_3(H_2O)_4]$.[2]

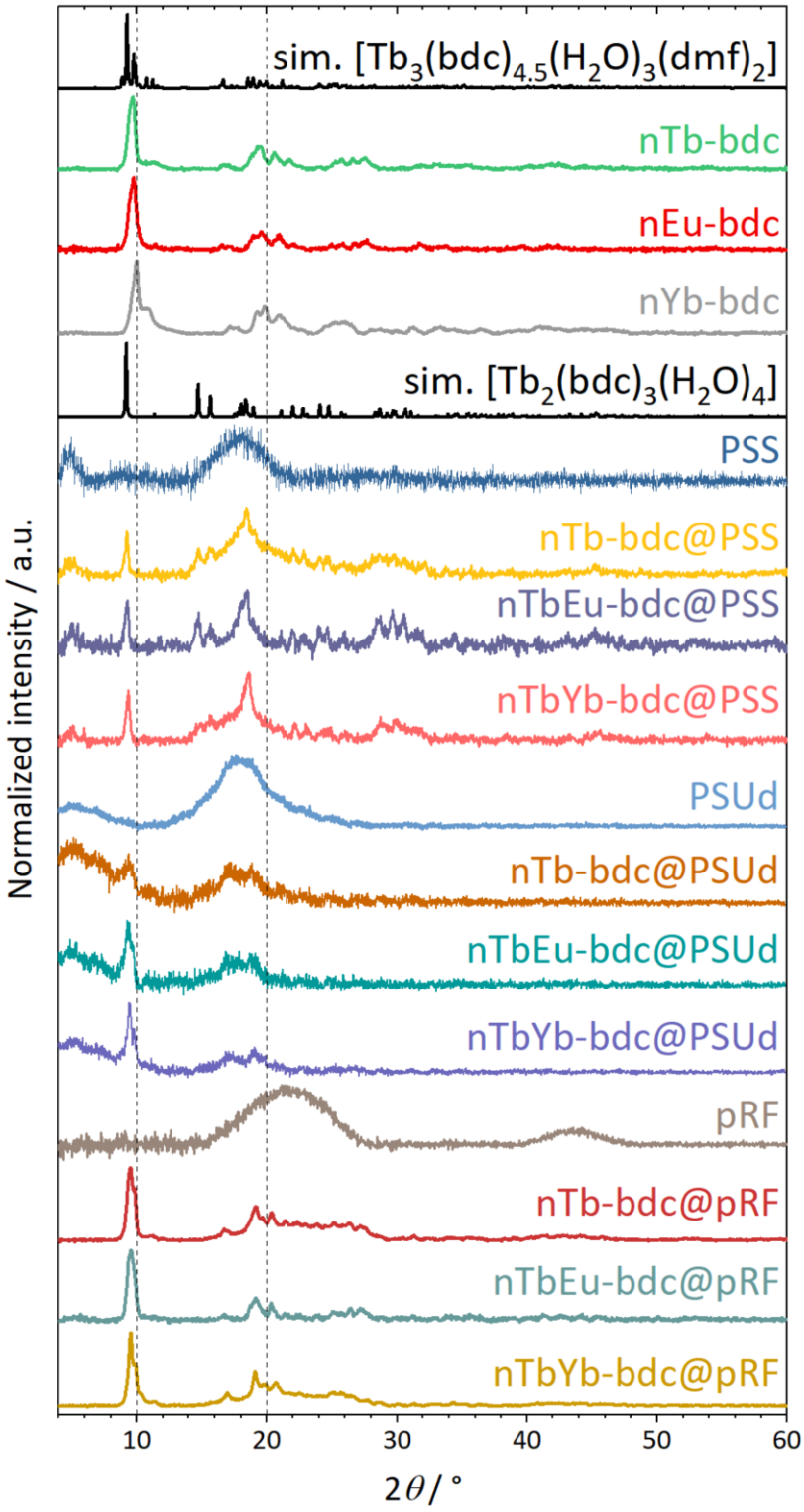

Figure S14. Comparison of simulated powder X-ray diffractograms based on single-crystal data of $[Tb_3(bdc)_{4.5}(H_2O)_3(dmf)_2]$[50] and $[Tb_2(bdc)_3(H_2O)_4]$,[51] and experimental powder diffractograms of the nanoMOFs nLn-bdc (with Ln= Eu, Tb, Yb), of the responder materials nLn-bdc@PSS, nLn-bdc@PSUd and nLn-bdc@pRF, as well as of the matrices pRF, PSS and PSUd. Dotted reference lines are set at $2\theta = 10°$ and $2\theta = 20°$ for clarity.

Supporting Information

WILEY-VCH

9 Procedure as Overview

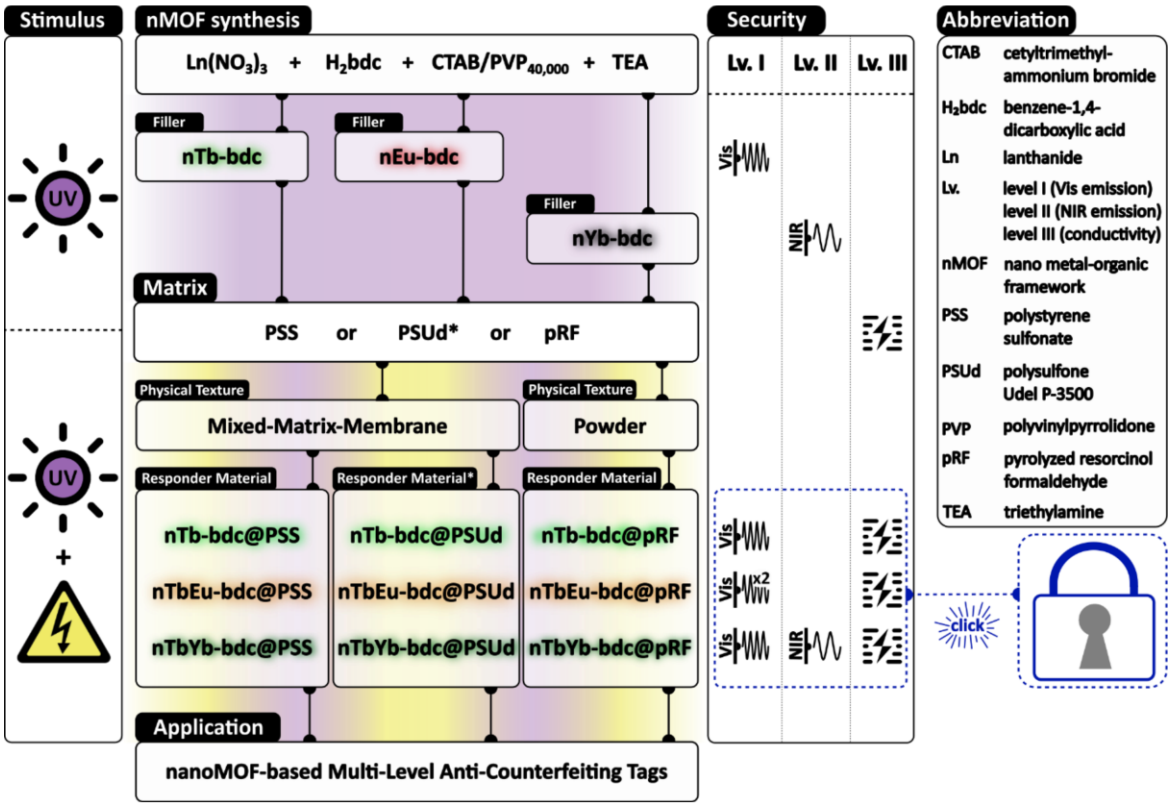

Scheme S2. Overview of the additive compositions and functions of external stimuli, nMOFs and matrices used for the development of nanoMOF-based multi-level anti-counterfeiting tags. Since PSUd is a representative for a non-conductive matrix, pure PSUd as well as responder materials made with PSUd are marked with an asterisk. The used colors do not represent the exact color impressions seen by the eye but were chosen to depict the effect of mixing nEu-bdc and nTb-bdc. Moreover, nYb-bdc does not influence the emitted Vis-light, yet is depicted as black for clarity.

10 Raman Spectroscopy

10.1 Characterization of pyrolyzed resorcinol-formaldehyde (pRF)

The spectrum exhibits two broad bands centered approximately at 1350 cm^{-1} (D band) and 1590 cm^{-1} (G band), which are characteristic for graphitic carbon (**Figure S15**). The intensity ratio of these two bands (I_D/I_G) is commonly used to evaluate the degree of graphitization, whereby high values correspond to high degrees of graphitization.[4] The rather low degree of graphitization of the herein used pRF (I_D/I_G = 0.80) can be attributed to the mild pyrolysis conditions (2 h, 600 °C). These conditions represent a compromise to obtain sufficient conductivity, but also to keep some functional groups intact, that enable further processing of the pRF spheres, i.e., redispersion in solvents.

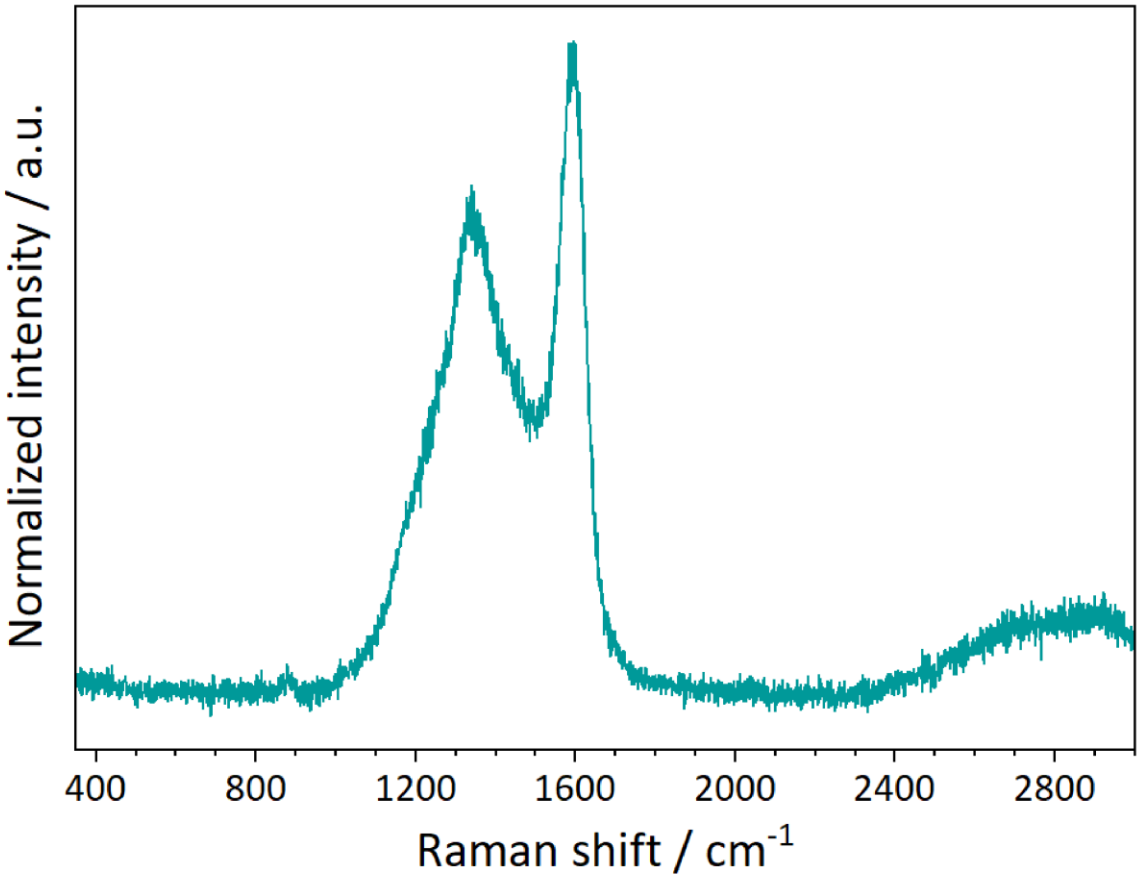

Figure S15. Raman spectrum recorded of the substrate RF after pyrolysis yielding pRF.

11 Scanning Electron Microscopy (SEM)

11.1 Electron microscopy images of polystyrene sulfonate (PSS), polysulfone Udel® P-3500 (PSUd) and pyrolyzed resorcinol-formaldehyde (pRF) in comparison

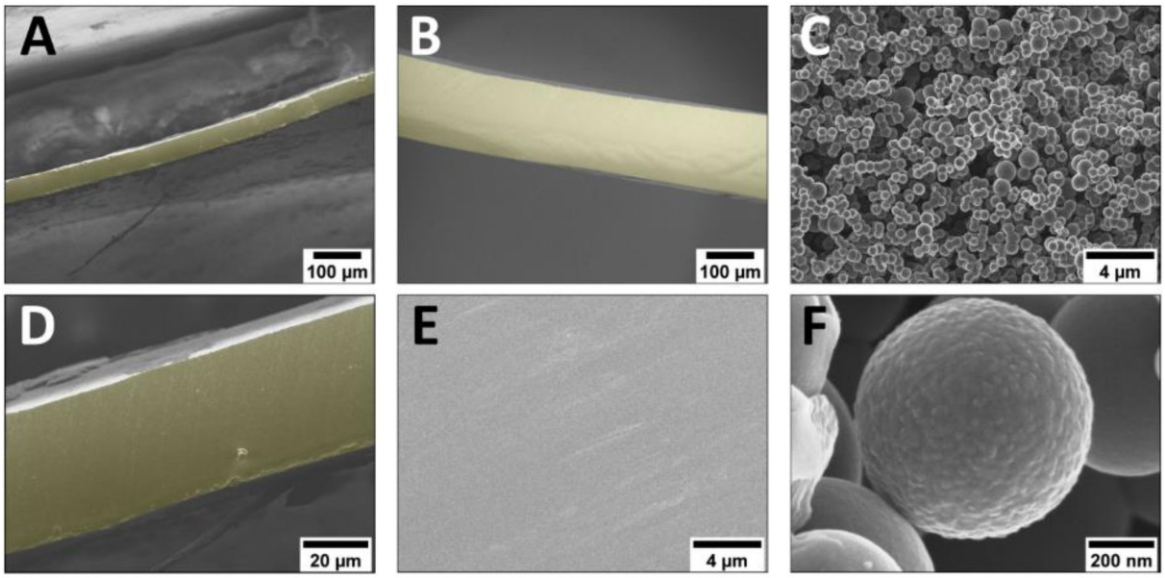

Figure S16. SEM images of the neat polymer matrices PSS, PSUd and pRF as overview (A, B, C) and detailed view (D, E, F). The corresponding cross-sections of the membranes are highlighted in yellow for the sake of clarity.

11.2 Electron microscopy images of polystyrene sulfonate (PSS)

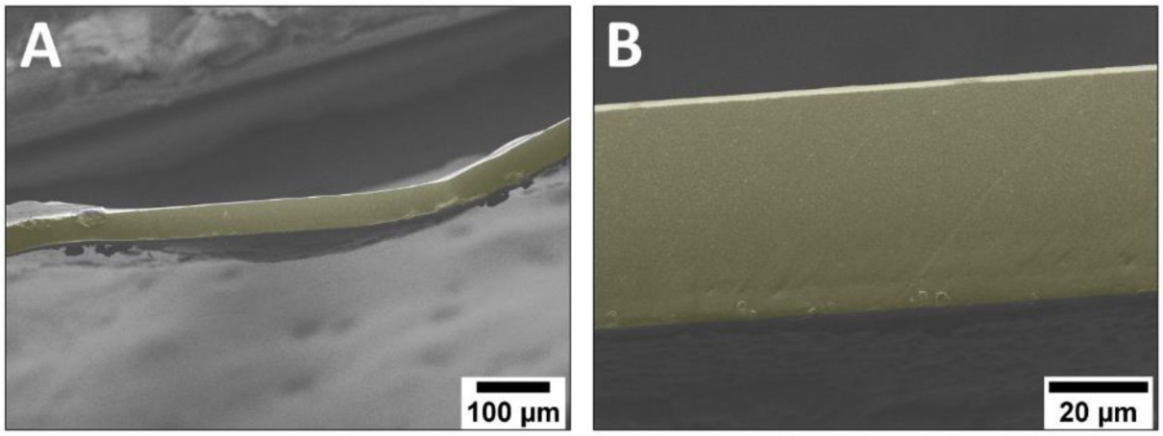

Figure S17. SEM images of the cross-section of PSS as overview (A) and detailed view (B). The corresponding cross-section of the membrane is highlighted in yellow for the sake of clarity.

11.3 Electron microscopy images of polysulfone Udel® P-3500 (PSUd)

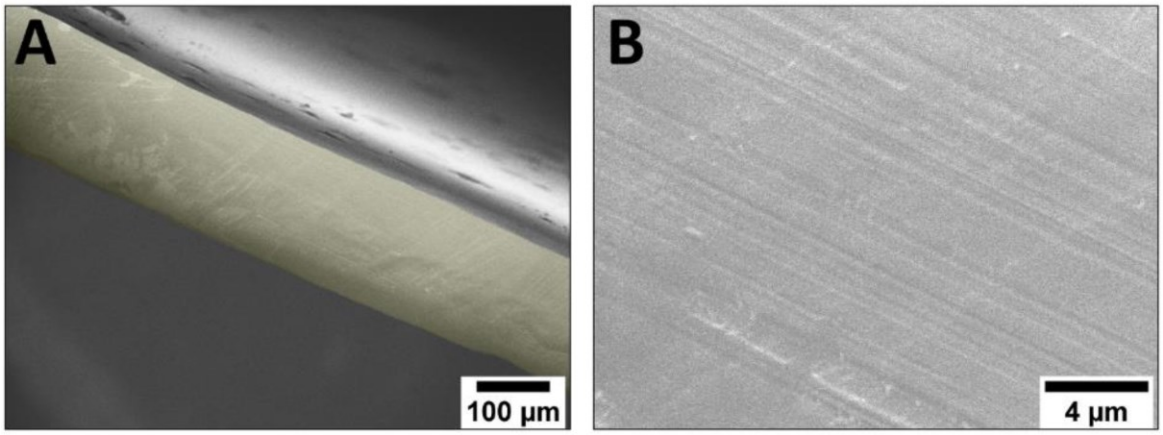

Figure S18. SEM images of the cross-section of PSUd as overview (A) and detailed view (B). The corresponding cross-section of the membrane is highlighted in yellow for the sake of clarity.

11.4 Electron microscopy images of pyrolyzed resorcinol-formaldehyde (pRF)

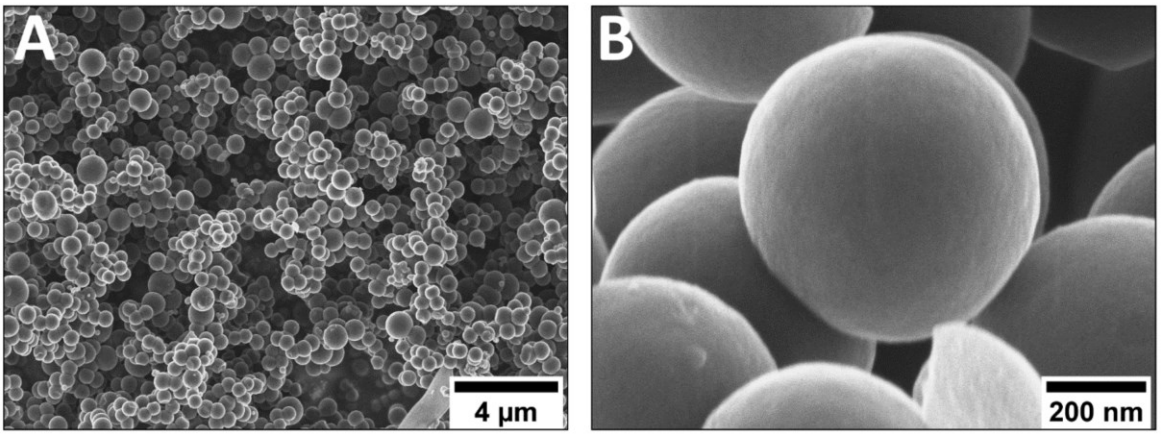

Figure S19. SEM images of pRF spheres as overview (A) and detailed view (B).

11.5 Electron microscopy images of nLn-bdc@PSS, nLn-bdc@PSUd and nLn-bdc@pRF (Ln= Eu, Tb, Yb)

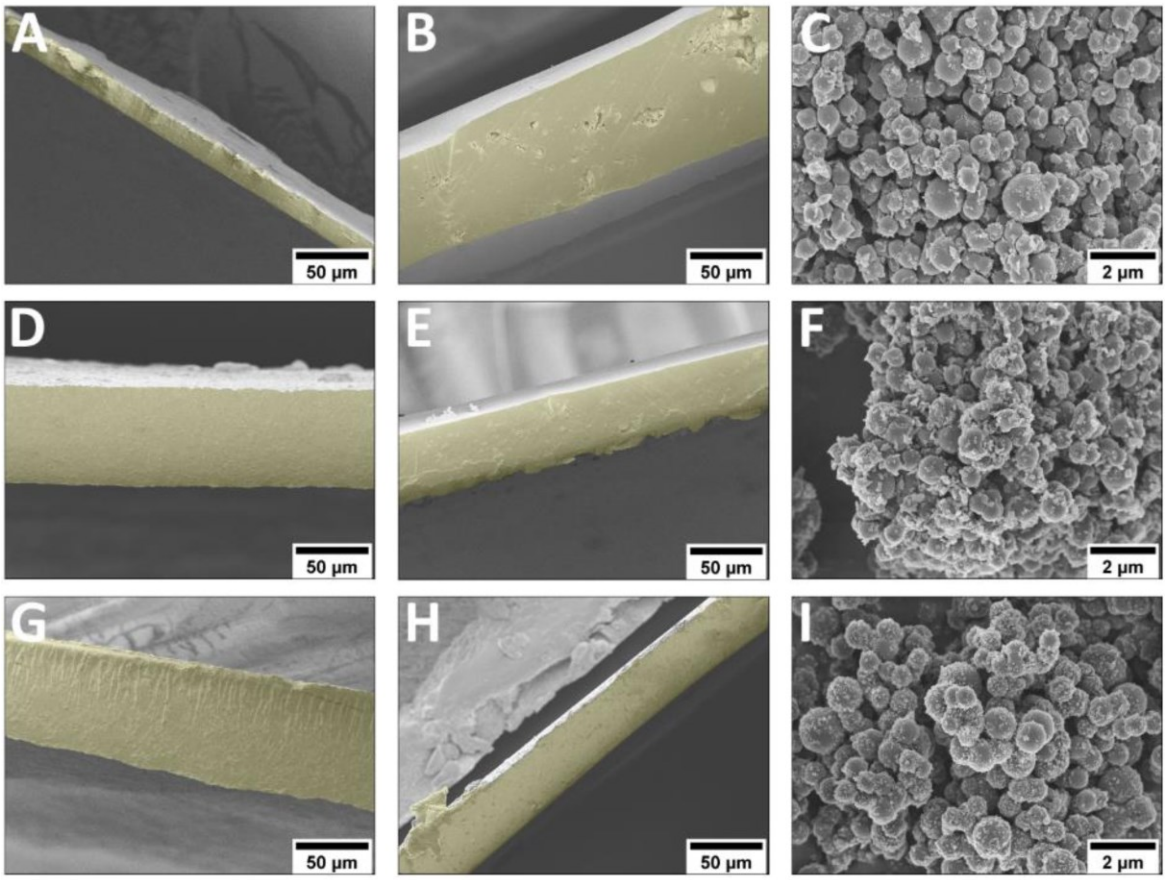

Figure S20. SEM images of responder materials in overview. The corresponding cross-sections of the membranes are highlighted in yellow for the sake of clarity. nTb-bdc@PSS (A), nTb-bdc@PSUd (B), nTb-bdc@pRF (C), nTbEu-bdc@PSS (D), nTbEu-bdc@PSUd (E), nTbEu-bdc@pRF (F), nTbYb-bdc@PSS (G), nTbYb-bdc@PSUd (H) and nTbYb-bdc@pRF (I).

11.6 SEM image of post-synthetically modified water-soaked nEu-bdc as $[Eu_2(bdc)_3(H_2O)_4]$

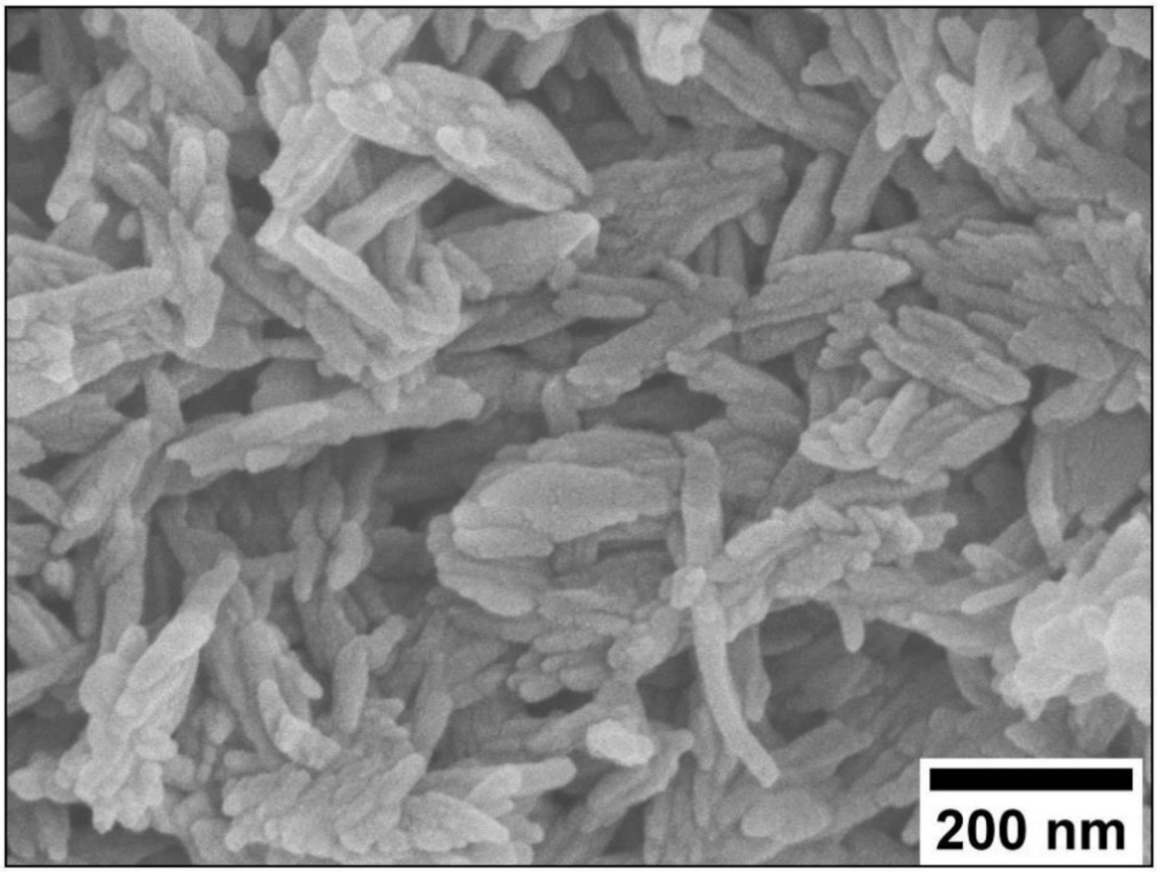

Figure S21. SEM image of post-synthetically modified water-soaked nEu-bdc as $[Eu_2(bdc)_3(H_2O)_4]$ as detailed view.

12 References

[1] X. Guo, G. Zhu, F. Sun, Z. Li, X. Zhao, X. Li, H. Wang, S. Qiu, *Inorg. Chem.* **2006**, *45*, 2581.

[2] T. M. Reineke, M. Eddaoudi, M. Fehr, D. Kelley, O. M. Yaghi, *J. Am. Chem. Soc.* **1999**, *121*, 1651.

[3] P.-W. Seo, G.-J. Kim, J.-S. Kim, *Appl. Microbiol. Biotechnol.* **2024**, *108*, 208.

[4] X. Zhao, M. Zhang, X. Sun, X. Li, J. Li, *Appl. Surf. Sci.* **2020**, *506*, 144591.

7.3 Supporting Information – Chapter 3.3

ADVANCED FUNCTIONAL MATERIALS

– Supporting Information –

Biodegradable and Recyclable Luminescent Mixed-Matrix-Membranes, Hydrogels, and Cryogels based on Nanoscale Metal-Organic Frameworks and Biopolymers

*Moritz Maxeiner, Julian Burkhart, Kateryna Borysova, Chiara Mazzariol and Klaus Müller-Buschbaum**

Content

WILEY-VCH

Supporting Information

List of Figures

Supporting Information

List of Tables

List of Schemes

WILEY-VCH

Supporting Information

1 Asymmetry ratio of Eu^{3+} luminescence in nEu-bdc@biopolymer

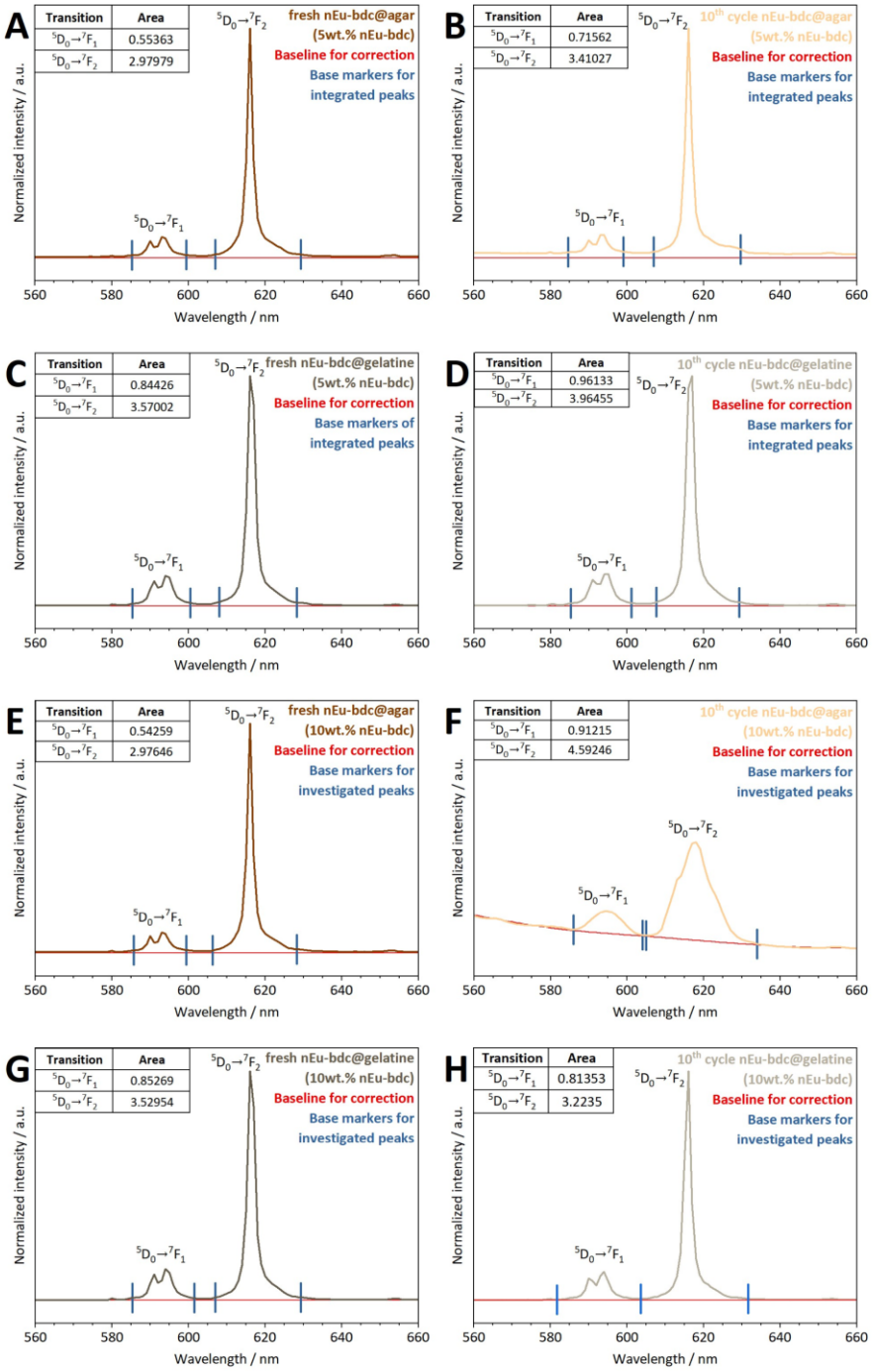

Figure S1. Spectra of the integrated peaks used for the calculation of the asymmetry ratios. Bio-nMOF-MMMs containing 5wt.% nEu-bdc: (A) fresh nEu-bdc@agar, (B) 10th cycle nEu-bdc@agar, (C) fresh nEu-bdc@gelatine and (D) 10th cycle nEu-bdc@gelatine. Bio-nMOF-MMMs containing 10wt.% nEu-bdc: (E) fresh nEu-bdc@agar, (F) 10th cycle nEu-bdc@agar, (G) fresh nEu-bdc@gelatine and (H) 10th cycle nEu-bdc@gelatine. Table inserts showing the f-f transitions of Eu with the corresponding integrated areas used for calculation.

WILEY-VCH

Supporting Information

2 Mass-Luminescence Correlation

Table S1. Experimental results of the mass loss determination and the loss of intensity of luminescence of nEu-bdc@biopolymer (with 5wt.% nEu-bdc) for the analysis of the mass-luminescence correlation. The luminescence intensity was determined at the intense transition $^5D_0 \rightarrow {}^7F_2$ at 616 nm of Eu^{3+}.

	nEu-bdc@agar	**nEu-bdc@gelatine**
m(fresh)	124.3 mg	98.3 mg
m(10th cycle)	43.6 mg	54.1 mg
Δm_{abs}(fresh−10th cycle)	80.7 mg	44.2 mg
Δm_{rel}(fresh−10th cycle)	**65 %**	**45 %**
I_{616}(fresh)	974582 cps	945485 cps
I_{616}(10th cycle)	88784 cps	802409 cps
$\Delta I_{616,abs}$(fresh−10th cycle)	885798 cps	143076 cps
$\Delta I_{616,rel}$(fresh−10th cycle)	**≈90 %**	**≈20 %**
$R_{MMM} = \Delta I_{616,abs}/\Delta m_{abs}$	**≈11000 cps·mg^{-1}** **≈1100 cps·mg^{-1}·cycle^{-1}** **≈0.1 %·mg^{-1}·cycle^{-1}**	**≈3000 cps·mg^{-1}** **≈300 cps·mg^{-1}·cycle^{-1}** **≈0.04 %·mg^{-1}·cycle^{-1}**

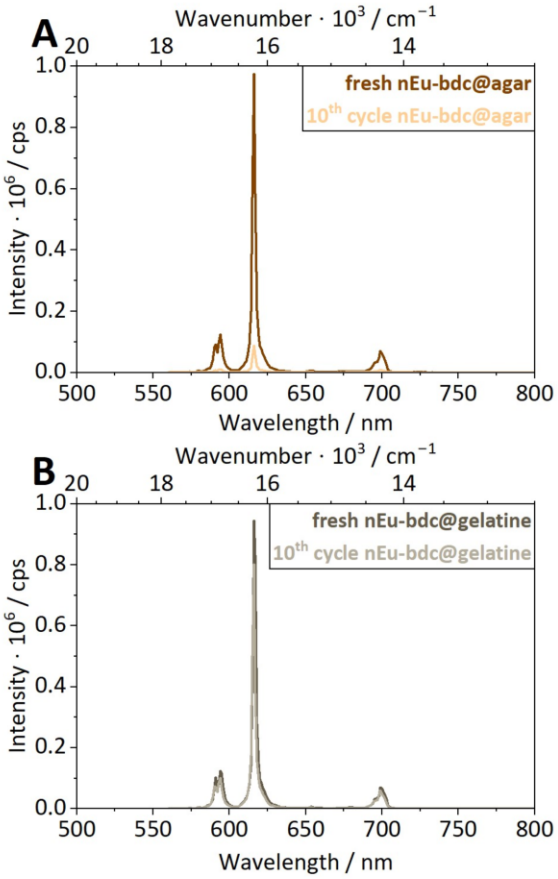

Figure S2. Emission spectra (λ_{ex}= 313 nm) of (A) fresh nEu-bdc@agar and ten times recycled nEu-bdc@agar as well as (B) fresh nEu-bdc@gelatine and ten times recycled nEu-bdc@gelatine each with 5wt.% nEu-bdc.

Supporting Information

3 Structures of the surfactants PVP and CTAB

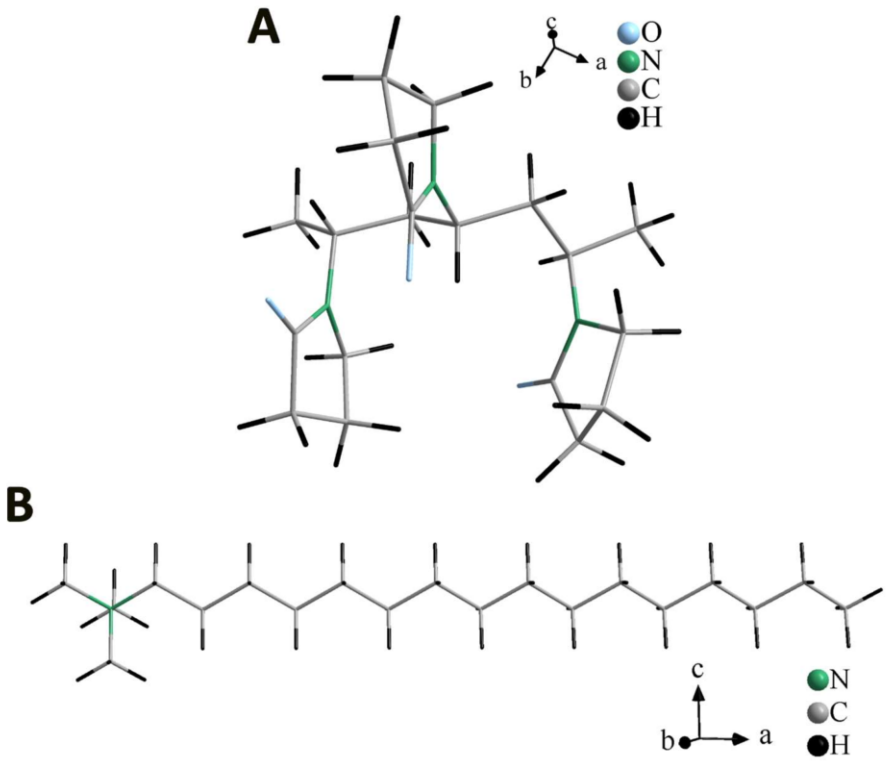

Scheme S1. Polymer structure of (A) polyvinyl pyrrolidone (PVP) and molecular structure of (B) cetyltrimethylammonium bromide (CTAB). The molecular unit of PVP is shown three times to indicate the chain route. The counterion bromide of CTAB is not shown for the sake of clarity.

Supporting Information

4 Stepwise recycled nEu-bdc@agar and nEu-bdc@gelatine (5wt.% nEu-bdc) - Photographs

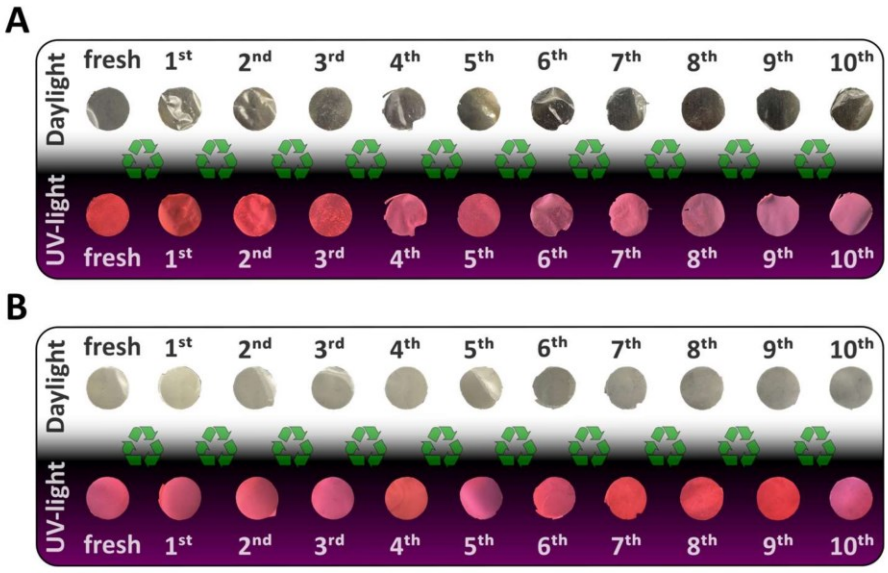

Figure S3. Photographs of (A) nEu-bdc@agar and (B) nEu-bdc@gelatine (both with 5wt.% nEu-bdc) starting with the freshly synthesized bio-nMOF-MMM and continuing through each subsequent recycling step. Imaging was conducted under both daylight and UV light (302 nm), focusing on circular cutouts.

5 Powder X-Ray Diffraction (PXRD)

5.1 Result of the decomposition of nEu-bdc during DTA/TG-MS analysis

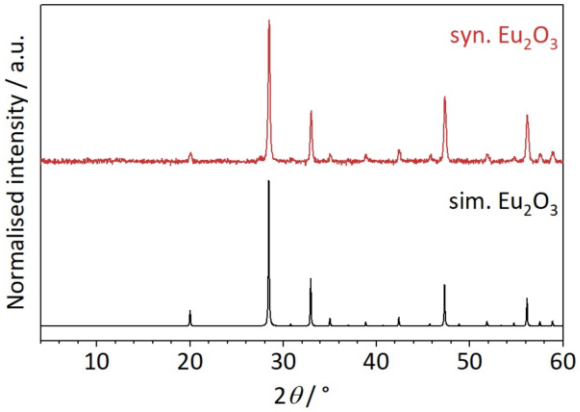

Figure S4. Diffractograms of the synthesized Eu_2O_3 during DTA/TG-MS analysis by decomposition of nEu-bdc and the simulated diffractogram of single crystal data[1] of Eu_2O_3.

5.2 Bio-nMOF-MMMs nEu-bdc@agar and nEu-bdc@gelatine with 5wt.% nEu-bdc

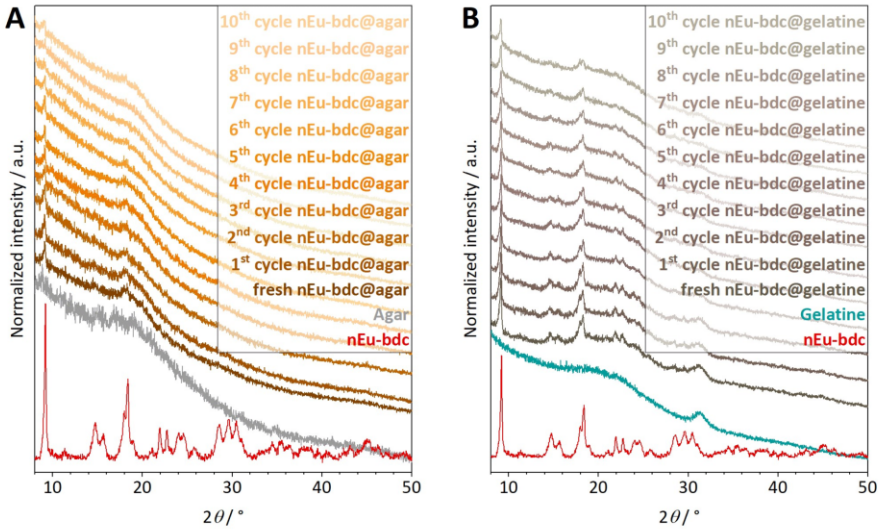

Figure S5. Powder patterns of (A) nEu-bdc@agar and (B) nEu-bdc@gelatine with 5wt.% nEu-bdc, the pure biopolymers agar and gelatine as well as the pure nMOF nEu-bdc prior to inserting into the biopolymer.

Supporting Information

6 Photoluminescence Spectroscopy (PL)

6.1 Excitation and Emission spectra of nEu-bdc at 77 K

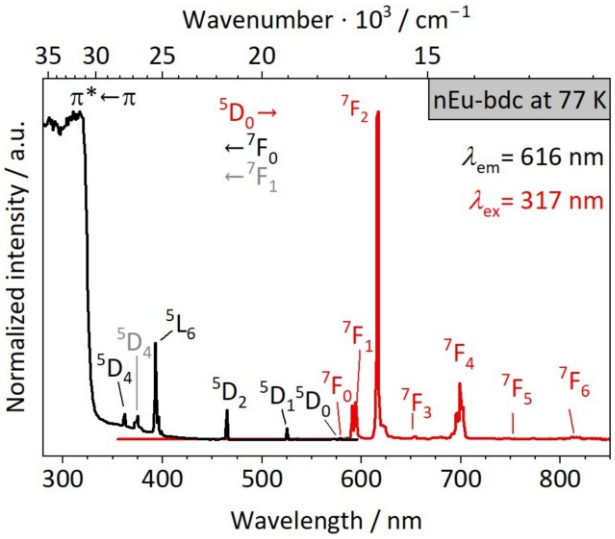

Figure S6. Normalized photoluminescence excitation (black) and emission (red) spectra of nEu-bdc at 77 K. The observed transitions are denoted with the respective term symbols.

6.2 Excitation and emission spectra of nEu-bdc@biopolymer with 5wt.% nEu-bdc

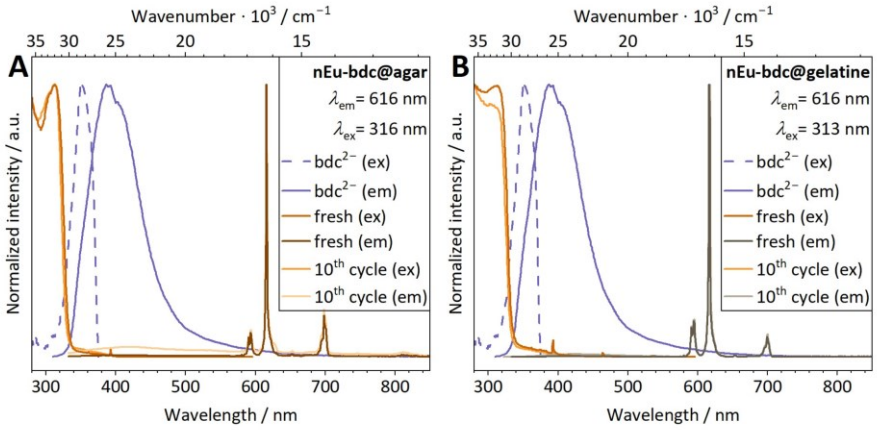

Figure S7. Normalized excitation (ex) and emission (em) spectra were obtained for (A) nEu-bdc@agar and (B) nEu-bdc@gelatine, both containing 5wt.% nEu-bdc. The freshly synthesized nEu-bdc@biopolymer and the sample from the 10th recycling cycle represent the initial and final bio-nMOF-MMM in a ten-cycle high-quality recycling cycle. The linker bdc^{2-} is also given for the evaluation of the stability of nEu-bdc (λ_{ex}= 350 nm, λ_{em}= 395 nm).

Supporting Information

6.3 Excitation and emission spectra of pure biopolymers agar and gelatine

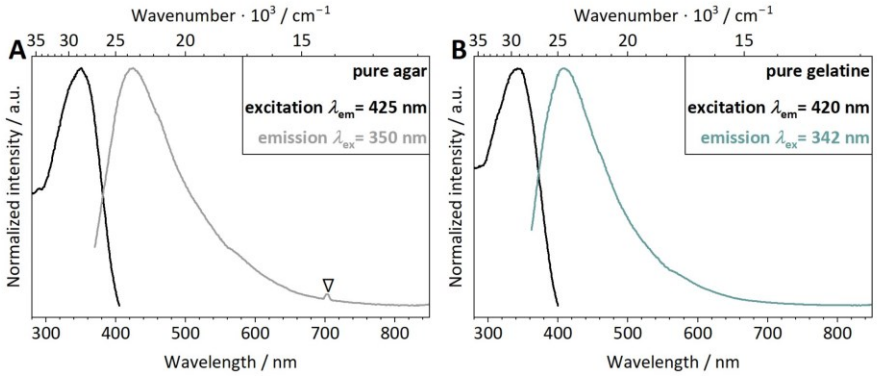

Figure S8. Normalized excitation and emission spectra of pure agar (A) and gelatine (B). ∇ in the emission spectrum of agar marks an artifact derived from the second-order diffraction of the source lamp.

Supporting Information

7 Scanning Electron Microscopy (SEM) + Energy-dispersive X-Ray Spectroscopy (EDS)

7.1 SEM and elemental mappings of bio-nMOF-MMMs nEu-bdc@agar and nEu-bdc@gelatine with 5wt.% nEu-bdc

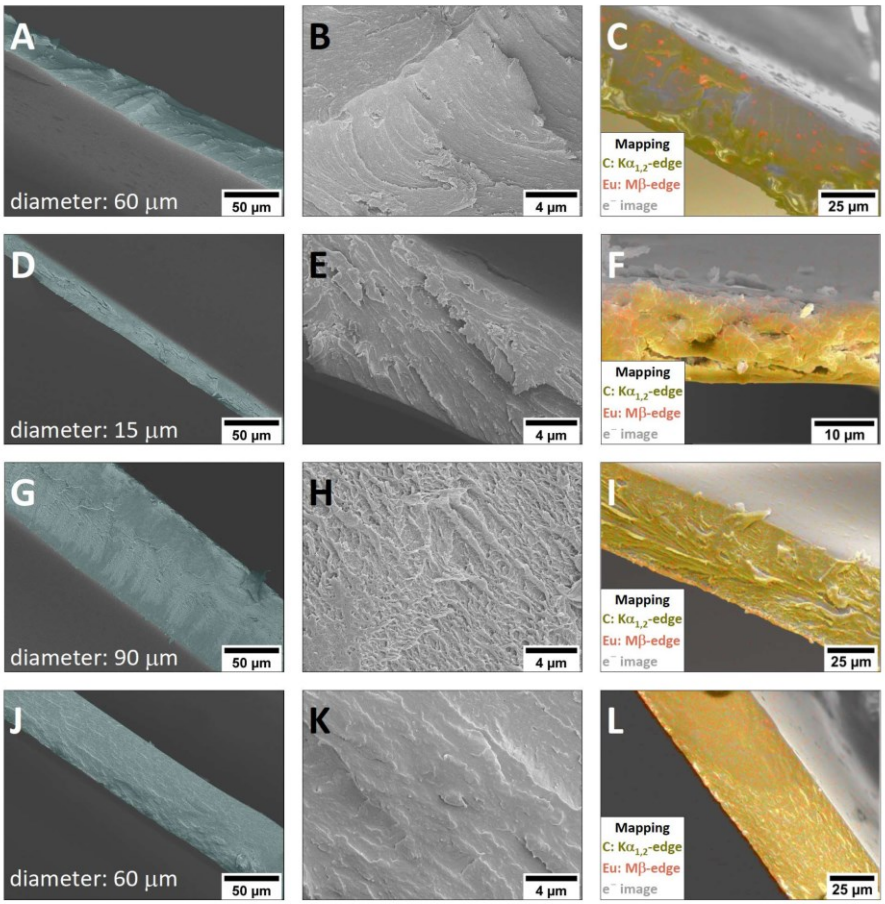

Figure S9. SEM images and elemental mappings (carbon: yellow, europium: red) of fresh nEu-bdc@agar (A, B, C), 10th cycle nEu-bdc@agar (D, E, F), fresh nEu-bdc@gelatine (G, H, I), 10th cycle nEu-bdc@gelatine (J, K, L) with each 5wt.% nEu-bdc at different magnifications. Cross-sections are highlighted in blue for clarity with denoted cross-section diameter.

7.2 SEM of pure agar freeze-dried cryogel

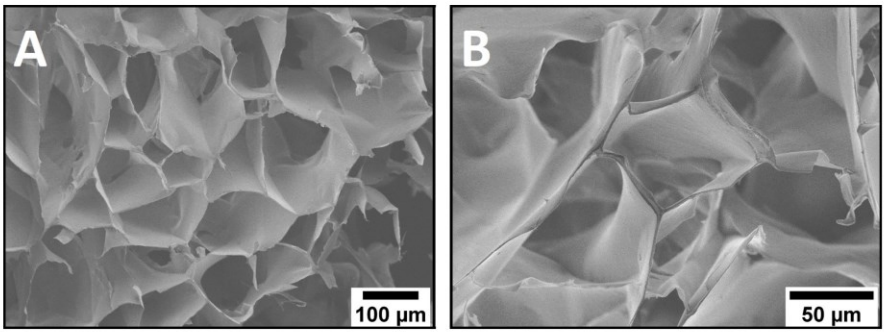

Figure S10. SEM images of pure agar as freeze-dried agar at larger scale (A) and lower scale (B).

Supporting Information

8 UV-Vis Absorption Spectroscopy

8.1 Absorption spectra of pure biopolymers agar and gelatine

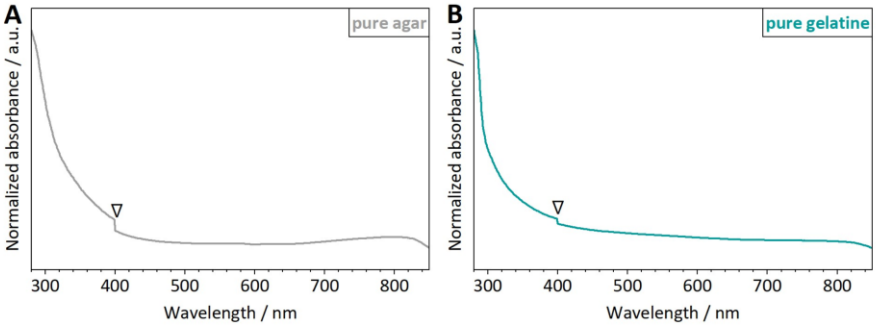

Figure S11. UV-Vis absorption spectra of pure agar (A) and pure gelatine (B). A systematic artifact (∇) is observable and is attributed to the light source change of the instrument.

8.2 Absorption spectra of fresh nEu-bdc@biopolymers and ten times cycled nEu-bdc@biopolymers

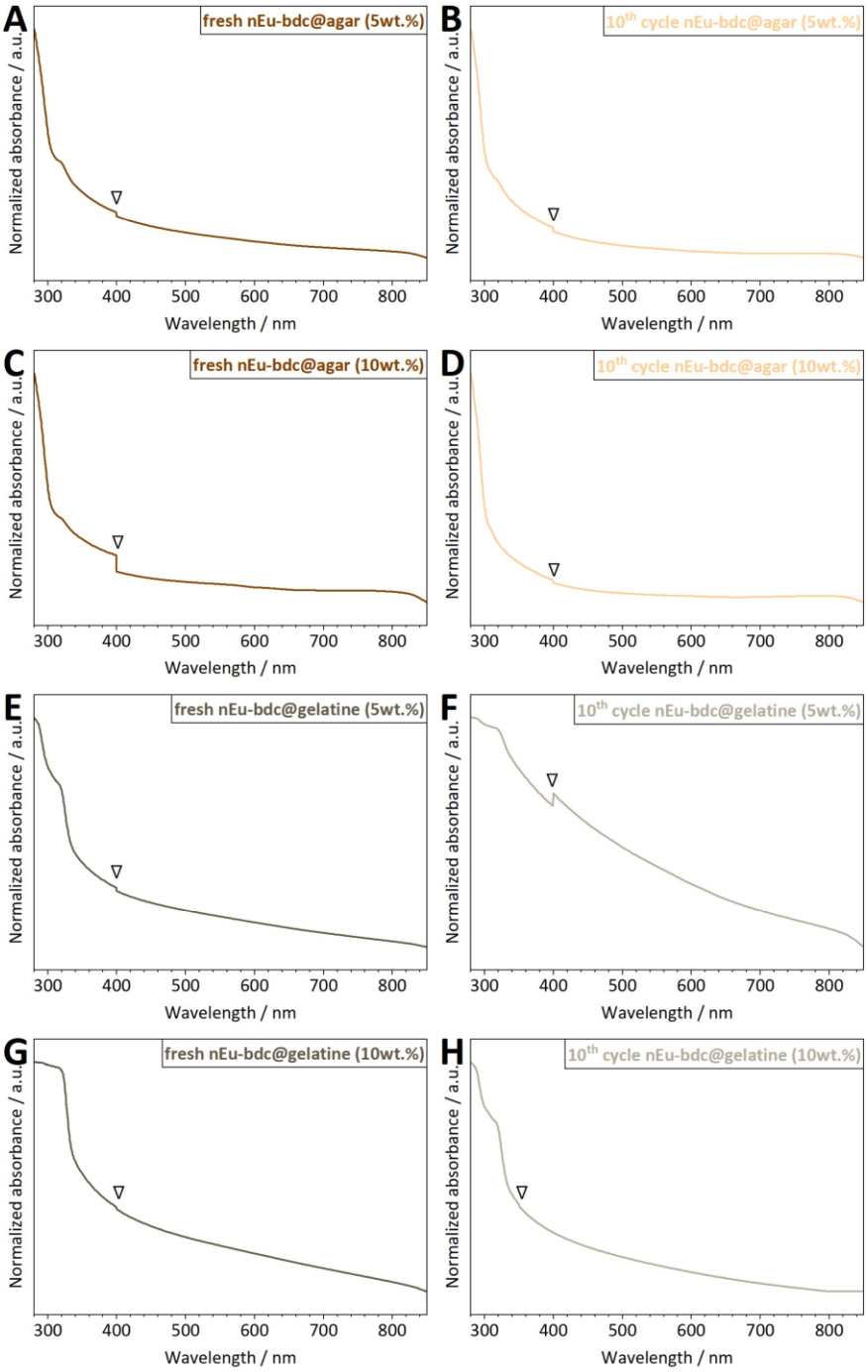

Figure S12. UV-Vis absorption spectra of investigated nEu-bdc@biopolymers. Spectra of nEu-bdc@biopolymer with 5wt.% nEu-bdc: (A) fresh nEu-bdc@agar, (B) 10th cycle nEu-bdc@agar, (C) fresh nEu-bdc@gelatine and (D) 10th cycle nEu-bdc@gelatine. Spectra of nEu-bdc@biopolymer with 10wt.% nEu-bdc: (E) fresh nEu-bdc@agar, (F) 10th cycle nEu-bdc@agar, (G) fresh nEu-bdc@gelatine and (H) 10th cycle nEu-bdc@gelatine. A systematic artifact (∇) is observable and is attributed to the light source change of the instrument.

Supporting Information

9 Characteristics of controlled artificial seawater

Table S2. List of artificial seawater properties as well as salt suppliers provided by the *Marine Holobiomics Lab*, JLU Giessen.

Salt	
Tropic Marine "Classic"	*Tropic Marin*, Wartenberg, Germany
Deep Blue	*Aquaperfekt*, Bergheim, Germany
Reef Salt	*Aquaforest*, Breszko, Poland
Ion concentration (selected)	
Ca^{2+}	416 mg · L^{-1}
Mg^{2+}	1300 mg · L^{-1}
Salinity	35‰
O_2 saturation	100% (saturated)
pH (at *T* °C)	8.12 (at 22.1 °C)
Alkalinity	
°dH	7.7
Total hardness	2.75 meq · L^{-1}
Carbonate hardness	137.68 mg · L^{-1}

10 Luminescence decay analysis of nEu-bdc, nEu-bdc@agar and nEu-bdc@gelatine

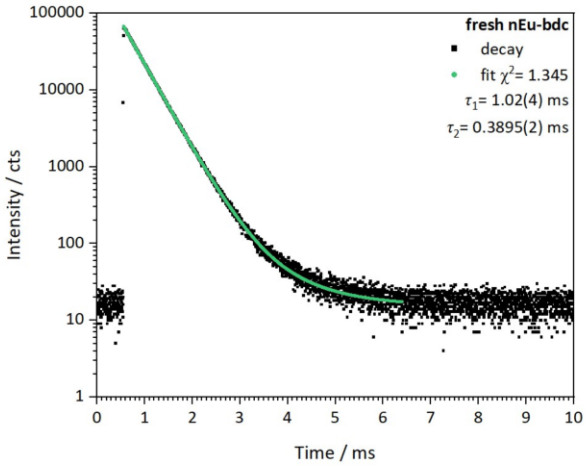

Figure S13. Luminescence decay measurement of fresh nEu-bdc with λ_{ex}= 288 nm and λ_{em}= 617 nm.

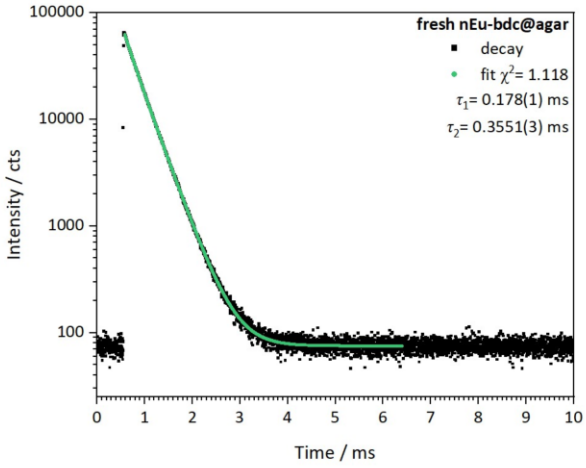

Figure S14. Luminescence decay measurement of fresh nEu-bdc@agar with λ_{ex}= 316 nm and λ_{em}= 616 nm.

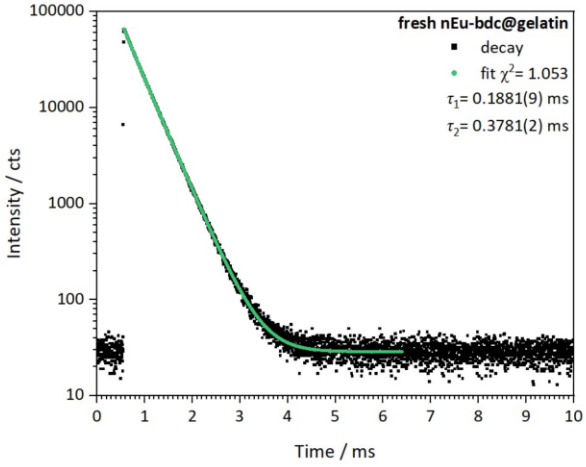

Figure S15. Luminescence decay measurement of fresh nEu-bdc@gelatine with λ_{ex}= 316 nm and λ_{em}= 616 nm.

Supporting Information

11 Physisorption - BET (Brunauer–Emmett–Teller) analysis of nEu-bdc

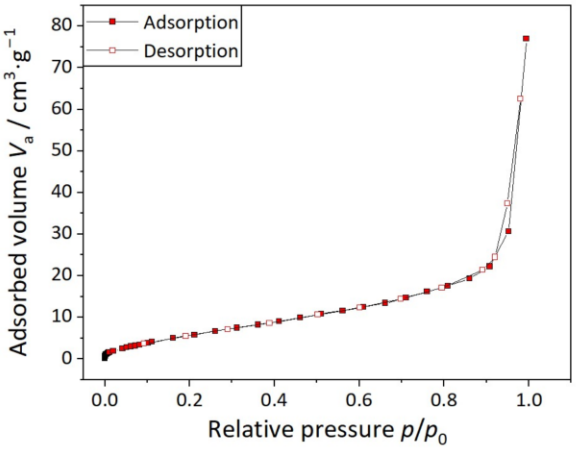

Figure S16. N_2 sorption isotherm of nEu-bdc.

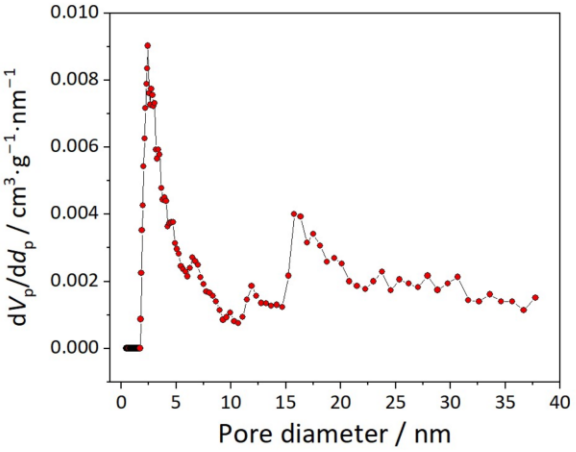

Figure S17. Pore size distribution of nEu-bdc.

Table S3. Pore system characteristics of nEu-bdc obtained from N_2 sorption analysis.

Specific surface area	24.6 m^2 g^{-1}
Average pore radius	3.9 nm
Total pore volume (for pores <1.8 nm, given for p/p$_0$= 0.95192)	4.7·10^{-2} cm^3 g^{-1}

12 References

[1] A. Saiki, N. Ishizawa, N. Mizutani, M. Kato, *J. Ceram. Assoc.* **1985**, *93*, 649.

8 Appendix B

8.1 List of abbreviations

AP	Anthropogenic polymers
BET	Brunauer-Emmett-Teller
C.N.	Coordination number
COF	Covalent organic framework
CP	Coordination polymer
DLS	Dynamic light scattering
DMF	Dimethyl formaldehyde
DTA/TG-MS	Differential thermal analysis/thermogravimetry-mass spectrometry
DUT	Dresden University of Technology
ED	Electric dipole
EDS	Energy-dispersive X-ray spectroscopy
EIS	Electrochemical impedance spectroscopy
EQ	Electric quadrupole
HKUST	Hong Kong University of Science and Technology
HQ	High-quality
HSAB	Hard and soft acids and bases
IBU	Inorganic building unit
IED	Induced electric dipole
IUPAC	International Union of Pure and Applied Chemistry
Ln	Lanthanide
MD	Magnetic dipole
MIL	Matériaux de l'Institut Lavoisier
MMM	Mixed matrix membrane
MP-AES	Microwave-induced plasma atomic emission spectroscopy
n(ano)MOF	Nanoscale metal-organic framework
NIR	Near-infrared
NPC	Nanoporous carbons
PL	Photoluminescence
PLQY	Photoluminescence quantum yield
REE	Rare earth elements

SEM	Scanning electron microscopy
UN	United Nations
UV	Ultraviolet
Vis	Visible
ZIF	Zeolitic imidazolate framework

8.2 List of chemical substances

Agar Agarose (polysaccharide)

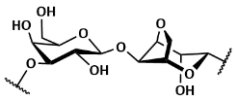

Agaropectin (polysaccharide)

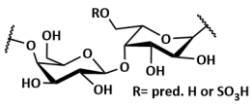

BDC^{2-} Benzene-1,4-dicarboxylate

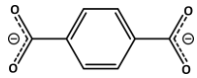

$BPDC^{2-}$ 1,1'-biphenyl-4,4'-dicarboxylate

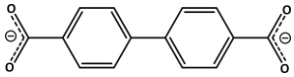

$BPyDC^{2-}$ 2,2'-bipyridine-5,5'-dicarboxylate

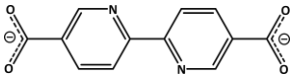

BTC^{3-} Benzene-1,3,5-tricarboxylate

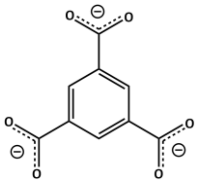

CTAB Cetyltrimethylammonium bromide

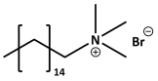

FDC^{2-} Ferrocenyl dicarboxylate

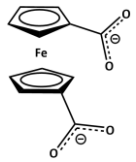

Gelatine Hydrolysed collagen (polypeptide)

Ala-Gly-Pro-Arg-Gly-Glu-4Hyp-Gly-Pro

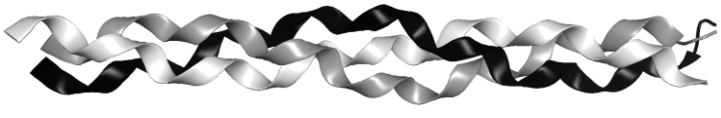

HL^{3-}	5,5’-(pyridine-2,5-diyl)-diisophthalate	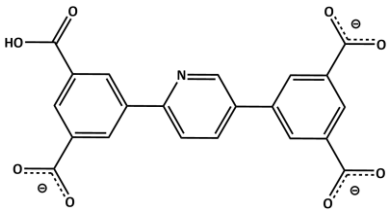
IM^{-}	Imidazolate	
PI	Polyimide	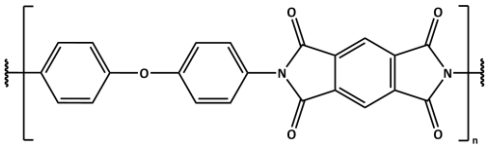
PSS	Polystyrene sulfonate	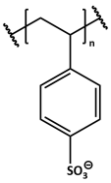
pRF	Pyrolyzed resorcinol-formaldehyde	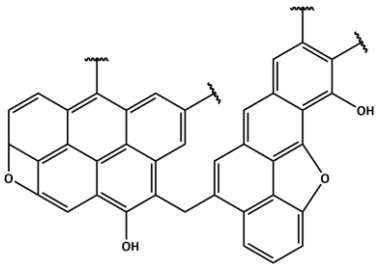
PSUd	Polysulfone (Udel® P-3500)	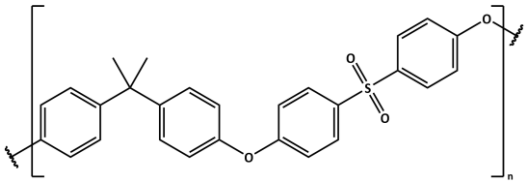
PVDF	Polyvinylidene fluoride	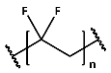
PVP	Polyvinyl pyrrolidone	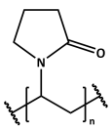

9 Appendix C

9.1 Awards

(1) **Poster award** (Titel: "Control of Photophysical and Morphological Properties of Luminescent, Nanoscale MOFs via a Surfactant-assisted Bottom-Up Synthesis Route") awarded by the **GDCh-division of solid-state chemistry and materials research**, *GDCh Science Forum Chemistry*, Leipzig (DE), **2023**.

9.2 Publication record

Lead authorship

(1) **M. Maxeiner**, J. Burkhart, K. Borysova, C. Mazzariol, K. Müller-Buschbaum "Biodegradable and Recyclable Luminescent Mixed-Matrix-Membranes, Hydrogels, and Cryogels based on Nanoscale Metal-Organic Frameworks and Biopolymers" *Adv. Funct. Mater.* **2025**, 2506570.

(2) **M. Maxeiner**, R. Maile, M. Cuvalli, A. Wolf, A. Komal, R. Oestreich, C. Janiak, K. Mandel, A. Knebel, K. Müller-Buschbaum "NanoMOF-based Multi-Level Anti-Counterfeiting by a Combination of Visible and Invisible Photoluminescence and Conductivity" *Adv. Funct. Mater.* **2025**, 2500794.

(3) **M. Maxeiner**, L. Wittig, A. E. Sedykh, T. Kasper, K. Müller-Buschbaum "Nano *vs.* bulk: surfactant-controlled photophysical and morphological features of luminescent lanthanide MOFs" *J. Mater. Chem. A* **2023**, *11*, 22478–22491.

Co-authorship

(4) J. Burkhart, L. Bemfert, E. Mitura, **M. Maxeiner**, R. Maile, A. Sedykh, K. Müller-Buschbaum "Tellurium Recovery from the Thermoelectric Materials Bismuth Telluride and Antimony Telluride by Chemical Vapour Transport" *Green Chem.* **2025**, DOI: 10.1039/D5GC00108K.

(5) A. E. Sedykh, **M. Maxeiner**, M. T. Seuffert, D. Heuler, D. G. Kurth, K. Müller-Buschbaum "Enhancing the Analysis of Eu^{3+} Photoluminescence in Coordination Compounds in the Solid State by Determining their Refractive Index" *Eur. J. Inorg. Chem.* **2024**, e202400078.

(6) L. H. Bemfert, J. Burkhart, A. E. Sedykh, S. Richter, E. L. Mitura, **M. Maxeiner**, G. Sextl, K. Müller-Buschbaum "Combinatorial Separation of Cd and Te from CdTe via Chemical Vapour Transport with Sulfur and Air/Methane Treatment for the Recovery of Critical Resources from Thin Film Solar Cells" *ChemSusChem* **2024**, e202400785.

(7) A.E. Sedykh, M. Becker, M. T. Seuffert, D. Heuler, **M. Maxeiner**, D. G. Kurth, C. E. Housecroft, E. C. Constable, K. Müller-Buschbaum "Air-Stable Solid-State Photoluminescence Standards for Quantitative Measurements Based on 4'-Phenyl-2,2' : 6',2''-Terpyridine Complexes with Trivalent Lanthanides" *ChemPhotoChem* **2023**, *7*, e202200244.

(8) M. A. Zhernakov, A. E. Sedykh, J. Becker, **M. Maxeiner**, K. Müller-Buschbaum, V. G. Shtyrlin "Three ytterbium(III) complexes with aromatic N-donors: Synthesis, structure, photophysical properties and thermal stability" *Z. Anorg. Allg. Chem.* **2022**, *648*, e202200230.

9.3 Conference contributions

(1) **Poster presentation** (Titel: "Nano *vs.* Bulk: Surfactant-controlled Photophysical and Morphological Features of Luminescent Lanthanide MOFs"), *26th JCF Spring Symposium*, Ulm (DE), **2024**.

(2) **Poster presentation** (Titel: "Control of Photophysical and Morphological Properties of Luminescent, Nanoscale MOFs via a Surfactant-assisted Bottom-Up Synthesis Route"), *GDCh Science Forum Chemistry*, Leipzig (DE), **2023**.

(3) **Poster presentation** (Titel: "Impact of Surfactant-Assisted Downsizing to Luminescent nanoMOFs on Morphological and Photophysical Properties"), *18th European Conference on Solid State Chemistry*, Prague (CZ), **2023**.